

THE UNIVERSITY OF SHEFFIELD



# **Oxide Ion Conduction in A-site Bi-containing Perovskite-type Ceramics**

By

Linhao Li

A thesis submitted for the degree of Doctor of Philosophy

Supervisors: Prof. D. C. Sinclair

Prof. Anthony R. West

Department of Material Science and Engineering

Faculty of Engineering

November 2016

## Publications from this thesis:

1. Li, L., Li, M., Zhang, H., Reaney, I. M. & Sinclair, D. C. Controlling mixed conductivity in  $\text{Na}_{1/2}\text{Bi}_{1/2}\text{TiO}_3$  using A-site non-stoichiometry and Nb-donor doping. *J. Mater. Chem. C* **4**, 5779–5786 (2016).
2. Li, M., Li, L., Zang, J. & Sinclair, D. C. Donor-doping and reduced leakage current in Nb-doped  $\text{Na}_{0.5}\text{Bi}_{0.5}\text{TiO}_3$ . *Appl. Phys. Lett.* **106**, 102904 (2015).
3. Li, M., Zhang, H., Cook, S. N., Li, L., Kilner, J. A., Reaney, I. M. & Sinclair, D. C. Dramatic Influence of A-Site Nonstoichiometry on the Electrical Conductivity and Conduction Mechanisms in the Perovskite Oxide  $\text{Na}_{0.5}\text{Bi}_{0.5}\text{TiO}_3$ . *Chem. Mater.* **27**, 629–634 (2015).
4. Yang, F., Zhang, H., Li, L., Reaney, I. M. & Sinclair, D. C. High Ionic Conductivity with Low Degradation in A-Site Strontium-Doped Nonstoichiometric Sodium Bismuth Titanate Perovskite. *Chem. Mater.* **28**, 5269–5273 (2016).

# Acknowledgments

I would like to take this opportunity to express my sincerest gratitude to my Ph.D. research supervisor, Prof. Derek C. Sinclair, for his guidance, invaluable support, and encouragement during the project. I benefited from his profound insight, experience, and scientific thinking.

I would like to thank Prof. Anthony R. West and Prof. Ian M. Reaney for their guidance throughout this project. I would also like to thank Dr. Ming Li for his continuous support and suggestions throughout this project.

Thanks to Dr. Huairuo Zhang (for performing the Electron Diffraction and Transmission Electron Microscopy), Dr. Roger A. De Souza (for performing O<sup>18</sup> Time-of-Flight Secondary Ion Mass Spectrometry), Dr. Fan Yang, Dr. Denis Cumming, Dr. Le Ma, Dr. Peng Zeng, Mr. Andrew Mould, Dr. Yang Liu, Mr. Patrick Wu and Dr. Zhilun Lu for their help and useful discussions. I also would like to thank all members in the functional ceramic group for their help throughout the last four year.

I would like to thank my parents, my parents in law, and my wife. I would never have finished this study without their encouragement and support.

# Abstract

Oxide ion conductors have drawn significant attention due to their important technical applications in electrochemical devices. This project is based on a new oxide ion conductor  $\text{Na}_{0.5}\text{Bi}_{0.5}\text{TiO}_3$  (NBT) which indicates (undoped) conducting NBT is a potential electrolyte material that possesses a high level of nearly pure oxide ion conduction.

Na non-stoichiometry in the starting composition (Na-series), acceptor doping ( $\text{Mg}^{2+} \rightarrow \text{Ti}^{4+}$ ,  $\text{Na}_{0.5}\text{Bi}_{0.5}\text{Ti}_{1-x}\text{Mg}_x\text{O}_{3-x}$ ) and donor doping ( $\text{Nb}^{5+} \rightarrow \text{Ti}^{4+}$ ,  $\text{Na}_{0.5}\text{Bi}_{0.5}\text{Ti}_{1-x}\text{Nb}_x\text{O}_{3+x/2}$ ) in NBT have been investigated. It has been shown that similar to a previously reported Bi non-stoichiometric series (Bi-series), the electrical properties of NBT are highly sensitive to low levels of Na non-stoichiometry. However, the defect mechanisms for Na and Bi non-stoichiometry are different and leads to a contrasting influence on the properties of NBT ceramics. Na-rich samples from the Na-series behave like Bi-deficient samples from the Bi-series whereas Na-deficient samples from the Na-series behave like Bi-rich samples from the Bi-series. Generally speaking, the bulk conductivity (oxide ion conduction) of NBT is dependent on the Na/Bi ratio in the nominal starting composition. Samples with a Na/Bi ratio  $\geq 1$  exhibit high, nearly pure oxygen ion conduction with a low activation energy ( $< 0.9$  eV) for bulk conduction whereas samples with a Na/Bi ratio  $< 1$  are electronic insulators with a high activation energy ( $\sim 1.6$  eV) for bulk conduction.

Mg B-site acceptor doping,  $(\text{Na,Bi})\text{Ti}_{1-x}\text{Mg}_x\text{O}_{3-x}$ , can further enhance the bulk conductivity and produces oxide ion transport numbers,  $t_{\text{ion}}$ , close to unity. This doping also stabilises NBT ceramics to reducing atmospheres (eg 5% $\text{H}_2$ /95% $\text{N}_2$  at 500 °C) to demonstrate their potential as an electrolyte material for Intermediate Temperature Solid Oxide Fuel Cells. In contrast, Nb donor doping,  $(\text{Na,Bi})\text{Ti}_{1-x}\text{Nb}_x\text{O}_{3+x/2}$ , systematically suppresses the oxide-ion conductivity; very low levels of Nb doping

(0.002 ~ 0.003) leads to a mixed oxide ion and n-type conduction and an intermediate  $t_{ion}$  (~ 0.5). A further increase of Nb doping level ( $\geq 0.005$ ) suppresses the oxide ion conduction and results in dielectric materials with predominant n-type electronic bulk conduction with  $t_{ion} \leq 0.07$  at elevated temperature (eg  $> 600$  °C). It is worth noting that, extremely Bi-rich (undoped) NBT ( $Bi \geq 0.52$ ) also induces mixed ionic/electronic behaviour by reintroducing higher oxide-ion conductivity with  $t_{ion} \sim 0.4-0.6$ .

The ferroelectric Aurivillius phase  $Bi_4Ti_3O_{12}$  (BiT) has also been determined to exhibit high levels of oxide ion conduction. Un-doped BiT shows mixed p-type and oxide ion conduction at low temperature; however,  $t_{ion}$  approaches near unity close to the Curie Temperature,  $T_C \sim 675$  °C. As BiT contains both extrinsic and intrinsic defects, the Bi nonstoichiometry has limited influence on its electrical properties. Isovalent doping ( $La^{3+} \rightarrow Bi^{3+}$ ;  $Bi_{4-x}La_xTi_3O_{12}$ ) acceptor doping ( $Sr^{2+} \rightarrow Bi^{3+}$ ;  $Bi_{4-x}Sr_xTi_3O_{12-x/2}$ ) and donor doping ( $Nb^{5+} \rightarrow Ti^{4+}$ ;  $Bi_4Ti_{3-x}Nb_xO_{12+x/2}$ ) are all investigated. La-doping ( $x \leq 2$ ) can shift  $T_C$  to lower temperature and makes BiT a potentially good oxygen ion conductor at  $\sim 600$  °C, but the bulk conductivity gradually reduces with increasing  $x$ . Sr-doping has a rather limited solid solution limit ( $x \leq 0.12$ ) compared to La doping but can maintain the bulk conductivity while lowering the  $T_C$ . Nb donor doping on Ti-site can compensate oxygen vacancies and suppress the oxide ion conduction.

$K_{0.5}Bi_{0.5}TiO_3$  (KBT) has been determined to be a mixed conductor where the ionic contribution can be oxide ions and/or protons. The proton conduction in KBT is controlled by the K/Bi ratio in the nominal starting composition. Samples with a starting K/Bi ratio  $> 1$  exhibit substantial proton conductivity whereas samples with a starting K/Bi ratio  $\leq 1$  exhibit lower proton conduction. Compared to NBT, the oxide ion conduction in KBT is significantly lower and relatively independent of the starting A-site non-stoichiometry.

# Introduction

In the past decades, oxide ion conductors have drawn significant interest due to their important technical applications in electrochemical devices such as solid-oxide fuel cells (SOFCs), oxygen separation membranes and oxygen sensors.<sup>1,2</sup> Taking SOFCs as an example, it is an energy generating device which fits the development strategy of sustainable energy and environmental protection. Compared with traditional combustion engines, the advantages of SOFCs include high efficiency, long-term stability, fuel flexibility, low emissions and relatively low cost. On the other hand, the main drawback for SOFCs is the high operating temperature which leads to issues of mechanical compatibility and chemical stability.<sup>3</sup> In order to overcome these disadvantages and enhance device efficiency, new materials with higher oxide ion conduction and better stability are required for SOFCs and most other oxide ion conductor related devices. The main aim for this project is therefore to discover new materials to fulfil such a requirement.

In 2014 our group reported that the electrical properties of a well known piezoelectric material  $\text{Na}_{1/2}\text{Bi}_{1/2}\text{TiO}_3$  (NBT) are highly sensitive to low levels of A-site non-stoichiometry that can lead to two different types of electrical behaviour.<sup>4</sup> It can either be an oxygen ion conductor with a low activation energy for bulk conduction or an electronic insulator with a high activation energy for bulk conduction. The difference in conductivity between these two kinds of NBTs can be more than 3 orders of magnitude. It is worth to note that conducting NBT exhibits a high level of nearly pure oxide ion conduction and is therefore a potential solid electrolyte. In addition, a low level of acceptor-type Mg doping on the Ti-site gives NBT good chemical stability against reduction that can tolerate a low  $\text{pO}_2$  at intermediate temperatures such as 5% $\text{H}_2$ /95% $\text{N}_2$  at 600 °C. With all of these properties, NBT has the promising prospect of being used as an electrolyte material in the above mentioned electrochemical

devices.

This project is based on an initial finding reported by our group<sup>4</sup> and starts with a more extensive study of the level and type of non-stoichiometry in undoped NBT before investigating acceptor- and donor-type doping to modify the electrical properties to either optimise the oxide ion conductivity for electrolyte applications or to suppress the ionic conduction for dielectric applications. Subsequently, two perovskite-related, Bi-containing phases  $\text{Bi}_4\text{Ti}_3\text{O}_{12}$  and  $\text{K}_{0.5}\text{Bi}_{0.5}\text{TiO}_3$  were investigated to establish if oxide-ion conduction was also present in these materials, and to establish if acceptor- and donor-doping mechanisms had a similar influence in fine-tuning their electrical properties.

## References

1. Steele, B. & Heinzel, A. Materials for fuel-cell technologies. *Nature* **414**, 345–352 (2001).
2. Wachsman, E. D. & Lee, K. T. Lowering the Temperature of Solid Oxide Fuel Cells. *Science*. **334**, 935–939 (2011).
3. Singhal, S. C. & Kendall, K. *High-temperature solid oxide fuel cells: fundamentals, design and applications*. (Elsevier, 2003).
4. Li, M. *et al.* A family of oxide ion conductors based on the ferroelectric perovskite  $\text{Na}_{0.5}\text{Bi}_{0.5}\text{TiO}_3$ . *Nat. Mater.* **13**, 31–5 (2014).

# Contents

Chapter 1.	Literature review .....	1
1.1	Perovskites .....	1
1.2	Oxygen ion conductors .....	3
1.3	$\text{Na}_{0.5}\text{Bi}_{0.5}\text{TiO}_3$ .....	5
1.4	$\text{K}_{0.5}\text{Bi}_{0.5}\text{TiO}_3$ .....	14
1.5	$\text{Bi}_4\text{Ti}_3\text{O}_{12}$ .....	18
1.6	Motivation and aim of this study .....	29
1.7	References.....	30
Chapter 2.	Experimental procedures .....	49
2.1	Fabrication of ceramics .....	49
2.2	Ceramic density.....	50
2.3	X-Ray diffraction.....	51
2.4	Scanning electron microscopy (SEM).....	51
2.5	Transmission electron microscopy (TEM) .....	52
2.6	Thermogravimetric analysis (TGA) .....	52
2.7	Differential scanning calorimetry (DSC) .....	53
2.8	Inductance-capacitance-resistance (LCR) Meter .....	53
2.9	Impedance spectroscopy .....	54
2.10	Piezoelectric property measurements.....	58
2.11	Oxygen ion transport number measurements .....	59
2.12	$^{18}\text{O}$ tracer diffusion coefficient measurements with time-of-flight secondary ion mass spectrometry (ToF-SIMS).....	61
2.13	Reference .....	62
Chapter 3.	Non-stoichiometry in the perovskite phase ' $\text{Na}_{0.5}\text{Bi}_{0.5}\text{TiO}_3$ ' .....	63
3.1	Bi non-stoichiometry.....	66
3.2	Na non-stoichiometry .....	78
3.3	The influence of drying reagents .....	84
3.4	Discussion.....	86
3.5	Conclusions .....	93
3.6	References.....	95
Chapter 4.	Doped NBT .....	97
4.1	Donor doping .....	99
4.2	Acceptor doping.....	107
4.3	Discussion.....	113
4.4	Conclusions .....	116
4.5	References.....	117
Chapter 5.	Fast oxide ion conduction in $\text{Bi}_4\text{Ti}_3\text{O}_{12}$ .....	118
5.1	Bismuth non-stoichiometry .....	119

5.2	Discussion.....	140
5.3	Conclusions .....	145
5.4	References.....	146
Chapter 6.	Chemical doping of $\text{Bi}_4\text{Ti}_3\text{O}_{12}$ .....	148
6.1	Nb-doped BiT .....	148
6.2	La doped BiT.....	156
6.3	Sr-doping.....	164
6.4	Discussion.....	171
6.5	Conclusions .....	177
6.6	References.....	177
Chapter 7.	Non-stoichiometry in the perovskite phase ' $\text{K}_{0.5}\text{Bi}_{0.5}\text{TiO}_3$ ' .....	180
7.1	Phase purity and microstructure .....	181
7.2	Electrical properties .....	189
7.3	Ionic conduction in KBT.....	200
7.4	Discussion.....	208
7.5	Conclusions .....	212
7.6	References.....	212
Chapter 8.	General discussion .....	215
Chapter 9.	Conclusions .....	221
Chapter 10.	Future Work .....	224

# 1. Literature review

## 1.1. Perovskites

Perovskites are named after a Russian mineralogist Lev Perovski who discovered the first material with this structure, calcium titanium oxide ( $\text{CaTiO}_3$ ) in 1839. Now the term perovskite is used to describe a series of metal oxides and halides with the same crystal structure and a common formula  $\text{ABX}_3$  where A and B are cations and X is anion.<sup>1</sup> In the first perovskite  $\text{CaTiO}_3$ , A is a large divalent cation and B is a medium-sized tetravalent cation. However, A and B can adopt various charges or even multiple elements with different charge can be located on these sites. The large number of possible combinations leads to great flexibility and make perovskites a 'tool box' with a wide range of functional properties including dielectric materials such as piezoelectrics and ferroelectrics. From a conduction point of view, oxides with the perovskite structure cover a wide range of materials from insulators to superconductors and also ionic conductors and mixed ionic-electronic conductors.

The ideal perovskite structure is based on a simple cubic cell with the space group  $Pm\bar{3}m$  as shown in Figure 1-1. The larger A cation occupies the cubo-octahedral interstice site with a co-ordination number of 12 whereas the smaller B cation occupies an octahedral site with a co-ordination number of 6. In 1926 Goldschmidt proposed an equation to describe an ideal perovskite:

$$R_A + R_O = \sqrt{2}(R_B + R_O)$$

where  $R_A$ ,  $R_B$  and  $R_O$  are the ionic radii for the A cation, B cation and the anion, respectively.<sup>2</sup> However, only a very limited number of compounds meet this requirement. To allow for distortion, the tolerance factor,  $t$ , has been introduced and the equation is modified to

$$R_A + R_O = t\sqrt{2}(R_B + R_O)$$

The structure can be considered as an ideal perovskite if  $t = 1$  is fulfilled. If  $t \neq 1$ , the perovskite is distorted. This normally involves a tilting of the  $\text{BO}_6$  octahedra and/or a displacement of the A and/or B cations. If it deviates significantly from 1, then the perovskite structure becomes unstable and will not form. In most cases, the perovskite structure is generally stable if  $0.8 < t < 1.05$ .<sup>3</sup>

Figure 1-1. Cubic perovskite unit cell where blue spheres are A cations, the orange sphere is the B cation and red spheres are the anions.<sup>4</sup>

When a perovskite has  $t < 1$ , it often results in tilting of the octahedra and this lowers the crystal symmetry.<sup>5</sup> This tilting is because the A-site cations are too small to fully occupy the site and so the octahedra tilt to reduce the volume of the site. In many cases, this will lower the symmetry of the perovskite to an orthorhombic structure.<sup>6</sup> On the other hand,  $t > 1$  occurs when the B-site cation is too small to fully occupy the octahedral site. In this case, there are two possibilities; all B-site ions can displace in the same direction or adjacent ions displace in opposite directions. The former is named as parallel displacement and the latter as anti-parallel displacement. In the case of more than one cation co-occupying either the A or B-site, the structure will be dependent on the bond lengths and preferred bonding environment(s) of the cations.

## 1.1. Electrical conduction

Electrical conduction occurs when long range migration of electrically charged particles (charge carriers) takes place, normally via drift in an electric field. The particular migration mechanism depends on the type of charge carrier and the host material. Typically, only one charge carrier dominates the electrical conduction, e.g. an electron or a cation but in some cases mixed electronic and ionic conduction can

occur within a material. For any charge carrier, the conductivity  $\sigma$  is determined by the equation:

$$\sigma = nq\mu$$

where  $n$  is the number of charge carriers,  $q$  is the electrical charge (e.g.  $1.6 \times 10^{-19}$  C for electron) and  $\mu$  is the mobility. In the case of mixed conductors (i.e. multiple charge carriers), the total conductivity is the sum of all types of conduction present.

In solid materials, charge carriers can be separated into two groups, electronic and ionic charge carriers. The former includes the electron and the electron hole whereas the latter can either be cations or anions such as  $\text{Li}^+$ ,  $\text{Na}^+$  and  $\text{F}^-$ ,  $\text{O}^{2-}$ , respectively.

## 1.2. Oxygen ion conductors

Oxygen ion conductors are a class of oxides that exhibit oxygen ion conductivity. There has been continued interest in these materials because of their applications such as electrolytes in solid oxide fuel cells (SOFCs) and as oxygen separation membranes.<sup>7,8</sup> All these devices are aiming towards the creation of a sustainable and environmental friendly future.

In oxygen ion conductors, the predominate charge carriers are oxygen ions. A current flow occurs in an oxide ion conductor when the thermally activated hopping of oxygen ions are driven by an electric field. Such migration of oxygen ions is feasible when a) there are unoccupied sites equivalent to those occupied by the lattice oxygen ions (i.e. oxygen vacancies) and b) a relatively low energy barrier for the hopping process. The energy barrier for an oxide ion conductor is normally lower than 1 eV but still higher than most other conduction mechanisms. This suggests relatively high oxide ion conductivity can be achieved at high temperatures in many materials. The charge carrier concentration is strongly temperature dependent but can also be enhanced by acceptor dopants, e.g. yttria stabilised zirconia. Increasing the dopant

concentration results in more oxygen vacancies in the lattice and normally a higher conductivity. Initially these vacancies enhance the conductivity but when it reaches a certain concentration (relatively low in most cases), the aliovalent dopants will start to interact with the oxygen vacancies and 'trap' them from free movement. A further increase of dopant concentration will reduce the conductivity, as shown in Figure 1-2. For instance, the conductivity of acceptor-doped ceria solid solutions start to decrease when the dopant concentration reaches ~8 mole percent.<sup>9</sup> Computer modelling reveals such interactions are due to the elastic strain introduced by size mismatch of the dopant and host ions.<sup>10,11</sup> This explains why materials like Scandia-stabilised Zirconia and Gadolinium-doped Ceria where the dopant and host ions are of similar size exhibit the best properties as acceptor-doped oxygen ion conductors.

Fig. 4 in reference [9].

Figure 1-2. Isothermal conductivity of different acceptor-doped ceria solid solutions close to 200°C.<sup>9</sup>

To obtain a pure oxygen ion conductor (also known as a solid electrolyte), the contribution from any other conduction mechanisms such as electronic or proton conduction needs to be minimised. However, due to the high mobility of electrons and holes, a low electronic carrier concentration can lead to a significant electronic contribution to the total conductivity. Hence most oxide ion conductors are actually mixed conductors and only a small number of them can be referred to as pure oxide ion conductors, i.e. solid electrolytes. Nevertheless, both pure oxide ion conductors and mixed conductors have their applications. For example, in Solid Oxide Fuel Cells (SOFC's) the electrolyte is required to be a pure ionic conductor to prevent any electronic leakage whereas mixed conductors can be used as electrodes to provide pathways for both electronic and ionic conduction.<sup>12</sup> In addition, most applications of oxygen ion conductors rely on an oxygen partial pressure gradient. For instance, the anode of an SOFC operates in a reduced (fuel) atmosphere like H<sub>2</sub>. Under such

conditions many oxygen ion conductors will be reduced and introduce a higher level of electronic conduction, therefore from an applications point of view chemical stability is a critical property of oxide ion conductors.<sup>13</sup>

From a structural point of view, most oxygen ion conductors possess a fluorite- or perovskite-related structure.<sup>14</sup> The fluorite oxides are classic oxygen ion conductors which have been studied for several decades. Some oxides already form in the cubic fluorite structure at room temperature such as  $\text{CeO}_2$  and  $\text{ThO}_2$  whereas others (e.g.  $\text{ZrO}_2$ ) only form at higher temperatures or with dopants to stabilise the structure. For example, yttria-stabilised zirconia (YSZ) with a fluorite structure is now the standard electrolyte material to use in high temperature SOFCs and gadolinium-doped ceria (GDC) is a very promising candidates for intermediate temperature SOFCs which can operate at a temperature as low as 550 °C (Figure 1-3).<sup>15</sup>

From reference [18]

Figure 1-3. Temperature dependent conductivity of some well-known oxygen ion conductors.<sup>18</sup>

Perovskite is another structure-type that many oxygen ion conductors adopt. Perovskite oxides often have advantages at intermediate temperatures from 600 ~ 800 °C. Strontium and magnesium co-doped  $\text{LaGaO}_3$  (LSGM) exhibits superior performance compared to many fluorite oxides (Figure 1-3).<sup>16,17</sup> The conductivity of some of the most promising oxygen ion conductors is shown in Figure 1-3.

## 1.3. $\text{Na}_{0.5}\text{Bi}_{0.5}\text{TiO}_3$

### 1.3.1. Crystal structure

Sodium bismuth titanate,  $\text{Na}_{0.5}\text{Bi}_{0.5}\text{TiO}_3$  (NBT) adopts a Perovskite structure in which the A-site contains half Bi and half Na (Figure 1-4). The Na and Bi ions are randomly

distributed on the A-site. NBT is a promising lead-free piezoelectric material which exhibits both ferroelectric and piezoelectric properties. The crystal structure-electrical property relationships of NBT have attracted considerable attention; however, after decades of study, both the room temperature and high temperature crystal structure of NBT are still under debate as are the links with the electrical properties.

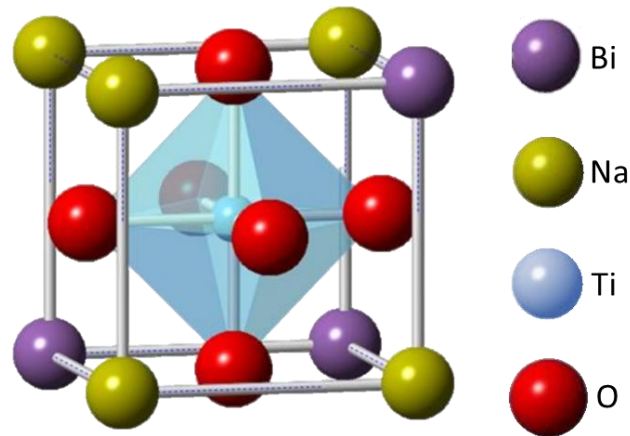


Figure 1-4. Schematic of NBT unit cell.<sup>33</sup>

Early XRD studies indicated NBT at room temperature exhibits rhombohedral<sup>19</sup> symmetry or as some authors referred to as pseudo-cubic<sup>20,21</sup> symmetry with a very small deviation from a cubic structure (e.g.  $\alpha = 89.83^\circ$ ).<sup>22</sup> Later studies suggested the space group for this rhombohedral structure is  $R3m$  without octahedral tilting.<sup>23,24</sup> However, a neutron diffraction study suggested the space group is actually  $R3c$  with  $a^-a^-a^-$  anti-phase octahedral tilting with a tilt angle of  $8.24^\circ$ .<sup>25</sup> This model has been widely accepted and adopted by many researchers.

On the other hand, Isuyov et al. performed temperature dependent birefringence and opalescence measurements on NBT single crystals and suggested the symmetry is actually lower than rhombohedral.<sup>26</sup> Furthermore, a high-pressure, x-ray scattering study indicated, at least on a local scale, some Bi ions move off the  $[111]$  axis and towards one of the  $[001]$  directions. Such displacements will effectively reduce the local symmetry to monoclinic while the overall symmetry may still remain

rhombohedral.<sup>27</sup> In addition, X-ray absorption fine structure (XAFS) data revealed variable Bi-O bond lengths with a minimum value of  $\sim 2.2 \text{ \AA}$ .<sup>28</sup> However, refinement of neutron diffraction data based on R3c symmetry only allows Bi-O bond lengths larger than  $\sim 2.5 \text{ \AA}$  which means Bi was in a under-bonded coordination environment.<sup>29</sup> High resolution XRD data from single crystals revealed peak splitting in reciprocal-space maps, suggesting the average structure of NBT is lower than rhombohedral and should be described more properly using a monoclinic space group Cc.<sup>22</sup> This model was later confirmed by high resolution powder XRD data on crushed powder of a sintered pellet.<sup>30</sup> The lattice parameters of the Cc model are similar to the R3c model but the octahedral tilting is  $a^-a^-c^-$  instead of  $a^-a^-a^-$ , which means the tilting angle is different in the z-direction compared to the other two directions. A multiphase model has also been considered with a combination of monoclinic (Cc) and cubic (Pm3m) phases giving the best fit to the diffraction data.<sup>31</sup>

TEM has also been employed to reveal local structural features in NBT. A TEM study on single crystals revealed an inhomogeneous distribution of nanometre-scale platelets with a few unit cells thick of a tetragonal phase with an  $a^0a^0c^+$  tilt system within a matrix of a rhombohedral  $a^-a^-a^-$  R3c phase.<sup>32,33</sup> The existence of these platelets lead to a lower matrix symmetry from R3c to Cc in powder diffraction refinements. Alternatively, the loss of symmetry can also be explained by a single-phase “continuous tilting” model where both in-phase ( $a^-a^-c^+$ ) and out-of-phase tilting ( $a^-a^-a^-$ ) are present.<sup>34</sup> However, the in-phase tilting only lasts a few unit cells long and is superimposed on an out-of-phase tilting matrix.

Another thing worth noting is the Na/Bi ordering. Na and Bi ions have similar radii thus the ordering of sodium and bismuth ions does not provide any gain in elastic energy, but on the other hand the charge difference between them ( $\text{Na}^+$  and  $\text{Bi}^{3+}$ ) should favour cation ordering. So far there is little evidence support long range Na/Bi

ordering, either experimentally or in computer simulations.<sup>35,36</sup> However, local or short range ordering has been observed in Raman spectroscopy data.<sup>34</sup>

In terms of phase transitions at elevated temperature, it is generally accepted that NBT exists as a cubic  $Pm\bar{3}m$  phase above  $\sim 520$  °C. On cooling, NBT undergoes a first order phase transition to a  $P4bm$  tetragonal phase with a weak but distinct peak on DSC measurements; however, such a phase transition does not introduce any obvious dielectric permittivity anomaly.<sup>37</sup> On the other hand, the phases that occur from room temperature to  $\sim 520$  °C remain controversial. Several early investigations have taken place but none have made a definitive structural determination. In 1995, Suchanicz and Kwapulinski first established a fundamental sequence of phase transitions by high temperature XRD in this temperature range. On cooling, NBT transforms from a cubic to tetragonal structure at 510-540 °C then to a rhombohedral structure at a temperature of  $\sim 260$  °C. It has been suggested that more than one phase may exist in certain temperature ranges (Figure 1-5).<sup>38</sup>

Figure 2 in reference [38]

Figure 1-5. Evolution of phase volumes with different symmetry versus temperature for NBT. <sup>38</sup> R = Rhombohedral, T = Tetragonal and C = Cubic.<sup>38</sup>

Most of the debates concerning the phase transition temperatures, the phase coexistence and electrical behaviour of NBT occur for the range between 200-320 °C. For example, relative permittivity,  $\epsilon_r$ , DSC <sup>37</sup> and electrostrictive strain  $x_{11}$ <sup>39</sup> all exhibit a maximum at  $\sim 320$  °C but X-ray and neutron diffraction data indicate no phase transition at this temperature.<sup>31,40</sup> Some early studies suggested there is a paraelectric – antiferroelectric - ferroelectric phase transition that occurs in this temperature range based on the double hysteresis loops observed around 150~240 °C and the loss of remanent polarization at  $\sim 220$  °C.<sup>37,41</sup> However, this hypothesis has not been supported by subsequent X-ray diffraction<sup>23</sup>, neutron scattering<sup>25</sup> and Raman

spectroscopy<sup>42</sup> studies. Later Vakhrushev proposed a new name for the state in this temperature range as a 'low temperature non-polar' (LTNP) phase with coexistence of tetragonal and rhombohedral symmetry.<sup>25</sup> This mixture contains rhombohedral clusters dispersed within a tetragonal matrix whose volume fraction increases as the temperature decreases, until the rhombohedral phase is stable.

High temperature in-situ TEM studies showed a phase transition sequence different from that reported using XRD or neutron diffraction. In the rhombohedral to tetragonal phase transition between 200-320 °C, an intermediate modulated phase was revealed which is an *Pnma* orthorhombic phase (as sheets) dispersed in the *R3c* matrix and exhibiting a (*a*<sup>-</sup>*a*<sup>+</sup>*a*<sup>-</sup>) tilting system.<sup>43,44</sup> Such a phase starts to appear slightly above 200 °C through a micro-twinning process and keeps growing with increasing temperature. At around 290~320 °C, the orthorhombic phase forms and almost immediately transforms into the tetragonal phase. Nevertheless, so far the existence of this orthorhombic *Pnma* phase has not been supported by any XRD or neutron diffraction studies.

In summary, structural and physical characterisation studies reveal four different phases occur during the whole temperature range. Five different phase/phase mixtures have been observed by TEM, electron diffraction and four different phase/phase mixtures by X-ray/neutron diffraction data (Figure 1-6). The complex crystal structure of NBT is caused by a combination of complex octahedral tilting, long range random with short range A-site cation ordering, co-existence of different phases as well as various defects that are extremely sensitive to the synthesis and processing conditions.

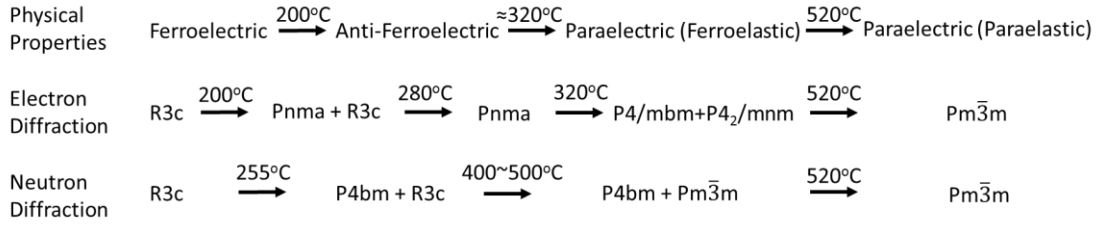


Figure 1-6. Reported phase transition routes based on physical properties, TEM and X-ray/neutron diffraction data.<sup>40,43-45</sup>

### 1.3.2. Electrical properties

As mentioned above, the relative permittivity,  $\epsilon_r$  of NBT undergoes a maximum at about 320 °C which is frequency independent. A hump on the  $\epsilon_r$  vs. T response has also been observed and suggested as an additional phase transition at ~200 °C.<sup>37,46</sup> Below 200 °C, there is a dielectric dispersion, the phase is determined to be ferroelectric according to Polarisation-Electric field (P-E) hysteresis loops (Figure 1-9 (a)). With a small amount of Sr-doping on the A-site, the NBT-SrTiO<sub>3</sub> solid solution shows typical, double P-E hysteresis loop behaviour in the temperature range between 150 and 240 °C (Figure 1-7).<sup>41</sup> Together with the disappearance of spontaneous polarisation (Figure 1-8) this phase transition was proposed as a ferroelectric-antiferroelectric transition.<sup>41</sup>

Figure 2 in reference [41]

Figure 1-7. P-E hysteresis loops of Sr<sub>0.15</sub>(Na<sub>0.5</sub>Bi<sub>0.5</sub>)<sub>0.85</sub>TiO<sub>3</sub> for a frequency of 50 Hz at: (a) 250 , b) 100 and (c) 170 °C.<sup>41</sup>

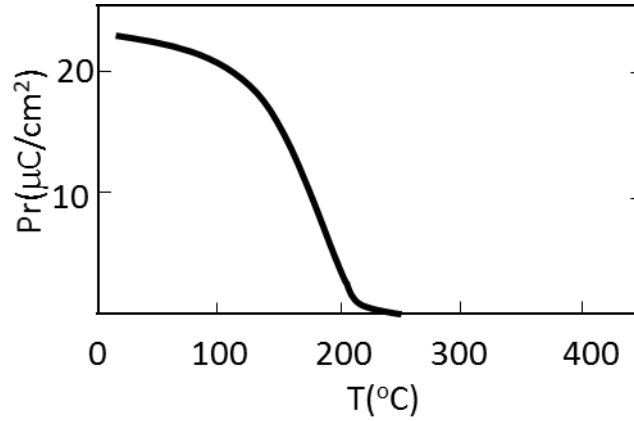


Figure 1-8. Temperature dependence of the remanent polarization of  $(\text{Na}_{0.5}\text{Bi}_{0.5})\text{TiO}_3$  from pyroelectric current measurements.<sup>41</sup>

Further investigations showed a large thermal hysteresis of  $\epsilon_r$  near  $\epsilon_{r,\text{max}}$  for a range over 50– 55 °C in NBT single crystals (Figure 1-9 (b)).<sup>37</sup> This hysteresis was attributed to the appearance and disappearance of an antiferroelectric phase on cooling and heating, respectively.

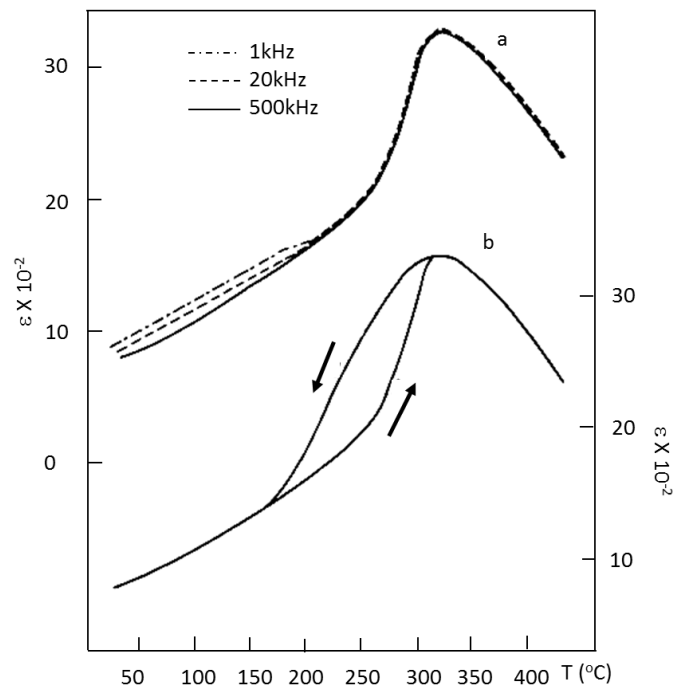


Figure 1-9. a)  $\epsilon_r$  of NBT at 1, 20 and 500 kHz and b) temperature hysteresis at 500 kHz.<sup>41</sup>

Many researchers have focused on the influence of A-site<sup>47-51</sup> and Ti-site<sup>52</sup> non-stoichiometry of NBT. Figure 1-10 shows the influence of non-stoichiometry on the dielectric constant,  $\epsilon_r$  and loss tangent,  $\tan \delta$ . Both Na and Bi non-stoichiometry have a modest influence on  $\epsilon_{r,max}$  and  $T_{max}$ . However, Na-deficiency or Bi-excess in the nominal starting composition will lower the depolarisation temperature ( $T_d$ ) and adopt a low  $\tan \delta$ . On the other hand, either Na-excess or Bi-deficiency enhances  $T_d$  and introduces high loss. The change in depolarization temperature and  $d_{33}$  are summarised in Figure 1-11.

(a)Figure 3 in reference [47], (b) figure 3 in reference [48] and (c) figure 4 in reference [52]

Figure 1-10. The influence of a) Na, b) Bi and c) Ti non-stoichiometry on the dielectric constant and loss tangent of NBT. <sup>47,48,52</sup>

(a)Figure 4 in reference [47] and (b) figure 4 in reference [48]

Figure 1-11. The influence of a) Na and b) Bi non-stoichiometry in NBT on the depolarisation temperature and  $d_{33}$ .<sup>47,48</sup>

As a ferroelectric material, a drawback of NBT is its relatively high conductivity which leads to significant leakage current. Avramenko et al. measured the conductivity of NBT single crystals at room temperature to be  $\sim 10^{-13} \text{S}\cdot\text{cm}^{-1}$ .<sup>53</sup> The Activation energy ( $E_a$ ) associated with the conductivity changed from 0.8 to 1.3 eV at the depolarization temperature  $T_d = 200 \text{ }^\circ\text{C}$  and then to 1.92 eV at the permittivity maximum,  $T_{max} = 320 \text{ }^\circ\text{C}$ . Hiruma et al. investigated the influence of non-stoichiometry on DC resistivity.<sup>50</sup> They showed that both Bi-deficient and Na-excess starting compositions induce low resistivity whereas Bi-excess and Na-deficient compositions lead to high resistivity (Figure 1-12). The difference in resistivity due to non-stoichiometry can be more than 3 orders of magnitude.

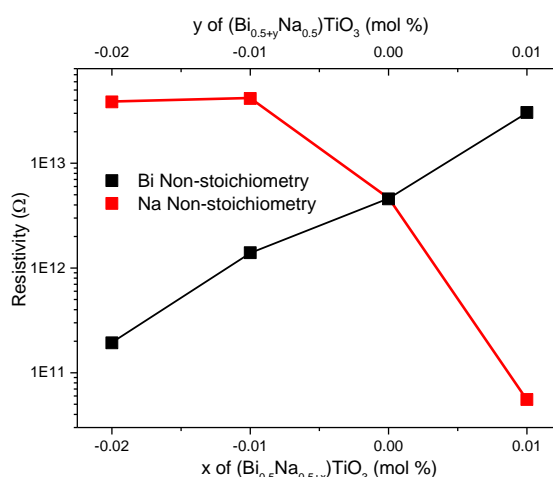


Figure 1-12. Variation of room temperature resistivity versus A-site non-stoichiometry in NBT ceramics.<sup>50</sup>

It is worth to note that for many properties such as room temperature resistivity,  $T_d$  and  $d_{33}$  the Na and Bi non-stoichiometry showed opposite trends. P-E hysteresis loops show Na-deficient and/or Bi-rich to have lower remanent polarisation, whereas Na-rich and/or Bi-deficient samples cannot reach a saturated state due to high leakage current which is in agreement with the RT DC resistivity and loss tangent data (Figure 1-13).<sup>51,54</sup>

(a) Figure 4 in reference [54] and (b) figure 9 in reference [51]

Figure 1-13. Polarization hysteresis loop of a)  $\text{Na}_{(0.5-x)}\text{Bi}_{(0.5+x)}\text{TiO}_{(3+x)}$  and b)  $\text{Na}_{0.5-x}\text{Bi}_{0.5}\text{TiO}_{3-x/2}$ .<sup>51,54</sup>

Recently the electrical conduction mechanisms of NBT were investigated using a combination of impedance spectroscopy, electromotive force and  $^{18}\text{O}$  tracer diffusion measurements.<sup>55</sup> This study showed the electrical properties of NBT are significantly different from other perovskite titanates like  $(\text{Ba,Sr})\text{TiO}_3$ ; NBT can exhibit high, nearly pure oxide ion conductivity for certain Na/Bi ratios in the starting reagents whereas the conductivity in  $(\text{Ba,Sr})\text{TiO}_3$  is dominated by electronic conduction. It was shown that small compositional variations (<1 at%) in the  $\text{Na}_2\text{CO}_3$  and  $\text{Bi}_2\text{O}_3$  starting reagents can induce significant changes in the electrical properties of NBT and can switch the

behaviour from an electronic insulator (Bi-rich or Na-deficient) with a high activation energy for conduction ( $\sim 1.6$  eV) to an oxide ion conductor (nominally stoichiometric and Bi-deficient or Na-excess, Figure 1-14) with a low activation energy for conduction (changes from  $\sim 0.9$  eV below  $320$  °C to  $\sim 0.4$  eV above  $320$  °C). The difference in bulk conductivity can be more than three orders of magnitude. A more detailed description of this study will be given in chapter 3 and 4.<sup>56–58</sup>

Figure 1 in reference [55]

Figure 1-14. Arrhenius-type plots of bulk conductivity with response activation energy for nominal stoichiometry, Bi non-stoichiometry and Mg doped NBT.<sup>55</sup>

#### 1.4. $K_{0.5}Bi_{0.5}TiO_3$

Similar to NBT, Potassium Bismuth Titanate,  $K_{0.5}Bi_{0.5}TiO_3$  (KBT) is another perovskite with 2 elements on the A-site. It has also been considered as a promising lead-free ferroelectric material. For piezoelectric materials, a morphotropic phase boundary (MPB) between rhombohedral and tetragonal phases can normally induce superior piezoelectric properties.<sup>59</sup> However, there are only limited perovskite materials which possess a tetragonal structure at room temperature, e.g.  $BaTiO_3$  and  $PbTiO_3$ . Therefore the room temperature tetragonal KBT is acting as an important end member which is adopted in many lead-free piezoelectric solid solutions such as KBT-NBT, BKT– $BiFeO_3$  and  $BiFeO_3$ –KBT– $PbTiO_3$ .<sup>59–65</sup>

KBT was firstly reported by Smolensky within the same paper as NBT followed by a few early stage studies about its structure and dielectric properties.<sup>19,46,66</sup> However, it is rather less intensely investigated when compared to NBT mostly because of the difficulty in obtaining dense ceramics using traditional solid state sintering. Therefore, a number of different fabrication routes have been employed to achieve higher density such as hot pressing,<sup>67–69</sup> sol-gel,<sup>70–72</sup> molten salts,<sup>73</sup> hydrothermal synthesis<sup>70,74–76</sup> and

a polymerised complex method<sup>77</sup>. Recently Tabuchi et al. report that with nano-sized TiO<sub>2</sub> and using KHCO<sub>3</sub> to replace the normal starting material K<sub>2</sub>CO<sub>3</sub>, dense ceramics (>95% density) can be obtained with solid state sintering for a relatively short period (2 hours).<sup>78,79</sup>

Due to the well-known volatilisation problems of both Potassium and Bismuth, many studies on KBT show the presence of secondary phase(s) in the final, sintered ceramics. Hiruma and Hou detected a K<sub>2</sub>Ti<sub>6</sub>O<sub>13</sub><sup>68,72</sup> phase while K<sub>4</sub>Ti<sub>3</sub>O<sub>12</sub><sup>70,71,80</sup> has been reported by other groups. König et al. have given a detailed analysis about the thermal decomposition of KBT ceramics.<sup>81</sup> They confirmed the volatilization of both K and Bi during calcination and sintering and revealed the bulk of KBT ceramics after sintering could be non-stoichiometric with K-deficiency and a Bi-excess.

#### 1.4.1. Crystal structure and phase transitions

An early structural investigation using XRD in the 1960s suggested the perovskite-type ferroelectric KBT adopts a tetragonal cell at room temperature with lattice parameters  $a = 3.913$  and  $c = 3.993$  Å.<sup>19</sup> Subsequent XRD and Neutron powder diffraction studies indicate the space group at room temperature is  $P4mm$  and it is polar without any octahedral tilting ( $a^0a^0a^0$ ).<sup>82,83</sup> Ivanova et al. point out the high temperature XRD shows the tetragonal structure remains until about 270 °C then a phase transition to an intermediate pseudo-cubic phase was observed. However, they failed to determine the character of this transition because the distortion is very small and due to a lack of quality in their samples. This intermediate phase remains stable up to 420 °C where KBT becomes a cubic phase with space group  $Pm\bar{3}m$ .<sup>19</sup>

Subsequent studies generally agree with Ivanova's results below the first phase transition temperature at 270 °C.<sup>66,84,85</sup> For the intermediate phase, Emel'yanov et al. suggested the symmetry remains tetragonal from 270 ~ 380 °C then becomes cubic.

On heating, the lattice parameter  $c$  decreases at first then starts to increase above 250 °C, oppositely, lattice parameter  $a$  initially increases then decreases slightly and finally increases again. On the other hand, Elkechai et al. report an XRD study where the change from tetragonal to cubic symmetry with increasing temperature is quite smooth with a continuous decrease of  $c$  and an increase of  $a$ , unlike other tetragonal perovskites such as BaTiO<sub>3</sub> or PbTiO<sub>3</sub> that show a discontinuous change in lattice parameters at the tetragonal to cubic phase transition. This result was supported by TEM and selected-area electron diffraction (SAED) data reported by Otoniča et al. On cooling, they observed a gradual appearance of domains, the associated SAED patterns do not appear immediately below  $T_c$  but appear progressively within a wide temperature range (on cooling) from 450 to 280 °C. On the other hand, some studies suggest KBT changes to a cubic structure above the first phase transition temperature at 250 or 300 °C.<sup>71,86</sup>

Both of the phase transitions in KBT have been determined to be variable due to different preparation routes. Hiruma et al. showed with hot-pressed ceramics that  $T_c$  varied from 410 to 440 °C and that the first phase transition also increased from 315 to 340 °C.<sup>68</sup> Other groups have reported similar results; Thongtha et al. reported  $T_c$  for their samples to vary from 358 to 377 °C depending on the sintering temperature.<sup>87</sup> Other factors that influence the phase transition temperature include; the starting material particle size<sup>78</sup>, external stress<sup>88</sup> and making KBT into a thin film<sup>89</sup>. In addition, despite the size of the K ion being larger than the Bi ion and the difference in charge, no A-site ordering has been reported in KBT.<sup>82</sup>

#### 1.4.2. Electrical properties

Forming solid solutions of KBT with other perovskite structured materials such as KBT-BaTiO<sub>3</sub>, KBT-NBT, KBT-PbTiO<sub>3</sub> and KBT-BiFeO<sub>3</sub> are known to result in good dielectric

properties.<sup>86,90-92</sup> Sometimes these solid solutions can contain more than 2 end member compositions.<sup>93</sup> As an end member, the permittivity of pure KBT reaches a maximum value at  $\sim 350$  to  $400$  °C according to various reports.<sup>71,84,94,95</sup> The maximum permittivity at  $T_c$  is  $\sim 3900$ . However, processing conditions can influence it significantly. Thongtha et al. showed with minor changes in the sintering temperature ( $\sim 975$  to  $1025$  °C)  $\epsilon_{max}$  can vary from  $\sim 1500$  to  $\sim 4000$ .<sup>87</sup> In addition, Hagiwara et al. suggest for the same sintering temperature, the dwelling time is also critical for the maximum permittivity. For samples sintered at  $1050$  °C for 5 and 100 hr, the maximum permittivity is  $\sim 4000$  and  $\sim 8000$ , respectively (Figure 1-15).<sup>96</sup> The  $\epsilon_{max}$  of KBT is also influenced by the K non-stoichiometry. Excess K in the starting material leads to a decrease in  $\epsilon_{max}$  and an increase in  $\tan\delta$ .<sup>97</sup>

Figure 2 in reference [76]

Figure 1-15. Variation of temperature dependent dielectric properties of KBT ceramics as a function of sintering dwell time.<sup>76</sup>

Thermal hysteresis and a frequency dispersion has also been observed in the dielectric properties of KBT. Li et al. reported thermal hysteresis of the dielectric constant in the range  $100 \sim 300$  °C.<sup>98</sup> This result has been confirmed by several other studies and one of the most recent papers suggests both the thermal hysteresis and frequency dispersion are strongly dependent on the grain size of KBT ceramics (Figure 1-16).<sup>76,85,88</sup> Hagiwara et al. attribute the thermal hysteresis and frequency dispersion to a relaxor-to-ferroelectric phase transition which is proposed to occur just below  $T_c$ . When the grain size is below a critical size, it makes the formation of domains energetically unfavourable. Therefore, the phase transition in small grained samples requires a wider temperature range and the relaxor phase can exist at lower temperature.

Figure 3 in reference [76]

Figure 1-16. Thermal hysteresis and frequency dispersion for KBT sintered for a) 100

hours and b) 5 hours.<sup>76</sup>

For decades, KBT and its solid solutions have been treated as a candidate lead-free ferroelectric material. KBT undergoes a depolarization temperature at  $\sim 280$  °C where most of its spontaneous polarization is lost and then it completely disappears around  $T_c$  ( $\sim 380$  °C) where the structure of KBT changes to become cubic (Figure 1-17).<sup>67</sup> Suchanicz et al. first measured the relationship between remanent polarization,  $P_r$  and temperature and gave the value at RT to be  $\sim 49$   $\mu\text{C}/\text{cm}^2$ . According to literature,  $P_r$  of KBT can vary in a range of  $\sim 22.2$  to  $49$   $\mu\text{C}/\text{cm}^2$  depending on the sintering temperature, dwelling time and grain size.<sup>67,78,99</sup>

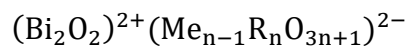
Figure 2 in reference [88]

Figure 1-17. Temperature dependence of  $P_r$  for KBT under 0 and 100 bar axis pressure.<sup>88</sup>

## 1.5. $\text{Bi}_4\text{Ti}_3\text{O}_{12}$

### 1.5.1. Aurivillius phases

$\text{Bi}_4\text{Ti}_3\text{O}_{12}$  was first synthesised by Aurivillius in 1949.<sup>100</sup> At that time he had synthesised a series of bismuth oxides with a general formula:



where Me is a mono, di, trivalent ion or a mixture of them, R can be an element such as V, Ti, W, Ta, etc., and n represent the number of perovskite-like layers between the  $(\text{Bi}_2\text{O}_2)^{2+}$  sheets and can be any number from 1 to 5.<sup>101</sup> In the case of  $\text{Bi}_4\text{Ti}_3\text{O}_{12}$ , Me is Bi, R is Ti and  $n = 3$  (Figure 1-18). In fact, the general formula of Aurivillius phases originally suggested by Aurivillius was  $(\text{Me}_2\text{O}_2)^{2+}(\text{Me}_{n-1}\text{R}_n\text{O}_{3n+1})^{2-}$  rather than the formula shown above. The change was made due to some studies indicating the

Bi in the  $\text{Bi}_2\text{O}_2$  layer cannot be replaced without destroying the structure, for instance  $\text{La}_4\text{Ti}_3\text{O}_{12}$  has a different structure to  $\text{Bi}_4\text{Ti}_3\text{O}_{12}$ .<sup>102</sup>

Figure 1 in reference [102]

Figure 1-18. The structure of  $\text{Bi}_4\text{Ti}_3\text{O}_{12}$  ( $n = 3$ ). A is the perovskite-like layers, B shows a unit cell of perovskite structure and C is the  $(\text{Bi}_2\text{O}_2)^{2+}$  layer.<sup>103</sup>

Initially the Aurivillius phases were studied for their ferroelectric properties as they contain perovskite-like blocks.<sup>104</sup> However, with time, numerous research groups have found many phases in this family can exhibit oxide ion conduction. The first reported phase was  $\text{Bi}_2\text{WO}_6$  ( $n=1$ ) by Takahashi.<sup>101</sup> Later, a single crystal study on the same phase by Yanovskii indicated the conductivity in the a-b plane is about 100 times higher than the conductivity in the c direction which indicated the ionic conduction was blocked by the  $(\text{Bi}_2\text{O}_2)^{2+}$  layers and can only occur within the perovskite-like blocks.<sup>105</sup> Following studies suggested some of these phases to have intrinsic oxygen vacancies and others need to be aliovalent-doped to introduce extrinsic oxygen vacancies. Among all these phases,  $\text{Bi}_2\text{VO}_{5.5}$  and its solid solution which is named as BIMEVOX has the highest oxide-ion conductivity and is one of the best anionic conductor reported to date.

Different dopants have been tried to replace Me, R and the Bi site in the  $(\text{Bi}_2\text{O}_2)^{2+}$  layers. In the early 90s, Castro et al. tried a number of dopants on three different Aurivillius phases. They found Bi in the  $(\text{Bi}_2\text{O}_2)^{2+}$  layer can be replaced by some p-block elements such as Sb, Pb and Te<sup>106</sup> but the conductivity showed no significant difference with these dopants.<sup>107</sup>

In terms of oxide ion conduction, doping on the Me or R site can produce two effects. For phases that do not contain any intrinsic oxygen vacancies, such as  $\text{Bi}_2\text{Sr}_2\text{B}_2\text{TiO}_{12}$  ( $\text{B}=\text{Nb}, \text{Ta}$ ) which is an n-type conductor, an aliovalent dopant like  $\text{Ga}^{3+}$  can introduce extrinsic oxygen vacancies and increase the conductivity while

decreasing the activation energy associated with the conduction. Secondly, for phases with intrinsic oxygen vacancies, the dopants can be used to stabilize the higher temperature phase at lower temperature if the higher temperature phase is more conductive such as some Me-site dopants in BIMEVOX. <sup>108–110</sup>

### 1.5.2. The crystal structure and phase transitions of Bi<sub>4</sub>Ti<sub>3</sub>O<sub>12</sub>

The basic structure of Bi<sub>4</sub>Ti<sub>3</sub>O<sub>12</sub> (BiT) can be described as three layers of pseudo-perovskite with Bi on the A-site and Ti on the B-site which are interleaved by [Bi<sub>2</sub>O<sub>2</sub>]<sup>2+</sup> sheets.<sup>101</sup> The idealized crystal structure for Aurivillius phases is tetragonal with the space group *I4/mmm* and BiT adopts this structure at temperatures above 675 °C (T<sub>C</sub>).<sup>111</sup> For the low temperature (< T<sub>C</sub>) structure, Newnham et al. stated that it depends on the number of perovskite blocks between the [Bi<sub>2</sub>O<sub>2</sub>]<sup>2+</sup> sheets. In order to minimise the strain, compounds with an odd number of perovskite layers tend to crystallize in a *B2cb* structure whereas with an even number of perovskite layers a structure based on *A2<sub>1</sub>am* is preferred.<sup>112</sup> Several studies have been performed on BiT below T<sub>C</sub>, most of them aiming to find the origin of BiT's ferroelectricity. The structure originally reported by Aurivillius when he discovered this material was pseudo-tetragonal with lattice parameters *a* = 3.841 and *b* = 32.83 Å but later by using single crystals he corrected the structure to be orthorhombic with *a* = 5.410, *b* = 5.448 and *c* = 32.84 Å.<sup>113,114</sup> This result was confirmed by a combination of X-ray and neutron diffraction studies which also indicated BiT to be a polar orthorhombic structure with space group *B2cb*.<sup>111</sup> Oppositely, Cummins et al. declared the results of an optical study on a single crystal not to be consistent with the orthorhombic symmetry but suggested monoclinic symmetry with a space group of *F4/mmm*.<sup>115</sup> Moreover, ferroelectric measurements gave the value of polarisation along *a* and *c* directions as 50 ± 5 and 4.0 ± 0.1 μC/cm<sup>2</sup>, respectively. These values show the spontaneous polarisation makes an angle of ~4.5° to the *a* direction and support the report of the

space group for BiT to be monoclinic  $F4/mmm$ . Some controversy has taken place regarding this finding. Newnham et al. point out that since  $Pc$  is the only monoclinic subgroup of  $B2cb$  that it should be the correct structure for BiT.<sup>112</sup> Based on a combination of single crystal X-ray diffraction and electron diffraction Rea and co-workers suggest there are some very minor monoclinic distortions in BiT which essentially makes the monoclinic space group  $B1a1$  a better fit than the  $B2cb$  orthorhombic structure.<sup>101</sup> Nevertheless, in general people tend to believe Rea's result because the orthorhombic  $B2cb$  fails to explain the polarisation along the  $c$  axis, but normally in order to obtain the reflection which can distinguish  $B1a1$  from  $B2cb$  requires a long period of data collection time which is not always feasible. Therefore both of the two space groups  $B2cb$  and  $B1a1$  have been reported or adopted in other studies.<sup>116–123</sup>

(a) Figure 1 and (b) figure 5 in reference [120]

Figure 1-19. The structure of (a)  $I4/mmm$  ideal structure of  $\text{Bi}_4\text{Ti}_3\text{O}_{12}$  observed at 800 °C and (b) Distorted  $B2cb$  structure observed at room temperature.<sup>120</sup>

BiT adopts a well-known phase transition from the lower temperature orthorhombic  $B2cb$  (monoclinic  $B1a1$ ) phase to a tetragonal  $I4/mmm$  phase at around 675 °C (Figure 1-19). Multiple groups have confirmed this via different techniques such as high temperature XRD/neutron diffraction, in-situ TEM/electron diffraction and Raman spectroscopy.<sup>6,119,122,124,125</sup> On heating, all three axes expand with increasing temperature but the structure of BiT does not change too much between room temperature and just below  $T_c$ . At  $T_c$ , the  $b$  axis exhibits a rapid decrease and becomes similar to  $a$  and overall the structure changes to  $I4/mmm$  (Figure 1-20).<sup>119</sup>

Figure 2 in reference [119]

Figure 1-20. Lattice parameters,  $b/a$  and cell volume of  $\text{Bi}_4\text{Ti}_3\text{O}_{12}$  as a function of temperature.<sup>119</sup>

The low temperature structure of BiT deviates from the parent  $I4/mmm$  structure by two features. First, Bi ions in the perovskite blocks displace along the a-axis with respect to the corner sharing  $TiO_6$  octahedra. Secondly, the  $TiO_6$  octahedra undergo tilting which can be described by Glazer's notation as  $a^-a^0c^0$  with a rotation angle of  $\sim 4^\circ$ .<sup>112,126</sup> Kojima and co-workers state if BiT exhibits a first order phase transition at 675 °C then these two features must take place simultaneously.<sup>127</sup> However, Zhou et al. observe a phase which is neither  $B2cb$  nor  $I4/mmm$  at a temperature of  $\sim 684$  °C. They suggest the Bi ion displacements and octahedral tilting actually occur in a sequence which means an additional intermediate phase exists in a narrow temperature range around  $T_C$ . With reference to other materials in the Aurivillius family, they suggest the octahedral tilting (on cooling) should happen first which means the phase transition is actually  $B2cb \xrightarrow{670^\circ C} Cmca \xrightarrow{695^\circ C} I4/mmm$ .<sup>126</sup> A bond valence sum analysis indicates the main driving force for this transition is a requirement to attain optimum bonding of the cations, especially those in the perovskite blocks.<sup>124</sup> Subsequent Rietveld analysis of high resolution neutron powder diffraction and electronic structure calculations show the stereoactivity of the  $Bi^{3+}$  lone pairs is not enough to cause this phase transition on its own. The primary driving force is attributed to the hybridisation of the Bi 6p orbitals and the O 2p orbitals in the perovskite layers.

Some reports indicate the 675°C phase transition is not the only one. Several Raman spectroscopy studies have reported a low temperature phase transition at  $\sim 200$  °C on both single crystal and polycrystalline BiT where the soft mode decreases its frequency.<sup>125,127-129</sup> The temperature of this phase transition is also reported to be dependent on grain size. However, such a phase transformation is absent in studies based on other techniques. In addition, in-situ electron diffraction results suggest another cell-doubling phase transition at  $\sim 900$  °C.<sup>6</sup> The authors also mention that 900 °C is sufficiently high to cause significant Bi volatilisation and that the actual phase

transition temperature can be altered by a change in composition.

### 1.5.3. Dielectric, ferroelectric and piezoelectric properties

For decades the Aurivillius oxide BiT has been regarded as a promising high-temperature, lead-free ferroelectric material. The two main advantages of this material are its high Curie temperature and high polarisation. As mentioned in the previous section,  $T_c$  of BiT is  $\sim 675$  °C which is high enough to maintain its ferroelectricity for most applications such as ferroelectric random access memories (FRAMs), radar technologies (phased arrays) and microwave high electron mobility transistors (HEMTs). The polarisation of BiT was first reported by Tambovtsev et al. based on single crystal measurements with a value of  $\sim 50$   $\mu\text{C}/\text{cm}^2$  whereas Van Uitert et al. suggest  $3.5$   $\mu\text{C}/\text{cm}^2$ . The value for ceramic samples was reported by Subbarao et al. to be  $\sim 6$   $\mu\text{C}/\text{cm}^2$ .<sup>114,130</sup> It clearly does not reach saturation, probably because of leakage current. Fang and Subbarao have investigated the polar axes of BiT based on single crystals and lattice parameter data, respectively. Fang et al. suggest the c-axis is the main polar axis whereas Subbarao propose the b-axis is more likely. Subsequent single crystal P-E hysteresis measurements indicate both a and c are polar axes with spontaneous polarisation of  $50 \pm 5$   $\mu\text{C}/\text{cm}^2$  for the a axis and  $4.0 \pm 0.1$   $\mu\text{C}/\text{cm}^2$  for the c axis.

The origin of ferroelectricity in BiT has also been investigated. Early investigations conclude two different modes. The first one attributes the spontaneous polarisation to off-centre movement of  $\sim 0.4$  Å by the Ti ions in the perovskite blocks towards an octahedral edge, similar to other perovskite materials such as BaTiO<sub>3</sub>.<sup>112</sup> The second one is the change of Bi-O bonding between the [Bi<sub>2</sub>O<sub>2</sub>]<sup>2+</sup> layers and the adjacent perovskite blocks; above  $T_c$  the 4 Bi-O bonds have the same length but become different to each other during cooling. This change introduces tilting of the octahedra

which leads to ferroelectricity.<sup>112,131</sup> However, recent studies cast doubts about the two old models and suggest the main cause should be the displacement of Bi cations along the a-axis in the perovskite blocks with respect to the TiO<sub>6</sub> octahedra, instead of the displacement of Ti.<sup>123</sup>

The piezoelectricity of BiT is difficult to measure due to the high leakage current, especially along the a-b plane. Seth et al. first measured the d<sub>33</sub> by using the pulse poling technique at room temperature to overcome the high leakage. Their results show for the a-b plane a d<sub>33</sub> of 26.0 pC/N, whereas along the c-direction d<sub>33</sub> was 11.0 pC/N.<sup>132</sup> Similar values have been reported in the range 11-26 pC/N for ceramics by other groups.<sup>133,134</sup>

The dielectric constant of BiT has been widely reported for both ceramic and single crystal samples.<sup>114,134,135</sup> Fouskova illustrated the dielectric constant of BiT single crystals show significant anisotropy parallel/perpendicular to the c-axis and in all directions exhibit a maximum at T<sub>c</sub>. The ε value within the a-b plane is ~1750 and about one order of magnitude higher along the c-axis (Figure 1-21).<sup>136</sup> Low temperature dielectric behaviour was measured by Sawaguchi and co-workers and revealed a continuous decrease with decreasing temperature (Figure 1-22).<sup>137</sup>

(a) Figure 2 and (b) figure 3 in reference [136]

Figure 1-21. The relative permittivity and conductivity of single crystal BiT at 5 MHz in a) a-b and b) c direction.<sup>136</sup>

Figure 1 in reference [137]

Figure 1-22. The relative permittivity of BiT at 1 kHz as a function of temperature.<sup>137</sup>

#### 1.5.4. Conduction mechanism and defects

As a candidate high-temperature lead-free ferroelectric material, BiT is known to exhibit undesirable leakage current. Takahashi et al. reported the electrical

conductivity of BiT ceramic at 100 kHz (Figure 1-23 (a)). A rapid increase can be observed around  $T_c$ . As Figure 1-23 (b) shows, the conductivity of BiT ceramic is  $pO_2$  dependent and increases with increasing  $pO_2$ . This demonstrates an electronic, p-type contribution to the total conductivity. Fouskova et al. performed ac conductivity measurements along all three axes of BiT single crystals.<sup>136</sup> As Figure 1-21 shows, similar to other compounds in the Aurivillius family, higher conductivity was observed in the a-b plane compared to the conductivity along the c axis. The difference is even larger at higher temperature ( $> 500$  °C). It is worth noting that at  $T_c$  the conductivity of the a-b plane undergoes a rapid increase whereas the conductivity along the c-axis suffers a rapid decrease. The  $pO_2$  dependence of conductivity in BiT single crystals shows  $pO_2$  dependent c-axis conductivity and nearly  $pO_2$  independent a-axis conductivity, Figure 1-24.<sup>138</sup> The minor  $pO_2$  independence along the a-axis indicates the conductivity in this direction is dominated by ionic conduction. Stronger  $pO_2$  dependence along the c-axis shows a larger contribution from the p-type electronic conduction. It is worth noting the  $pO_2$  dependence of BiT ceramics also shown in Figure 1-23 (b) illustrate a change of  $pO_2$  dependence. Below  $T_c$ , the conductivity of BiT ceramic has a much stronger  $pO_2$  dependence than above  $T_c$ , which means the ionic conduction has a larger contribution to the total conductivity above  $T_c$ .

(a) Figure 2 and (b) figure 4 in reference [139]

Figure 1-23. a) Temperature dependence and b)  $pO_2$  dependence of the ac electrical conductivity of a BiT ceramic.<sup>139</sup>

Figure 5 in reference [138]

Figure 1-24.  $pO_2$  dependence of the conductivity of BiT single crystal.<sup>138</sup>

Masatake et al. estimated the contribution of ionic and p-type conduction from the  $pO_2$  dependence in Figure 1-23 (b) and the impedance results by treating them as two different components in an equivalent circuit (Figure 1-25 (a)). The results from the two methods were in agreement with each other and they found the oxygen ion

conduction is higher than the hole conduction below  $T_C$  and the difference becomes even larger above  $T_C$  (675 °C). This result is consistent with the  $pO_2$  dependent measurements. (Figure 1-25 (b)).

(a) Figure 6 and (b) figure 7 in reference [139]

Figure 1-25. a) Schematic of equivalent circuit used to separate oxide ion and hole conduction where  $R_0$  and  $L_0$  is the resistance and inductance of sample holder; b) the change of  $\sigma_{hole}$  and  $\sigma_{ion}$  of BiT ceramic above and below the Curie point.<sup>139</sup>

The presence of oxygen vacancies are critical for oxygen ion conduction. The location of oxygen ion vacancies in BiT has therefore attracted a lot of attention. Noguchi et al. studied the defects in BiT and their effect on the polarisation properties.<sup>140</sup> They used a combination of high temperature neutron diffraction analysis and ab-initio electronic structure calculations to calculate possible defect locations. Assuming some loss of  $Bi_2O_3$ , they stated that Bi in the perovskite layers were more favourable to lose and create an adjacent oxygen vacancy than Bi in the  $Bi_2O_2$  layer. Some other researchers support this point of view.<sup>103,107</sup> Conversely, a first-principles calculation study indicated from an energy point of view the oxygen vacancies prefer the oxygen site in the  $[Bi_2O_2]^{2+}$  layers.<sup>141</sup> This suggestion is also supported by several other groups.<sup>142</sup> In addition, Park et al. suggest that oxygen vacancies can exist in both the perovskite block and  $[Bi_2O_2]^{2+}$  layers.<sup>143</sup> Computer modelling has also shown oxygen vacancies are feasible to form under reducing atmosphere.<sup>103</sup> On the other hand, they suggest the formation of  $Ti^{3+}$  is also favourable under reducing atmospheres therefore may lead to an increase in the electronic contribution.

#### 1.5.5. Dopants and solid solutions

Both the the A- and B-sites of BiT can host many different dopants. Hyatt et al. determined that Bi can be half substituted by La ( $Bi_2La_2Ti_3O_{12}$ ) and still maintain a

single phase.<sup>144</sup> Subbarao et al. investigated several different co-dopants in BiT which can significantly change the crystal structure and Curie point.<sup>114</sup>  $Pb^{2+}$ ,  $Ba^{2+}$  and  $Sr^{2+}$  have all been successfully used to replace  $Bi^{3+}$  with different solid solution limits, whereas small amounts of  $Ti^{4+}$  were replaced by  $Nb^{5+}$  ( $Bi^{3+} + Ti^{4+} = A^{2+} + Nb^{5+}$ ,  $A = Pb, Ba, Sr$ ).<sup>114</sup>  $T_c$  decreased significantly with all three combinations of substitution up to  $x = 1.25$  corresponding to the peak in dielectric constant (Figure 1-26). On the other hand, substitution of Bi by Dy and Ti by Zr failed to yield any single phase materials.

Snedden et al. performed a series of simulations based on energy minimisation procedures.<sup>103</sup> They investigated the feasibility of different doping mechanisms. Simulations suggested lanthanide cations (Yb, Gd, Nd, La) are more favourable to substitute Bi in the  $[Bi_2O_2]^{2+}$  layers but can be doped on both the  $[Bi_2O_2]^{2+}$  layers and the perovskite blocks with higher doping levels. For trivalent ions like Al, Ga and In, doping is more favourable to occur on the Bi-site on the  $[Bi_2O_2]^{2+}$  layers.

Figure 7 in reference 114

Figure 1-26. Curie temperature change with  $Me^{2+}$  doping level in  $Bi_{4-x}Me_xTi_{3-x}Nb_xO_{12}$  ( $Me=Pb, Ba, Sr$ ).<sup>114</sup>

Among all the dopants, La is a well-studied one for BiT. After the initial discovery by Popper et al., Shimazu et al. studied the relationship between the phase transition temperature and La-doping.<sup>145</sup> They showed with increasing La-doping, the a and b axes start to become similar and finally become the same when the composition  $(Bi_3La)Ti_3O_{12}$  was reached. Consequently, the Curie temperature and phase transition enthalpy,  $\Delta H$  decrease with increasing La-doping and become less than 0 when  $La=1$  (Figure 1-27). La substitution has also been used to reduce leakage current by reducing the volatility of  $Bi_2O_3$  and thus suppressing the creation of oxygen vacancies and electron holes.<sup>116</sup> In addition,  $(Bi_{3.25}La_{0.75})Ti_3O_{12}$  shows fatigue-free P-E characteristics

up to  $10^7$  cycles which makes it a more attractive candidate as a lead-free ferroelectric material.<sup>146</sup> After this discovery, La-doped BiT attracted significant interest and a series of studies on both La-doped BiT ceramics and single crystals were performed. La substitution of Bi can lead to modification of the grain size and grain morphology<sup>147</sup> and broaden the dielectric constant peak and lead to relaxor-like behaviour<sup>148</sup>. However, the location(s) of the La-ions remains controversial. All three suggested doping mechanisms of La (i.e. only substituting for Bi either in the  $[\text{Bi}_2\text{O}_2]^{2+}$  layer<sup>103</sup>, perovskite blocks<sup>116,149</sup> or in both<sup>150</sup>) have been suggested by different research groups.

Figure 3 in reference [145]

Figure 1-27 Ferroelectric Curie temperature and phase transition enthalpy for  $(\text{Bi}_{4-x}\text{La}_x)\text{Ti}_3\text{O}_{12}$ .<sup>145</sup>

Niobium is another well investigated dopant in BiT. The substitution of  $\text{Ti}^{4+}$  by  $\text{Nb}^{5+}$  has been used as a common route to eliminate undesired leakage for many years. It has been well reported this substitution can reduce the oxygen vacancy concentration via an ionic compensation mechanism ( $2\text{Ti}_{\text{Ti}}^{\times} + V_{\text{O}}^{\bullet\bullet} + \text{Nb}_2\text{O}_5 = 2\text{Nb}_{\text{Ti}}^{\cdot} + \text{O}_{\text{O}}^{\times} + 2\text{TiO}_2$ ) and thus reduce both oxygen ion and p-type conductivity. Shulman et al. reported evidence that ion hopping can no longer be observed with 0.05at% Nb doping in BiT.<sup>151</sup> They measured the conductivity of BiT and showed the Nb donor-doping can decrease conductivity by more than three orders of magnitude.<sup>133</sup> The reduction in oxygen vacancy concentration by Nb doping can enhance domain wall movement and hence improve the remanent polarisation ( $P_r$ ) and coercive field ( $E_c$ ) (Figure 1-28).<sup>152</sup> From a crystal structure point of view, Nb doping can induce more distortion of the  $\text{TO}_6$  octahedral chains.<sup>153,154</sup>

Figure 2 in reference [152]

Figure 1-28. Hysteresis loops of  $\text{Bi}_{4-x}(\text{Ti}_{1-x}\text{Nb}_x)_3\text{O}_{12}$  ceramic.<sup>152</sup>

In addition to La and Nb, other elements have also been studied.  $\text{Nd}^{3+}$  doping on

the A-site exhibits similar behaviour to La-doping and results in a decrease in conductivity and an increase in remanent polarisation.<sup>121,155</sup> On the other hand, Ti<sup>4+</sup> substituted by W<sup>6+</sup> can lead to a continuous decrease of the Curie point with increasing dopant content. The oxygen vacancies are filled by a compensation mechanism which leads to a decrease in both conductivity and dielectric loss similar to Nb doping. The grain size also decreased with increasing W<sup>6+</sup> doping level.<sup>104</sup>

## 1.6. Motivation and aim of this study

Oxide ion conductors find important technical applications in electrochemical devices such as solid-oxide fuel cells, oxygen separation membranes and oxygen sensors. For commercial applications, oxide ion conductors require a number of properties including high oxide ion conductivity and good chemical stability under operating conditions. However, only a few materials meet these requirements to date.<sup>8</sup> This project is focused on finding new oxide ion conductors with advanced properties. Impedance spectroscopy and EMF measurements are two important techniques to be used in this project. The former is able to extract the bulk conductivity and identify ionic conduction whereas the latter gives the percentage of oxide ion conductivity in the total conductivity (oxide ionic transport number,  $t_{ion}$ ). In addition, <sup>18</sup>O tracer diffusion measurements have also been employed to provide direct evidence for oxide ion conduction. Three materials are investigated in this project, Na<sub>0.5</sub>Bi<sub>0.5</sub>TiO<sub>3</sub>, K<sub>0.5</sub>Bi<sub>0.5</sub>TiO<sub>3</sub> and Bi<sub>4</sub>Ti<sub>3</sub>O<sub>12</sub>. They are either known to or can potentially exhibit oxide ion conduction.

### 1.6.1. Na<sub>0.5</sub>Bi<sub>0.5</sub>TiO<sub>3</sub> (NBT)

Li et al. has shown NBT can exhibit a high level oxide ion conduction with a transport number close to unity.<sup>55</sup> For the NBT system, this project is focused on further enhancement of the functional properties (both as an oxide ion conductor and as

ferroelectric insulator) via controlling the Na/Bi ratio in the starting materials and via donor/acceptor doping on the B-site.

### 1.6.2. $\text{K}_{0.5}\text{Bi}_{0.5}\text{TiO}_3$ (KBT)

KBT is a ferroelectric perovskite where K replaces Na in NBT.<sup>19</sup> Na and K belong to the same group in the periodic table thus have similar physical and chemical characteristics. Previous studies have shown that low levels of A-site non-stoichiometry can significantly influence the dielectric constant and the loss tangent of KBT<sup>86</sup>, similar to that observed for NBT. In addition, an impedance spectroscopy study by Rao et al. showed the activation energy of KBT bulk conduction is  $1.16 \pm 0.04$  eV which is a typical value for oxide ion conduction (e.g.  $\sim 0.9$  eV for NBT).<sup>55</sup> Therefore, the possibility exists that KBT may also possess significant oxide ion conduction like NBT and this will be investigated in this study.

### 1.6.3. $\text{Bi}_4\text{Ti}_3\text{O}_{12}$ (BiT)

BiT adopts an Aurivillius structure with NBT-like perovskite blocks formed by Bi and Ti interleaved by  $[\text{Bi}_2\text{O}_2]^{2+}$  sheets.<sup>100</sup> Impedance spectroscopy and  $p\text{O}_2$  dependent measurements indicate BiT is a mixed conductor with both oxide ion and p-type conduction.<sup>68</sup> The reported relatively high oxide ion conduction and the fact many compounds in the Aurivillius family are oxide ion conductors makes it reasonable to presume BiT has the potential to be a good oxide ion conductor. The aim for the BiT system in this project is to improve the ionic conduction by chemical doping and to determine its potential as an oxide ion conductor.

## 1.7. References

1. Mitchell, R. H. Perovskites: modern and ancient. (2002).

2. Beskow, G. V. M. Goldschmidt: Geochemische Verteilungsgesetze der Elemente. *Geol. Foereningan i Stock. Foerhandlingar* **46**, 738–743 (1924).
3. Jaffe, B. *Piezoelectric ceramics*. **3**, (Elsevier, 2012).
4. Levy, M. *Crystal Structure and Defect Properties in Ceramic Materials*. (Imperial College, 2005).
5. Glazer, A. M. Simple ways of determining perovskite structures. *Acta Crystallogr. Sect. A* **31**, 756–762 (1975).
6. Reaney, I. M. & Ubic, R. Dielectric and structural characteristics of perovskites and related materials as a function of tolerance factor. *Ferroelectrics* **228**, 23–28 (1999).
7. Steele, B. & Heinzl, A. Materials for fuel-cell technologies. *Nature* **414**, 345–352 (2001).
8. Wachsman, E. D. & Lee, K. T. Lowering the Temperature of Solid Oxide Fuel Cells. *Science*. **334**, 935–939 (2011).
9. Skinner, S. J. & Kilner, J. A. Oxygen ion conductors. *Mater. Today* **6**, 30–37 (2003).
10. Butler, V., Catlow, C. R. A., Fender, B. E. F. & Harding, J. H. Dopant ion radius and ionic conductivity in cerium dioxide. *Solid State Ionics* **8**, 109–113 (1983).
11. Minervini, L. Defect cluster formation in M<sub>2</sub>O<sub>3</sub>-doped CeO<sub>2</sub>. *Solid State Ionics* **116**, 339–349 (1999).
12. Minh, N. Q. Ceramic Fuel Cells. *J. Am. Ceram. Soc.* **76**, 563–588 (1993).

13. Jacobson, A. J. Materials for Solid Oxide Fuel Cells. *Chem. Mater. Rev.* **22**, 660–674 (2010).
14. Steele, B. C. H. Oxygen ion conductors and their technological applications. *Mater. Sci. Eng. B* **13**, 79–87 (1992).
15. Kilner, J. Fast oxygen transport in acceptor doped oxides. *Solid State Ionics* **129**, 13–23 (2000).
16. Huang, K. Electrode Performance Test on Single Ceramic Fuel Cells Using as Electrolyte Sr- and Mg-Doped LaGaO<sub>3</sub>. *J. Electrochem. Soc.* **144**, 3620–3624 (1997).
17. Feng, M. & Goodenough, J. B. A superior oxide-ion electrolyte. *Eur. J. solid state Inorg. Chem.* **31**, 663–672 (1994).
18. Ishihara, T., Sammes, N. M. & Yamamoto, O. in *High Temperature and Solid Oxide Fuel Cells* 83–117 (Elsevier, 2003). doi:10.1016/B978-185617387-2/50021-0
19. Ivanova, V. V, Kapyshev, A. G., Venevtsev, Y. N. & Zhdanov, G. S. X-ray determination of the symmetry of elementary cells of the ferroelectric materials (K<sub>0.5</sub>Bi<sub>0.5</sub>)TiO<sub>3</sub> and (Na<sub>0.5</sub>Bi<sub>0.5</sub>)TiO<sub>3</sub> and of high-temperature phase transitions in (K<sub>0.5</sub>Bi<sub>0.5</sub>)TiO<sub>3</sub>. *Izv. Akad. Nauk SSSR* **26**, 354–356 (1962).
20. Buhner, C. F. Some Properties of Bismuth Perovskites. *J. Chem. Phys.* **36**, 798–803 (1962).
21. Smolenskii, G. A., Isupov, V. A., Agranovskaya, A. I. & Krainik, N. N. New ferroelectrics of complex composition. 4. *Sov. Physics-Solid State* **2**, 2651–2654 (1961).

22. Gorfman, S. & Thomas, P. A. Evidence for a non-rhombohedral average structure in the lead-free piezoelectric material  $\text{Na}_{0.5}\text{Bi}_{0.5}\text{TiO}_3$ . *J. Appl. Crystallogr.* **43**, 1409–1414 (2010).
23. Zvirgzds, J. A., Kapostin, P. P., Zvirgzde, J. V. & Kruzina, T. V. X-ray study of phase transitions in ferroelectric  $\text{Na}_{0.5}\text{Bi}_{0.5}\text{TiO}_3$ . *Ferroelectrics* **40**, 75–77 (1982).
24. Isupov, V. A. Ferroelectric  $\text{Na}_{0.5}\text{Bi}_{0.5}\text{TiO}_3$  and  $\text{K}_{0.5}\text{Bi}_{0.5}\text{TiO}_3$  Perovskites and Their Solid Solutions. *Ferroelectrics* **315**, 123–147 (2005).
25. Vakhrushev, S. B. *et al.* Phase transitions and soft modes in sodium bismuth titanate. *Ferroelectrics* **63**, 153–160 (1985).
26. Isuyov, V. A., Pronin, I. P. & Kruzina, T. V. Temperature dependence of birefringence and opalescence of the sodium-bismuth titanate crystals. *Ferroelectr. Lett. Sect.* **2**, 205–208 (1984).
27. Kreisel, J. *et al.* High-pressure x-ray scattering of oxides with a nanoscale local structure: Application to  $\text{Na}_{1/2}\text{Bi}_{1/2}\text{TiO}_3$ . *Phys. Rev. B* **68**, 14113 (2003).
28. Shuvaeva, V. A. *et al.* Local structure of the lead-free relaxor ferroelectric  $(\text{K}_x\text{Na}_{1-x})_{0.5}\text{Bi}_{0.5}\text{TiO}_3$ . *Phys. Rev. B* **71**, 174114 (2005).
29. Balagurov, A. M. *et al.* The rhombohedral phase with incommensurate modulation in  $\text{Na}_{1/2}\text{Bi}_{1/2}\text{TiO}_3$ . *Phase Transitions* **79**, 163–173 (2006).
30. Aksel, E. *et al.* Monoclinic crystal structure of polycrystalline  $\text{Na}_{0.5}\text{Bi}_{0.5}\text{TiO}_3$ . *Appl. Phys. Lett.* **98**, 13–16 (2011).
31. Aksel, E., Forrester, J. S., Kowalski, B., Jones, J. L. & Thomas, P. A. Phase

- transition sequence in sodium bismuth titanate observed using high-resolution x-ray diffraction. *Appl. Phys. Lett.* **99**, 222901 (2011).
32. Dorcet, V. & Trolliard, G. A transmission electron microscopy study of the A-site disordered perovskite  $\text{Na}_{0.5}\text{Bi}_{0.5}\text{TiO}_3$ . *Acta Mater.* **56**, 1753–1761 (2008).
  33. Beanland, R. & Thomas, P. A. Imaging planar tetragonal sheets in rhombohedral  $\text{Na}_{0.5}\text{Bi}_{0.5}\text{TiO}_3$  using transmission electron microscopy. *Scr. Mater.* **65**, 440–443 (2011).
  34. Levin, I. & Reaney, I. M. Nano- and Mesoscale Structure of  $\text{Na}_{1/2}\text{Bi}_{1/2}\text{TiO}_3$ : A TEM Perspective. *Adv. Funct. Mater.* **22**, 3445–3452 (2012).
  35. Tu, C.-S., Siny, I. G. & Schmidt, V. H. Sequence of dielectric anomalies and high-temperature relaxation behavior in  $\text{Na}_{1/2}\text{Bi}_{1/2}\text{TiO}_3$ . *Phys. Rev. B* **49**, 11550–11559 (1994).
  36. Petzelt, J. *et al.* Infrared, Raman and high-frequency dielectric spectroscopy and the phase transitions in  $\text{Na}_{1/2}\text{Bi}_{1/2}\text{TiO}_3$ . *J. Physics-Condensed Matter* **16**, 2719–2731 (2004).
  37. Pronin, I. P., Syrnikov, P. P., Isupov, V. A., Egorov, V. M. & Zaitseva, N. V. Peculiarities of phase transitions in sodium-bismuth titanate. *Ferroelectrics* **25**, 395–397 (1980).
  38. Suchanicz, J. & Kwapulinski, J. X-ray diffraction study of the phase transitions in  $\text{Na}_{0.5}\text{Bi}_{0.5}\text{TiO}_3$ . *Ferroelectrics* **165**, 249–253 (1995).
  39. Suchanicz, J., Roleder, K., Kania, A. & Hańderek, J. Electrostrictive strain and pyroeffect in the region of phase coexistence in  $\text{Na}_{0.5}\text{Bi}_{0.5}\text{TiO}_3$ . *Ferroelectrics* **77**, 107–110 (1988).

40. Jones, G. O. & Thomas, P. A. Investigation of the structure and phase transitions in the novel A-site substituted distorted perovskite compound  $\text{Na}_{0.5}\text{Bi}_{0.5}\text{TiO}_3$ . *Acta Crystallogr. Sect. B Struct. Sci.* **58**, 168–178 (2002).
41. Sakata, K. & Masuda, Y. Ferroelectric and antiferroelectric properties of  $(\text{Na}_{0.5}\text{Bi}_{0.5})\text{TiO}_3\text{-SrTiO}_3$  solid solution ceramics. *Ferroelectrics* **7**, 347–349 (1974).
42. Zhang, M.-S., Scott, J. F. & Zvirgzds, J. a. Raman spectroscopy of  $\text{Na}_{0.5}\text{Bi}_{0.5}\text{TiO}_3$ . *Ferroelectr. Lett. Sect.* **6**, 147–152 (1986).
43. Dorcet, V., Trolliard, G. & Boullay, P. Reinvestigation of phase transitions in  $\text{Na}_{0.5}\text{Bi}_{0.5}\text{TiO}_3$  by TEM. Part I: First order rhombohedral to orthorhombic phase transition. *Chem. Mater.* **77**, 5061–5073 (2008).
44. Trolliard, G. & Dorcet, V. Reinvestigation of phase transitions in  $\text{Na}_{0.5}\text{Bi}_{0.5}\text{TiO}_3$  by TEM. Part II: Second order orthorhombic to tetragonal phase transition. *Chem. Mater.* **25**, 5074–5082 (2008).
45. Dorcet, V., Trolliard, G. & Boullay, P. The structural origin of the antiferroelectric properties and relaxor behavior of  $\text{Na}_{0.5}\text{Bi}_{0.5}\text{TiO}_3$ . *J. Magn. Magn. Mater.* **321**, 1758–1761 (2009).
46. Smolensky, G. A., Isupov, V. A., Agranovskaya, A. I. & Krainic, N. N. New ferroelectrics with complex compounds. IV. *Fiz. Tverd. Tela* **2**, 2982–2985 (1960).
47. Sung, Y. S. *et al.* Effects of Na nonstoichiometry in  $(\text{Bi}_{0.5}\text{Na}_{0.5+x})\text{TiO}_3$  ceramics. *Appl. Phys. Lett.* **96**, 22901 (2010).
48. Sung, Y. S. *et al.* Effects of Bi nonstoichiometry in  $(\text{Bi}_{0.5+x}\text{Na}_{0.5})\text{TiO}_3$  ceramics.

- Appl. Phys. Lett.* **98**, 12902 (2011).
49. Hiruma, Y., Nagata, H. & Takenaka, T. Grain-Size Effect on Electrical Properties of  $(\text{Bi}_{1/2}\text{K}_{1/2})\text{TiO}_3$  Ceramics. *Jpn. J. Appl. Phys.* **46**, 1081–1084 (2007).
  50. Hiruma, Y., Nagata, H. & Takenaka, T. Thermal depoling process and piezoelectric properties of bismuth sodium titanate ceramics. *J. Appl. Phys.* **105**, 84112 (2009).
  51. Spreitzer, M., Valant, M. & Suvorov, D. Sodium deficiency in  $\text{Na}_{0.5}\text{Bi}_{0.5}\text{TiO}_3$ . *J. Mater. Chem.* **17**, 185–192 (2007).
  52. Naderer, M., Kainz, T., Schütz, D. & Reichmann, K. The influence of Ti-nonstoichiometry in  $\text{Bi}_{0.5}\text{Na}_{0.5}\text{TiO}_3$ . *J. Eur. Ceram. Soc.* **34**, 663–667 (2014).
  53. Avramenko, V. P., Kruzina, T. V., Kudzin, A. Y., Sokolyanskii, G. K. & Yudin, A. S. Electrical-properties of single-crystal Sodium bismuth titanate. *Fizika Tverdogo Tela* **31**, 325–327 (1989).
  54. Carter, J. *et al.* Structure and ferroelectricity of nonstoichiometric  $(\text{Na}_{0.5}\text{Bi}_{0.5})\text{TiO}_3$ . *Appl. Phys. Lett.* **104**, 0–4 (2014).
  55. Li, M. *et al.* A family of oxide ion conductors based on the ferroelectric perovskite  $\text{Na}_{0.5}\text{Bi}_{0.5}\text{TiO}_3$ . *Nat. Mater.* **13**, 31–5 (2014).
  56. Li, M. *et al.* Dramatic Influence of A-Site Nonstoichiometry on the Electrical Conductivity and Conduction Mechanisms in the Perovskite Oxide  $\text{Na}_{0.5}\text{Bi}_{0.5}\text{TiO}_3$ . *Chem. Mater.* **27**, 629–634 (2015).
  57. Li, M., Li, L., Zang, J. & Sinclair, D. C. Donor-doping and reduced leakage current in Nb-doped  $\text{Na}_{0.5}\text{Bi}_{0.5}\text{TiO}_3$ . *Appl. Phys. Lett.* **106**, 102904 (2015).

58. Li, L., Li, M., Zhang, H., Reaney, I. M. & Sinclair, D. C. Controlling mixed conductivity in  $\text{Na}_{1/2}\text{Bi}_{1/2}\text{TiO}_3$  using A-site non-stoichiometry and Nb-donor doping. *J. Mater. Chem. C* **4**, 5779–5786 (2016).
59. Bennett, J. *et al.* Variation of Piezoelectric Properties and Mechanisms Across the Relaxor-Like /Ferroelectric Continuum in  $\text{BiFeO}_3\text{-(K}_{0.5}\text{Bi}_{0.5})\text{TiO}_3\text{-PbTiO}_3$  Ceramics. *IEEE Trans. Ultrason. Ferroelectr. Freq. Control* **62**, 33–45 (2015).
60. Bennett, J., Bell, A. J., Stevenson, T. J. & Comyn, T. P. Exceptionally large piezoelectric strains in  $\text{BiFeO}_3\text{-(K}_{0.5}\text{Bi}_{0.5})\text{TiO}_3\text{-PbTiO}_3$  ceramics. *Scr. Mater.* **68**, 491–494 (2013).
61. Bennett, J. *et al.* Multiferroic properties of  $\text{BiFeO}_3\text{-(K}_{0.5}\text{Bi}_{0.5})\text{TiO}_3$  ceramics. *Mater. Lett.* **94**, 172–175 (2013).
62. Sasaki, A., Chiba, T., Mamiya, Y. & Otsuki, E. Dielectric and Piezoelectric Properties of  $(\text{Bi}_{0.5}\text{Na}_{0.5})\text{TiO}_3\text{-(Bi}_{0.5}\text{K}_{0.5})\text{TiO}_3$  Systems. *Jpn. J. Appl. Phys.* **38**, 5564–5567 (1999).
63. Zuo, R., Fang, X., Ye, C. & Li, L. Phase Transitional Behavior and Piezoelectric Properties of Lead-Free  $(\text{Na}_{0.5}\text{K}_{0.5})\text{NbO}_3\text{-(Bi}_{0.5}\text{K}_{0.5})\text{TiO}_3$  Ceramics. *J. Am. Ceram. Soc.* **90**, 2424–2428 (2007).
64. Bennett, J., Bell, a. J., Stevenson, T. J. & Comyn, T. P. Tailoring the structure and piezoelectric properties of  $\text{BiFeO}_3\text{-(K}_{0.5}\text{Bi}_{0.5})\text{TiO}_3\text{-PbTiO}_3$  ceramics for high temperature applications. *Appl. Phys. Lett.* **103**, 152901 (2013).
65. Matsuo, H. *et al.* Structural and piezoelectric properties of high-density  $(\text{Bi}_{0.5}\text{K}_{0.5})\text{TiO}_3\text{ - BiFeO}_3$  ceramics. *J. Appl. Phys.* **108**, 104103 (2010).
66. Bührer, C. F. Some Properties of Bismuth Perovskites. *J. Chem. Phys.* **36**, 798–

- 803 (1962).
67. Hiruma, Y., Marumo, K., Aoyagi, R., Nagata, H. & Takenaka, T. Ferroelectric and piezoelectric properties of  $(\text{Bi}_{1/2}\text{K}_{1/2})\text{TiO}_3$  ceramics fabricated by hot-pressing method. *J. Electroceramics* **21**, 296–299 (2008).
  68. Hiruma, Y., Aoyagi, R., Nagata, H. & Takenaka, T. Ferroelectric and Piezoelectric Properties of  $(\text{Bi}_{1/2}\text{K}_{1/2})\text{TiO}_3$  Ceramics. *Jpn. J. Appl. Phys.* **44**, 5040–5044 (2005).
  69. Hiruma, Y., Nagata, H. & Takenaka, T. Grain-Size Effect on Electrical Properties of  $(\text{Bi}_{1/2}\text{K}_{1/2})\text{TiO}_3$  Ceramics This. *Jpn. J. Appl. Phys.* **46**, 1081–1084 (2007).
  70. Hou, L. *et al.* Sol-gel-hydrothermal synthesis and sintering of  $\text{K}_{0.5}\text{Bi}_{0.5}\text{TiO}_3$  nanowires. *Mater. Res. Bull.* **41**, 1330–1336 (2006).
  71. Li, Z. F., Wang, C. L., Zhong, W. L., Li, J. C. & Zhao, M. L. Dielectric relaxor properties of  $\text{K}_{0.5}\text{Bi}_{0.5}\text{TiO}_3$  ferroelectrics prepared by sol–gel method. *J. Appl. Phys.* **94**, 2548–2552 (2003).
  72. Hou, Y.D. *et al.* Comparative study of  $\text{K}_{0.5}\text{Bi}_{0.5}\text{TiO}_3$  nanoparticles derived from sol–gel-hydrothermal and sol–gel routes. *Solid State Commun.* **137**, 658–661 (2006).
  73. Yang, J., Hou, Y., Wang, C., Zhu, M. & Yan, H. Relaxor behavior of  $(\text{K}_{0.5}\text{Bi}_{0.5})\text{TiO}_3$  ceramics derived from molten salt synthesized single-crystalline nanowires. *Appl. Phys. Lett.* **91**, 23118 (2007).
  74. Lim, J. B., Suvorov, D., Kim, M.-H. & Jeon, J.-H. Hydrothermal synthesis and characterization of  $(\text{Bi,K})\text{TiO}_3$  ferroelectrics. *Mater. Lett.* **67**, 286–288 (2012).

75. Hagiwara, M. & Fujihara, S. Fabrication of dense  $(\text{Bi}_{1/2}\text{K}_{1/2})\text{TiO}_3$  ceramics using hydrothermally derived fine powders. *J. Mater. Sci.* **50**, 5970–5977 (2015).
76. Hagiwara, M. & Fujihara, S. Grain-size-dependent spontaneous relaxor-to-ferroelectric phase transition in  $(\text{Bi}_{1/2}\text{K}_{1/2})\text{TiO}_3$  ceramics. *Appl. Phys. Lett.* **107**, 12903 (2015).
77. Wada, T., Fukui, A. & Matsuo, Y. Preparation of  $(\text{K}_{0.5}\text{Bi}_{0.5})\text{TiO}_3$  Ceramics by Polymerized Complex Method and their Properties. *Jpn. J. Appl. Phys.* **41**, 7025–7028 (2002).
78. Tabuchi, K., Inoue, Y., Nagata, H. & Takenaka, T. Effects of Starting Raw Materials for Fabricating Dense  $(\text{Bi}_{1/2}\text{K}_{1/2})\text{TiO}_3$  Ceramics. *Ferroelectrics* **457**, 124–130 (2013).
79. Tabuchi, K., Nagata, H. & Takenaka, T. Fabrication and electrical properties of potassium excess and poor  $(\text{Bi}_{1/2}\text{K}_{1/2})\text{TiO}_3$  ceramics. *J. Ceram. Soc. Japan* **121**, 623–626 (2013).
80. Zhao, S., Li, G., Ding, A., Wang, T. & Yin, Q. Ferroelectric and piezoelectric properties of  $(\text{Na}, \text{K})_{0.5}\text{Bi}_{0.5}\text{TiO}_3$  lead free ceramics. *J. Phys. D. Appl. Phys.* **39**, 2277–2281 (2006).
81. König, J. *et al.* The thermal decomposition of  $\text{K}_{0.5}\text{Bi}_{0.5}\text{TiO}_3$  ceramics. *J. Eur. Ceram. Soc.* **29**, 1695–1701 (2009).
82. Jones, G. O., Kreisel, J. & Thomas, P. A. A structural study of the  $(\text{Na}_{1-x}\text{K}_x)_{0.5}\text{Bi}_{0.5}\text{TiO}_3$  perovskite series as a function of substitution (x) and temperature. *Powder Diffr.* **17**, 301–319 (2002).
83. Otoničar, M., Škapin, S. D., Jančar, B., Ubič, R. & Suvorov, D. Analysis of the

- Phase Transition and the Domain Structure in  $K_{0.5}Bi_{0.5}TiO_3$  Perovskite Ceramics by In Situ XRD and TEM. *J. Am. Ceram. Soc.* **93**, 4168–4173 (2010).
84. Emel'yanov, S. M., Raevskii, I. P. & Prokopalo, O. I. Nature of phase transitions in potassium bismuth titanate. *Sov. Phys. solid state* **25**, 889–890 (1983).
  85. Emel'yanov, S. M. *et al.* Spontaneous polarizations and piezoelectric of potassium bismuth titanate. *Sov. Phys. solid state* **29**, 1446–1447 (1987).
  86. Wefring, E. T., Morozov, M. I., Einarsrud, M.-A. & Grande, T. Solid-State Synthesis and Properties of Relaxor  $(1-x)BKT-xBNZ$  Ceramics. *J. Am. Ceram. Soc.* **97**, 2928–2935 (2014).
  87. Thongtha, A., Laowanidwatana, A. & Bongkarn, T. Phase Formation, Microstructure and Dielectric Properties of Bismuth Potassium Titanate Ceramic Fabricated Using the Combustion Technique. *Integr. Ferroelectr.* **149**, 32–38 (2013).
  88. Suchanicz, J., Mercurio, J. P. & Said, S. Axial Pressure Effect on Dielectric and Ferroelectric Properties of  $K_{0.5}Bi_{0.5}TiO_3$  Ceramic. *Ferroelectrics* **290**, 169–175 (2003).
  89. Jing, X. *et al.* Structural and electrical properties of  $K_{0.5}Bi_{0.5}TiO_3$  thin films for ferroelectric field effect transistor applications. *J. Phys. D. Appl. Phys.* **42**, 45421 (2009).
  90. Morozov, M. I., Einarsrud, M.-A. & Grande, T. Polarization and strain response in  $Bi_{0.5}K_{0.5}TiO_3$ - $BiFeO_3$  ceramics. *Appl. Phys. Lett.* **101**, 252904 (2012).
  91. Hiruma, Y., Aoyagi, R., Nagata, H. & Takenaka, T. Piezoelectric Properties of  $BaTiO_3$ – $(Bi_{1/2}K_{1/2})TiO_3$  Ferroelectric Ceramics. *Jpn. J. Appl. Phys.* **43**, 7556–

- 7559 (2004).
92. Nemoto, M., Hiruma, Y., Nagata, H. & Takenaka, T. Fabrication and Piezoelectric Properties of Grain-Oriented  $(\text{Bi}_{1/2}\text{K}_{1/2})\text{TiO}_3$ – $\text{BaTiO}_3$  Ceramics. *Jpn. J. Appl. Phys.* **47**, 3829–3832 (2008).
  93. Li, Y., Chen, W., Xu, Q., Zhou, J. & Gu, X. Piezoelectric and ferroelectric properties of  $\text{Na}_{0.5}\text{Bi}_{0.5}\text{TiO}_3$ – $\text{K}_{0.5}\text{Bi}_{0.5}\text{TiO}_3$ – $\text{BaTiO}_3$  piezoelectric ceramics. *Mater. Lett.* **59**, 1361–1364 (2005).
  94. Elkechai, O., Manier, M. & Mercurio, J.  $\text{Na}_{0.5}\text{Bi}_{0.5}\text{TiO}_3$ – $\text{K}_{0.5}\text{Bi}_{0.5}\text{TiO}_3$  (NBT-KBT) system: A structural and electrical study. *Phys. status solidi* **499**, (1996).
  95. Yamada, Y. *et al.* Effect of B-Ions Substitution in  $[(\text{K}_{1/2}\text{Bi}_{1/2})-(\text{Na}_{1/2}\text{Bi}_{1/2})](\text{Ti} - \text{B})\text{O}_3$  System with  $\text{B}=\text{Zr}$ ,  $\text{Fe}_{1/2}\text{Nb}_{1/2}$ ,  $\text{Zn}_{1/3}\text{Nb}_{2/3}$  or  $\text{Mg}_{1/3}\text{Nb}_{2/3}$ . *Jpn. J. Appl. Phys.* **34**, 5462–5466 (1995).
  96. Hagiwara, M. & Fujihara, S. Grain size effect on phase transition behavior and electrical properties of  $(\text{Bi}_{1/2}\text{K}_{1/2})\text{TiO}_3$  piezoelectric ceramics. *Jpn. J. Appl. Phys.* **54**, 10ND10 (2015).
  97. Sung, Y. S. *et al.* Effects of K Nonstoichiometry in  $(\text{Bi}_{0.5}\text{K}_{0.5+x})\text{TiO}_3$  Ceramics. *Integr. Ferroelectr.* **114**, 92–99 (2010).
  98. Samara, G. a. The relaxational properties of compositionally disordered ABO<sub>3</sub> perovskites. *J. Phys. Condens. Matter* **15**, R367–R411 (2003).
  99. Nagata, H., Saitoh, M., Hiruma, Y. & Takenaka, T. Fabrication and Piezoelectric Properties of Textured  $(\text{Bi}_{1/2}\text{K}_{1/2})\text{TiO}_3$  Ferroelectric Ceramics. *Jpn. J. Appl. Phys.* **49**, 09MD08 (2010).

100. Aurivillius, B. Mixed bismuth oxides with layer lattices. 2. Structure of  $\text{Bi}_4\text{Ti}_3\text{O}_{12}$ . *Ark. kemi* **1**, 499–512 (1950).
101. Rae, A. D., Thompson, J. G., Withers, R. L. & Willis, A. C. Structure refinement of commensurately modulated bismuth titanate,  $\text{Bi}_4\text{Ti}_3\text{O}_{12}$ . *Acta Crystallogr. Sect. B Struct. Sci.* **46**, 474–487 (1990).
102. Subbarao, E. C. Crystal Chemistry of Mixed Bismuth Oxides with Layer-Type Structure. *J. Am. Ceram. Soc.* **45**, 166–169 (1962).
103. Snedden, A., Lightfoot, P., Dinges, T. & Islam, M. S. Defect and dopant properties of the Aurivillius phase  $\text{Bi}_4\text{Ti}_3\text{O}_{12}$ . *J. Solid State Chem.* **177**, 3660–3665 (2004).
104. Villegas, M., Jardiel, T. & Farías, G. Sintering and electrical properties of  $\text{Bi}_4\text{Ti}_{2.95}\text{W}_x\text{O}_{11.9+3x}$  piezoelectric ceramics. *J. Eur. Ceram. Soc.* **24**, 1025–1029 (2004).
105. Yanovskii, V. K. & Voronkova, V. I. Polymorphism and Properties of  $\text{Bi}_2\text{WO}_6$  and  $\text{Bi}_2\text{MoO}_6$ . *Phys. Status Solidi* **93**, 57–66 (1986).
106. Castro, A., Millan, P., Martinezlope, M. & Torrance, J. Substitutions for  $\text{Bi}^{3+}$  into  $(\text{Bi}_2\text{O}_2)^{2+}$  layers of the Aurivillius  $(\text{Bi}_2\text{O}_2)(\text{A}_{n-1}\text{B}_n\text{O}_{3n+1})$  oxides. *Solid State Ionics* **63–65**, 897–901 (1993).
107. Vannier, R., Mairesse, G., Abraham, F. & Nowogrocki, G. Double substitutions in  $\text{Bi}_4\text{V}_2\text{O}_{11}$ . *Solid State Ionics* **70–71**, 248–252 (1994).
108. Abraham, F., Boivin, J. C., Mairesse, G. & Nowogrocki, G. The bimevox series: A new family of high performances oxide ion conductors. *Solid State Ionics* **40–41**, 934–937 (1990).

109. Goodenough, J. B., Manthiram, A., Paranthaman, M. & Zhen, Y. S. Oxide ion electrolytes. *Mater. Sci. Eng. B* **12**, 357–364 (1992).
110. Sharma, V., Shukla, A. & Gopalakrishnan, J. Effect of aliovalent-cation substitution on the oxygen-ion conductivity of  $\text{Bi}_4\text{V}_2\text{O}_{11}$ . *Solid State Ionics* **58**, 359–362 (1992).
111. Dorrian, J. F., Newnham, R. E., Smith, D. K. & Kay, M. I. Crystal structure of  $\text{Bi}_4\text{Ti}_3\text{O}_{12}$ . *Ferroelectrics* **3**, 17–27 (1972).
112. Newnham, R. E., Wolfe, R. W. & Dorrian, J. F. Structural basis of ferroelectricity in the bismuth titanate family. *Mater. Res. Bull.* **6**, 1029–1039 (1971).
113. Van Uitert, L. G. & Egerton, L. Bismuth Titanate. A Ferroelectric. *J. Appl. Phys.* **32**, 959 (1961).
114. Subbarao, E. C. Ferroelectricity in  $\text{Bi}_4\text{Ti}_3\text{O}_{12}$  and Its Solid Solutions. *Phys. Rev.* **122**, 804–807 (1961).
115. Cummins, S. E. & Cross, L. E. Electrical and Optical Properties of Ferroelectric  $\text{Bi}_4\text{Ti}_3\text{O}_{12}$  Single Crystals. *J. Appl. Phys.* **39**, 2268 (1968).
116. Shimakawa, Y. *et al.* Crystal and electronic structures of  $\text{Bi}_{4-x}\text{La}_x\text{Ti}_3\text{O}_{12}$  ferroelectric materials. *Appl. Phys. Lett.* **79**, 2791–2793 (2001).
117. Chen, Y., Pen, Z., Wang, Q. & Zhu, J. Crystalline structure, ferroelectric properties, and electrical conduction characteristics of W/Cr co-doped  $\text{Bi}_4\text{Ti}_3\text{O}_{12}$  ceramics. *J. Alloys Compd.* **612**, 120–125 (2014).
118. Peng, Z. *et al.* Correlation between lattice distortion and electrical properties

- on Bi<sub>4</sub>Ti<sub>3</sub>O<sub>12</sub> ceramics with W/Ni modifications. *J. Alloys Compd.* **590**, 210–214 (2014).
119. Hirata, T. & Yokokawa, T. Variable-temperature X-ray diffraction of the ferroelectric transition in Bi<sub>4</sub>Ti<sub>3</sub>O<sub>12</sub>. *Solid State Commun.* **104**, 673–677 (1997).
  120. Chu, M. *et al.* Bulk and Surface Structures of the Aurivillius Phases: Bi<sub>4-x</sub>La<sub>x</sub>Ti<sub>3</sub>O<sub>12</sub> (0 ≤ x ≤ 2.00). *Chem. Mater.* **16**, 31–42 (2004).
  121. Qi, H., Qi, Y. & Xiao, M. Leakage mechanisms in rare-earth (La, Nd) doped Bi<sub>4</sub>Ti<sub>3</sub>O<sub>12</sub> ferroelectric ceramics. *J. Mater. Sci. Mater. Electron.* **25**, 1325–1330 (2014).
  122. Nistor, L., van Tendeloo, G. & Amelinckx, S. The paraelectric-ferroelectric phase transition of Bi<sub>4</sub>Ti<sub>3</sub>O<sub>12</sub> studied by electron microscopy. *Phase Transitions* **59**, 135–153 (1996).
  123. Withers, R. L., Thompson, J. G. & Rae, A. D. The crystal chemistry underlying ferroelectricity in Bi<sub>4</sub>Ti<sub>3</sub>O<sub>12</sub>, Bi<sub>3</sub>TiNbO<sub>9</sub>, and Bi<sub>2</sub>WO<sub>6</sub>. *J. Solid State Chem.* **94**, 404–417 (1991).
  124. Hervoche, C. H. & Lightfoot, P. A Variable-Temperature Powder Neutron Diffraction Study of Ferroelectric Bi<sub>4</sub>Ti<sub>3</sub>O<sub>12</sub>. *Chem. Mater.* **11**, 3359–3364 (1999).
  125. Fang, P. H., Robbins, C. R. & Aurivillius, B. Ferroelectricity in the compound Bi<sub>4</sub>Ti<sub>3</sub>O<sub>12</sub>. *Phys. Rev.* **126**, 892–892 (1962).
  126. Zhou, Q., Kennedy, B. J. & Howard, C. J. Structural Studies of the Ferroelectric Phase Transition in Bi<sub>4</sub>Ti<sub>3</sub>O<sub>12</sub>. *Chem. Mater.* **15**, 5025–5028 (2003).

127. Kojima, S. & Shimada, S. Soft mode spectroscopy of bismuth titanate single crystals. *Phys. B Condens. Matter* **219–220**, 617–619 (1996).
128. Jinfang, M., Yabin, H. & Guangtian, Z. Temperature dependence of the Raman active modes in nanocrystalline  $\text{Bi}_4\text{Ti}_3\text{O}_{12}$ . *Solid State Commun.* **97**, 887–890 (1996).
129. Idink, H., Srikanth, V., White, W. B. & Subbarao, E. C. Raman study of low temperature phase transitions in bismuth titanate,  $\text{Bi}_4\text{Ti}_3\text{O}_{12}$ . *J. Appl. Phys.* **76**, 1819–1823 (1994).
130. Tambovtsev, D. A., Skorikov, V. M. & Zheludev, I. S. Preparation and some properties of bismuth titanate single crystals. *Kristallografiya* **8**, 889–893 (1963).
131. Jardiel, T., Caballero, A. & Villegas, M. Aurivillius ceramics:  $\text{Bi}_4\text{Ti}_3\text{O}_{12}$ -based piezoelectrics. *J. Ceram. Soc. Japan* **116**, 511–518 (2008).
132. Seth, V. K. & Schulze, W. A. Grain-oriented fabrication of bismuth titanate ceramics and its electrical properties. *IEEE Trans. Ultrason. Ferroelectr. Freq. Control* **36**, 41–49 (1989).
133. Shulman, H. S., Testorf, M., Damjanovic, D. & Setter, N. Microstructure, Electrical Conductivity, and Piezoelectric Properties of Bismuth Titanate. *J. Am. Ceram. Soc.* **79**, 3124–3128 (1996).
134. Frit, B. & Mercurio, J. P. The crystal chemistry and dielectric properties of the Aurivillius family of complex bismuth oxides with perovskite-like layered structures. *J. Alloys Compd.* **188**, 27–35 (1992).
135. Ehara, S. *et al.* Dielectric Properties of  $\text{Bi}_4\text{Ti}_3\text{O}_{12}$  below the Curie Temperature.

- Jpn. J. Appl. Phys.* **20**, 877–881 (1981).
136. Fouskova, A. Dielectric Properties of Bismuth Titanate. *J. Appl. Phys.* **41**, 2834–2838 (1970).
  137. Sawaguchi, E. & Cross, L. E. Dielectric behavior of  $\text{Bi}_4\text{Ti}_3\text{O}_{12}$  at low temperature. *Mater. Res. Bull.* **5**, 147–152 (1970).
  138. Takahashi, M., Noguchi, Y. & Miyayama, M. Electrical Conduction Mechanism in  $\text{Bi}_4\text{Ti}_3\text{O}_{12}$  Single Crystal. *Jpn. J. Appl. Phys.* **41**, 7053–7056 (2002).
  139. Takahashi, M. Estimation of ionic and hole conductivity in bismuth titanate polycrystals at high temperatures. *Solid State Ionics* **172**, 325–329 (2004).
  140. Noguchi, Y., Matsumoto, T. & Miyayama, M. Impact of Defect Control on the Polarization Properties in  $\text{Bi}_4\text{Ti}_3\text{O}_{12}$  Ferroelectric Single Crystals. *Jpn. J. Appl. Phys.* **44**, L570–L572 (2005).
  141. Hashimoto, T. & Moriwake, H. Oxygen vacancy formation energy and its effect on spontaneous polarization in  $\text{Bi}_4\text{Ti}_3\text{O}_{12}$ : A first-principles theoretical study. *Phys. Rev. B* **78**, 92106 (2008).
  142. Jovalekić, C., Pavlović, M., Osmokrović, P. & Atanasoska, L. X-ray photoelectron spectroscopy study of  $\text{Bi}_4\text{Ti}_3\text{O}_{12}$  ferroelectric ceramics. *Appl. Phys. Lett.* **72**, 1051–1053 (1998).
  143. Park, B. H. *et al.* Differences in nature of defects between  $\text{SrBi}_2\text{Ta}_2\text{O}_9$  and  $\text{Bi}_4\text{Ti}_3\text{O}_{12}$ . *Appl. Phys. Lett.* **74**, 1907–1909 (1999).
  144. Hyatt, N. C., Hriljac, J. A. & Comyn, T. P. Cation disorder in  $\text{Bi}_2\text{Ln}_2\text{Ti}_3\text{O}_{12}$  Aurivillius phases (Ln = La, Pr, Nd and Sm). *Mater. Res. Bull.* **38**, 837–846

- (2003).
145. Shimazu, M., Tanaka, J., Muramatsu, K. & Tsukioka, M. Phase transition in the family  $\text{La}_x\text{Bi}_{4-x}\text{Ti}_3\text{O}_{12}$ : In relation to lattice symmetry and distortion. *Journal of Solid State Chemistry* **35**, 402–406 (1980).
  146. Park, B. H. *et al.* Lanthanum-substituted bismuth titanate for use in non-volatile memories. *Nature* **401**, 682–684 (1999).
  147. Roy, M., Bala, I., Barbar, S. K., Jangid, S. & Dave, P. Synthesis, structural and electrical properties of La and Nb modified  $\text{Bi}_4\text{Ti}_3\text{O}_{12}$  ferroelectric ceramics. *J. Phys. Chem. Solids* **72**, 1347–1353 (2011).
  148. Chen, X. B., Hui, R., Zhu, J., Lu, W. P. & Mao, X. Y. Relaxor properties of lanthanum-doped bismuth layer-structured ferroelectrics. *J. Appl. Phys.* **96**, 5697–5700 (2004).
  149. Rachna, S., Bhattacharyya, S. & Gupta, S. M. Correlating structure, dielectric and impedance studies with lanthanum-ion substitution in bismuth titanate. *Mater. Sci. Eng. B Solid-State Mater. Adv. Technol.* **175**, 207–212 (2010).
  150. Noguchi, Y., Soga, M., Takahashi, M. & Miyayama, M. Oxygen Stability and Leakage Current Mechanism in Ferroelectric La-Substituted  $\text{Bi}_4\text{Ti}_3\text{O}_{12}$  Single Crystals. *Jpn. J. Appl. Phys.* **44**, 6998–7002 (2005).
  151. Shulman, H. S., Damjanovic, D. & Setter, N. Niobium Doping and Dielectric Anomalies in Bismuth Titanate. *J. Am. Ceram. Soc.* **83**, 528–532 (2004).
  152. Bao, Z. H., Yao, Y. Y., Zhu, J. S. & Wang, Y. N. Study on ferroelectric and dielectric properties of niobium doped  $\text{Bi}_4\text{Ti}_3\text{O}_{12}$  ceramics and thin films prepared by PLD method. *Mater. Lett.* **56**, 861–866 (2002).

153. Hou, J., Kumar, R. V., Qu, Y. & Krsmanovic, D. B-site doping effect on electrical properties of  $\text{Bi}_4\text{Ti}_{3-2x}\text{Nb}_x\text{Ta}_x\text{O}_{12}$  ceramics. *Scr. Mater.* **61**, 664–667 (2009).
154. Yao, Y. Y. Doping effect on the dielectric property in bismuth titanate. *J. Appl. Phys.* **95**, 3126–3130 (2004).
155. Wei, T. *et al.* Strong green light emission in Ho doped  $\text{Bi}_4\text{Ti}_3\text{O}_{12}$  ferroelectric ceramics. *Ceram. Int.* **39**, 7211–7215 (2013).

## 2. Experimental procedures

### 2.1. Fabrication of ceramics

The traditional solid oxide route was adopted in this project to fabricate all compositions in the  $\text{Na}_{0.5}\text{Bi}_{0.5}\text{TiO}_3$  (NBT),  $\text{K}_{0.5}\text{Bi}_{0.5}\text{TiO}_3$  (KBT), and  $\text{Bi}_4\text{Ti}_3\text{O}_{12}$  (BiT) series. The reagents used were oxide and carbonate powders, i.e.  $\text{Bi}_2\text{O}_3$  (99.9% purity, across organics, Geel, Belgium),  $\text{Na}_2\text{CO}_3$  (99.5% purity, Alfa Aesar, Ward Hill, MA),  $\text{TiO}_2$  (99.9% purity, Sigma-Aldrich, Gillingham, UK),  $\text{TiO}_2$  (99.5% purity, < 100 nm particle size, Sigma-Aldrich, Gillingham, UK),  $\text{K}_2\text{CO}_3$  (99.9+% purity, Fisher Scientific, Loughborough, UK),  $\text{La}_2\text{O}_3$  (99.99% purity, Sigma-Aldrich, Gillingham, UK),  $\text{MgO}$  (99.9% purity, Alfa Aesar, Ward Hill, MA) and  $\text{Nb}_2\text{O}_5$  (99.9% purity, Sigma-Aldrich, Gillingham, UK). All the materials are dried first at various drying temperatures (300 °C for  $\text{Bi}_2\text{O}_3$ ,  $\text{Na}_2\text{CO}_3$  and  $\text{K}_2\text{CO}_3$ , and 900 °C for  $\text{TiO}_2$ ,  $\text{La}_2\text{O}_3$ ,  $\text{MgO}$  and  $\text{Nb}_2\text{O}_5$ ) for 8 h and mixed in stoichiometric amounts to obtain 30 g batches. In each case, the mixture was ball milled in a 500 mL HDPE bottle with isopropanol and 300 g of yttria-stabilized zirconia milling media for 6 h. The powder was dried at 80 °C in a chamber oven to remove the isopropanol and then sieved with a mesh size of 250  $\mu\text{m}$  to separate the milling media. The powder was reacted twice in the alumina crucible closed with a lid for 2 h. The reactions were carried out in a chamber furnace with a heating and cooling rate of 5 °C•min<sup>-1</sup>. Various suitable reaction temperatures were applied to different compositions. After each reaction, the same milling, drying and sieving procedure was applied; the only exception was the milling after the first reaction was 4 h. The powder was uniaxial pressed in an 8 mm diameter die with a pressure of 0.5 ton, and then Cold Isostatic Pressing with a pressure of 30 PSI was applied to the green pellets. The green pellets were sintered in an alumina boat with a heating and cooling rate of 5 °C•min<sup>-1</sup>. During sintering the green pellets were buried in sacrificial powder of the same composition.

## 2.2. Ceramic density

### 2.2.1. Theoretical density

The theoretical density of ceramics for each composition was calculated from the atomic weight and unit cell dimensions with following formula,

$$\rho_{th} = \frac{MW \cdot n}{V_{cell} \cdot N_A}$$

where  $\rho_{th}$  is theoretical density, MW is molecular weight, n is the number of atoms in the unit cell,  $V_{cell}$  is the unit cell volume and  $N_A$  is Avogadro's number.

The volume of a unit cell for each composition was obtained from the lattice parameters using X-ray Diffraction data from the fully reacted powder.

### 2.2.2. Measured Density

In this project, the measured density of each sample was recorded using Archimedes' principle, i.e. when an object is immersed in a liquid, the apparent weight will decrease by the same weight of the volume of the liquid it displaced. Here the liquid was distilled water and the object was a sintered pellet. The actual density was calculated using the following formula,

$$\rho_A = \frac{m_1}{m_1 - m_2} \cdot \rho_{H_2O}$$

where  $\rho_A$  is actual density,  $m_1$  is the weight of pellet in air,  $m_2$  is the weight of pellet in water and  $\rho_{H_2O}$  is the density of water corresponding to the water temperature during the experiment.

### 2.3. X-Ray diffraction

X-Ray Diffraction (XRD) was used to identify the phases present, establish phase purity and to calculate lattice parameters of single phase products in the series of samples. All compositions were measured by XRD during several stages of the ceramic processing. XRD was first employed on fully reacted powders after a double calcine and also on a crushed pellet of sintered ceramic.

A powdered sample was placed on a transparent plastic disc and mixed with PVA glue and dried with an electric blower. Pellet samples were crushed using a pellet crusher and then ground with a mortar and pestle in acetone to transform into a fine powdered sample. The disc was inserted to a sample holder and put into a STOE-STADI PSD diffractometer with Cu radiation. Scans to determine the phases present and establish phase purity were taken in the two theta range 20-80°, whereas to calculate lattice parameters the range was extended to 20-100°. A step size of 0.2° was used for all measurements with a scan rate of 20 or 80 s/step to determine the phase(s) or calculate lattice parameters, respectively. The diffraction patterns were analysed with Win X<sup>POW</sup> software (version 2.10, STOE & Cie GmbH, Germany). Silicon was used as a standard to calibrate peak positions to calculate the lattice parameters. A linear calibration polynomial was created according to the Silicon peaks and then the position of all peaks in the pattern could be calibrated. A least squares fit was used to obtain the final lattice parameters. For all refinements the final 2Theta window was less than 0.04° and the maximum delta (2Theta) was less than 3 times of average delta (2Theta).

### 2.4. Scanning electron microscopy (SEM)

To prepare samples for SEM, sintered pellets were firstly ground by 800 and 1200 Grit

waterproof sand paper, then polished with 6, 3 and 1  $\mu\text{m}$  diamond paste on a synthetic polishing cloth. The polished samples were cut in half and a thermal etching process with heating at 90% of the sintering temperature for 1 h was applied on one of them. Both etched and un-etched parts were fixed on an aluminum SEM sample holder by silver paste. The sample and sample holder were then carbon coated to prevent any charging effects during operation.

Determination of microstructure information was carried out using a JEOL JSM 6400 scanning electron microscope (JEOL Ltd., Tokyo, Japan) using an accelerating voltage of 20 kV and a probe diameter of 9 - 11  $\mu\text{m}$ . During operation, a Noran energy dispersive (EDS) X-ray analyzer (Link Analytical Ltd., High Wycombe, Bucks, UK) was used for most samples to verify the chemical composition. The data were recorded and analyzed by using LINK ISIS software.

## 2.5. Transmission electron microscopy (TEM)

Sintered ceramics were thinned using a Gatan Disc Grinder to a thickness of  $< 30 \mu\text{m}$  with a series of silicon carbide sand paper. A 2000  $\mu\text{m}$  copper support ring was then glued (Epoxy resin, Wellingbrough, UK) on to the sample. Ion milling was applied on a sample by a GATAN dual ion mill 600 model (Pleasanton, California, USA). The ion mill was firstly operated at 5 kV and 0.5 mA for both guns with an incidence angle of  $15^\circ$  and then change to  $12^\circ$  after the sample was sufficiently thinned.

All measurements were performed in house by Dr. Huairuo Zhang on a Philips EM420 TEM (120 kV, Eindhoven, Netherlands) and a JEOL 3010 TEM (300 kV, JEOL Ltd., Tokyo, Japan), both equipped with a high angle annular dark-field (HAADF) detector and a high tilt angle specimen holders.

## 2.6. Thermogravimetric analysis (TGA)

TGA is a method of thermal analysis. It measures the mass change as a function of temperature (with a heating/cooling rate) or time (with a constant temperature). The measurements were taken using a PerkinElmer Pyris 1 (PerkinElmer, Massachusetts, USA) and a Setaram SETSYS Evolution (SETARAM Instrumentation, Caluire, France). For each measurement, 20-30 mg of powder sample was placed on a piece of platinum and put into an alumina crucible. The heating/cooling rate was fixed at  $20\text{ }^{\circ}\text{C}\cdot\text{min}^{-1}$  but the measured temperature ranges varied according to each sample.

## 2.7. Differential scanning calorimetry (DSC)

DSC is a technique to determine the difference in amount of heat needed to maintain the same temperature within a sample and a reference. A Netzsch DSC 404 C Thermal analyzer (Netzsch, Selb, Germany) was used in this project. The samples used here were calcined powder or crushed pellet. 20-30 mg of powder was weighed and put into the sample crucible beside the reference crucible containing  $\text{Al}_2\text{O}_3$  and then subjected to a heating/ cooling rate of  $10\text{ }^{\circ}\text{C}\cdot\text{min}^{-1}$ . The measured temperature ranges were dependent on the sample.

## 2.8. Inductance-capacitance-resistance (LCR) Meter

The pellets were coated with gold paste (T-10112, Metalor Technologies UK Ltd., Birmingham, UK) on both side and heated to  $800\text{ }^{\circ}\text{C}$  for 2 h with a heating/cooling rate of  $10\text{ }^{\circ}\text{C}/\text{min}$ . The pellet was placed inside an alumina jig in a tube furnace. The results were taken by a Hewlett Packard 4284A Precision LCR meter (Hewlett-Packard GmbH, Böblingen, Germany). The capacitance and dielectric loss were measured at 4 fixed frequencies, 1, 10 and 100 kHz and 1 MHz. Most measurements were recorded every minute from room temperature to  $900\text{ }^{\circ}\text{C}$  with a heating/cooling rate of  $1\text{ }^{\circ}\text{C}/\text{min}$ . The permittivity was extracted from the capacitance using the following formulae,

$$\varepsilon_r = \frac{C}{\varepsilon_0} \cdot GF$$

$$GF = \frac{t}{A}$$

where  $\varepsilon_r$  is the relative permittivity, C is Capacitance,  $\varepsilon_0$  is the permittivity of free space, GF is the geometric factor for a normalised sample shape, t is sample thickness and A is the area of the face of a pellet.

## 2.9. Impedance spectroscopy

Impedance spectroscopy was used to determine the electrical properties of the ceramics. A small ac voltage is applied over a wide range of frequency, typically  $10^{-2}$  to  $10^7$  Hz. Compared with other techniques, the main advantage of Impedance Spectroscopy is the ability of distinguish different electro-active regions in a ceramic by their different time constants. In this project, Impedance measurements were performed using temperature and oxygen partial pressure as two variables.

The samples were prepared in the same way as the LCR samples. They were loaded into a jig and placed in a tube furnace. An Agilent E4980A Precision LCR Meter (Agilent Technology, California, USA) with a frequency range 2 Hz – 2 MHz was used for open air measurements and a Solartron SI 1260 Impedance analyser (Solartron Group Ltd, Farnborough, Hampshire, UK) with a frequency range from 10  $\mu$ Hz to 32 MHz was used for variable oxygen partial pressure and low frequency measurements. The applied voltage was 100 mV for all samples and a geometric factor was used to normalise the results for sample geometry. ZView (Scribner Associates Inc, USA) was used for data analysis.

The impedance data of each electrically active component (e.g. grain, grain boundary or surface layer) in an electroceramic can ideally be modelled as a 'parallel

RC element' which is characterised by its resistance (R) and capacitance (C). The various components can be separated by their different relaxation times or time constants ( $\tau$ ) which is determined only by R and C,

$$\tau = RC$$

$$\omega_{max}RC = 1$$

where  $\omega_{max}$  is the frequency of maximum loss.

To analyse Impedance data, there are 4 important complex formalisms: impedance  $Z^*$ ; admittance  $Y^*$ ; electric modulus  $M^*$ ; and permittivity  $\epsilon^*$ . They can be defined as follows:

$$Z^* = Z' - jZ''$$

$$Y^* = (Z^*)^{-1} = Y' + jY''$$

$$M^* = j\omega C_0 Z^* = M' + jM''$$

$$\epsilon^* = (M^*)^{-1} = \epsilon' + j\epsilon''$$

Since these four basic formalisms are interrelated, the same set of data may be plotted in four different forms. The most widely used complex plots to analyse data for electroceramics are  $Z^*$  and  $M^*$ .

A general strategy for analysis and interpretation of measured data is to establish an equivalent circuit that simulates the experimental response. The equivalent circuit shown in Figure 2-1 is a common 'parallel RC element' which represents the response of a single component. In this ideal case, both  $Z^*$  and  $M^*$  plots show a perfect semicircle where the diameter of the former is R and for the latter is  $1/C$ .

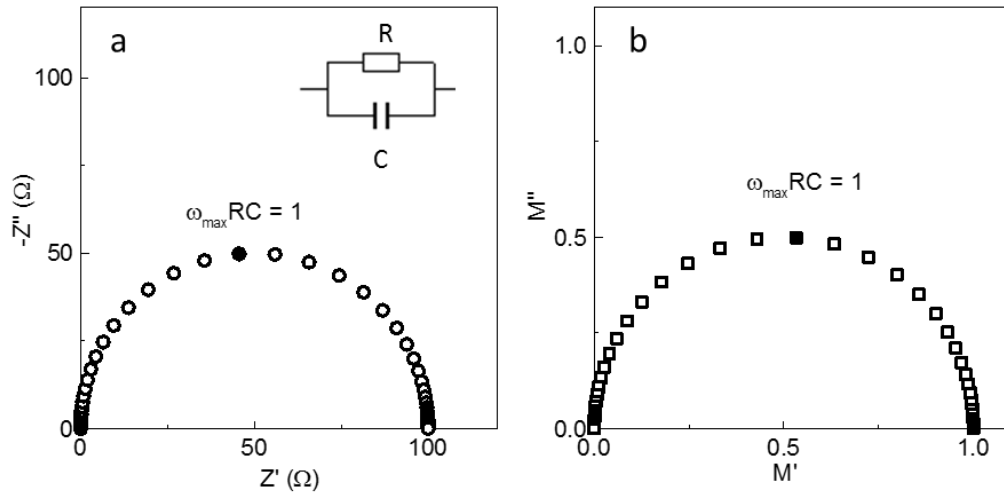


Figure 2-1. (a) Idealized  $Z^*$  and (b)  $M^*$  plots showing a single semi-circular arc for a parallel RC element.

In many case, however, it is inadequate to model the ac response of real materials based only on ideal resistive and capacitive circuit elements. Additional elements such as the constant phase element (CPE) and Warburg-type resistance (W) element have been created to simulate non-ideal behaviour such as departures from an ‘ideal’ Debye-like response and diffusion phenomena at the sample/electrode interface, respectively.

A CPE can simulate the so called ‘power law’ dependence of the impedance response on frequency which is commonly observed in ionic conductors and is responsible for non-ideal Debye peaks for the grain response in  $Z''$  and  $M''$  spectra. A CPE has an impedance defined as

$$Z_{CPE}^* = [A(j\omega)^n]^{-1}$$

where A and n are two frequency-independent parameters which usually depend on temperature. The values of A have been linked to intrinsic and extrinsic processes associated with various electroactive components such as sample/electrode interfaces and/or bulk conduction processes. The value of n is in the range  $0 \sim 1$  and a CPE simplifies to an ideal capacitor for  $n = 1$  and an ideal resistor for  $n = 0$ . In general, when  $n \neq 0$  or  $1$  a CPE describes a distribution of relaxation times. A high frequency

dispersion can be observed in  $Y'$  spectra which can be defined as

$$Y' = 1/R + A\omega^n \cos(n\pi/2)$$

as shown in Figure 2-2 (a).

The impedance response from the metal/electrode interface can be a source of useful information on the carrier type(s) in a material but often shows non-ideal behaviour. A good example is where metal electrodes applied on an ionic conductor can 'block' (either fully or partially) the charge carrier. For a perfect blocking electrode (i.e. migrating ions pile up at the electrode interface and can't penetrate the metal electrode) the material-electrode interface acts as an ideal capacitor. The impedance response of this interface can be expressed as

$$-Z'' = 1/\omega C$$

and introduces a low frequency, vertical spike-like response in  $Z^*$  plots. In many cases, blocking is never perfect and there will be some level of diffusion of the migrating ions into the metal electrode, i.e. leakage. This kind of leakage can be treated as an infinite diffusion process of charge carriers which essentially leads to  $|Z'| = |Z''|$  (a spike with an inclined angle of  $45^\circ$ ), Figure 2-2 (b). This type of response is commonly referred to as the Warburg semi-infinite linear diffusion response which is often a sign for the existence of ionic conduction in materials.

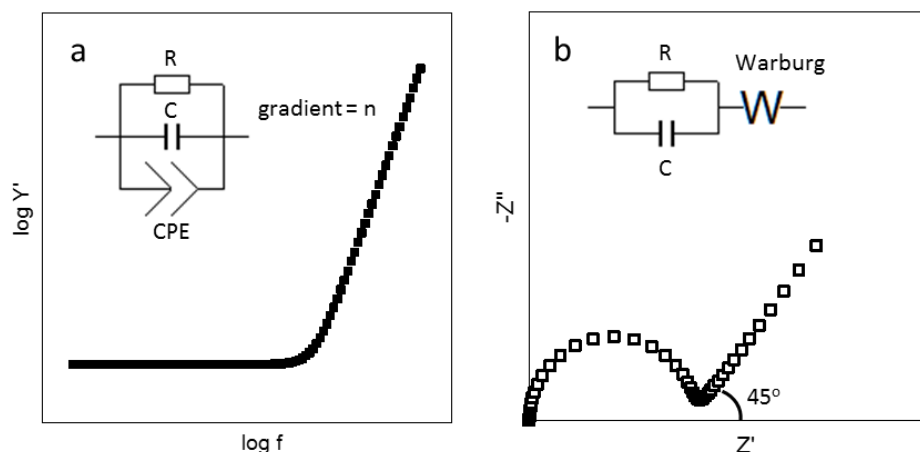


Figure 2-2. (a) Typical conductivity-frequency spectrum and (b) Warburg response in  $Z^*$  for an ionic conductor.

In this project, the largest Debye-like peak from the imaginary component of the complex electric modulus ( $M''$ ) spectroscopic plots was used to obtain the conductivity and capacitance of bulk region, Figure 2-3. This is because the  $M''$  plot is dominated by the element with the lowest capacitance which is normally the bulk. At the peak maximum, the following relationship holds:

$$\omega_{max}RC = 1$$

and the R and C can be calculated from the  $\omega_{max}$  and C where

$$C = \frac{1}{2M''}$$

Arrhenius plots of the log of conductivity (where conductivity =  $1/R$ ) versus  $1000/T$  were plotted and the activation energy associated with the bulk conduction process obtained from the slope of the plots.

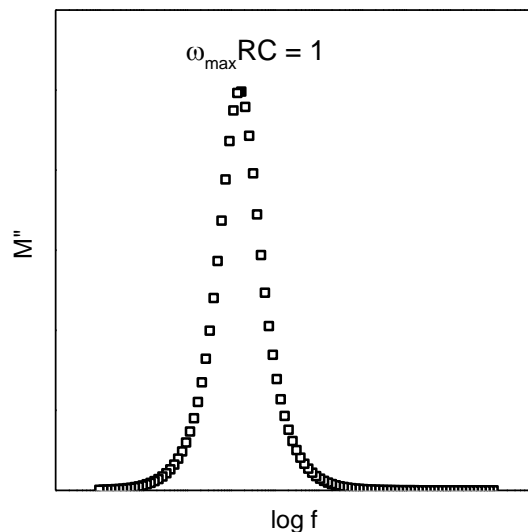


Figure 2-3. Debye-like peak in an  $M''$  spectrum for a parallel RC element.

## 2.10. Piezoelectric property measurements

Ceramics with less than 0.5 mm thickness were prepared for piezoelectric measurements. Gold electrodes were applied on both faces of pellets in the same way as for LCR samples. Samples were initially poled in a silicon bath at 150 °C for 10 min with an external electric field of 20-80  $\text{kV}\cdot\text{cm}^{-1}$ . The piezoelectric charge constant ( $d_{33}$ )

was measured immediately on a Berlincourt-type meter (Piezotest, Model PM300, London, UK) and further measurements were taken until a stable reading was obtained. The applied force was 0.25 N at a frequency of 110 Hz.

### 2.11. Oxygen ion transport number measurements

The EMF transport number measurement was taken by a ProboStat system (NorECs Norwegian Electro Ceramics AS, Oslo, Norway). A YSZ tube with electrodes on both sides was prepared and used as a  $pO_2$  monitor. A pellet sample was put at one end of the tube and sealed with a glass frit sealant. Pellet samples were 20 mm in diameter and 1 mm in thickness and coated with Pt electrodes on both sides. 4 Pt wires were connected to the inner sample face, outer sample face, inner YSZ tube and outer YSZ tube, respectively.

During measurements, the outer tube atmosphere was kept as air and the inner tube atmosphere changed between  $O_2$  and  $N_2$  to create a  $pO_2$  gradient. The  $pO_2$  difference was monitored by the voltage difference across the YSZ tube. As YSZ is a pure ionic conductor, the ratio of the voltage difference between the two sample electrodes to the YSZ electrodes was taken as the transport number for oxygen ions. Both the voltage across the YSZ tube and the sample were measured by a Keithley 182 sensitive digital voltmeter (Keithley, Ohio, USA). The set up for EMF measurements is shown in Figure 2-4.

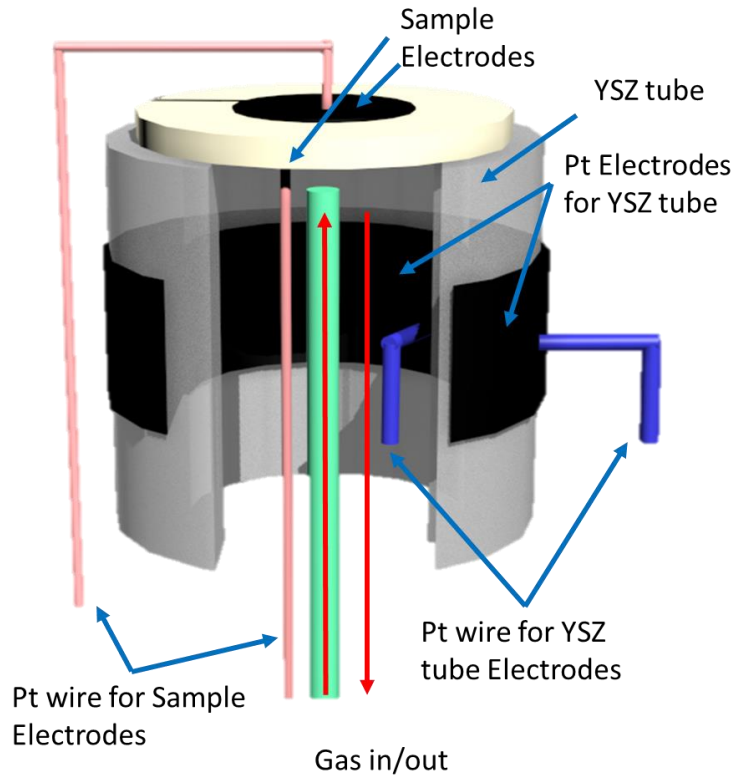


Figure 2-4. Schematic diagram of the set-up for EMF measurements.

When no external current is applied, the voltage between the inner and outer electrode is:

$$E = t_{ion} \frac{kT}{4e} \ln\left(\frac{P_{O_2}^{in}}{P_{O_2}^{out}}\right)$$

$$t_{ion} = \frac{\sigma_O}{\sigma_{tot}}$$

where  $k$  is the Boltzmann constant,  $T$  is temperature,  $e$  is the electronic charge,  $t_{ion}$  is the ion transport number and  $\sigma_O$  and  $\sigma_{tot}$  are the oxide ion and total conductivity of a material, respectively.

Since the YSZ tube and test sample are under the same conditions of  $pO_2$  gradient and temperature,  $t_{ion}$  for the test sample can be expressed as

$$t_{ion,sample} = \frac{E_{sample}}{E_{YSZ}} t_{ion,YSZ}$$

As YSZ is a solid electrolyte at high temperature ( $t_{\text{ion}} \sim 1$ ), the ratio of the voltage difference between the sample electrodes to the YSZ electrodes is taken as the oxygen ion transport number.

Various temperatures in the range 600 ~ 800 °C were chosen to take the measurements dependent on different compositions. All readings were taken on cooling with a cooling rate of 3 °C/min and each point was equilibrated for 24 hours prior to taking readings.

## 2.12. $^{18}\text{O}$ tracer diffusion coefficient measurements with time-of-flight secondary ion mass spectrometry (ToF-SIMS)

The  $^{18}\text{O}$  TOF-SIMS diffusion measurements were performed by Dr. Roger A. De Souza and members of his research group (RWTH Aachen University). The samples (ceramic pallets) were annealed in an  $\text{O}^{18}$  atmosphere at various temperatures then cut, rotated and reassembled as shown in Figure 2-5. The size of dashed box is not to scale compare to the rest of sketch as the actual diffusion profiles are normally equal to/less than several hundred  $\mu\text{m}$ . The sampling area (cross section) was then bombarded with  $\text{Ga}^{3+}$  ions and the resultant secondary ions analysed by Time-of-Flight Secondary Ion Mass Spectrometry (IONTOF GmbH, Münster, Germany) to determine their species and concentration. A depth profile of  $^{18}\text{O}$  ( $^{18}\text{O}$  concentration against distance) was then obtained. Time-of-Flight Secondary Ion Mass Spectrometry (IONTOF GmbH, Münster, Germany) was then used to measure the depth profile. The oxygen diffusion coefficient,  $D^*$  and surface exchange coefficient,  $k^*$  can then calculated from the depth profile. See Ref. 1 for more detail.

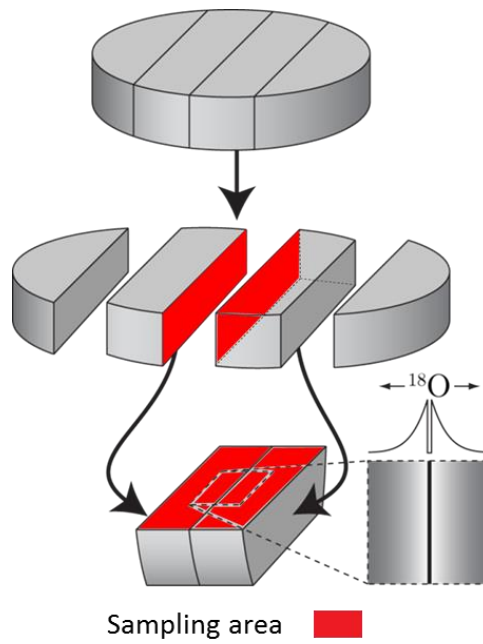


Figure 2-5. Sample preparation for  $^{18}\text{O}$  TOF-SIMS diffusion measurements.<sup>1</sup>

### 2.13. Reference

1. Li, M. *et al.* A family of oxide ion conductors based on the ferroelectric perovskite  $\text{Na}_{0.5}\text{Bi}_{0.5}\text{TiO}_3$ . *Nat. Mater.* **13**, 31–5 (2014).

### 3. Non-stoichiometry in the perovskite phase



As discussed in the literature review (Chapter 1),  $\text{Na}_{0.5}\text{Bi}_{0.5}\text{TiO}_3$ , NBT, is a well known ferroelectric material but depending on the initial composition and the processing conditions to fabricate single crystals and/or ceramics it can have high levels of leakage conductivity at modest temperatures. Hiruma et al. have shown the room temperature dc resistivity of NBT ceramics to be highly sensitive to A-site non-stoichiometry based on the nominal Na/Bi ratio of the starting reagents (Figure 3-1).<sup>1</sup> The difference in dc resistivity caused by this non-stoichiometry can be  $\sim 3$  orders of magnitude; however, they did not resolve the type of charge carrier(s) or the origin(s) of the leakage current.

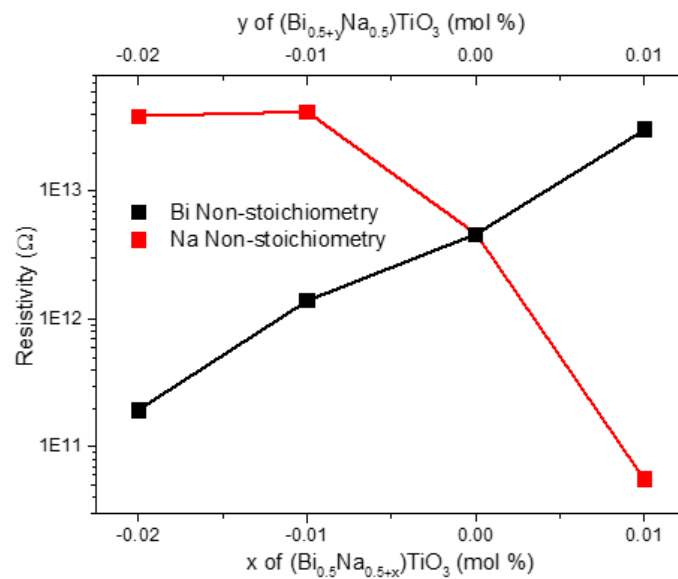


Figure 3-1. Variation of room temperature dc resistivity versus A-site non-stoichiometry in NBT ceramics.<sup>1</sup>

More recently, Li *et al.* have reported the electrical properties of NBT using impedance spectroscopy and have shown it to be highly sensitive to low levels of Bi non-stoichiometry.<sup>2</sup> It can either be an oxide ion conductor or an electrical insulator with more than 3 orders of magnitude difference in the bulk conductivity (Figure 3-2).

It is also noteworthy that the activation energy for bulk conduction of NBT for  $\text{Bi} \leq 0.50$  is relatively low and undergoes a change from  $\sim 0.85$  to  $\sim 0.40$  eV at  $\sim 320$  °C which is consistent with the permittivity maximum; whereas for insulating NBT with  $\text{Bi} > 0.50$  the activation energy for bulk conduction is much higher ( $\sim 1.7$  eV) which is close to half of the reported NBT optical band gap,  $E_g$ , of  $\sim 3.0$ – $3.5$  eV, indicating it is dominated by intrinsic electronic conduction.

Figure 1 in reference 2

Figure 3-2. Arrhenius-type plots of bulk conductivity for selected NBT samples.<sup>2</sup>

Electromotive force (EMF) measurements under the  $\text{pO}_2$  gradient created by air/ $\text{N}_2$  gas were reported to verify the presence of oxide ion conduction as well as to determine its share of the total conductivity. Results showed that in nominally stoichiometric NBT (i.e.  $\text{Na} = \text{Bi} = 0.50$ ) an oxide ion transport number,  $t_{\text{ion}} > 0.90$  was observed at  $600 \sim 700$  °C and reduced to  $\sim 0.84$  at  $800$  °C (Figure 3-3); whereas, Bi deficient and Mg-doped NBT ( $\text{Na}_{0.5}\text{Bi}_{0.49}\text{Ti}_{0.98}\text{O}_{2.965}$ ) possessed even higher  $t_{\text{ion}}$  compared to nominally stoichiometric NBT. On the other hand, insulating NBT showed  $t_{\text{ion}} \sim 0.1$  over the same temperature range proving the predominant intrinsic electronic conduction mechanism in this material.

Figure 2 in reference 2

Figure 3-3. Oxygen ionic transport number,  $t_{\text{ion}}$ , for selected NBT samples from EMF measurements using air/ $\text{N}_2$  gas.<sup>2</sup>

The predominance of oxide ion conduction in conducting NBT was further confirmed by  $^{18}\text{O}$  tracer diffusion measurements using isotopic exchange and time of flight secondary-ion mass spectrometry (Figure 3-4). The tracer diffusion coefficient,  $D^*$ , of stoichiometric NBT was  $2.64 \times 10^{-10}$   $\text{cm}^2/\text{s}$  with a surface exchange coefficient,  $k^*$ , of  $2.97 \times 10^{-9}$   $\text{cm}/\text{s}$  at  $632$  °C whereas a  $D^*$  of  $5.24 \times 10^{-10}$   $\text{cm}^2/\text{s}$  with  $k^* \sim 1.73 \times 10^{-6}$   $\text{cm}/\text{s}$  was observed at  $608$  °C. The total diffusion profile is  $\sim 150$   $\mu\text{m}$  in both cases,

considering the grain size of conducting NBT is  $\sim 20 \mu\text{m}$ , the  $^{18}\text{O}$  ions penetrated several grains in these measurements. Ionic conduction can be calculated from  $D^*$  with the Nernst–Einstein equation:

$$\sigma_i = \frac{C_i(Ze)^2}{kT} D^*$$

where  $C_i$  is the oxygen concentration ( $5.095 \times 10^{22} \text{ cm}^{-3}$ ),  $Z$  is the charge of charge carrier (2),  $k$  is the Boltzmann constant ( $1.38 \times 10^{-23} \text{ J/K}$ ). The calculated oxygen ion conductivity is  $1.105 \times 10^{-4} \text{ S/cm}$  at  $632 \text{ }^\circ\text{C}$  and  $2.254 \times 10^{-4} \text{ S/cm}$  at  $608 \text{ }^\circ\text{C}$ . The calculated conductivity is consistent with the total resistivity of NBT in the same temperature range  $\sim 4 \text{ k}\Omega\cdot\text{cm}$  ( $2.54 \times 10^{-4} \text{ S/cm}$ , Figure 3-11 (a)) which proves that NBT in this temperature range is dominated by oxide ion conduction.

(a) Figure 3 and (b) Figure S5 in reference [2]

Figure 3-4.  $^{18}\text{O}$  tracer diffusion profile of  $\text{Na}_{0.50}\text{Bi}_{0.50}\text{TiO}_3$  (a) after exchange at  $632 \text{ }^\circ\text{C}$  for  $\sim 22000 \text{ s}$  with  $p^{18}\text{O}_2 \sim 508 \text{ mbar}$  and (b) after exchange at  $608 \text{ }^\circ\text{C}$  for  $\sim 8040 \text{ s}$  with  $p^{18}\text{O}_2 \sim 750 \text{ mbar}$ .<sup>2</sup>

From the combination of impedance ( $p\text{O}_2$  independent bulk response and low frequency spike in  $Z^*$  plots), EMF (near unity  $t_{\text{ion}}$ ) and  $^{18}\text{O}$  tracer diffusion measurement (high  $D^*$  consistent with total conductivity measured using Impedance Spectroscopy) results, conducting NBT (with  $\text{Bi} \leq 0.50$ ) was established to be predominantly an oxide ion conductor; whereas, insulating NBT (with  $\text{Bi} > 0.5$ ) exhibit mixed ionic-electronic conduction that is dominated by the electronic component. It is well known that oxygen vacancies are critical in perovskites to provide hopping pathways for the oxide ions. The origin of oxygen vacancies in stoichiometric NBT was attributed to the loss of  $\text{Bi}_2\text{O}_3$  during processing. In order to compensate for the Bi-loss while maintaining charge balance, oxygen vacancies are generated according to the Kroger-Vink equation:



The level of oxygen vacancies produced in stoichiometric NBT was therefore

reported to be strongly dependent on the ceramic processing procedures/conditions employed and can explain the wide variation in leakage conductivity of NBT materials reported in the literature.

### 3.1. Bi non-stoichiometry

This chapter is an in-depth investigation on the influence of A-site non-stoichiometry and the importance of pre-drying the starting reagents (especially hygroscopic  $\text{Na}_2\text{CO}_3$ ) prior to fabrication of NBT ceramics. To investigate the A-site non-stoichiometry, two series (x and y) of materials have been prepared. The x-series investigates nominal Bi non-stoichiometry based on the general formula  $\text{Na}_{0.50}\text{Bi}_{0.50+x}\text{TiO}_{3+x/2}$  and the y-series investigates nominal Na non-stoichiometry based on the general formula  $\text{Na}_{0.50+y}\text{Bi}_{0.50}\text{TiO}_{3+1/2y}$ . This work follows on from that conducted by Dr Ming Li at Sheffield University with the aim of investigating finer increments of A-site non-stoichiometry in an attempt to fully establish the solid solution limits and to better characterise the insulating to oxide ion conducting switch over.

#### 3.1.1. Phase purity and microstructure

Samples in the x-series with both Bi-deficient and Bi-rich starting compositions based on the general formula  $\text{Na}_{0.50}\text{Bi}_{0.50+x}\text{TiO}_{3+x/2}$  ( $-0.01 < x < 0.20$ ) have been investigated to establish the influence of the Bi-content on the non-stoichiometry and electrical properties of NBT.

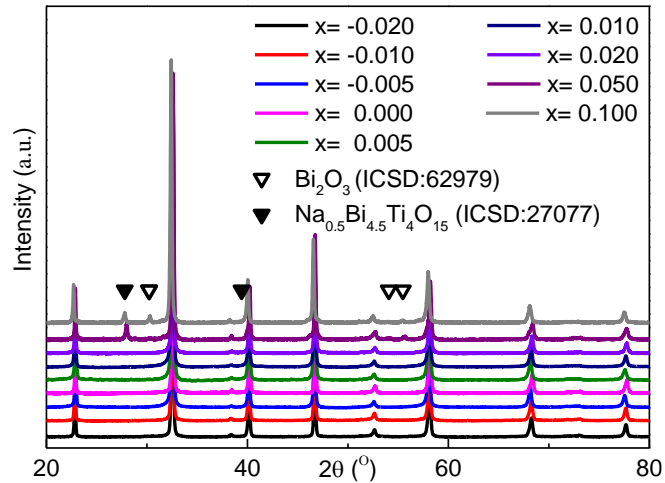


Figure 3-5. Room temperature X-ray powder diffraction data for the  $\text{Na}_{0.5}\text{Bi}_{0.5+x}\text{TiO}_{3+3/2x}$  series.

XRD patterns at room temperature obtained from crushed ceramics of selected samples from the  $x$ -series are shown in Figure 3-5. The peaks from the NBT phase suggest all compositions in this series adopt a monoclinic/rhombohedral structure at room temperature which is slightly distorted from the ideal cubic structure. No additional reflections are observed within the compositional range  $-0.02 \leq x \leq 0.02$  whereas secondary phases are clearly observed for  $x = 0.05$  and  $0.10$  (Figure 3-5);  $\text{Bi}_2\text{O}_3$  (space group  $P\bar{4}2_1c$ ) and  $\text{Na}_{0.5}\text{Bi}_{4.5}\text{Ti}_4\text{O}_{15}$  (space group  $I4/mmm$ ) were identified as secondary phases based on the XRD patterns.

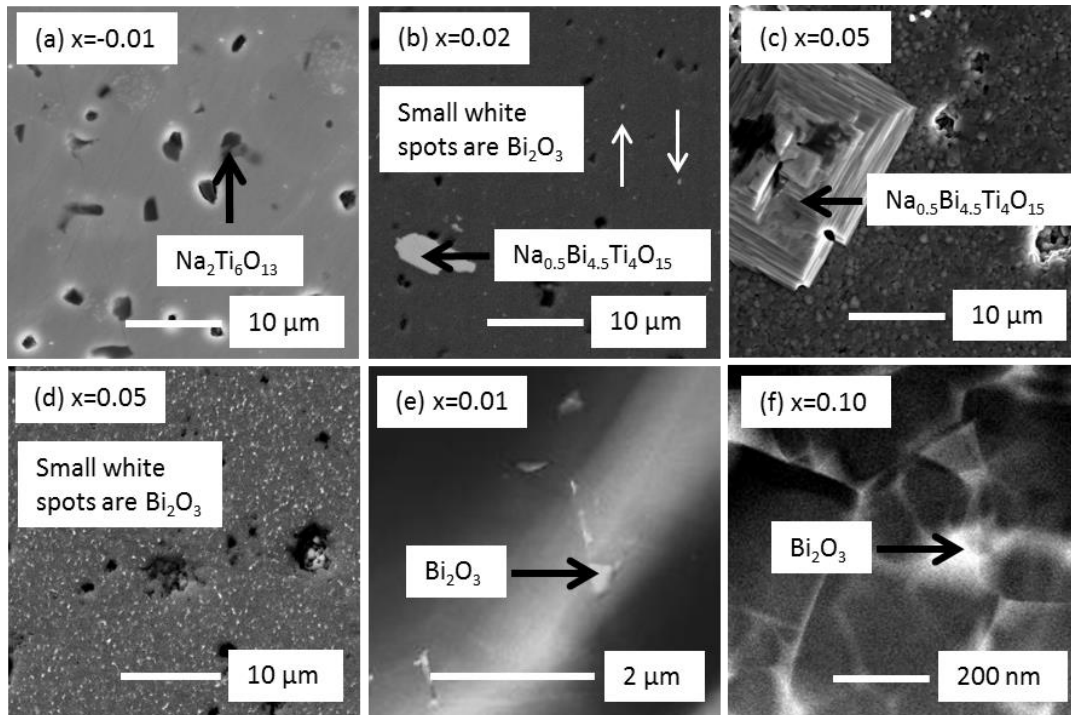


Figure 3-6. SEM Secondary electron images (a), (c) and back scattered electron images (b), (d) for selected  $\text{Na}_{0.50}\text{Bi}_{0.50+x}\text{TiO}_{3+3x/2}$  ceramics. Samples were polished without thermal etching for (a) and (b) and were polished then thermally etched for (c). HAADF-STEM (Z-contrast) images for (e)  $x = 0.01$  and (f)  $x = 0.10$  where bright areas represent the  $\text{Bi}_2\text{O}_3$  secondary phase.

The existence of  $\text{Na}_{0.5}\text{Bi}_{4.5}\text{Ti}_4\text{O}_{15}$  has been confirmed by SEM/EDX results on polished (without thermal etching)  $x = 0.02$  and  $0.05$  samples, Figure 3-6 (b) and (c). On the other hand,  $\text{Bi}_2\text{O}_3$  forms as very fine particles dispersed in the NBT matrix which can be observed as small bright dots in backscattering images, Figure 3-6 (b) and (d). It is unfeasible to confirm the composition of the small particles since the spot size of the EDX on the SEM is much larger than the particles. A combination of high angle annular dark field scanning transmission electron microscopy (HAADF-STEM, Z-contrast) images and EDX mapping (performed by Dr H Zhang) were therefore employed to confirm this phase. EDX mapping results in Figure 3-7 indicate this phase has a much higher Bi content and much lower Na, Ti content than the matrix which means it likely to be the  $\text{Bi}_2\text{O}_3$  phase observed by XRD. In addition, this secondary

phase is mostly located in the triple point junctions between grains and along selected grain boundaries as shown in Figure 3-6 (e) and (f).

Figure 3 in reference 8

Figure 3-7. (a) HAADF-STEM (Z-contrast) images for  $x = 0.01$  sample and EDX mapping results of the same area for (b) Bi-mapping, (c) Na-mapping and (d) Ti-mapping.

For the Bi-deficient samples, although XRD shows them to be single phase, SEM/EDX results reveal the presence of  $\text{Na}_2\text{Ti}_6\text{O}_{13}$  as a secondary phase, Figure 3-6 (a). The chemical composition of the main phase analysed by SEM/EDX is listed in Table 3-1. The bulk composition between these samples cannot be distinguished from each other within instrumental resolution and standard errors. The Bi content also influences the average grain size of the ceramics. The grain size of NBT decreases from  $\sim 10 \mu\text{m}$  for  $x \leq -0.01$  to  $\sim 100 \text{nm}$  for  $x \geq 0.10$ , Figure 3-6 (f) and Figure 3-8.

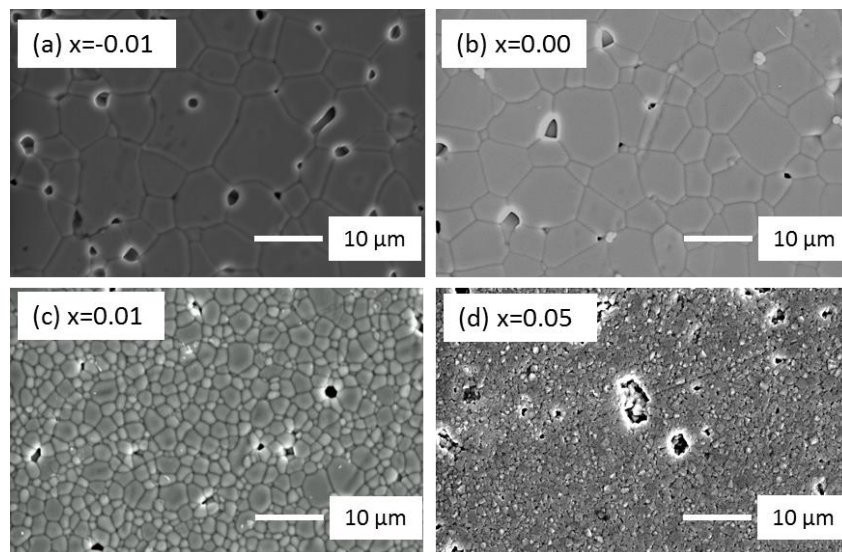


Figure 3-8. SEM micrographs for (a)  $x = -0.01$ , (b)  $x = 0.00$ , (c)  $x = 0.01$  and (d)  $x = 0.05$ . All samples were polished and thermally etched prior to SEM.

Table 3-1. Chemical composition (relative cation at%) of the main phase and associated error (standard deviation) by SEM/EDX of selected samples in the x-series.

Composition		Na (at%)	Bi (at%)	Ti (at%)
<b>x = 0.05</b>	Main phase	24.4 (±0.4)	25.8 (±0.5)	49.8 (±0.5)
	$\text{Na}_{0.5}\text{Bi}_{4.5}\text{Ti}_4\text{O}_{15}$	5.2 (±0.7)	50.9 (±0.7)	44.0 (±0.6)
<b>x = 0.02</b>	Main phase	24.3 (±0.7)	25.9 (±0.5)	49.9 (±0.3)
	$\text{Na}_{0.5}\text{Bi}_{4.5}\text{Ti}_4\text{O}_{15}$	5.5 (±0.1)	49.5 (±0.5)	45.1 (±0.4)
<b>x = 0.01</b>	Main phase	24.71 (±0.40)	25.43 (±0.36)	49.85 (±0.41)
<b>x = 0.00</b>	Main phase	25.03 (±0.43)	25.17 (±0.21)	49.80 (±0.36)
<b>x = -0.01</b>	Main phase	25.08 (±0.32)	24.98 (±0.13)	49.94 (±0.26)
<b><math>\text{Na}_{0.5}\text{Bi}_{0.5}\text{TiO}_3</math></b>		25	25	50
<b><math>\text{Na}_{0.5}\text{Bi}_{4.5}\text{Ti}_4\text{O}_{15}</math></b>		5.6	50	44.4

### 3.1.2. Electrical Properties

The temperature dependence of the permittivity,  $\epsilon_r$ , and the dielectric loss,  $\tan \delta$  are shown in Figure 3-9. A modest difference in the maximum permittivity,  $\epsilon_{r,\max}$ , with composition in the x-series is observed and the variation in the temperature for  $\epsilon_{r,\max}$  ( $T_m$ ) is small and within  $\pm 10$  °C (Figure 3-10 (a)). In this series,  $x = -0.02$  exhibits the highest  $\epsilon_{r,\max}$  of  $\sim 3200$  at  $T_m \sim 315$  °C.  $\epsilon_{r,\max}$  then decreases continuously with increasing Bi-content and the lowest value is reached for  $x = 0.05$  with  $\epsilon_{r,\max} \sim 1800$  (Figure 3-10 (a)). This indicates excess Bi may influence the lattice polarisability and/or the ferroelectric domain wall motion in NBT. Alternatively, it might be a microstructural effect associated with a decrease in average grain size and therefore an increasing volume fraction of grain boundaries with increasing Bi-content in the x-series ceramics.

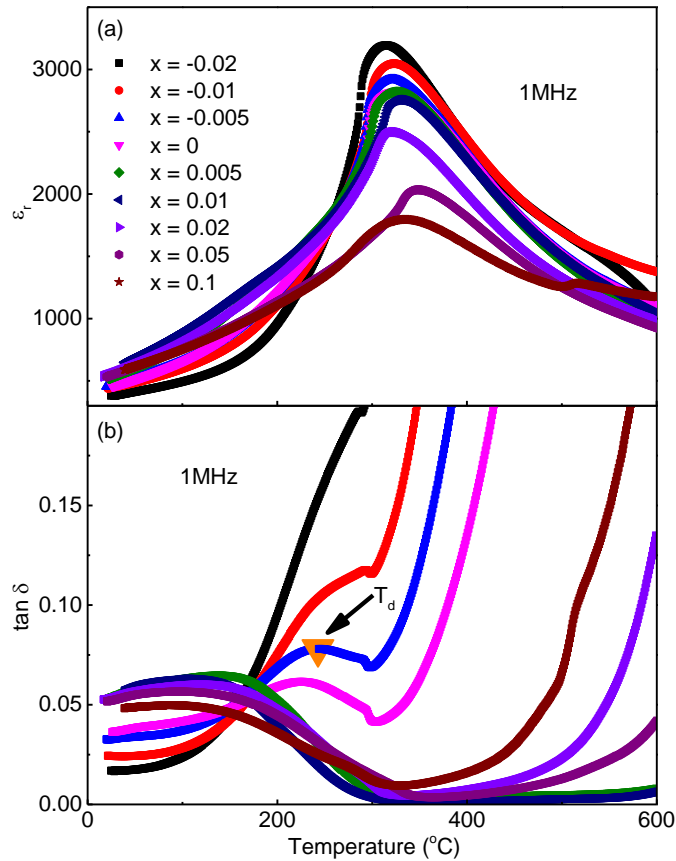


Figure 3-9. Temperature dependence of (a)  $\epsilon_r$  and (b)  $\tan \delta$  at 1 MHz for  $\text{Na}_{0.50}\text{Bi}_{0.50+x}\text{TiO}_{3+3/2x}$ .

In contrast, the dielectric loss,  $\tan \delta$  changes significantly in the  $x$ -series, especially at temperature higher than  $\sim 300$  °C (Figure 3-9 (b)). For  $x \leq 0$ ,  $\tan \delta$  increases rapidly above  $\sim 300$  °C and is greater than 0.2 above 400 °C. For a Bi-excess,  $0.02 > x \geq 0.005$  the loss remains below 0.005 in the range 300-600 °C but for a further increase in Bi ( $x \geq 0.02$ )  $\tan \delta$  starts to rise again in the same temperature range. Moreover, the so-called depolarisation temperature which has been taken as the temperature at the loss peak maximum between RT and  $T_{\epsilon_r, \max}$  shifts to higher temperature with decreasing Bi-content (Figure 3-10 (b)).

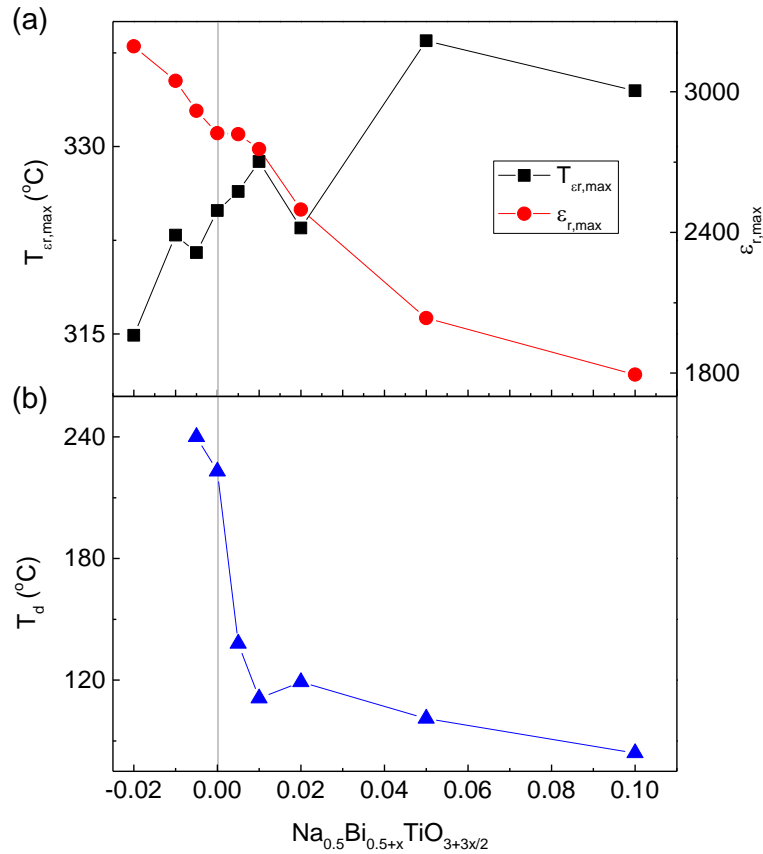


Figure 3-10. The influence of Bi non-stoichiometry on (a) maximum permittivity,  $\epsilon_{r,\max}$  and the corresponding temperature,  $T_{\epsilon_{r,\max}}$  and (b) depolarisation temperature,  $T_d$ .

Complex impedance plane ( $Z^*$ ) plots for selected  $x$ -series samples are shown in Figure 3-11. For  $x \leq 0$ , three components have been observed in  $Z^*$  plots, Figure 3-11 (a). The low frequency data consist of a spike, followed by a distorted semi-circle then an incomplete semi-circle at high frequency. The extracted capacitance (e.g. for stoichiometric  $\text{Na}_{0.5}\text{Bi}_{0.5}\text{TiO}_3$ ) associated with these three arcs from high to low frequency are  $\sim 1.1 \times 10^{-10}$  F/cm,  $\sim 4 \times 10^{-9}$  F/cm and  $\sim 3 \times 10^{-7}$  F/cm, respectively. The capacitance for the high frequency incomplete arc is consistent with permittivity values from the LCR meter ( $\sim 1200$  or  $1.06 \times 10^{-10}$  F/cm in capacitance) indicating this arc is associated with a grain (bulk) response. The value for the other two components are much higher due to their geometry, as capacitance is determined by the formula

$$C = \varepsilon_0 \varepsilon_r \frac{A}{d}$$

where A is the electrode area and d is the separation of the electrodes. For grain boundary and electrode effects, the effective thickness ( $d'$ ) is much smaller than d and leads to a much higher capacitance. Typical capacitance values for grain boundary and electrode effects are  $10^{-11} \sim 10^{-8}$  F/cm and  $10^{-7} \sim 10^{-5}$  F/cm, respectively.<sup>3</sup> The distorted semi-circle at intermediate frequencies is therefore attributed to a grain boundary response and the spike is an electrode effect response. These NBT samples possess the highest conductivity among all un-doped NBTs and are therefore referred to as conducting NBTs.

For  $0 < x < 0.02$ , Figure 3-11 (b), the  $Z^*$  plots were dominated by a single arc associated with the bulk response and a small low frequency spike response associated with an electrode effect as shown in the insert graph of Figure 3-11 (b). The difference in bulk conductivity of samples in these two groups can be more than 3 orders of magnitude, therefore samples with low conductivity are referred to as insulating NBTs.

The bulk conductivity of samples with  $x \geq 0.02$  start to increase again. Although the  $Z^*$  plots are still dominated by a single arc associated with the bulk response and a small low frequency spike similar to insulating NBTs, the bulk conductivity increased significantly compared with insulating NBTs (Figure 3-11 (c)). At the same temperature of 650 °C, the resistivity decreased from  $\sim 120$  k $\Omega \cdot$ cm for  $x = 0.005$  to  $\sim 25$  k $\Omega \cdot$ cm for  $x = 0.02$  and 0.05. In order to distinguish these samples from the other two type of NBTs, samples with  $x \geq 0.02$  are referred to as intermediate NBTs.

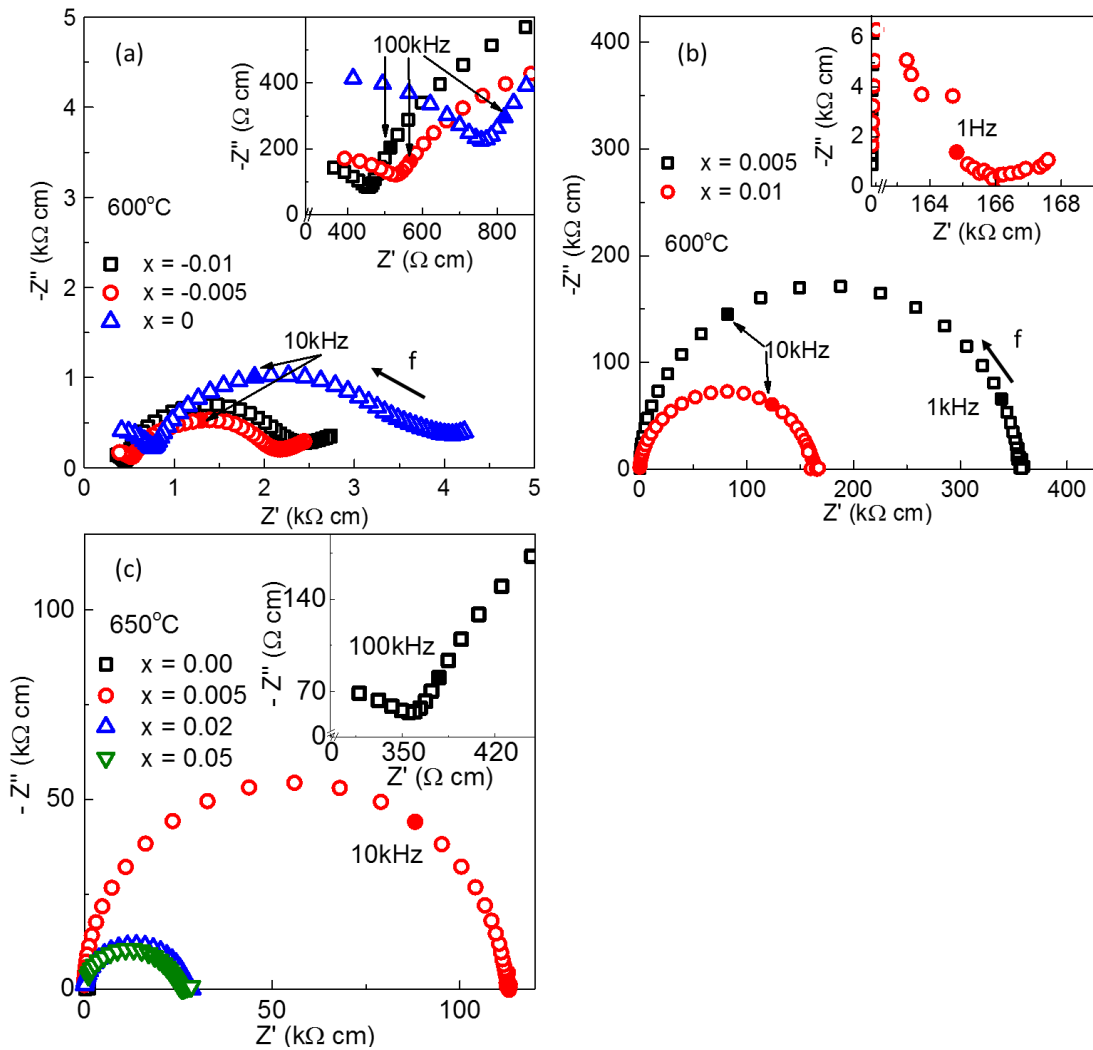


Figure 3-11.  $Z^*$  plots of selected (a) conducting, (b) insulating and (c) intermediate samples of  $\text{Na}_{0.50}\text{Bi}_{0.50+x}\text{TiO}_{3+3x/2}$  ceramics.

For conducting NBTs, the high frequency bulk response is independent of  $p\text{O}_2$  on switching the flowing gas from  $\text{O}_2$  to  $\text{N}_2$  Figure 3-12 (a); however, the grain boundary response is  $p\text{O}_2$  dependent. The behaviour of the low frequency spike is a typical Warburg semi-infinite linear diffusion response. Combining the response of the low frequency spike with the  $p\text{O}_2$  independence of the high frequency bulk response strongly supports these samples to be predominantly oxide-ion conductors.

In contrast, the  $p\text{O}_2$  dependence of insulating/intermediate NBTs presented in Figure 3-12 (b) and (c) shows the bulk conductivity increasing with decreasing  $p\text{O}_2$ ,

suggesting these two types of NBTs possess a much larger contribution from (n-type) electronic conduction as compared to the conducting NBTs.

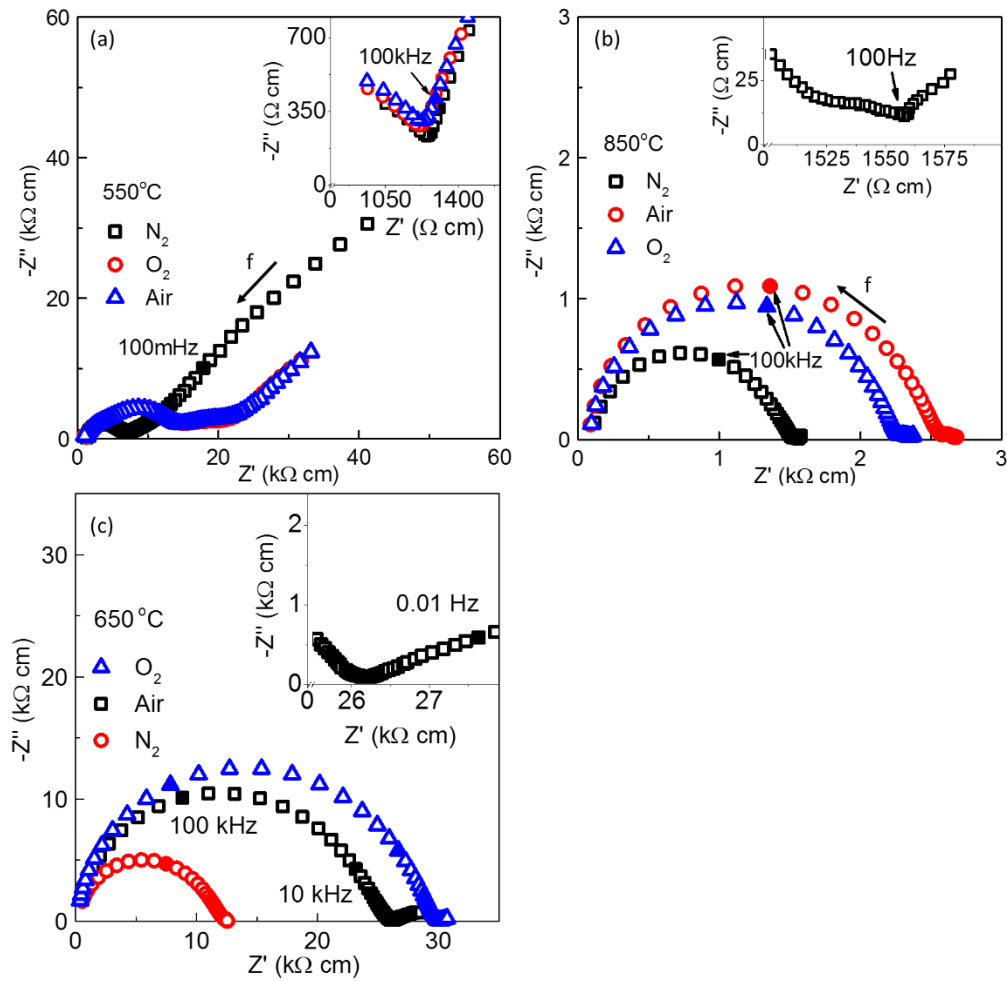


Figure 3-12.  $Z^*$  plots for (a)  $x = -0.005$ , (b)  $x = 0.005$  and (c)  $x = 0.05$  under different flowing gas atmospheres.

Based on the bulk conductivity results from Impedance spectroscopy data, x-series samples show three different types of behaviour, as summarised in the Arrhenius plot shown in Figure 3-13. They can be a conductor, an insulator or a mixed conductor. The conductivity difference between conducting and insulating NBTs can be more than 3 orders of magnitude. On the other hand, intermediate NBTs possess a conductivity  $\sim 1$  order of magnitude higher than the insulating NBTs but still much lower than the conducting NBTs.

A significant difference in activation energy,  $E_a$ , for the bulk conductivity has also been observed. Insulating and intermediate NBTs have a higher bulk  $E_a$  of  $\sim 1.7$  eV compared to the conducting NBTs with  $E_a \sim 0.8\text{--}0.9$  eV and  $\sim 0.4\text{--}0.5$  eV for the temperature ranges below and above  $\sim 320$  °C, respectively. The cross-over temperature for the change in  $E_a$  for the conducting samples is consistent with the temperature of the maximum permittivity,  $\epsilon_{r,\max}$ . In addition, the activation energy for insulating NBTs are  $1.66 \sim 1.70$  eV (Figure 3-13), which is about half of the value reported for the band gap of NBT.<sup>4</sup> The electrical conduction in insulating NBTs are nearly intrinsic since for intrinsic (direct band gap) semi-conductors  $E_g \sim 2E_a$ . The low frequency spike in both insert graphs of Figure 3-11 (b) and Figure 3-12 (b), (c) indicate the presence of some ionic conduction in insulating and intermediate NBTs.

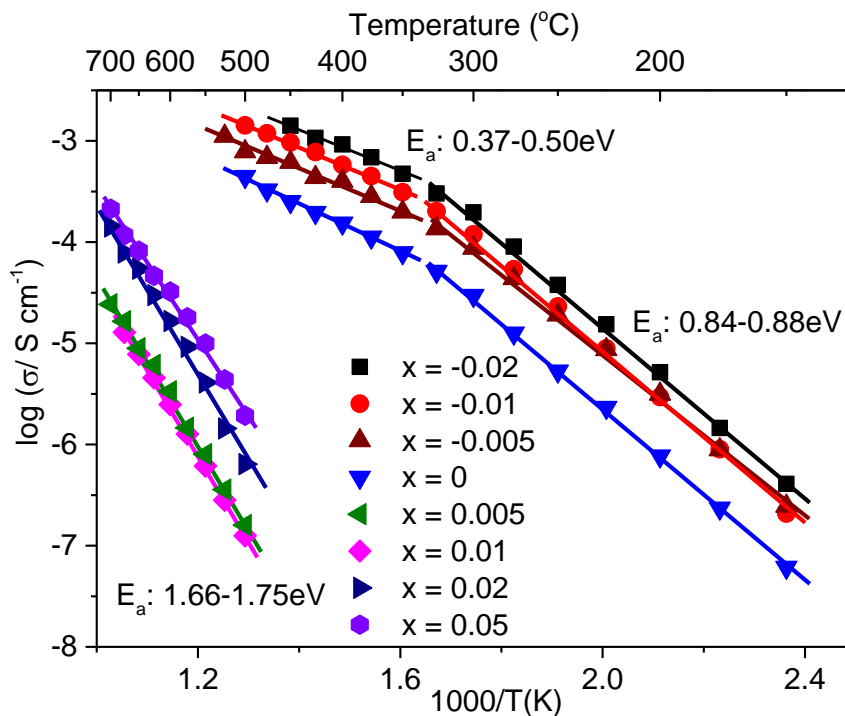


Figure 3-13. Arrhenius plot of bulk conductivity,  $\sigma_b$ , versus reciprocal temperature for selected  $\text{Na}_{0.50}\text{Bi}_{0.500+x}\text{TiO}_{3+3x/2}$  ceramics. Activation energy,  $E_a$ , values for  $\sigma_b$  are included.

$t_{\text{ion}}$  measurements were performed on all ceramics in the range 600 to 800 °C and

are listed in Table 3-2 together with some previously reported values.<sup>2</sup> The behaviour is subdivided into three categories based on the magnitude of  $t_{ion}$ . As mentioned in the introduction,  $x = 0$  and  $-0.01$  samples are predominantly oxide ion conductors with high  $t_{ion} \sim 0.9$  whereas  $x = 0.10$  is an electronic insulator with a small  $t_{ion} < 0.1$ . The intermediate NBTs are different from the other two types of NBTs with  $t_{ion} \sim 0.5$  which indicates predominantly mixed ionic-electronic conduction.

Table 3-2.  $t_{ion}$  values between 600 and 800 °C for selected  $Na_{0.50}Bi_{0.500+x}TiO_{3+3x/2}$  ceramics.

Starting composition	$t_{ion}$ (600 °C)	$t_{ion}$ (700 °C)	$t_{ion}$ (800 °C)
<b>Oxygen ion conductor</b>			
$x = 0.00$	0.93	0.93	0.85
$x = -0.01$	0.92	0.92	0.90
<b>Mixed conductor</b>			
$x = 0.02$	0.46	0.45	0.46
$x = 0.05$	0.62	0.64	0.65
<b>Insulator</b>			
$x = 0.01$	0.07	0.07	0.10

## 3.2. Na non-stoichiometry

### 3.2.1. Phase purity and microstructure

To be systematic, the starting Na-content non-stoichiometry of NBT was also investigated as the  $y$ -series. The general formula of the  $y$ -series samples is written as  $\text{Na}_{0.50+y}\text{Bi}_{0.50}\text{TiO}_{3+1/2y}$  where  $-0.01 \leq y \leq 0.01$ .

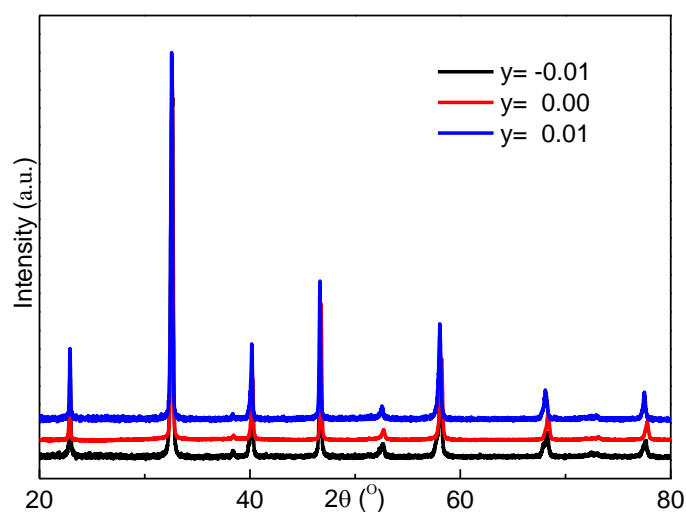


Figure 3-14. Room temperature X-ray powder diffraction data for the  $\text{Na}_{0.50+y}\text{Bi}_{0.50}\text{TiO}_{3+1/2y}$  series.

XRD pattern of all three samples showed no evidence of any secondary phases (Figure 3-14). However, TEM HAADF-STEM (Z-contrast) images (performed by Dr H Zhang, University of Sheffield) and SEM/EDX results revealed the presence of  $\text{TiO}_2$  and a Na-rich phase as a secondary phase in Na-deficient and Na-rich NBT, respectively (Figure 3-15). Table 3-3 summarises EDX data for  $x = 0.01$  and  $-0.01$ . The bulk composition of these two samples cannot be distinguished from each other within instrument resolution and standard errors. EDX results for the Na-rich phase in  $y = 0.01$  gave a composition similar to  $\text{Na}_2\text{TiO}_3$ . However, this data can be influenced from the contribution of the matrix since the size of the secondary phase particles are smaller compared to the spot size of the EDX detective beam. The average grain size of the  $y$ -

series showed a reversed trend compared to the x-series as it increases with increasing Na content from  $\sim 50 \mu\text{m}$  for  $y = 0.01$  to  $\sim 5 \mu\text{m}$  for  $y = -0.01$ , Figure 3-16. It is worth noting that  $y = 0.01$  possess the largest average grain size among all un-doped NBT samples.

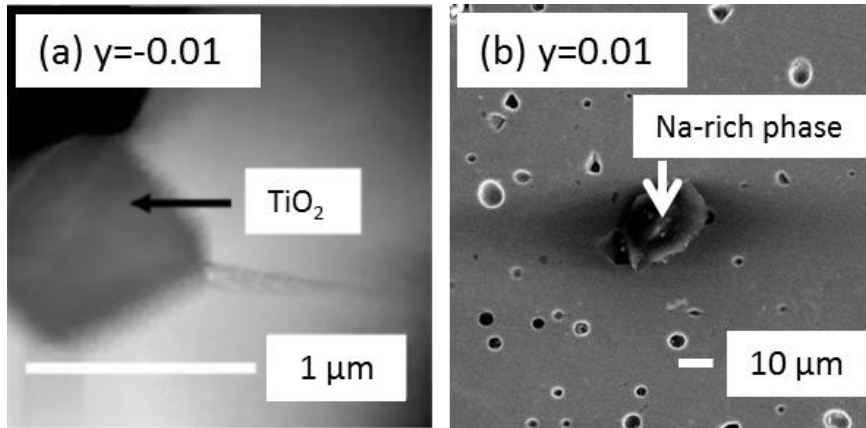


Figure 3-15. (a) STEM high angle annular dark field (HAADF) Z-contrast image showing the TiO<sub>2</sub> secondary phase in  $y = -0.01$  and (b) secondary electron image of an  $y = 0.01$  ceramic (polished without thermal etching) showing the Na-rich secondary phase.

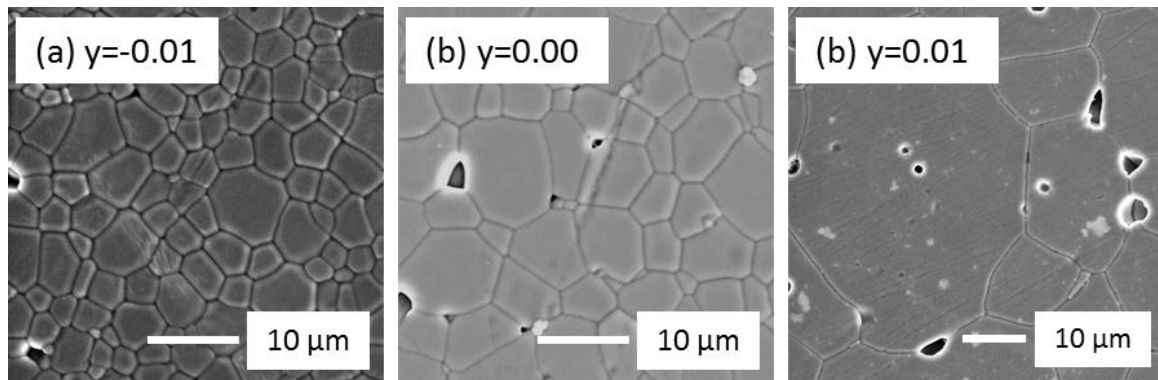


Figure 3-16. SEM micrographs of (a)  $y = -0.01$ , (b)  $y = 0$  and (c)  $y = 0.01$ . All samples were polished and thermally etched prior to SEM.

Table 3-3. Chemical composition (relative cation at%) and associated error (standard deviation) by SEM/EDX of the main and secondary phases present in  $y = 0.01$  and  $-0.01$ .

Start Composition		Na (at%)	Ti (at%)	Bi (at%)
<b>y = 0.01</b>	Main phase	25.3 ( $\pm 0.4$ )	49.7 ( $\pm 0.4$ )	25.0 ( $\pm 0.3$ )
	Na-rich phase	63.2 ( $\pm 2.1$ )	31.0 ( $\pm 1.5$ )	5.8 ( $\pm 1.1$ )
<b>y = -0.01</b>	Main phase	24.8 ( $\pm 0.6$ )	49.8 ( $\pm 0.5$ )	25.4 ( $\pm 0.2$ )
	TiO <sub>2</sub>		TiO <sub>2</sub>	
<b>Na<sub>0.5</sub>Bi<sub>0.5</sub>TiO<sub>3</sub></b>		25	25	50

### 3.2.2. Electrical properties

$\epsilon_r$  and  $\tan \delta$  for the  $y$ -series samples are summarised in Figure 3-17.  $y = 0.01$  has the highest  $\epsilon_{r,max}$  of  $\sim 3200$  whereas  $y = -0.01$  has the lowest with  $\sim 2800$ , Figure 3-18.  $y = 0.01$  possess  $\tan \delta > 0.05$  above  $300^\circ\text{C}$ , whereas  $\tan \delta$  for  $y = -0.01$  remains lower than  $0.06$  below  $600^\circ\text{C}$ . The maximum temperature  $T_{\epsilon_r,max}$  decreases linearly with increasing  $y$  from  $\sim 334^\circ\text{C}$  for  $y = -0.01$  to  $\sim 318^\circ\text{C}$  for  $y = 0.01$ , whereas  $T_d$  shows the opposite trend and increases linearly from  $\sim 130^\circ\text{C}$  for  $y = -0.01$  to  $\sim 260^\circ\text{C}$  for  $y = 0.01$ , Figure 3-18.

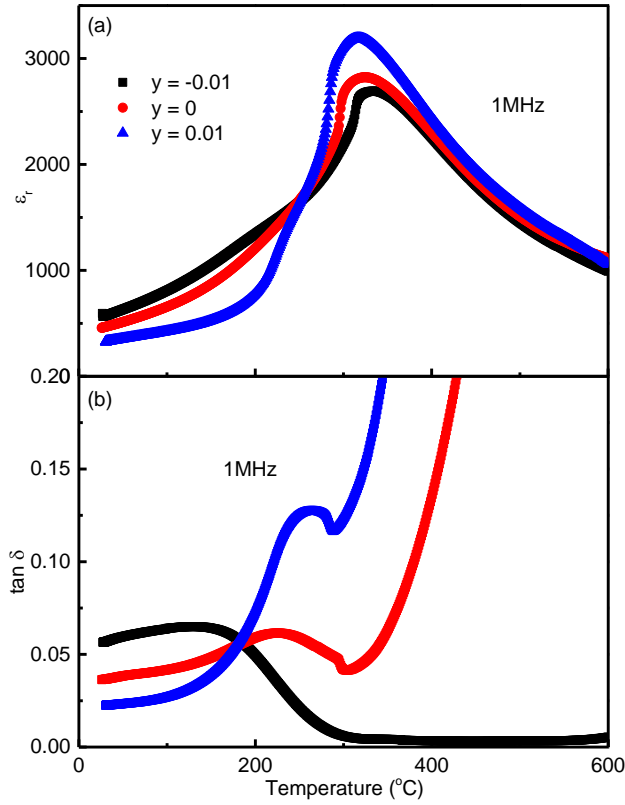


Figure 3-17. Temperature dependence of (a)  $\epsilon_r$  and (b)  $\tan \delta$  at 1 MHz for  $\text{Na}_{0.50+y}\text{Bi}_{0.500}\text{TiO}_{3+1/2y}$  ceramics.

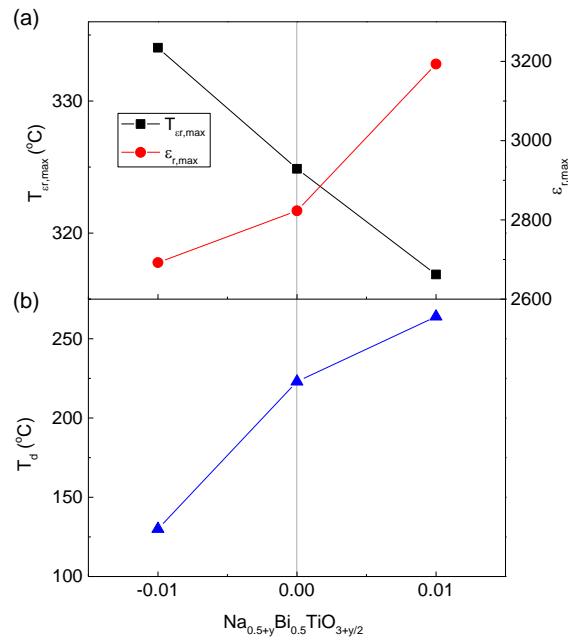


Figure 3-18. The influence of Na non-stoichiometry on (a) maximum permittivity,  $\epsilon_{r, \max}$  and the corresponding temperature,  $T_{\epsilon_r, \max}$  and (b) depolarisation temperature,  $T_d$ .

$Z^*$  plots of  $y$ -series samples at 600 °C are shown in Figure 3-19. Similar to the  $x$ -series,  $y$ -series samples also display two different types of behaviour, plots for  $y = 0.10$  consist of three arcs including an incomplete high frequency semi-circle corresponding to the bulk response followed by a distorted semi-circle corresponding to the grain boundary response and a low frequency spike indicating the presence of ionic conduction (Figure 3-19 (b) and Figure 3-20 (b)).  $Z^*$  plots for  $y = -0.01$  only have a significant larger semi-circular arc consistent with a resistive, bulk response, Figure 3-19 (a).

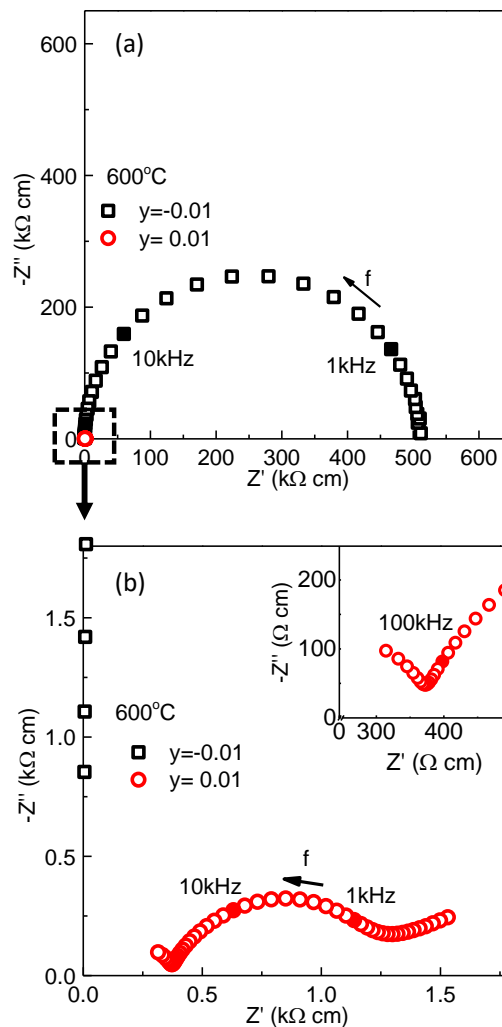


Figure 3-19. (a)  $Z^*$  plots for  $y = -0.01$  and  $0.01$  and (b) enlarged view of  $y = 0.01$ , the inset shows bulk response of  $y = 0.01$  ceramic.

$pO_2$  tests of  $\gamma = -0.01$  showed an increase in bulk conductivity with a decrease of  $pO_2$ . When combined with the lack of any significant low frequency spike (Figure 3-20 (a)), this suggested n-type conduction with limited ionic conduction. On the other hand,  $\gamma = 0.01$  exhibited a  $pO_2$  independent bulk conductivity similar too Bi-deficient NBT (for example,  $x = -0.01$ ) which suggests the bulk conductivity is dominated by ionic conduction (Figure 3-20 (b)).

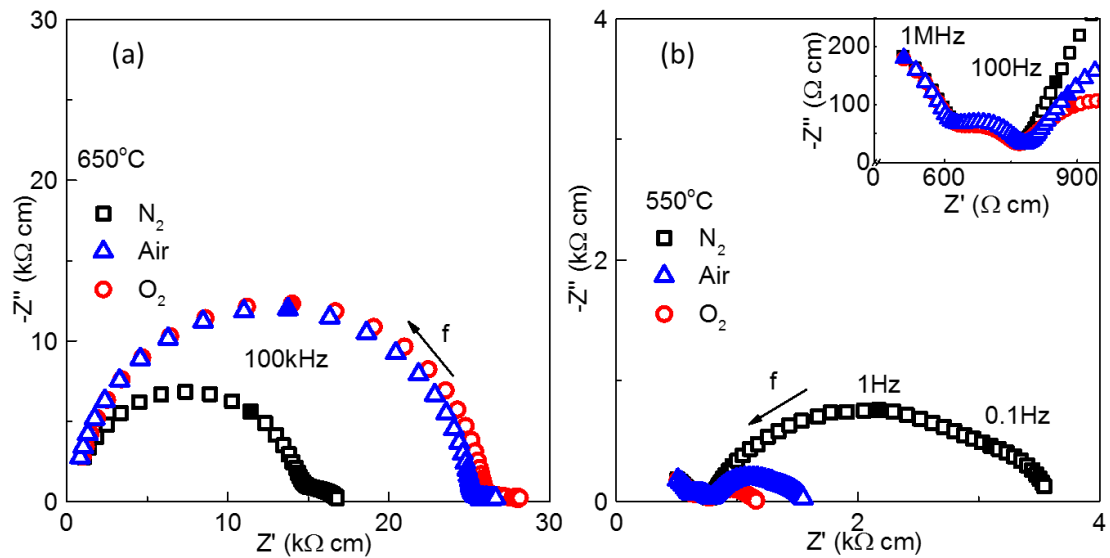


Figure 3-20. (a)  $\gamma = -0.01$  and (b)  $\gamma = 0.01$  ceramic under different atmosphere.

The bulk conductivity of  $\gamma$ -series samples is summarised in Figure 3-21. The difference in bulk conductivity between conducting  $\gamma = 0.01$  and insulating  $\gamma = -0.01$  was more than 3 orders of magnitude below  $\sim 500$  °C. The bulk activation energy was high for insulating samples ( $\sim 1.7$  eV) and low for conducting samples (0.4  $\sim$  0.9 eV). For conducting samples,  $E_a$  decreases from 0.85 – 0.94 eV to 0.34 – 0.46 eV when the temperature increases to above  $\sim 320$  °C from low temperature. The activation energy for insulating samples of  $\gamma = -0.01$  ( $\sim 1.7$  eV) is close to half of the reported NBT optical band gap,  $E_g$ , of  $\sim 3.0$ – $3.5$  eV, indicating  $\gamma = -0.01$  samples are dominated by intrinsic electronic conduction.

The lack of ionic conduction in  $\gamma = -0.01$  was also verified by  $^{18}O$  tracer diffusion

measurements. The diffusion profile at 608 °C is less than 2 μm which indicates very low bulk diffusion (grain size ~ 5 μm, Figure 3-22). Using a  $D^* = 3.2 \times 10^{-13} \text{ cm}^2/\text{s}$  for  $y = -0.01$  (exchange at 608 °C) in the Nernst–Einstein equation, the oxide ion conductivity can be calculated as  $\sim 1.38 \times 10^{-7} \text{ S/cm}$  which is less than ~10% of the total conductivity measured by impedance spectroscopy at 600 °C ( $\sim 2 \times 10^{-6} \text{ S/cm}$ , Figure 3-19).

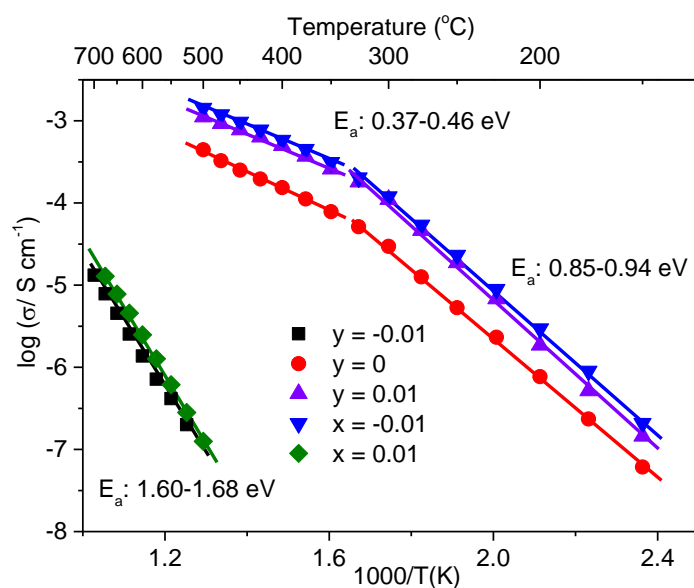


Figure 3-21. Arrhenius plot of bulk conductivity,  $\sigma_b$ , versus reciprocal temperature for selected  $\text{Na}_{0.50+y}\text{Bi}_{0.50}\text{TiO}_{3+y/2}$  ceramics. Activation energy,  $E_a$ , values for  $\sigma_b$  are included.

Figure 4 in reference [11]

Figure 3-22.  $^{18}\text{O}$  diffusion tracer profile of  $y = -0.01$  exchange at 608 °C for 8040 s with  $p^{18}\text{O}_2 \sim 750 \text{ mbar}$ .

### 3.3. The influence of drying reagents

As mentioned in the experimental procedure chapter, the raw materials used in this chapter are  $\text{Na}_2\text{CO}_3$ ,  $\text{Bi}_2\text{O}_3$  and  $\text{TiO}_2$ . Among these three raw materials,  $\text{Na}_2\text{CO}_3$  is much more hygroscopic than the other two. As shown in Figure 3-23,  $\text{Na}_2\text{CO}_3$  reagent directly taken out from the bottle undergoes an irreversible weight loss of ~1.0 wt % on

heating in air which can be attributed to loss of adsorbed water whereas the weight loss for the other two reagents under the same conditions is negligible. Although the precise weight loss due to water will depend on the condition of production and storage of the reagent; in this case the actual formula for a nominal stoichiometric NBT made by un-dried reagents will be  $\text{Na}_{0.495}\text{Bi}_{0.50}\text{TiO}_{2.9975}$  (wet NBT) instead of  $\text{Na}_{0.50}\text{Bi}_{0.50}\text{TiO}_3$  (dry NBT). In other words, wet NBT is effectively sodium-deficient.

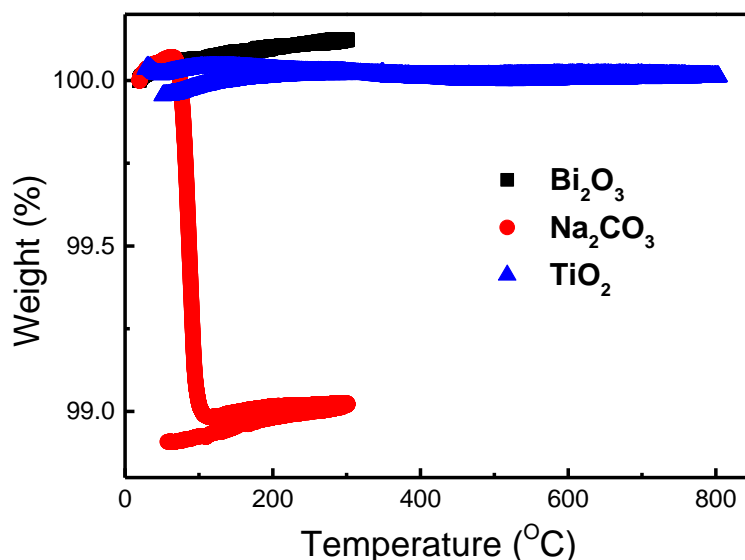


Figure 3-23. Weight loss of  $\text{Na}_2\text{CO}_3$ ,  $\text{Bi}_2\text{O}_3$ , and  $\text{TiO}_2$  reagents on a single heating and cooling cycle in air.

A  $Z^*$  plot of wet and dry NBT processed under identical conditions shows a significant difference in bulk conductivity at 600 °C (Figure 3-24 (a)). It is clear that wet NBT possesses a much higher resistivity than dry-NBT. However, the wet NBT also possesses a grain boundary response that is merged with the bulk response which made it difficult to extract accurate bulk conductivity values from  $Z^*$  plots. Therefore,  $M''$  spectroscopic plots were used to extract bulk conductivity since the bulk response dominates this plot due to its low capacitance. The bulk conductivity can be obtained by the equation:

$$\omega RC = 1$$

at the peak point of the  $M''$  peak. An Arrhenius plot of the bulk conductivity confirmed the wet-NBT sample to behave like intermediate NBTs with a much lower bulk conductivity and a higher  $E_a$  compared to the dry NBT sample (Figure 3-25).

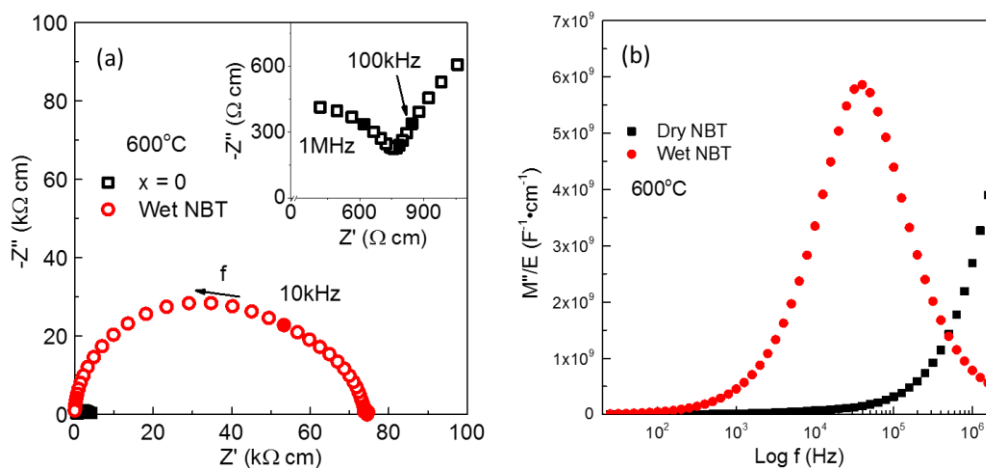


Figure 3-24. (a)  $Z^*$  plots and (b)  $M''$  plot for wet-NBT and dry-NBT at 600°C.

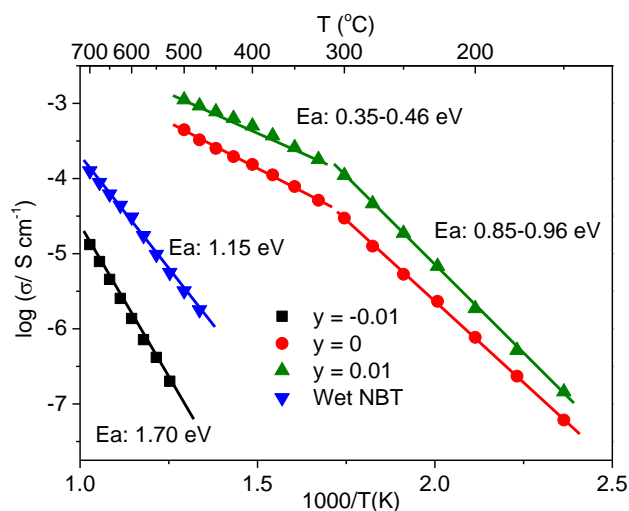


Figure 3-25. Arrhenius plot of bulk conductivity for wet- and dry-NBTs with  $y$ -series samples

### 3.4. Discussion

The conductivity and phase purity of samples in the  $x$ -series are listed in Table 3-4 to act as a summary of the results obtained.  $\text{Na}_2\text{Ti}_6\text{O}_{12}$  and  $\text{TiO}_2$  are the two secondary phases that appear in conducting NBT whereas  $\text{Bi}_2\text{O}_3$  and  $\text{Na}_{0.5}\text{Bi}_{4.5}\text{Ti}_4\text{O}_{15}$  are the

secondary phases that appear in insulating NBT. Among all the compositions in the x-series,  $\text{Na}_{0.50}\text{Bi}_{0.505}\text{TiO}_{3.0075}$  ( $x = 0.005$ ) is the only one that remains single phase under the inspection of TEM. However, due to the volatility of both Na and Bi the level of required Bi-excess to obtain single phase samples will be dependent on the particular ceramic processing conditions employed. These results demonstrate the Bismuth non-stoichiometry is very limited in NBT and single phase NBT can only be obtained with a small Bi-excess in the starting material to compensate for Bi-loss during processing.

Table 3-4. Summary of conductivity type and phase purity of  $\text{Na}_{0.5}\text{Bi}_{0.5+x}\text{TiO}_{3+3/2x}$  series of ceramics

Composition	Conductivity	XRD	SEM	TEM
$x = -0.020$	Conductor	$\text{Na}_2\text{Ti}_6\text{O}_{13}$	$\text{Na}_2\text{Ti}_6\text{O}_{13}$	
$x = -0.010$	Conductor	Clean	$\text{Na}_2\text{Ti}_6\text{O}_{13}$	$\text{TiO}_2$
$x = -0.005$	Conductor	Clean	$\text{Na}_2\text{Ti}_6\text{O}_{13}$	$\text{TiO}_2$
$x = 0.000$	Conductor	Clean	Clean	$\text{TiO}_2$
$x = 0.005$	Insulator	Clean	Clean	Clean
$x = 0.010$	Insulator	Clean	Clean	$\text{Bi}_2\text{O}_3$
$x = 0.020$	Mixed	Clean	Clean	$\text{Bi}_2\text{O}_3$
$x = 0.050$	Mixed	$\text{Bi}_2\text{O}_3, \text{Na}_{0.5}\text{Bi}_{4.5}\text{Ti}_4\text{O}_{15}$	$\text{Bi}_2\text{O}_3, \text{Na}_{0.5}\text{Bi}_{4.5}\text{Ti}_4\text{O}_{15}$	$\text{Bi}_2\text{O}_3$
$x = 0.100$	Mixed	$\text{Bi}_2\text{O}_3, \text{Na}_{0.5}\text{Bi}_{4.5}\text{Ti}_4\text{O}_{15}$		$\text{Bi}_2\text{O}_3$
$x = 0.200$	Mixed	$\text{Bi}_2\text{O}_3, \text{Na}_{0.5}\text{Bi}_{4.5}\text{Ti}_4\text{O}_{15}$		$\text{Bi}_2\text{O}_3$

Table 3-5 shows the phase purity and conductivity type of samples in the y-series. Generally speaking, the y-series samples behave in the opposite way in terms of non-stoichiometry compared to the x-series samples. Na-rich samples in the y-series are conducting similar to Bi-deficient samples from the x-series and Na-deficient samples

from the y-series are insulating similar to Bi-rich samples in the x-series. These results indicate the defect mechanism of the y-series is different to the x-series.

Table 3-5. Summary of conductivity type and phase purity of  $\text{Na}_{0.50+y}\text{Bi}_{0.50}\text{TiO}_{3+1/2y}$  series of ceramics.

Composition	Conductivity	XRD	SEM	TEM
<b>y = -0.01</b>	Insulator	Clean	Clean	$\text{TiO}_2$
<b>y = 0.00</b>	Conductor	Clean	Clean	$\text{Na}_2\text{Ti}_6\text{O}_{13}$ , $\text{TiO}_2$
<b>y = 0.01</b>	Conductor	Clean	Na-Rich phase	

In order to increase the oxide ion conduction in NBT, two possible routes can be employed, either by a non-stoichiometric Bi-deficient starting composition or acceptor doping, only the former was covered in this chapter. Compared with stoichiometric NBT the bulk conductivity increased half order of magnitude with  $x = -0.005/0.01$  and a further increase can be achieved with reducing Bi to  $x = -0.02$ . The  $t_{\text{ion}}$  at 800 °C also increased to  $\sim 0.90$  from  $\sim 0.85$  (Figure 3-11 (a), Figure 3-13 and Table 3-2).

On the other hand, since the oxygen ion conduction of nominally stoichiometric NBT is raised by Bi-loss during processing, then compensating the Bi-loss with sufficient excess Bi in the starting material should be able to eliminate oxygen vacancies and lead to insulating behaviour. Figure 3-13 shows only a very small amount of Bi excess ( $x = 0.005$  in this case but will be dependent on the processing procedure) is enough to make NBT a good dielectric (insulator).

SEM/EDX results showed that despite the contrasting insulating and conducting electrical properties of NBT, the compositional differences cannot be distinguished from each other within instrument resolution and standard errors. Therefore, the level of Bi non-stoichiometry in nominal stoichiometric NBT is very low and essentially it

means the level of oxygen vacancy concentration is very low. This implies the mobility of oxygen ions in NBT is very high in order to obtain such high levels of oxide ionic conductivity. The pathway for anion hopping inside a perovskite is called the saddle-point which is a triangle formed by two A-site cations and one B-site cation (Figure 3-26). Computer simulation have shown the cation polarisability, weak Bi-O bonds and local atomistic configurations in NBT are all important factors that favour oxygen ion migration. Cation polarisability influences lattice relaxation and how cations can displace away from the mobile oxygen ions (Figure 3-26).<sup>5,6</sup> Weak Bi-O bonds are caused by the  $6s^2$  lone pair electrons of Bi hybridising with oxygen 2p orbitals which also leads to an off-centring of Bi ions and a variety of Bi-O bond lengths due to a reduction in the coordination number. The high polarisability of Bi and the weak Bi-O bonds on the A-site are critical to obtain high oxygen ion conductivity. This has been supported by computer simulations that estimate the migration energy barrier for different pathways are different and the Bi-Bi-Ti saddle-point has the lowest barrier (0.22 eV) whereas the Na-Na-Ti saddle-point has the highest barrier (1.3 eV).<sup>6</sup>

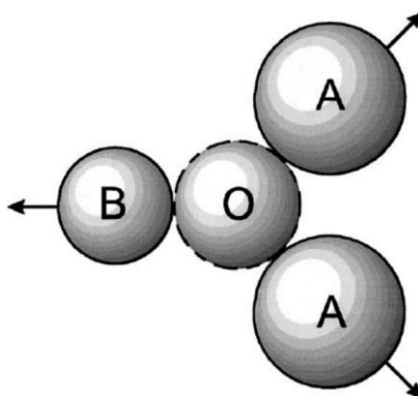


Figure 3-26. Cation displacement at the saddle-point for oxygen ion migration in perovskite.<sup>5</sup>

At this stage it is unclear why samples in the x-series with starting compositions  $x \geq 0.02$  exhibit mixed conduction and higher conductivity than insulating NBTs but it must be linked to the presence of secondary phases, both of which are Bi-rich compared to

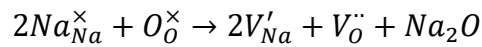
NBT, i.e.  $\text{Na}_{0.5}\text{Bi}_{4.5}\text{Ti}_4\text{O}_{15}$  and a  $\text{Bi}_2\text{O}_3$  phase.<sup>7</sup> Two possible explanations are; (i) a change in the Bi-content in the NBT main phase, and (ii) a space-charge model. We outline both below.

Firstly, the Bi-rich secondary phases may deplete the NBT main phase of Bi in  $x > 0.01$ , therefore reducing its Bi-content resulting in an increase in oxide-ion conduction. The results sections have shown that conventional analytical methods such as EDX are unable to distinguish the low level of A-site non-stoichiometry (Na:Bi ratio) required to switch from conducting to insulating behaviour in NBT-based ceramics.<sup>2</sup> As a consequence, it is not possible to unequivocally prove a change in stoichiometry associated with the main NBT phase in the ceramics, especially due to the fine scale distribution of the  $\text{Bi}_2\text{O}_3$ -type phase in the x-series, Figure 3-6 (b), (d) - (f). The level of x required to obtain insulating NBTs will be dependent on the ceramic processing conditions employed as they control the extent of thermodynamic equilibrium within the ceramics and this will influence the chemical potential and therefore concentration (strictly, the activity) of Bi between the three co-existing phases. In this case, NBT powders are prepared at  $\sim 850$  °C and ceramics are sintered at 1100 to 1150 °C for 2 h in air, covered in sacrificial powder of the same composition. This results in  $x = 0$  being conducting and the requirement for a small excess of starting  $\text{Bi}_2\text{O}_3$  ( $x \sim 0.01$ ) to compensate for losses during processing prior to the formation of Bi-rich secondary phases to obtain insulating behaviour. x values are likely to be significantly different for processing conditions that don't use sacrificial powders to limit Na, Bi volatilisation and/or for higher/longer sintering periods as these factors will influence the final phase assemblage, i.e. composition and weight percentage of the phases present.

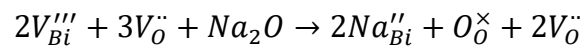
Secondly, enhanced ionic conductivity based on a space charge model has been observed in mixtures of two phases, based either on one ionic conductor and one insulator or mixtures of two ionic conductors.<sup>8</sup> For example, additions of  $\text{Al}_2\text{O}_3$  to

lithium iodide LiI led to an increase in ionic conductivity by a factor of  $\sim 50$  at room temperature<sup>9</sup> and additions of ZrO<sub>2</sub> nano-powder to AgI increased ionic conductivity by more than three orders of magnitude at room temperature.<sup>10</sup> The interfacial space charge effect is widely considered as a driving force for the enhancement of ionic conductivity.<sup>8</sup> This effect may account for the enhanced oxide-ion conduction and the  $t_{ion}$  of  $\sim 0.4-0.6$  in starting compositions with higher Bi-excess ( $x \geq 0.02$ ) where NBT, Bi<sub>2</sub>O<sub>3</sub>-type and Na<sub>0.5</sub>Bi<sub>4.5</sub>Ti<sub>4</sub>O<sub>15</sub>-type phases coexist. The fine scale distribution of the Bi<sub>2</sub>O<sub>3</sub>-type phase with the NBT matrix, Figure 2 (g) and (h), combined with the fact that many Bi<sub>2</sub>O<sub>3</sub>-type materials exhibit high levels of oxide-ion conductivity would appear to be the most likely source of any space charge model in these ceramics. In addition,  $t_{ion}$  of these ceramics may be overestimated if the Bi<sub>2</sub>O<sub>3</sub>-type phase present is a good oxide-ion conductor. Further study is needed to clarify the composition and properties of this Bi<sub>2</sub>O<sub>3</sub>-type phase to elucidate its influence on the measured electrical properties of these ceramics and in attempts to try and distinguish between the two possible explanations outlined above.

In terms of the y-series, if the defect mechanism is the same as in the x-series then Na-deficient samples in the y-series should contain more oxygen vacancies, consequently should be more conductive than nominal stoichiometric NBT according to the equation:



In contrast, Na-rich NBT in the y-series should exhibit lower conductivity than stoichiometric NBT as the excess Na should fill the Bi vacancies and lead to partial elimination of oxygen vacancies:



However, the conductivity of the y-series act opposite to both of these two assumptions. The results show the conducting Na-rich y-series have a high level of

oxygen vacancies which is comparable to the Bi-deficient x-series NBT whereas the Na-deficient y-series fail to create oxygen vacancies by introducing Na-vacancies and somehow have a low level of oxygen vacancies as they remain insulating. With that in mind, and combined with the secondary phases present in both Na-rich/deficient samples, the odd behaviour of the y-series samples can be explained.

For the case of  $y = 0.01$ , a Na-rich secondary phase has been detected, which indicates the extra Na in the starting material does not enter the lattice. The bulk composition is again Bi-deficient due to the Bi-loss during processing. Consequently, oxygen vacancies and therefore oxygen ion conduction are introduced into the Na-rich y-series samples.

For  $y = -0.01$ , STEM HAADF Z-contrast images showed the presence of  $\text{TiO}_2$  secondary phase. Thus the final bulk composition is deficient in both Na and Ti, and therefore Bi-rich. So the formula  $\text{Na}_{0.49}\text{Bi}_{0.50}\text{Ti}_1\text{O}_{2.99}$  can be rewritten as  $\text{Na}_{0.50}\text{Bi}_{0.51}\text{Ti}_{1.02-z}\text{O}_{3.055-2z}$  where the  $z\text{TiO}_2$  is present as a secondary phase in the final product (Figure 3-15). Therefore, the starting composition of  $y = -0.01$  was essentially Bi-rich similar to  $x = 0.01$  and the “extra” Bi compensates the loss of Bi during processing, preventing the formation of oxygen vacancies and therefore ensuring the material is an insulator.

The result of wet and dry NBT demonstrate the sensitivity of NBT to exceptionally small compositional variations in the starting material which can vary the bulk conductivity and activation energy (conduction mechanism). The level of adsorbed moisture in  $\text{Na}_2\text{CO}_3$  will be different according to different production and storage conditions of the reagent and therefore to fully control and obtain reproducible results, it is important to control the moisture level in the raw materials (e.g. use pre-dried reagents). It also proves the electrical properties of NBT are highly sensitive to synthesis procedures which is a likely explanation for the significant variation in dielectric properties of NBTs reported in the literature.

### 3.5. Conclusions

In summary, the electrical properties of NBT are highly sensitive to low levels of A-site non-stoichiometry which can lead to distinctly different kinds of electrical behaviour. Figure 3-27 and Figure 3-28 summarise most of the electrical properties in un-doped NBT.

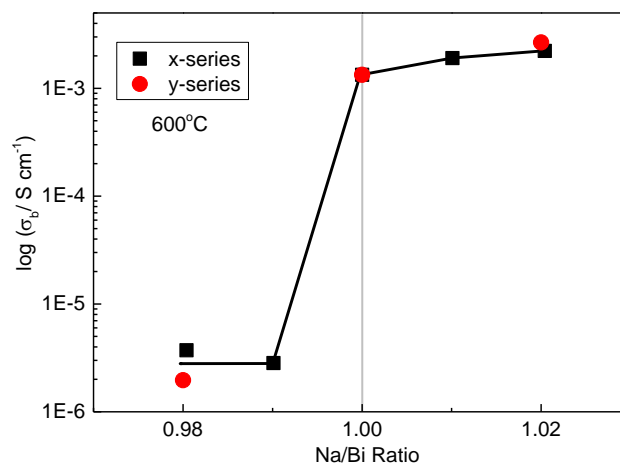


Figure 3-27. Bulk conductivity of un-doped NBTs at 600 °C versus Na/Bi ratio.

In general, samples with a Na/Bi ratio  $\geq 1$  exhibit high, nearly pure oxygen ion conduction with a low activation energy ( $< 1$  eV) and high  $\tan \delta$  above  $T_m$ . Conversely, samples with a Na/Bi ratio  $< 1$  are electronic insulators and are dominated by electronic conduction with  $E_a \sim 1.7$  eV at elevated temperatures;  $\tan \delta$  remains  $< 0.05$  below 600 °C. The difference in bulk conductivity between these two kinds of NBTs can be more than 3 orders of magnitude. However, further increases in the starting Bi-content ( $0.02 \leq x \leq 0.10$ ) leads to more Bi-rich secondary phases which can induce mixed ionic/electronic behaviour by reintroducing significant oxide-ion conductivity with  $t_{\text{ion}} \sim 0.4 - 0.6$ . From the ferroelectric point of view,  $\epsilon_{r,\text{max}}$  clearly shows a decrease with decreasing Na/Bi ratio. If the two compositions which are far beyond the solid

solution limit are neglected, e.g.  $x = 0.05$  and  $0.1$  ( $\text{Na/Bi}$  ratio =  $0.91$  and  $0.83$ ), then  $T_{\epsilon_r, \max}$  can be seen to decrease with increasing  $\text{Na/Bi}$  ratio.  $T_d$  also displays a trend that decreases with the decreasing  $\text{Na/Bi}$  ratio and a rapid decrease can be observed from  $\text{Na/Bi} \geq 1$  to  $\text{Na/Bi} < 1$ . It is worth noting that from the  $\text{Na/Bi}$  ratio point of view, the electrical properties of both x-series and y-series samples in Figure 3-27 and Figure 3-28 fall into the same trend which means the electrical properties of NBT ceramics are controlled by the  $\text{Na/Bi}$  ratio in the starting composition instead of a simple A-site rich/deficient concept.

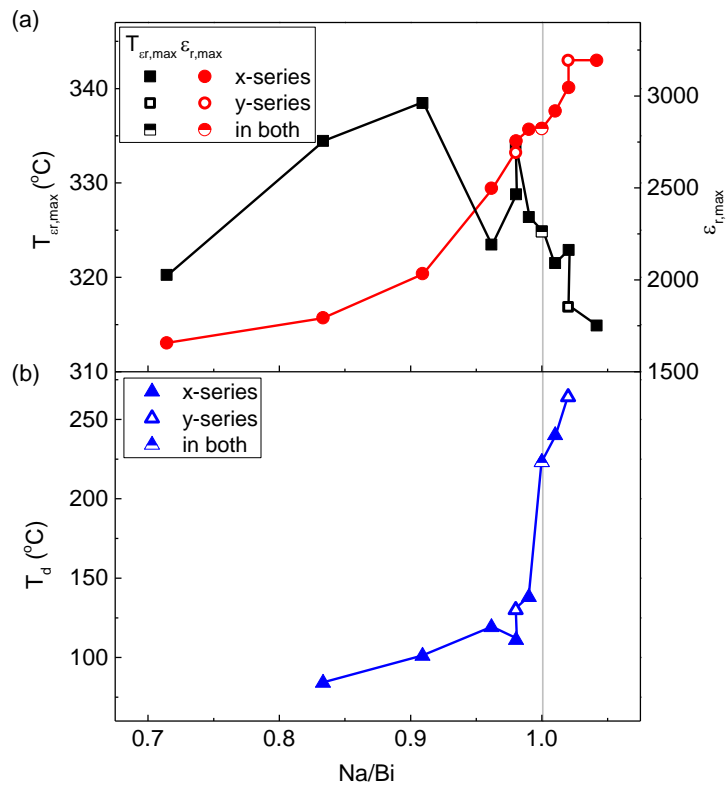


Figure 3-28. (a) Maximum permittivity,  $\epsilon_{r, \max}$  and the corresponding temperature,  $T_{\epsilon_r, \max}$  and (b) depolarisation temperature,  $T_d$  of undoped NBTs versus  $\text{Na/Bi}$  ratio.

The level of allowed non-stoichiometry within NBT is below the detection limit of most readily available analytical methods but is easily detected by electrical property

measurements. In addition, pre-dried reagents significantly influence the bulk conductivity of nominally stoichiometric NBT and reinforce the point that the electrical properties of undoped NBT are very sensitive to extremely small changes in the starting stoichiometry.

### 3.6. References

1. Hiruma, Y., Nagata, H. & Takenaka, T. Thermal depoling process and piezoelectric properties of bismuth sodium titanate ceramics. *J. Appl. Phys.* **105**, 84112 (2009).
2. Li, M. *et al.* A family of oxide ion conductors based on the ferroelectric perovskite  $\text{Na}_{0.5}\text{Bi}_{0.5}\text{TiO}_3$ . *Nat. Mater.* **13**, 31–5 (2014).
3. Irvine, J. T. S., Sinclair, D. C. & West, A. R. Electroceramics: characterization by impedance spectroscopy. *Adv. Mater.* **2**, 132–138 (1990).
4. Bousquet, M. *et al.* Optical properties of an epitaxial  $\text{Na}_{0.5}\text{Bi}_{0.5}\text{TiO}_3$  thin film grown by laser ablation: Experimental approach and density functional theory calculations. *J. Appl. Phys.* **107**, 104107 (2010).
5. Saiful Islam, M. Ionic transport in  $\text{ABO}_3$  perovskite oxides: a computer modelling tour. *J. Mater. Chem.* **10**, 1027–1038 (2000).
6. He, X. & Mo, Y. Accelerated Materials Design of  $\text{Na}_{0.5}\text{Bi}_{0.5}\text{TiO}_3$  Oxygen Ionic Conductors Based on First Principles Calculations. *Phys. Chem. Chem. Phys.* **17**, 18035–18044 (2015).
7. Li, L., Li, M., Zhang, H., Reaney, I. M. & Sinclair, D. C. Controlling mixed conductivity in  $\text{Na}_{1/2}\text{Bi}_{1/2}\text{TiO}_3$  using A-site non-stoichiometry and Nb-donor doping. *J. Mater. Chem. C* **4**, 5779–5786 (2016).

8. Maier, J. Ionic conduction in space charge regions. *Prog. Solid State Chem.* **23**, 171–263 (1995).
9. Liang, C. C. Conduction Characteristics of the Lithium Iodide-Aluminum Oxide Solid Electrolytes. *J. Electrochem. Soc.* **120**, 1289–1292 (1973).
10. Tadagana, K., Imai, K., Tatsumisago, M. & Minami, T. Preparation of AgI-Al<sub>2</sub>O<sub>3</sub> Composites with High Ionic Conductivity Using Al<sub>2</sub>O<sub>3</sub> Aerogel and Xerogel. *J. Electrochem. Soc.* **147**, 4061–4064 (2000).
11. Li, M.; Zhang, H.; Cook, S. N.; Li, L.; Kilner, J. A.; Reaney, I. M.; Sinclair, D. C. Dramatic Influence of A-Site Nonstoichiometry on the Electrical Conductivity and Conduction Mechanisms in the Perovskite Oxide Na<sub>0.5</sub>Bi<sub>0.5</sub>TiO<sub>3</sub>. *Chem. Mater.* **2015**, 27 (2), 629–634.

## 4. Doped NBT

Low levels of A-site non-stoichiometry in NBT can lead to three different types of electrical behaviour, as discussed in Chapter 3. It can be; a conductor with a high level of nearly pure oxide ion conduction; a mixed conductor with both n-type and oxide ion conduction; an electrical insulator with predominantly n-type conduction at elevated temperature. To further improve the electrical properties of NBT, either as an oxide ion conductor or as a ferroelectric material, chemical doping is required to either create or compensate for defects; however, the A-site non-stoichiometry is rather limited in NBT and can be difficult to control.

Chemical doping is a long-known, well-established way that can induce significant changes in functional properties. Li et al. have reported that 2 at% Mg-doping on the Ti site of conducting  $\text{NB}_{0.49}\text{T}$  can lead to  $\sim 0.5$  an order of magnitude increase in bulk conductivity (Figure 4-1).<sup>1</sup> The increase in bulk conductivity was attributed to the increase in the concentration of oxygen vacancies according to the equation:

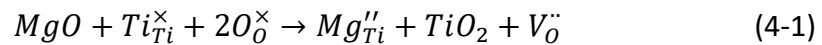


Figure 1 in reference [1]

Figure 4-1. Arrhenius-type plots of bulk conductivity for selected NBT samples.<sup>1</sup>

With 2 at% Mg doping,  $^{18}\text{O}$  tracer diffusion measurements showed the diffusion coefficient  $D^*$  at 632 °C increased by 2 orders of magnitude, from  $2.64 \times 10^{-10} \text{ cm}^2 \text{ s}^{-1}$  for  $\text{NB}_{0.49}\text{T}$  to  $1.17 \times 10^{-8} \text{ cm}^2 \text{ s}^{-1}$  indicating the Mg doping does as expected from the equation above and improves the oxide ion conduction by increasing the oxygen vacancy concentration (Figure 4-2). The oxide ion transport number  $t_{\text{ion}}$  from EMF measurements also increased from  $\sim 0.93$  at 600 °C for  $\text{NB}_{0.49}\text{T}$  to  $\sim 0.98$  (Figure 4-3).

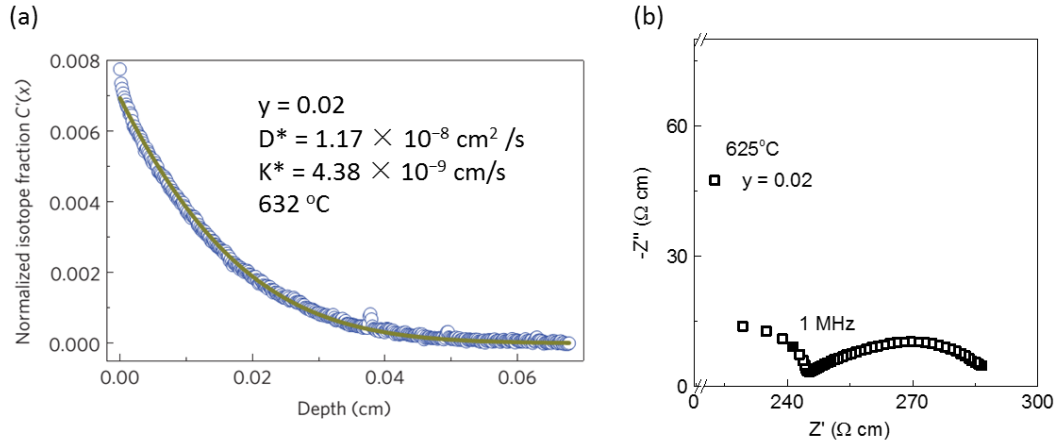
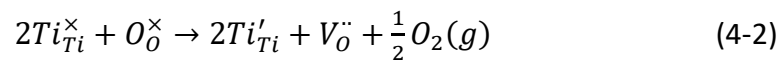


Figure 4-2. (a)  $^{18}\text{O}$  tracer diffusion profile after exchange at 632 °C for  $\sim 22000$  s with  $p^{18}\text{O}_2 \sim 508$  mbar and (b) a  $Z^*$  plot for  $y = 0.02$  at 625 °C. <sup>1</sup>

The results of  $^{18}\text{O}$  tracer diffusion measurements, combined with EMF measurements giving values close to unity for the transport number of oxygen, proves Mg doping can enhance the oxide ion conduction in NBT without introducing any significant contribution from electronic conduction and result in Mg-doped  $\text{NB}_{0.49}\text{T}$  being a solid electrolyte. Moreover, Mg doping also extends the oxide ion conduction window (e.g. as an electrolyte in SOFCs) for the bulk conductivity to a lower  $p\text{O}_2$  range. For un-doped NBT, no change in bulk electrical conductivity at 600 °C occurs by varying the  $p\text{O}_2$  from  $\text{O}_2$  to  $\text{N}_2$  but it undergoes an increase in conductivity when annealed under 5% $\text{H}_2$ /95% $\text{N}_2$  due to oxygen loss with accompanied partial reduction of  $\text{Ti}^{4+}$  to  $\text{Ti}^{3+}$  (Figure 4-4 (a) and (b)) following the equation:



In the case of 2 at% Mg doped NBT, the bulk conductivity remains unchanged after  $\sim 45$  h under the same conditions (Figure 4-4 (c) and (d)). The sintering temperature of the NBT ceramics can be significantly reduced by Mg-doping.

Figure 2 in reference [1]

Figure 4-3. Oxygen ionic transport number,  $t_{\text{ion}}$ , for selected NBT samples from EMF measurements using air/ $\text{N}_2$  gas.<sup>1</sup>

Figure S7 in reference [1]

Figure 4-4.  $Z^*$  plots for (a) NBT and (c) 1 at% Mg doped NBT at 600 °C under different atmospheres, (b) and (d) are expanded scales of (a) and (c) to highlight low impedance data.<sup>1</sup>

In this chapter both donor (Nb, x-series) and acceptor (Mg, y-series) doping on the Ti-site are reported; the former is aimed at providing a more reliable and efficient way to reduce the leakage conductivity since excess Bi in the starting material can reintroduce oxide ion conduction once a certain amount of extra Bi is exceeded in the starting composition ( $\geq 2$  at% extra Bi in this project but will depend on different synthesis procedures and conditions); the latter is to explore Mg-doped NBT in more depth regarding the switch from dielectric to solid-electrolyte behaviour to further enhance the oxide ion conduction, improve the stability of NBT under reducing atmosphere and to lower the sintering temperature required to make dense ceramics.

## 4.1. Donor doping

### 4.1.1. Phase purity and microstructure

Niobium donor-doping on the Ti-site of NBT ceramics has been investigated based on a general formula  $\text{Na}_{0.5}\text{Bi}_{0.5}\text{Ti}_{1-x}\text{Nb}_x\text{O}_{3+1/2x}$  ( $0 \leq x \leq 0.100$ , x-series). A combination of XRD and SEM/EDX were employed to determine the phase purity.

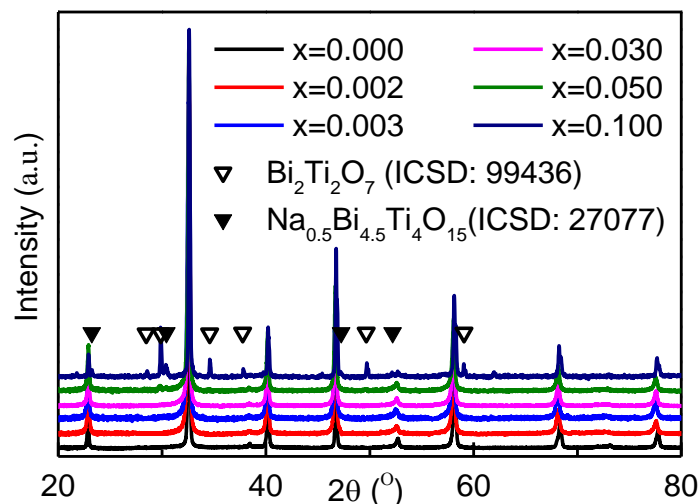


Figure 4-5. Room temperature X-ray powder diffraction data for selected Nb-doped NBTs.

Results indicate Nb-doped NBTs remain single phase in the range  $0.000 \leq x < 0.030$ . Although XRD data suggests  $x = 0.030$  to be phase pure (Figure 4-5), SEM/EDX revealed the presence of an  $A_5B_4O_{15}$  secondary phase, Figure 4-6 (a). EDX analysis of the composition of the bulk and secondary phases are summarised in Table 4-1.

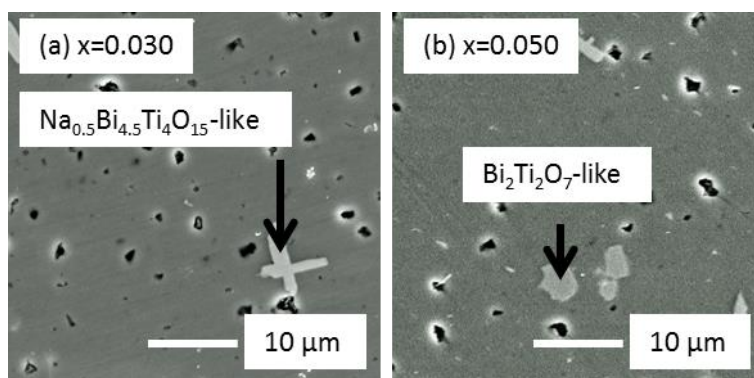


Figure 4-6. Secondary electron image for  $x = 0.030$  and  $0.050$  ceramics (polished without thermal etching) showing the  $Na_{0.5}Bi_{4.5}Ti_4O_{15}$ -like and  $Bi_2Ti_2O_7$ -like secondary phases.

Both a pyrochlore-based ' $Bi_2Ti_2O_7$ ' phase and a  $A_5B_4O_{15}$  phase were detected by XRD and SEM/EDX for samples with  $x \geq 0.050$ . The average composition for the  $A_2B_2O_7$  pyrochlore-type phase contains Na and Bi on the A-site and Ti and Nb on the Ti-site

with an average composition of  $\text{Na}_{0.34}\text{Bi}_{1.59}\text{Ti}_{1.63}\text{Nb}_{0.37}\text{O}_{6.74}$ . For the layered perovskite phase  $\text{A}_5\text{B}_4\text{O}_{15}$ , both Ti and Nb are on the Ti-site with a slight excess of Na for Bi on the A-site with an average composition of  $\text{Na}_{0.57}\text{Bi}_{4.43}\text{Ti}_{3.78}\text{Nb}_{0.22}\text{O}_{15.04}$  (Table 4-1). In addition, despite secondary phases appearing in samples with  $x \geq 0.030$ , EDX results suggest a continuous increase in Nb-content with an increase of the  $\text{Nb}_2\text{O}_5$  content in the starting composition. SEM images show a systematic decrease in grain size of NBT with increasing Nb content from  $\sim 10 \mu\text{m}$  for  $x = 0.000$  to  $\sim 1 \mu\text{m}$  for  $x = 0.050$  (Figure 4-7).

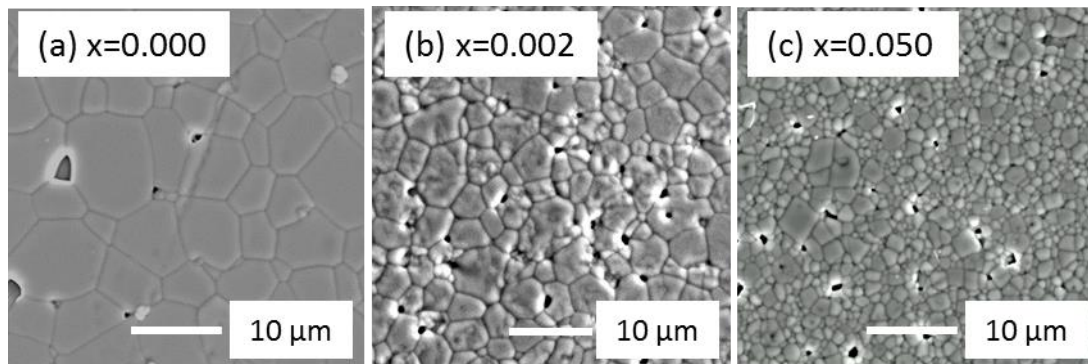


Figure 4-7. SEM micrographs of (a)  $x = 0.000$ , (b)  $x = 0.005$  and (c)  $x = 0.050$ . All samples were polished and thermally etched prior to SEM.

Table 4-1. Bulk chemical composition (relative cation at%) and associated error (standard deviation) by SEM/EDX of the main and secondary phases present in selected Nb-doped NBT ceramics.

Starting Composition		Na (at%)	Bi (at%)	Ti (at%)	Nb (at%)
<b>x = 0.010</b>	Main phase	25.3(±0.8)	25(±0.4)	48.7(±0.3)	0.9(±0.4)
	Theoretical value	25	25	49.5	0.5
<b>x = 0.020</b>	Main phase	25.2(±0.6)	24.8(±0.4)	48.6(±0.6)	1.3(±0.5)
	Theoretical value	25	25	49	1

	Main phase	25.5 ( $\pm 0.3$ )	24.7 ( $\pm 0.2$ )	48.0 ( $\pm 0.3$ )	1.8 ( $\pm 0.2$ )
<b>x = 0.030</b>	Theoretical value	25	25	48.5	1.5
	Na <sub>0.5</sub> Bi <sub>4.5</sub> Ti <sub>4</sub> O <sub>15</sub> phase	6.3 ( $\pm 0.8$ )	49.1 ( $\pm 0.7$ )	42.2 ( $\pm 0.5$ )	2.5 ( $\pm 0.2$ )
	Main Phase	26.9 ( $\pm 0.4$ )	24.2 ( $\pm 0.4$ )	46.3 ( $\pm 0.5$ )	2.6 ( $\pm 0.4$ )
<b>x = 0.050</b>	Theoretical value	25	25	47.5	2.5
	Bi <sub>2</sub> Ti <sub>2</sub> O <sub>7</sub> phase	8 ( $\pm 1$ )	40 ( $\pm 2$ )	42 ( $\pm 2$ )	10 ( $\pm 2$ )

#### 4.1.2. Electrical properties

As shown in Figure 4-8, both the maximum permittivity,  $\epsilon_{r,max}$ , and the corresponding temperature,  $T_{\epsilon_{r,max}}$  of samples in the x-series are influenced by an increase in the Nb content.  $\epsilon_{r,max}$  decreases from a highest value of  $\sim 2800$  for un-doped NBT to a lowest value of  $\sim 1400$  for  $x = 0.10$  (Figure 4-9 (a)). On the other hand,  $T_{\epsilon_{r,max}}$  was initially unchanged up to  $x = 0.03$  and then continuously decreased from  $\sim 320$  to  $\sim 270$  °C for  $x = 0.10$ .

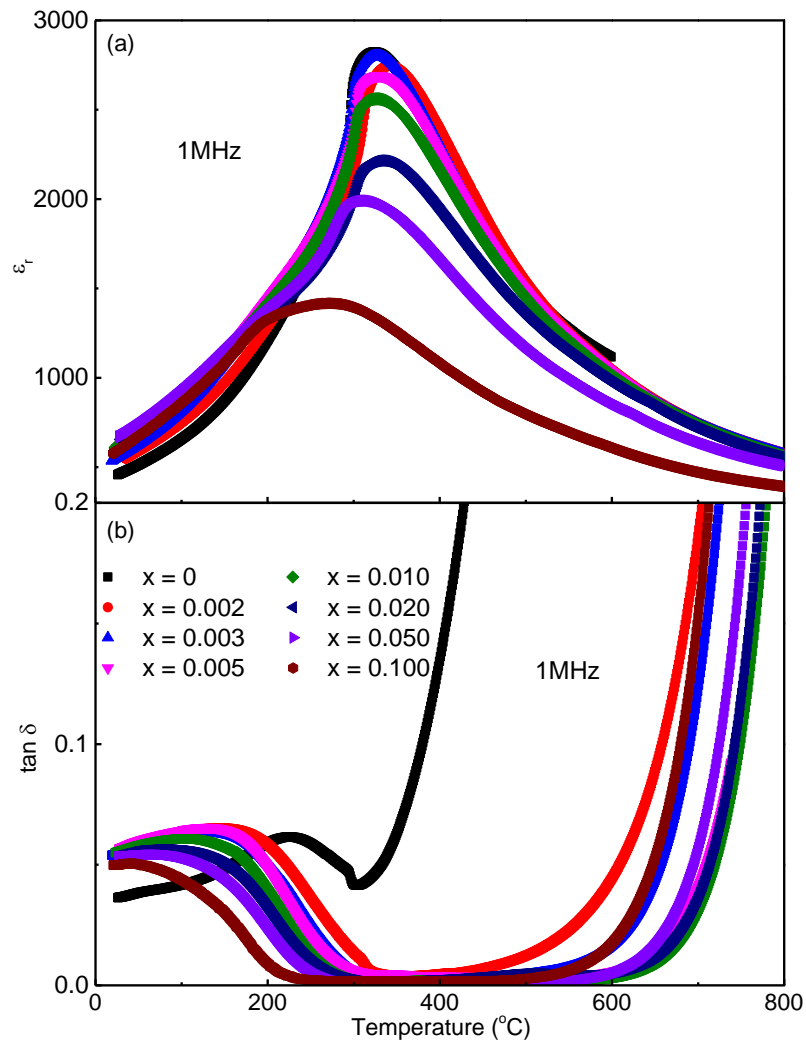


Figure 4-8. Temperature dependence of (a)  $\epsilon_r$  and (b)  $\tan \delta$  at 1 MHz for Nb-doped NBTs.

A significant change is observed in the dielectric loss,  $\tan \delta$  versus temperature. For un-doped NBT,  $\tan \delta$  increased rapidly above  $\sim 300$  °C, but the  $\tan \delta$  became significantly lower in the range  $300 \sim 600$  °C with even a low level of Nb doping ( $x = 0.002-0.003$ ); for  $x \geq 0.005$   $\tan \delta$  remained below 0.03 in the same range. It is worth to note that the depolarisation temperature also decreased with increasing Nb-doping from  $\sim 200$  °C for un-doped NBT to  $\sim 50$  °C for  $x = 0.10$  (Figure 4-9 (b)).

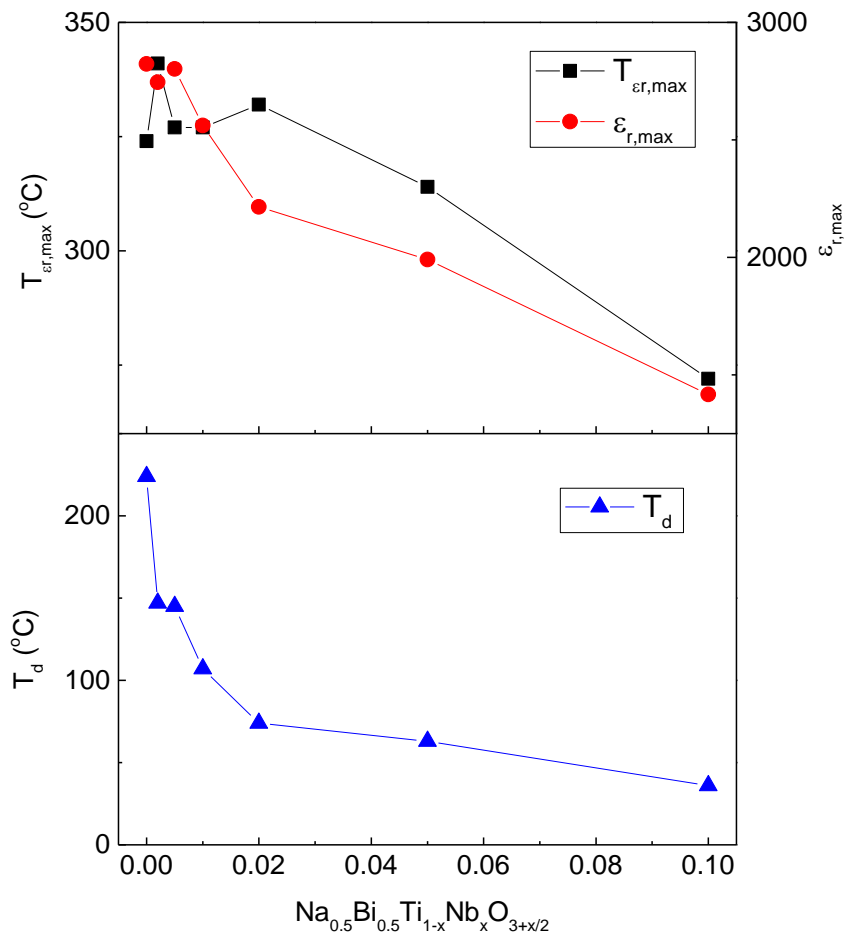


Figure 4-9. The influence of Nb-doping on (a) maximum permittivity,  $\epsilon_{r,\max}$  and the corresponding temperature,  $T_{\epsilon_{r,\max}}$  and (b) depolarisation temperature,  $T_d$ .

Z\* plots revealed a change in electrical behaviour of NBT with increasing Nb doping level, from conducting NBT-type of behaviour (three components with high bulk conductivity) for un-doped NBT to intermediate behaviour (one component with a bulk conductivity similar to intermediate NBTs) for  $x = 0.002 - 0.003$  and finally insulating NBT-type of behaviour (one component with low bulk conductivity) for  $x = 0.050$  (Figure 4-10 (a)). The difference in bulk conductivity between undoped and  $x \geq 0.005$  samples at  $600\text{ }^\circ\text{C}$  is more than 3 orders of magnitude.

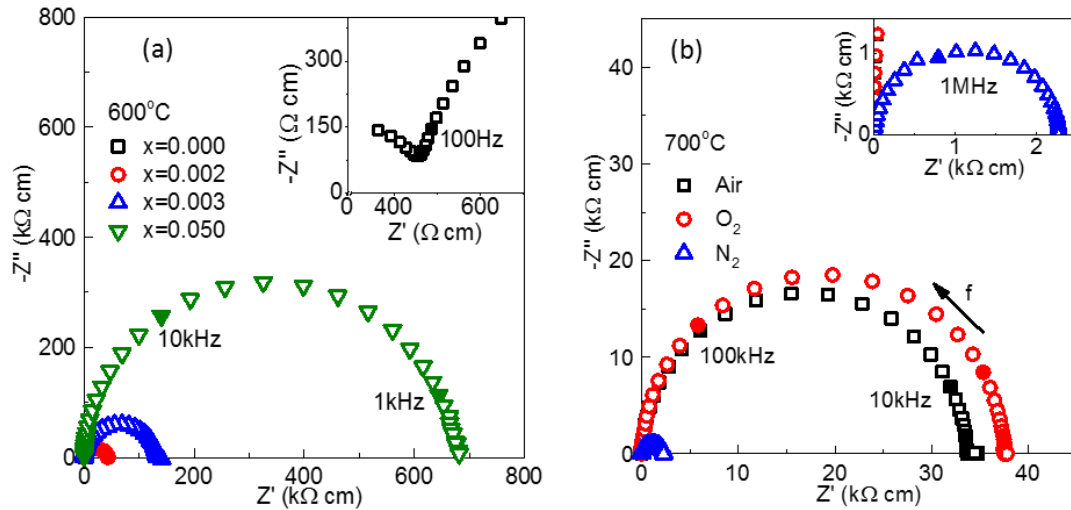


Figure 4-10. Z\* plots for a) selected Nb-doped NBTs at 600°C and b)  $x = 0.010$  under different atmospheres.

The temperature dependence of bulk conductivity for all samples in this series is summarised in an Arrhenius type plot shown in Figure 4-11. Nb-donor doping on the Ti-site induces a significant influence on the bulk conductivity of NBT (Figure 4-11 and Figure 4-10 (a)). The bulk conductivity of samples in the range  $0 \leq x \leq 0.010$  decrease continuously, first from conducting NBT to an intermediate NBT with a very low level of Nb doping ( $x = 0.002 - 0.003$ ), then higher Nb doping levels lead to a further decrease in bulk conductivity until  $x = 0.010$  is reached. Samples with  $x \geq 0.010$  have roughly the same bulk conductivity which is more than 3 orders of magnitude lower than un-doped NBT (Figure 4-11). The bulk conduction activation energy also changed from  $< 1$  eV for un-doped NBT to 0.92-1.55 eV for low levels of Nb doping and finally to 1.5-1.8 eV for relatively high level Nb-containing NBT. Such a change in activation energy normally implies a change in conduction mechanism. As mentioned in Ch.3, the optical band gap of NBT is about 3.0 ~ 3.5 eV which is about twice of the activation energy for high level Nb-doped NBT. This suggests the oxide ion conduction has been minimised and the bulk conduction in high level Nb-doped NBT is dominated by intrinsic electronic conduction.

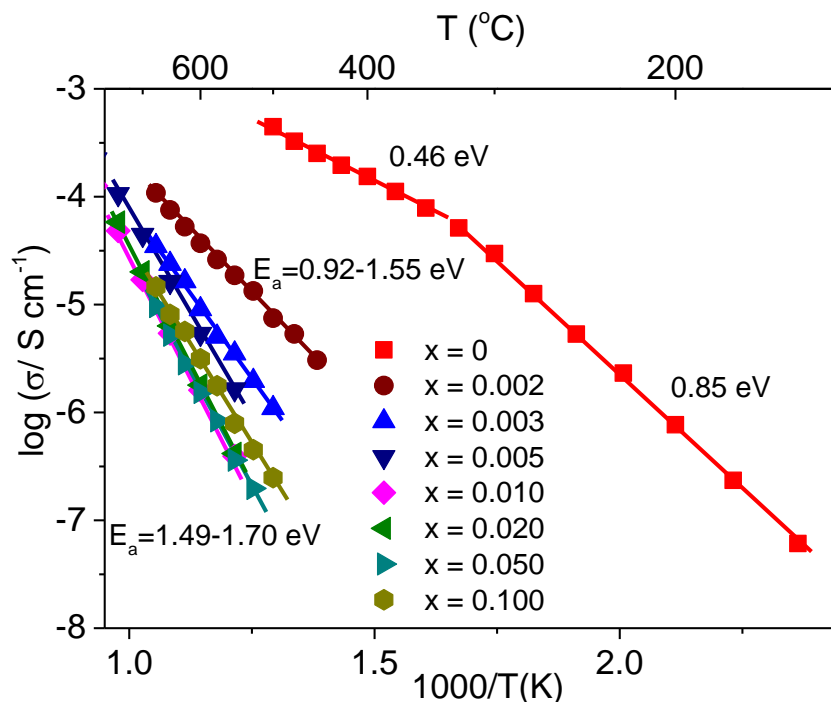


Figure 4-11. Arrhenius plot of bulk conductivity,  $\sigma_b$ , versus reciprocal temperature for Nb doped NBTs.

$pO_2$  dependent impedance measurements showed a decrease in bulk resistivity for  $x = 0.010$  from  $\sim 38 \text{ k}\Omega\cdot\text{cm}$  in  $O_2$  to  $\sim 35 \text{ k}\Omega\cdot\text{cm}$  in air and eventually to  $\sim 2.2 \text{ k}\Omega\cdot\text{cm}$  in  $N_2$  (Figure 4-10 (b)). No clear evidence of a low frequency spike associated with Warburg diffusion was observed. The  $pO_2$  dependence of the bulk conductivity and absence of Warburg diffusion indicate  $x = 0.010$  is dominated by n-type electronic conduction as opposed to ionic conduction.

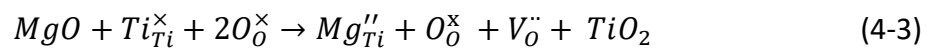
EMF results are consistent with impedance and  $pO_2$  dependent impedance measurements as they show the oxide ion conduction is suppressed with Nb doping (Table 4-2). Mixed conduction with  $t_{ion} \sim 0.5$  is observed at very low doping levels ( $x \leq 0.003$ ), further increases in doping level ( $x \geq 0.005$ ) eliminate most of the oxide ion conduction and leads to an electronic dominated bulk conduction ( $t_{ion} \leq 0.07$ ).

Table 4-2.  $t_{ion}$  values between 600 and 800 °C for selected samples in x-series.

Starting composition	$t_{ion}$ (600 °C)	$t_{ion}$ (700 °C)	$t_{ion}$ (800 °C)
<b>x = 0</b>	0.93	0.93	0.85
<b>x = 0.002</b>	0.57	0.63	0.63
<b>x = 0.003</b>	0.47	0.49	0.53
<b>x = 0.005</b>	0.06	0.06	0.07
<b>x = 0.020</b>	0.05	0.06	0.06
<b>x = 0.100</b>	0.02	0.02	0.03

## 4.2. Acceptor doping

Acceptor doping is a possible way to increase the ionic conductivity in NBT by increasing the oxygen vacancy concentration. In this chapter, Mg will be used as an acceptor dopant on the Ti-site to enhance oxide ion conduction by inducing more oxygen vacancies following the equation:



In order to maximise the oxide ion conduction, NB<sub>0.49</sub>T was chosen as the starting point base composition for the  $\gamma$ -series since it has a higher oxygen vacancy concentration than nominally stoichiometric NBT.  $\gamma$ -series Mg-doped NBT samples were prepared based on the general formula Na<sub>0.5</sub>Bi<sub>0.49</sub>Ti<sub>1- $\gamma$</sub> Mg $\gamma$ O<sub>3- $\gamma$</sub>  ( $0 \leq \gamma \leq 0.05$ ,  $\gamma$ -series).

### 4.2.1. Phase purity and microstructure

The phase purity of Mg-doped NBTs were determined by a combination of XRD and SEM/EDX. No extra peaks were observed in XRD data indicating good phase purity for all 6 samples in this series (Figure 4-12). However, secondary phases were detected by

SEM/EDX analysis which reveals the presence of  $\text{MgTiO}_3$  which exists in  $y \geq 0.02$  (Figure 4-13, Figure 4-14 (c) and Table 4-3).

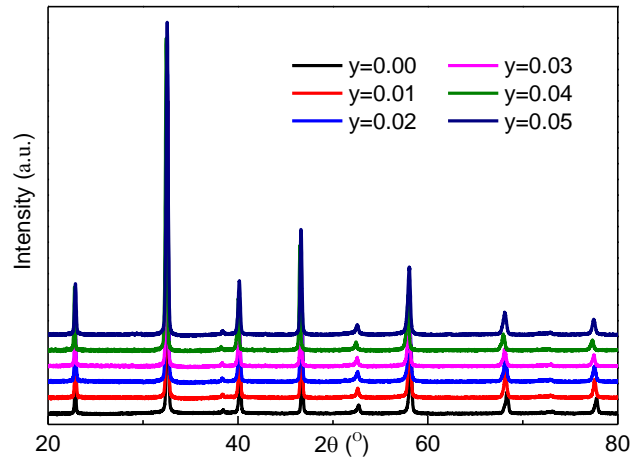


Figure 4-12. Room temperature X-ray powder diffraction data for  $y$ -series Mg-doped NBTs

EDX analysis shows a small amount of Na and Bi exist in the  $\text{MgTiO}_3$  secondary phase. This may be caused by the influence of the signal from the NBT matrix since the spot size of EDX on SEM is slightly larger than the size of the  $\text{MgTiO}_3$  phase. EDX results also showed no significant change in the Mg content of the bulk with an increase of  $y$  from 0.02 to 0.05, indicating the solid solution limit of Mg in NBT is  $\sim 2$  at%. The average grain size of Mg-doped NBT initially remained unchanged at low levels of Mg doping ( $y \leq 0.02$ ) but then started to decrease with increasing Mg content (Figure 4-14).

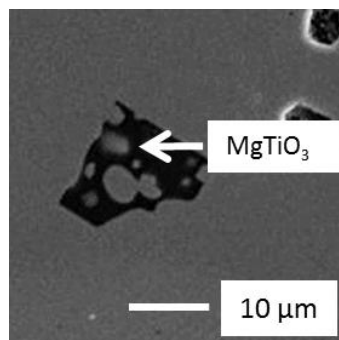


Figure 4-13. Secondary electron image for a  $y = 0.02$  ceramic (polished without thermal etching).

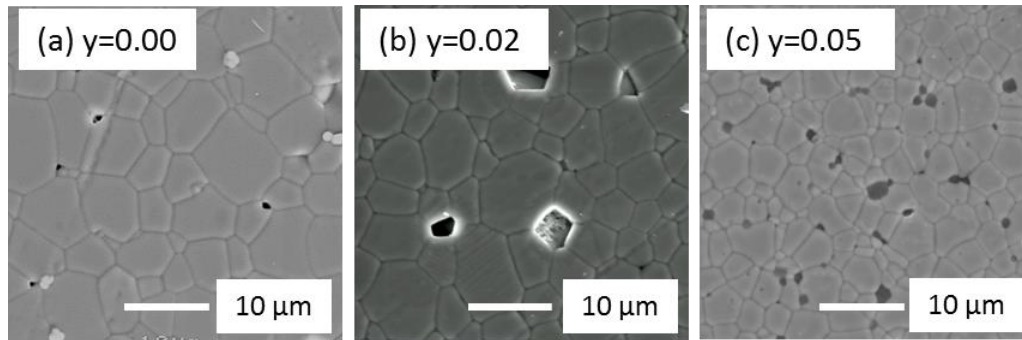


Figure 4-14. SEM micrographs for samples in the  $\gamma$ -series.

Table 4-3. Bulk chemical composition (relative cation at%) and associated error (standard deviation) by SEM/EDX of the main and secondary phases present in  $\gamma = 0.02, 0.04$  and  $0.05$  ceramics.

Starting Composition		Na (at%)	Bi (at%)	Ti (at%)	Mg (at%)
<b><math>\gamma = 0.02</math></b>	Main phase	25.3 ( $\pm 0.3$ )	25 ( $\pm 0.1$ )	49.1 ( $\pm 0.2$ )	0.6 ( $\pm 0.2$ )
	Theoretical value	25	25	49	1
	MgTiO <sub>3</sub>	2 ( $\pm 1$ )	1 ( $\pm 1$ )	49 ( $\pm 1$ )	48 ( $\pm 1$ )
<b><math>\gamma = 0.04</math></b>	Main phase	26.0 ( $\pm 0.6$ )	24.5 ( $\pm 0.1$ )	48.6 ( $\pm 0.9$ )	0.7 ( $\pm 0.3$ )
	Theoretical value	25	25	48	2
	MgTiO <sub>3</sub>	2 ( $\pm 1$ )	5 ( $\pm 2$ )	46 ( $\pm 1$ )	45 ( $\pm 1$ )
<b><math>\gamma = 0.05</math></b>	Main phase	26.2 ( $\pm 0.9$ )	25.7 ( $\pm 0.7$ )	47.2 ( $\pm 1.4$ )	0.8 ( $\pm 0.4$ )
	Theoretical value	25	25	47.5	2.5

#### 4.2.2. Electrical properties

The temperature dependence of the maximum permittivity,  $\epsilon_{r,\max}$  and the dielectric loss,  $\tan \delta$  are shown in Figure 4-15.

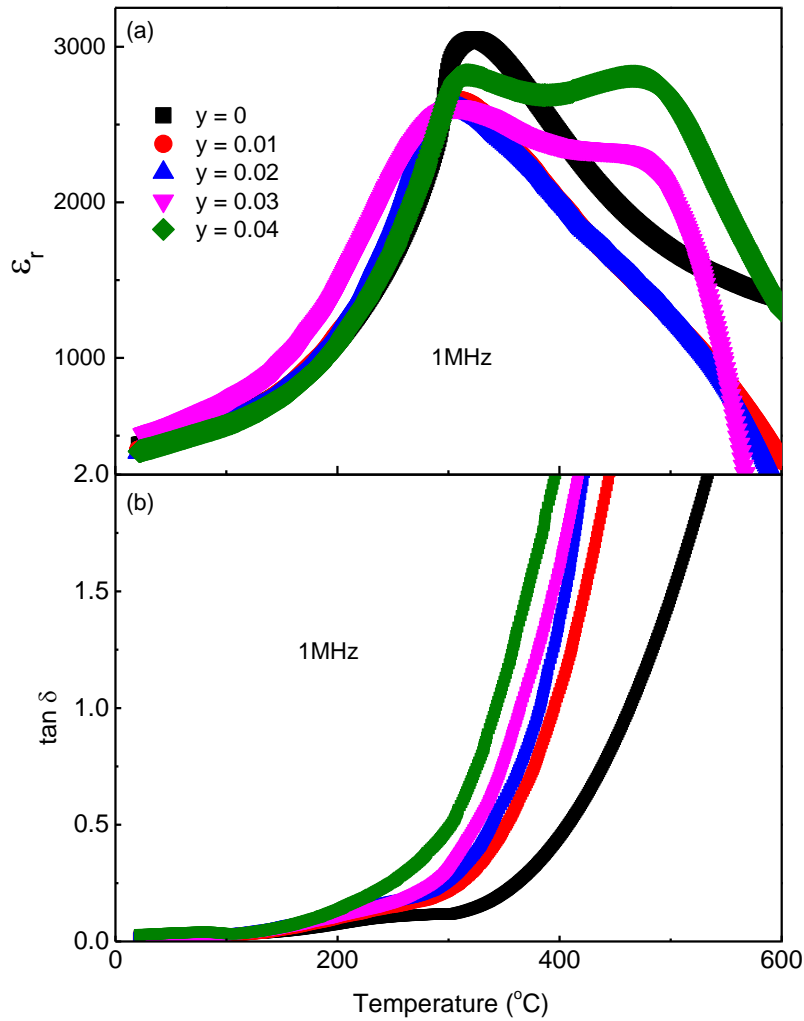


Figure 4-15. Temperature dependence of (a)  $\epsilon_r$  and (b)  $\tan \delta$  at 1 MHz for  $\text{Na}_{0.50}\text{Bi}_{0.49}\text{Ti}_{1-y}\text{Mg}_y\text{O}_{3-x}$ .

A modest difference in the maximum permittivity,  $\epsilon_{r,\max}$ , with composition in the  $y$ -series is observed. The  $T_{\epsilon_r,\max}$  initially decreases from 323 °C for  $x = 0$  to  $\sim 305$  °C for  $x = 0.01 \sim 0.03$  and then increases to  $\sim 315$  °C for  $x = 0.04$ , Figure 4-16. Similar to  $T_{\epsilon_r,\max}$ ,  $\epsilon_{r,\max}$  also initially decreases from  $\sim 2800$  to  $\sim 2600$  with Mg doping and remains similar in the range  $0.01 \leq y \leq 0.03$  and finally increases again to  $\sim 2800$  for  $y = 0.04$ . For all Mg doped samples,  $\epsilon_{r,\max}$  showed abnormal behaviour which is a rapid decrease at high temperature ( $> 500$  °C). This phenomenon is caused by the high leakage conductivity of the  $y$ -series samples at high temperature. Figure 4-15 (b) shows a significant

increase in  $\tan \delta$  with the increase of Mg content at temperature  $> 300$  °C. It was not possible to establish the depolarisation temperature,  $T_d$ , for any samples in this series due to their high loss at low temperature.

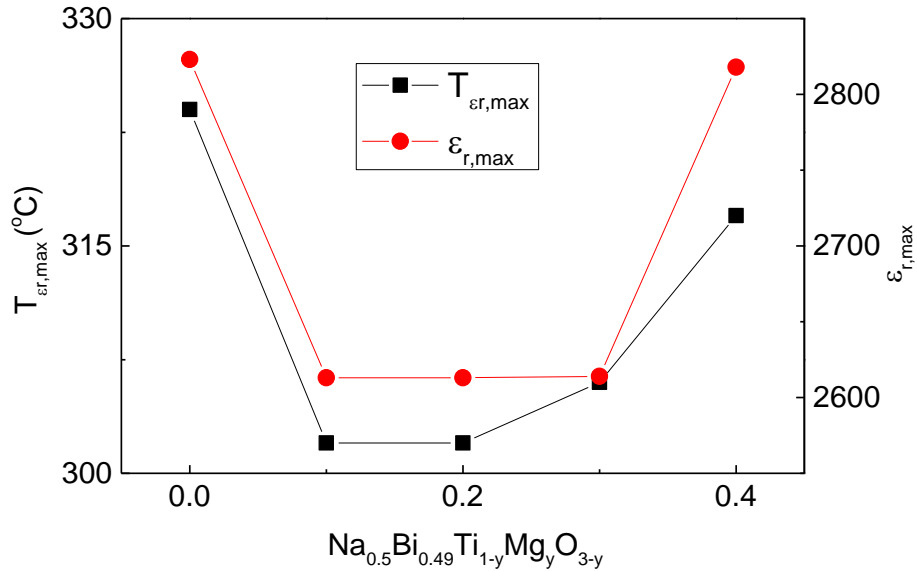


Figure 4-16. The influence of Mg doping on (a) maximum permittivity,  $\epsilon_{r,max}$  and the corresponding temperature,  $T_{\epsilon_{r,max}}$

$Z^*$  plots for all samples in the y-series consisted of three components representing the bulk, grain boundary and electrode effect responses (from high to low frequency) similar to un-doped conducting NBTs. However, with relatively high doping level, the grain boundary response in Mg-doped NBTs merged with the electrode effect response leading to a distorted quarter circle (instead of a distorted semicircle) followed by a spike (Figure 4-17 (a)).

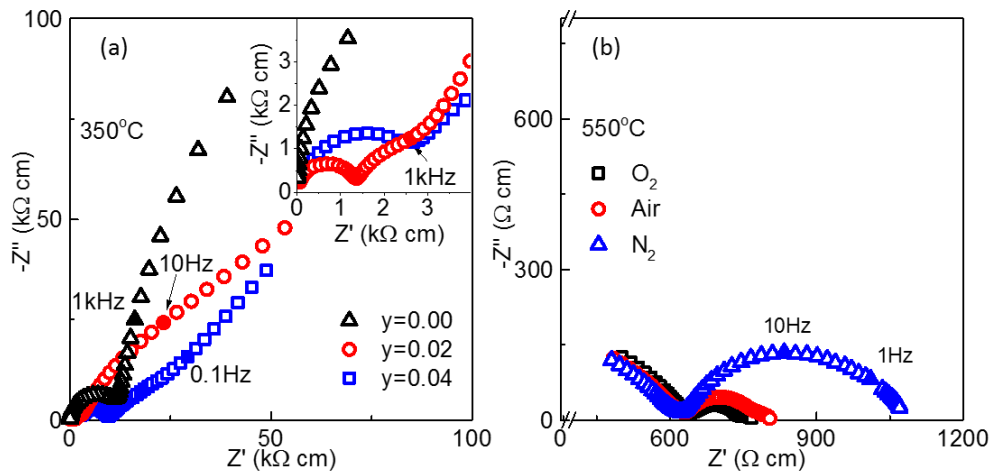


Figure 4-17.  $Z^*$  plots of (a) selected  $y$ -series samples at 350 °C and (b)  $y = 0.04$  at 550 °C under different atmospheres.

Temperature dependent bulk conductivity behaviour of selected  $y$ -series samples are summarised in the Arrhenius plot in Figure 4-18. Compared with undoped  $\text{NB}_{0.49}\text{T}$  ceramics, low levels of Mg doping can increase the bulk conductivity by  $\sim 0.5$  order of magnitude. However, further increases in Mg content showed very limited further influence on the bulk conductivity, supporting the SEM/EDX results that indicated the solid solution limit of Mg on the Ti-site in NBT is about 1 ~ 2 at%.

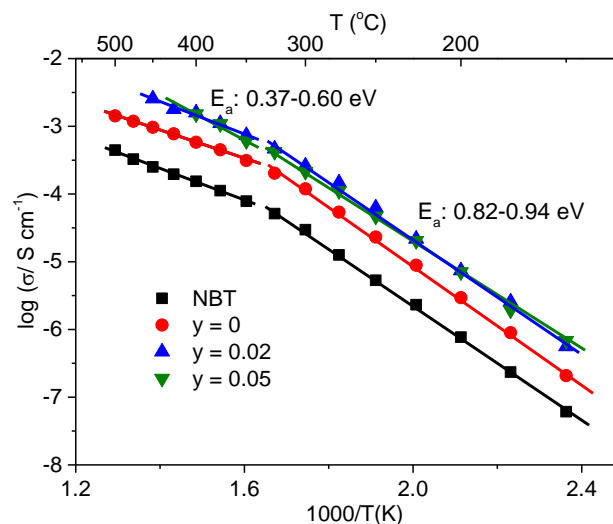
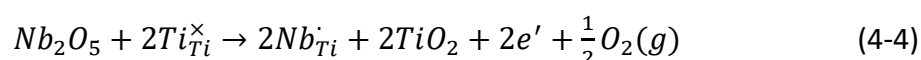


Figure 4-18. Arrhenius plot of bulk conductivity,  $\sigma_b$ , versus reciprocal temperature for selected  $y$ -series and un-doped NBT ceramics. Activation energy,  $E_a$ , values for  $\sigma_b$  are included.

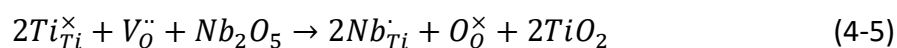
Mg-doped NBTs show a  $pO_2$  independent bulk conduction mechanism and a p-type grain boundary conduction mechanism which indicates Mg-doped NBTs possess ionic dominated bulk conduction. EMF and  $^{18}O$  tracer diffusion measurements are consistent with the  $pO_2$  independent bulk conductivity measurements.

### 4.3. Discussion

For Nb doping, two compensation mechanisms are possible, either electronic (or donor) doping:



or ionic charge compensation:



The electronic (or donor-doping) mechanism is commonly adopted in (Ba,Sr)TiO<sub>3</sub>-related titanates where low levels of electron doping can induce high levels of semiconductivity. However, given the bulk conductivity of NBT decreased significantly with Nb doping indicates the excess positive charge from the Nb ions is compensated by filling oxygen vacancies with oxygen. Consequently the oxide ion conductivity is suppressed due to a suppression of charge carriers (oxygen vacancies) and Nb-doped ceramics with sufficient Nb to fill-up many of the oxygen vacancies exhibits near intrinsic electronic conduction. The intrinsic electronic conduction is confirmed by samples with  $x \geq 0.010$  where the activation energy for bulk conduction is  $\sim 1.8$  eV which is close to half of the reported band gap (3.0 - 3.5 eV).

The different donor doping mechanisms of NBT (ionic compensation) and (Ba,Sr)TiO<sub>3</sub> (electronic compensation) is related to their different band structures.<sup>2</sup> In NBT, the  $6s^2$  electron lone pairs of Bi-ions hybridise with the oxygen  $2p$  orbitals. For (Ba,Sr)TiO<sub>3</sub>, the valence band is formed mainly by O  $2p$  states, but for NBT the interaction of  $6s$  orbitals with the O  $2p$  orbitals give rise to a higher valence band

maximum, Figure 4-19. The high conduction band minimum and high valance band maximum of NBT compared to (Ba,Sr)TiO<sub>3</sub> is less favourable for an n-type doping mechanism and therefore is a reason for the lack of n-type conduction (electronic donor-doping) in NBT system.

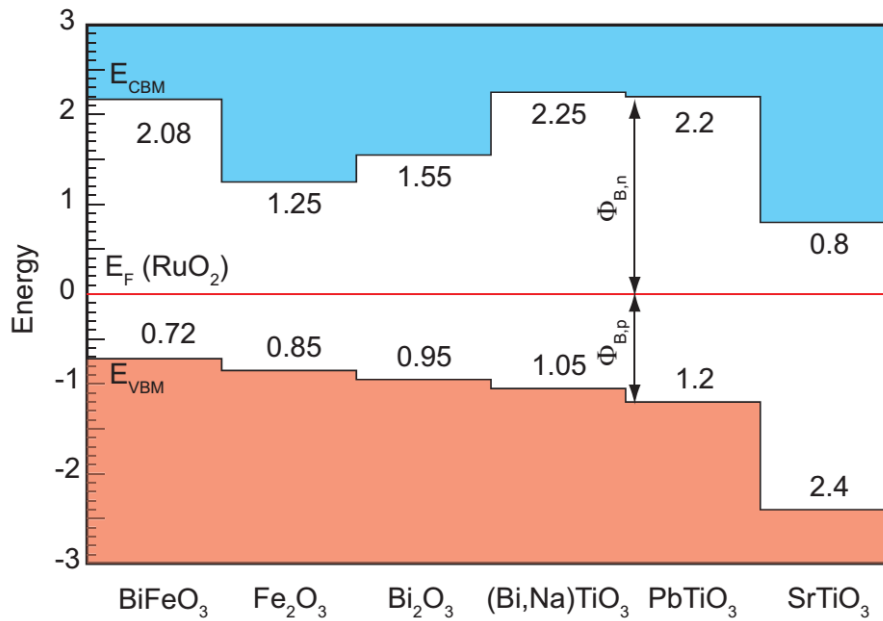


Figure 4-19. Energy band alignment of various oxides with respect to the Fermi level of RuO<sub>2</sub>.<sup>2</sup>

Mixed oxide ion and n-type conduction behaviour similar to NB<sub>0.52/0.55</sub>T can be obtained with very low levels of Nb doping, e.g. an intermediate bulk conductivity compared to conducting/insulating NBTs with tan δ remaining low (< 0.1) below 500 °C. The remaining oxide ion conduction level was confirmed by EMF measurements with values of t<sub>ion</sub> ~ 0.5.

Nb-doping in the x-series is systematic and effective in ‘mopping-up’ and compensating for any oxygen deficiency associated with Bi<sub>2</sub>O<sub>3</sub> loss during processing; t<sub>ion</sub> (600 °C) decreases from 0.93 (undoped) to 0.47 for x = 0.003 and is < 0.06 for 0.010 ≤ x ≤ 0.100, Table 4-2. As a consequence, bulk conductivity and tan δ remain low up to

$x = 0.100$ . Unlike Bi-rich NBT, all samples in this series with  $x \geq 0.010$  retain insulating behaviour and exhibit excellent, high temperature low dielectric loss behaviour in the range  $\sim 300 - 650$  °C (Figure 4-8 (b)). The temperature dependent permittivity profile remains similar to undoped NBT up to  $x = 0.010$ , then a significant decrease occurs in  $\epsilon_{r,max}$  for  $0.020 \leq x \leq 0.100$  indicating Nb-doping for Ti influences the lattice polarisability/ferroelectric domain wall motion (Figure 4-8 (a) and Figure 4-9 (a)). Again, the level of  $x$  required to fully suppress oxide-ion conduction in NBT ceramics to promote, high temperature, low dielectric low behaviour will be dependent on the employed ceramic processing conditions.

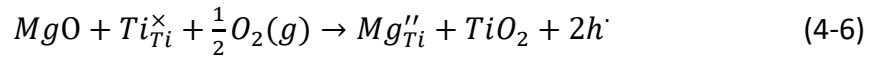
The Bi-loss in NBT due to processing can be quantified since the amount of Nb required to fill up the oxygen vacancies is in the range  $x = 0.005-0.010$ . It can be calculated that the oxygen non-stoichiometry in nominal stoichiometric NBT is in the range of  $0.0025-0.0050$  and the bismuth non-stoichiometry is in the range of  $0.0017-0.0033$ . This demonstrates the level of oxygen vacancies in NBT is very low compared to other oxide ion conductors (e.g.  $\delta\text{-Bi}_2\text{O}_3$ ) and therefore the mobility of oxygen ions in NBT must be very high in order to promote such a comparable oxygen ion conductivity although the actual Bi and O non-stoichiometry is dependent on different processing conditions.

It is worth mentioning that for samples with  $x \geq 0.010$ , the presence of ionic conduction was not readily observed by low frequency impedance data (low frequency spike) but residual levels can still be detected by EMF measurements ( $t_{ion} \sim 0.03-0.05$ ).

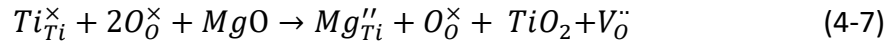
Mg has been adopted as an acceptor dopant on the Ti-site of NBT to enhance oxide ion conduction by creating more oxygen vacancies. Figure 4-18 reveals a low level of Mg doping ( $y = 0.02$ ) can increase bulk conductivity by  $\sim 0.5$  order of magnitude. However, further increases in Mg doping level show very limited further enhancement

of the bulk conductivity.

As discussed above, compared to normal titanates, NBT adopts a higher conduction band minimum and higher valence band maximum which is un-favourable for n-type doping. On the other hand, NBT is more favourable for p-type doping. Therefore, for Mg doping on the Ti-site, the two possible compensation mechanisms are electronic acceptor-doping:



or ionic charge compensation:



Based on experiment results of Mg doped NBT, there is an increase in bulk conductivity but also an increase in oxygen diffusion coefficient and oxide ion transport number. This shows only the ionic charge compensation is taking place which means Mg doping is a reliable way to increase oxygen vacancy concentration without introducing p-type conduction.

The increase in bulk conduction also influences the temperature dependent permittivity and  $\tan \delta$ . NBTs with Mg-doping show an abnormal rapid decrease at high temperature (500-600 °C) and some samples with high doping levels even possess a 'negative' permittivity (e.g.  $\gamma = 0.03$  above 550 °C). Such a negative permittivity is normally an instrument related error caused by inductance when the sample is too conductive compared to the sample holder and connection wires. The rise of  $\tan \delta$  with Mg doping also supports the conclusion the  $\gamma$ -series of NBT are leaky.

#### 4.4. Conclusions

In this chapter both Nb donor (x-series) and Mg acceptor ( $\gamma$ -series) doping on the Ti-site are reported. Very low level of Nb doping ( $x \leq 0.003$ ) will partially fill oxygen vacancies introduced by Bi-loss during processing and lead to mixed oxide ion and n-

type conduction in NBT ( $t_{\text{ion}} \sim 0.5$ ). Further increases in doping level ( $x \geq 0.005$ ) systematically suppresses oxide ion conduction and leads to predominant electronic bulk conduction ( $t_{\text{ion}} \leq 0.07$ ). It is worth to note that, opposite to Bi excess, secondary phases introduced by excess Nb-doping have very limited influence on NBT bulk conductivity.

The solid solution limit of Mg doping on Ti-site has been determined to be  $\sim 2$  at%. NBT bulk conductivity can be enhanced by low levels of Mg-doping ( $y \leq 0.02$ ) but further increases in Mg content shows little influence. Moreover, Mg-doping can extend the bulk oxide ion conduction window (e.g. as an electrolyte in SOFCs) to lower  $p\text{O}_2$  and reduce the required sintering temperature to obtain dense NBT ceramics.

## 4.5. References

1. Li, M. *et al.* A family of oxide ion conductors based on the ferroelectric perovskite  $\text{Na}_{0.5}\text{Bi}_{0.5}\text{TiO}_3$ . *Nat. Mater.* **13**, 31–5 (2014).
2. Li, S. *et al.* Influence of orbital contributions to the valence band alignment of  $\text{Bi}_2\text{O}_3$ ,  $\text{Fe}_2\text{O}_3$ ,  $\text{BiFeO}_3$ , and  $\text{Bi}_{0.5}\text{Na}_{0.5}\text{TiO}_3$ . *Phys. Rev. B* **88**, 45428 (2013).
3. Smyth, D. M. Effects of dopants on the properties of metal oxides. *Solid State Ionics* **129**, 5–12 (2000).

## 5. Fast oxide ion conduction in $\text{Bi}_4\text{Ti}_3\text{O}_{12}$

$\text{Bi}_4\text{Ti}_3\text{O}_{12}$  (BiT) is a member of the Aurivillius family with 3 layers of perovskite-like blocks interleaved by  $[\text{Bi}_2\text{O}_2]^{2+}$  sheets. On heating, it changes from a monoclinic ( $B1a1$ ) to a tetragonal cell ( $I4/mmm$ ) at  $\sim 675$  °C.<sup>1,2</sup> For decades it has been seen as a high-temperature, lead-free ferroelectric material.<sup>3,4</sup> However, as the perovskite blocks are formed by Bi and Ti and the  $[\text{Bi}_2\text{O}_2]^{2+}$  layers are similar to  $\text{Bi}_2\text{O}_3$  and the fact many compounds in the Aurivillius family are good oxide ion conductors, it is reasonable to presume BiT also possesses a high level of oxide ion conduction.<sup>5,6</sup>

It was reported in the literature that BiT possesses high leakage conductivity which is problematic for its ferroelectric applications. A series of studies showed the leakage conduction in BiT is a combination of oxide ion and p-type electronic conduction.<sup>7-10</sup> However, in the interpretation of the impedance data Noguchi *et al.*<sup>7-8</sup> incorrectly assigned the total conductivity based on a combination of several component responses as the grain response which means the bulk conductivity of BiT has been underestimated (see later). Furthermore, most researchers focus only on suppressing the conduction mechanism in BiT to minimize the leakage current. There has been no attempts, therefore, to try and enhance it and to treat BiT as a potential oxide ion conductor. In this chapter, one of the aims is to improve the oxide ion conduction in BiT to determine its potential as a solid electrolyte. Another aim is to maximise the oxide ion conduction by use of non-stoichiometry in the undoped material, similar to that of  $(\text{Na}_{1/2}\text{Bi}_{1/2})\text{TiO}_3$ , NBT.

## 5.1. Bismuth non-stoichiometry

### 5.1.1. Phase purity and microstructure

The sensitivity of oxide ion conduction in NBT with A-site non-stoichiometry is rather surprising and pronounced. As BiT has perovskite blocks containing only Bi ions as opposed to Na and Bi ions in NBT, it is worth exploring the influence of Bi non-stoichiometry on the electrical properties of BiT. In this series, samples with both Bi-excess and Bi-deficient starting compositions were prepared based on the general formula  $\text{Bi}_{4.00+x}\text{Ti}_3\text{O}_{12+3x/2}$  ( $-0.10 < x < 0.10$ , x-series). A combination of XRD and SEM/EDX was employed to determine the phase purity.

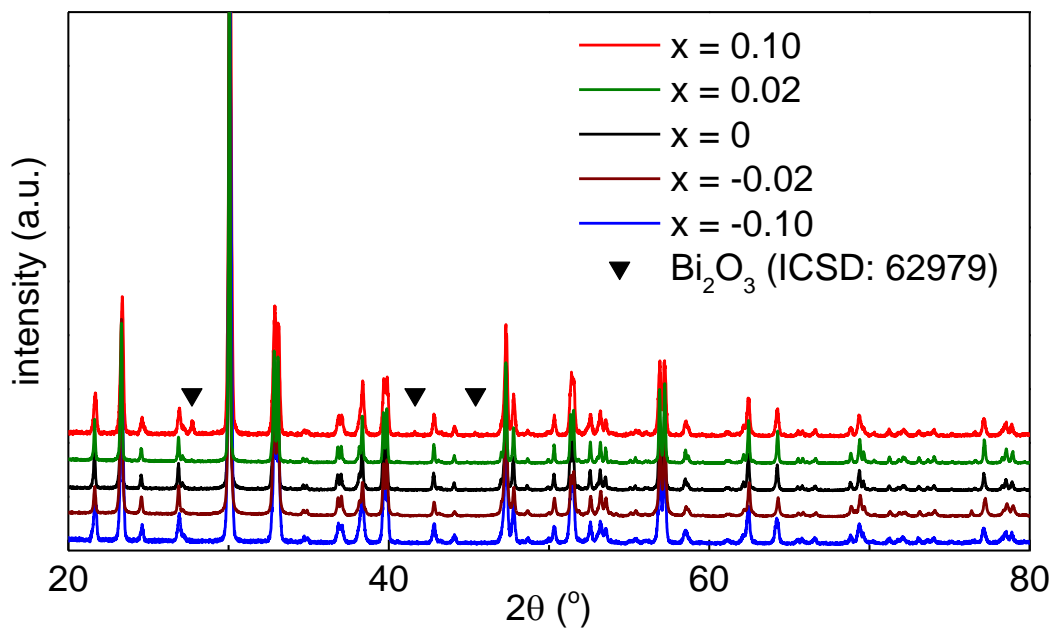


Figure 5-1. Room temperature X-ray powder diffraction data for  $\text{Bi}_{4.00+x}\text{Ti}_3\text{O}_{12+3x/2}$  ceramics.

XRD patterns obtained from crushed ceramics of selected samples from the x-series are shown in Figure 5-1. At room temperature, BiT has a monoclinic (*B1a1*) structure which has been observed in all samples in this series. No additional reflections are observed by XRD in the range  $-0.10 \leq x \leq 0.02$  but do appear in  $x = 0.10$ .

The secondary phase is identified as  $\text{Bi}_2\text{O}_3$  (space group  $P\bar{4}2_1c$ ) based on XRD data. The lattice parameters calculated from the XRD patterns are shown in Figure 5-2. The variation of lattice parameters are small, b and c decrease with increasing Bi content whereas a remains almost unchanged.

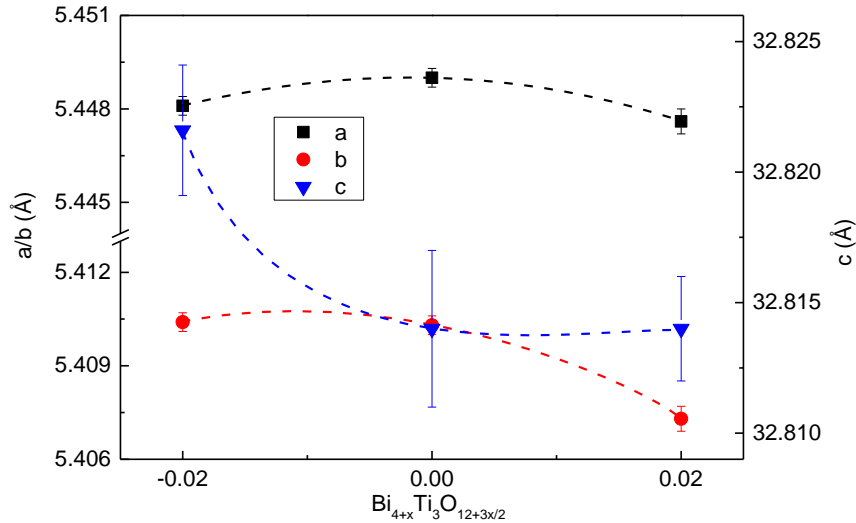


Figure 5-2. Lattice parameters a, b and c versus x content for  $\text{Bi}_{4+x}\text{Ti}_3\text{O}_{12+3x/2}$  crushed ceramics.

A combination of SEM and EDX reveals there are secondary phases present in both Bi-excess and Bi-deficient samples. For Bi-deficient samples  $x = -0.10$  and  $-0.02$ , a secondary phase is observed in backscattering images with a darker colour that indicates a lower average atomic number compared to the matrix. EDX results show the secondary phase has a Bi:Ti ratio close to 1:2 and the only known oxide that matches this ratio is  $\text{Bi}_2\text{Ti}_4\text{O}_{12}$ , Table 5-1. On the other hand, SEM fails to detect any bulk  $\text{Bi}_2\text{O}_3$  secondary phase in  $x = 0.10$  as the XRD result implies, instead, some small white spots have been observed in backscattering images with a morphology similar to the  $\text{Bi}_2\text{O}_3$  secondary phase in Bi-excess NBT, Figure 5-3 (b). EDX measurements taken near those spots show a higher Bi content than the matrix (Table 5-1), therefore the white spots in  $x = 0.10$  are suggested to be  $\text{Bi}_2\text{O}_3$ . The bulk composition shows no

significant variation with the change of  $\text{Bi}_2\text{O}_3$  content in the starting composition; all variation is within instrumental resolution and standard errors.

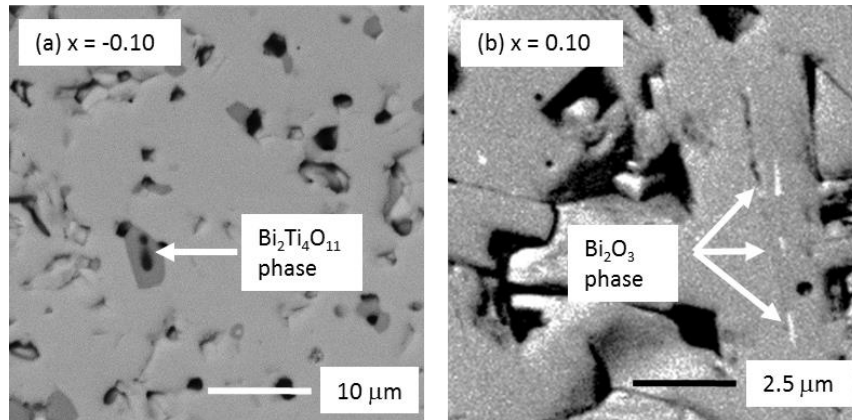


Figure 5-3. SEM back scattered electron images for  $x = -0.10$  and  $0.10$ . The bright areas in  $x = 0.10$  represent the  $\text{Bi}_2\text{O}_3$  secondary phase.

The grain size of un-doped BiT ceramics increases with an increase of  $\text{Bi}_2\text{O}_3$  content in the starting composition, Figure 5-4.  $x = -0.10$  possesses the smallest grain size of  $\sim 5 \mu\text{m}$  with a polygon morphology. With increasing Bi content, the grains in  $x = -0.02$  are slightly larger,  $\sim 10 \mu\text{m}$  and there is a change into a plate-like morphology. For samples with  $x \geq 0$ , the grain size is significantly larger, the prolate axis (a-b plane) can be more than  $\sim 100 \mu\text{m}$  long (some grains can be hundreds of micro-metres) and increases with increasing Bi content.

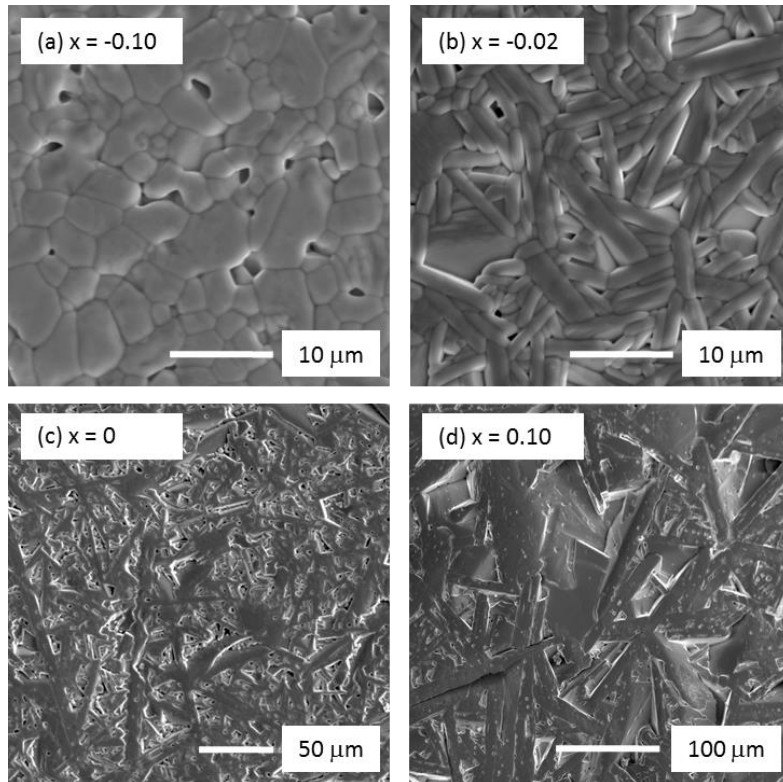


Figure 5-4. SEM secondary electron images for (a)  $x = -0.10$ , (b)  $x = -0.02$ , (c)  $x = 0$  and (d)  $x = 0.10$ . All samples were polished and thermally etched prior to SEM. The scales are different in these images.

Table 5-1. Chemical composition (relative cation at%) of the main phase and secondary phase with associated errors (standard deviation) by SEM/EDX of samples in the x-series.

Composition		Bi (at%)	Ti (at%)
<b>x = 0.10</b>	Main phase	56.8 ( $\pm 0.8$ )	43.2 ( $\pm 0.8$ )
	Bi-rich phase	62 ( $\pm 1$ )	38 ( $\pm 0.1$ )
<b>x = 0.02</b>	Main phase	57.5 ( $\pm 0.6$ )	42.8 ( $\pm 0.6$ )
<b>x = 0</b>	Main phase	56.8 ( $\pm 0.3$ )	43.2 ( $\pm 0.3$ )
<b>x = -0.02</b>	Main phase	57.2 ( $\pm 0.2$ )	42.8 ( $\pm 0.2$ )
	Bi <sub>2</sub> Ti <sub>4</sub> O <sub>11</sub>	34.3 ( $\pm 0.9$ )	65.7 ( $\pm 0.9$ )
<b>x = -0.10</b>	Main phase	57.0 ( $\pm 0.4$ )	43.0 ( $\pm 0.4$ )
	Bi <sub>2</sub> Ti <sub>4</sub> O <sub>11</sub>	36 ( $\pm 2$ )	64 ( $\pm 2$ )
<b>Bi<sub>4</sub>Ti<sub>3</sub>O<sub>12</sub></b>		57.1	42.9
<b>Bi<sub>2</sub>Ti<sub>4</sub>O<sub>11</sub></b>		33.3	66.7

### 5.1.2. Electrical properties

The temperature dependence of the maximum permittivity,  $\epsilon_{r,max}$  and the dielectric loss,  $\tan \delta$  are shown in Figure 5-5. Nominally stoichiometric BiT possesses the highest  $\epsilon_{r,max} \sim 1800$  which is reduced by either excess or deficient Bi non-stoichiometry, Figure 5-6. The lowest  $\epsilon_{r,max}$  is observed for  $x = 0.02$  with a value  $\sim 500$ . The corresponding temperature for  $\epsilon_{r,max}$ ,  $T_{\epsilon_{r,max}}$  varies within 5 °C with Bi non-stoichiometry which means  $T_C$  is essentially the same within experimental errors for all samples. It is worth to note that a permittivity abnormality is observed just below  $T_{\epsilon_{r,max}}$  in  $x = 0$ .

The dielectric loss,  $\tan \delta$  is relatively large for all samples in the x-series with  $\tan$

$\delta > 0.2$  above 300 °C, Figure 5-5. (b).  $\tan \delta$  for the x-series samples is similar to each other at low temperature but for temperatures  $> 300$  °C, nominally stoichiometric BiT has the highest loss. Both Bi-excess and Bi-deficient samples reduce  $\tan \delta$  and the lowest  $\tan \delta$  observed was for  $x = 0.02$ .

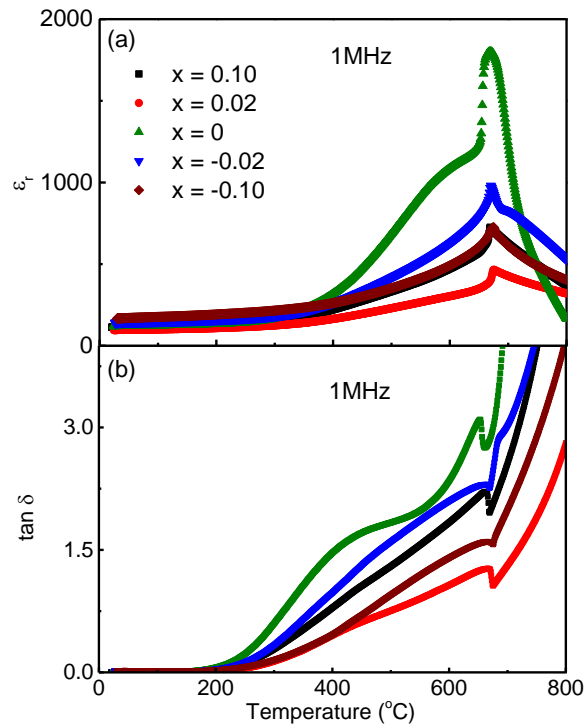


Figure 5-5. Temperature dependence of (a)  $\epsilon_r$  and (b)  $\tan \delta$  at 1 MHz for  $\text{Bi}_{4.00+x}\text{Ti}_3\text{O}_{12+3x/2}$  ceramics.

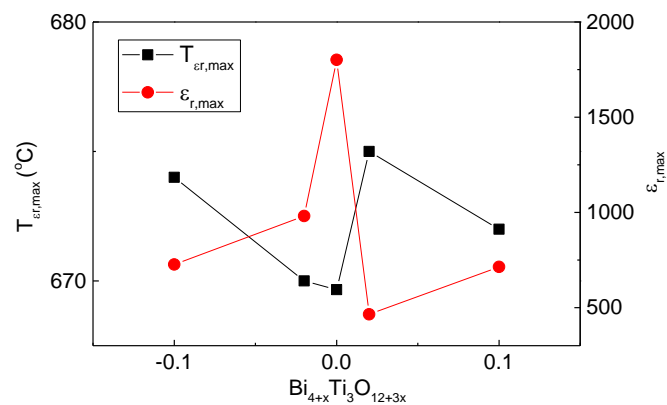


Figure 5-6. The influence of Bi non-stoichiometry on maximum permittivity,  $\epsilon_{r, \max}$  and the corresponding temperature,  $T_{\epsilon_r, \max}$  for  $\text{Bi}_{4.00+x}\text{Ti}_3\text{O}_{12+3x/2}$  ceramics.

$Z^*$  plots for un-doped BiT samples are shown in Figure 5-7 (a). Samples with  $x \leq 0$  contain 3 poorly resolved arcs. A small distorted high frequency quarter circle, a large spike which become a distorted semicircle at high temperature and a low frequency spike which also appears only at higher temperatures, Figure 5-7 (b). On the other hand, Bi-rich samples ( $x > 0$ ) show only a single curve. However, the  $Z''$  and  $M''$  spectroscopic plots show this single curve in  $x > 0$  samples actually contains more than one response which are merged together, Figure 5-10 (c) and (d). It is also worth to note that the influence of Bi non-stoichiometry on the magnitudes of the electrical properties in BiT is much smaller than in NBT, especially from the viewpoint of the bulk conductivity.

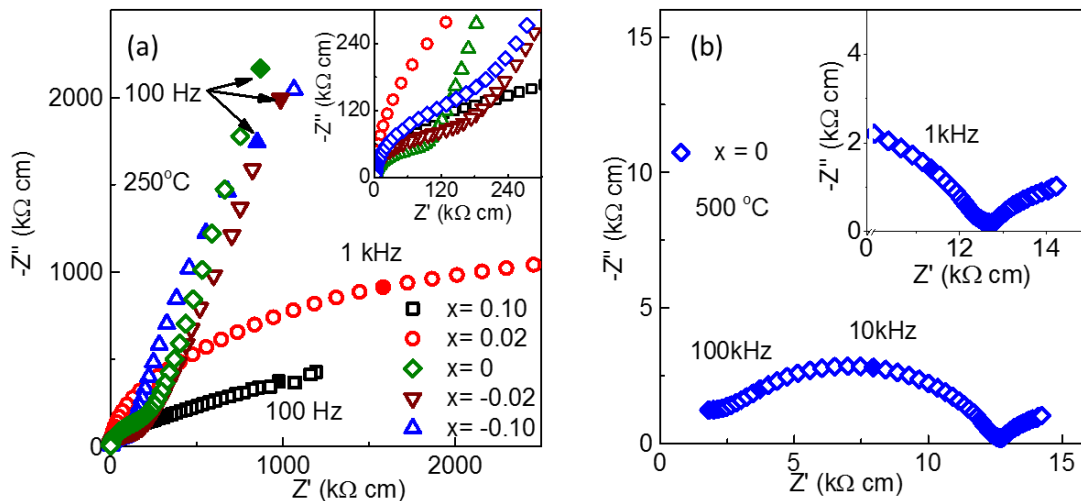


Figure 5-7.  $Z^*$  plots of (a)  $x$ -series samples at  $250^\circ\text{C}$  and (b)  $x = 0$  at  $500^\circ\text{C}$ . The insert in (a) shows the bulk response arc and the insert in (b) is the low frequency spike.

One of the differences between BiT and NBT in terms of data processing is how well the arcs in  $Z^*$  plots are resolved. The bulk and grain boundary arcs and the electrode response for NBT ceramics are relatively well resolved, but in BiT they tend to merge with each other and make it difficult to extract data from individual responses. In the worst cases ( $x > 0$ ), several responses merge together and form a large distorted semicircle which makes it look like a single response. Therefore,  $Z''$  and

$M''$  spectroscopic plots are adopted here to extract resistance and permittivity for different responses, see Figure 5-8 and Figure 5-10. In most cases, the frequency dependent  $Z''$  and  $M''$  data are plotted on a log scale to help differentiate the responses. In ideal conditions, an individual response is normally represented as a peak which is connected to other responses by a slope of + or - 1 based on log-log scale plots.

Figure 5-8 shows combined  $Z''$  and  $M''$  spectroscopic plots for  $x = 0$ . At 300 °C, two responses are observed in both  $Z''$  and  $M''$  plots, one at higher frequency and one at lower frequency. When the temperature increased to 400 °C, the higher frequency response in Figure 5-8 (a) moved to higher frequency which is beyond the measurement window and can no longer be observed but a new low frequency response appears in the low frequency range with a much higher capacitance (the capacitance is inversely proportional to the  $M''$  value). Components with such a high capacitance is rare and combined with the low frequency spike in the  $Z''$  plot it is reasonable to believe this is a Warburg semi-infinite linear diffusion response from an electrode effect.

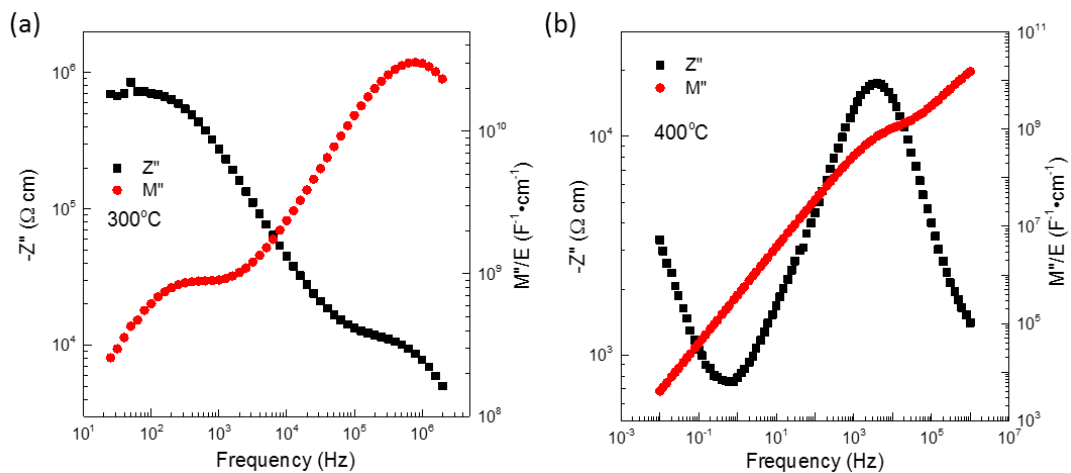


Figure 5-8. log-log  $Z''$  and  $M''$  spectroscopic plots for  $x = 0$  at (a) 300 °C and (b) 400 °C.

Figure 5-9 shows the  $M''$  spectroscopic plot of  $x = 0$  on a linear scale which is dominated by the high frequency response in Figure 5-8 (a) due to the low capacitance. The height of the  $M''$  peak shows a systematic decrease with increasing temperature, implying the permittivity of this component increases with increasing temperature. Furthermore, the calculated permittivity of this component at 300 °C is  $\sim 186$  which is in agreement with the permittivity measured using the LCR meter at the same temperature ( $\sim 168$ ). This high frequency  $M''$  response is therefore attributed to the BiT bulk (grain) response.

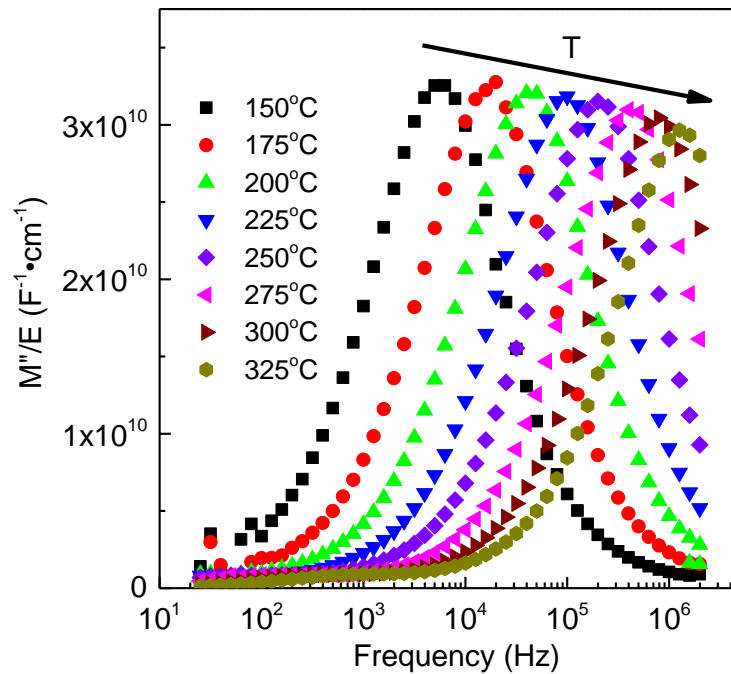


Figure 5-9.  $M''$  spectroscopic plots for  $x = 0$  in the temperature range  $\sim 150$  to  $325$  °C.

The  $Z''$  and  $M''$  spectroscopic plots of non-stoichiometric BiTs are shown in Figure 5-10. For the  $M''$  spectroscopic plots, the two Bi-deficient samples ( $x = -0.02$  and  $-0.10$ ) show two components whereas the two Bi-rich samples ( $x = 0.02$  and  $0.10$ ) show only one component which is consisted with bulk response. On the other hand, the  $Z''$  spectroscopic plots show 3 or 4 different responses in all samples instead of one or two as in the  $M''$  plots. These 4 components will be referred to as R1 to R4 (C1 to C4

in terms of capacitance and assumed to all be parallel RC elements connected in series) from high to low frequency in the following discussion.

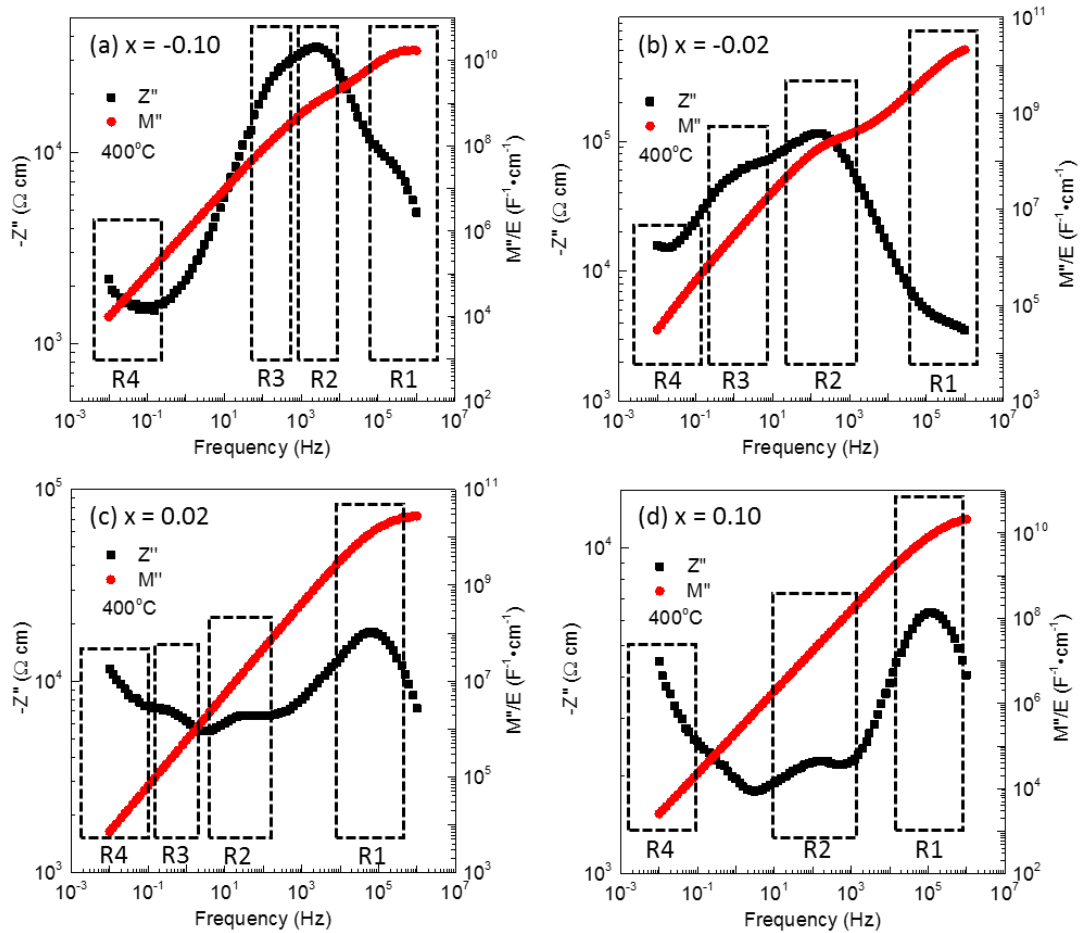


Figure 5-10.  $Z''$  and  $M''$  spectroscopic plots for (a)  $x = -0.10$ , (b)  $x = -0.02$ , (c)  $x = 0.02$  and (d)  $x = 0.10$  at  $400\text{ }^{\circ}\text{C}$ .

Figure 5-11 summarises the resistance and capacitance values (where possible) of R1 to R4 for the x-series samples at  $400\text{ }^{\circ}\text{C}$ . Analysis of time constants (reciprocal of corresponding frequency maximum) shows R1 and R4 are relatively insensitive to the Bi non-stoichiometry. From the resistance and capacitance point of view, again the value of the bulk response R1C1 is relatively insensitive to Bi non-stoichiometry. R1 varies within half an order of magnitude and C1 remains almost unchanged for all x-series samples. R4C4 is the electrode effect response whose resistance is very high and

therefore not shown in the figure since the Au electrode is considered to be predominantly 'blocking' the oxygen migration. R2C2 and R3C3 are sensitive to the Bi non-stoichiometry and are different from sample to sample. In general, R2 and R3 decrease with increasing x whereas the C2 and C3 show the opposite trend.

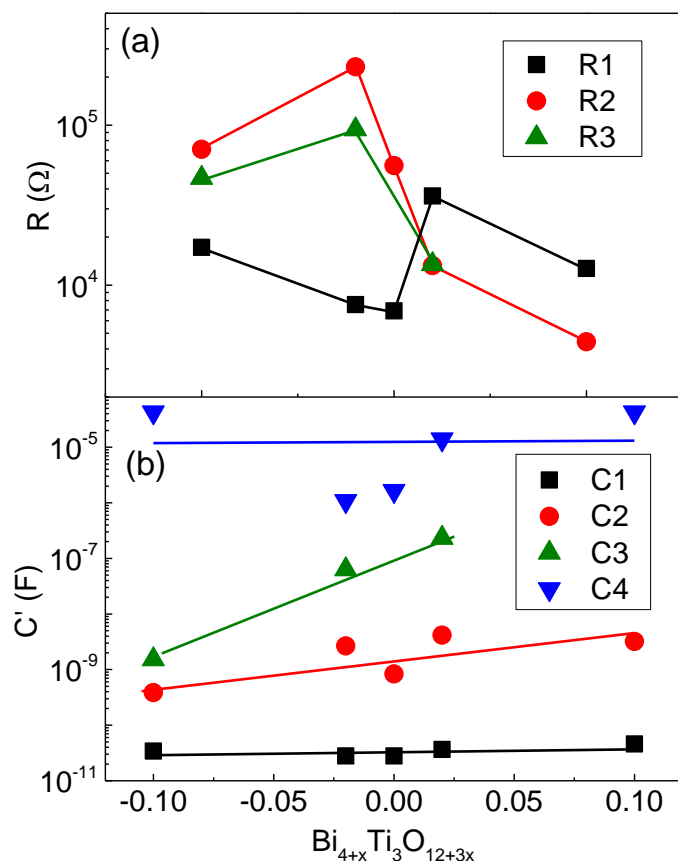


Figure 5-11. (a) Resistance and (b) capacitance for the four components in x-series samples at 400 °C.

An Arrhenius type plot of bulk conductivity (extracted from the largest  $M''$  peak and taken as  $1/R_1$ ) for all x-series samples is shown in Figure 5-12.  $x = 0$  BiT possesses the highest bulk conductivity among all samples whereas  $x = 0.02$  has the lowest which is about one order of magnitude lower than  $x = 0$ . The activation energy for samples in this series vary only in a relatively narrow range,  $\sim 0.57 - 0.75$  eV, unlike un-doped non-stoichiometric NBTs where there is a large difference in both the magnitude of the

bulk conductivity and the associated activation energy values on going from Bi-deficient to Bi-excess starting compositions.

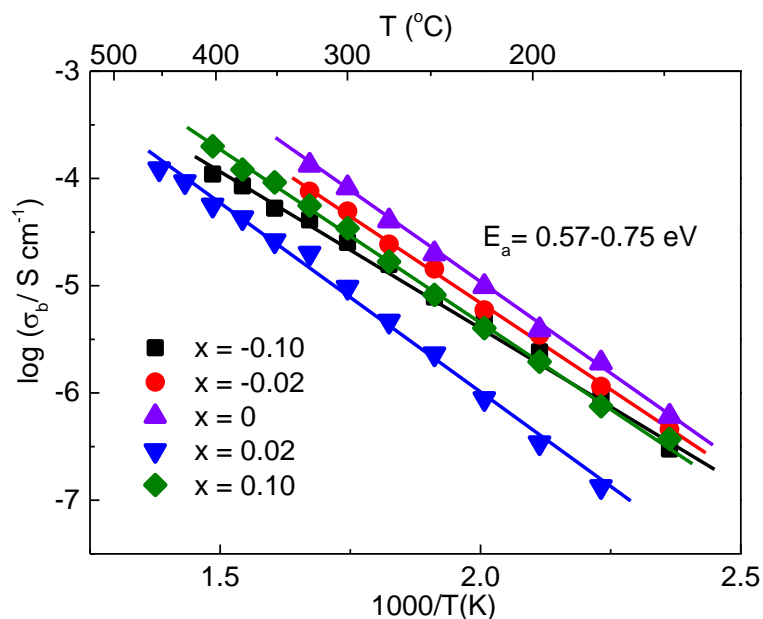


Figure 5-12. Arrhenius plot of bulk conductivity,  $\sigma_b$ , versus reciprocal temperature for selected  $x$ -series ceramics. Activation energy,  $E_a$ , values for  $\sigma_b$  are included.

Since the influence of Bi non-stoichiometry on the electrical properties of BiT is rather limited compared to NBT, sets of  $x = 0$  ceramics were annealed in flowing  $N_2$  or  $O_2$  for 10 hours at 900 °C in an attempt to generate more/fill up oxygen vacancies and to investigate their influence on the electrical properties. After annealing, the samples were slow cooled in the same gas atmosphere to room temperature and then measured by impedance spectroscopy (using the same type of flowing gas).  $Z^*$  plots of annealed ceramics are shown in Figure 5-13 with an as-sintered sample (sintered in air without annealing) as reference. In general, the  $N_2$  annealed samples behave similar to as-sintered samples whereas the bulk conductivity of  $O_2$  annealed samples is significantly reduced by  $\sim 1$  order of magnitude compared to as-sintered samples and the different components are better resolved.

The  $Z''$  and  $M''$  spectroscopic plots of  $O_2$  and  $N_2$  annealed stoichiometric BiT are shown in Figure 5-14. For the  $M''$  plot, only one response has been observed for all samples whereas in  $Z''$  plots four different responses can be observed. R1 in Figure 5-14 (a) and (c) is the bulk response whereas R4 in Figure 5-14 (b) and (c) is the electrode effect. The different R and C values are summarised in Figure 5-15. The capacitance values for different samples remain relatively similar. In contrast, R1 is significantly larger after annealing in  $O_2$  whereas R2 is smaller in both annealed samples as compared to as-sintered samples.

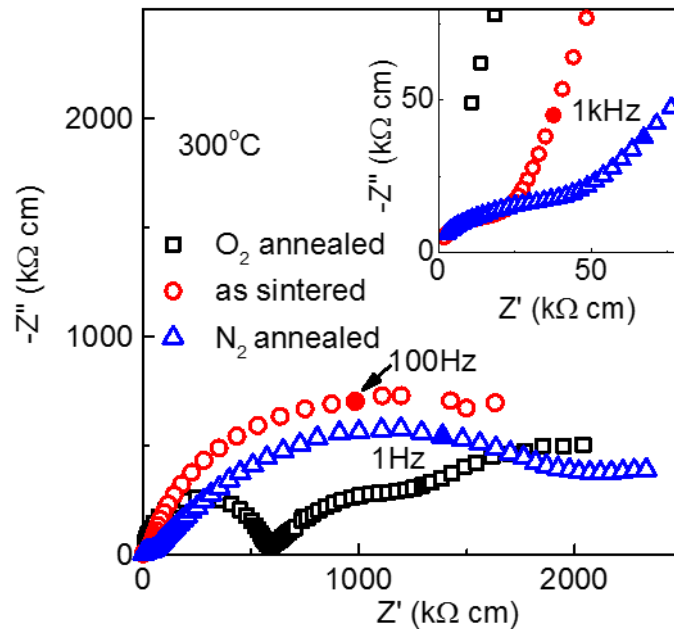


Figure 5-13.  $Z^*$  plots of as-sintered and after annealing in  $O_2/N_2$  for 10 h at 900 °C for  $x = 0$  ceramics at 300 °C.

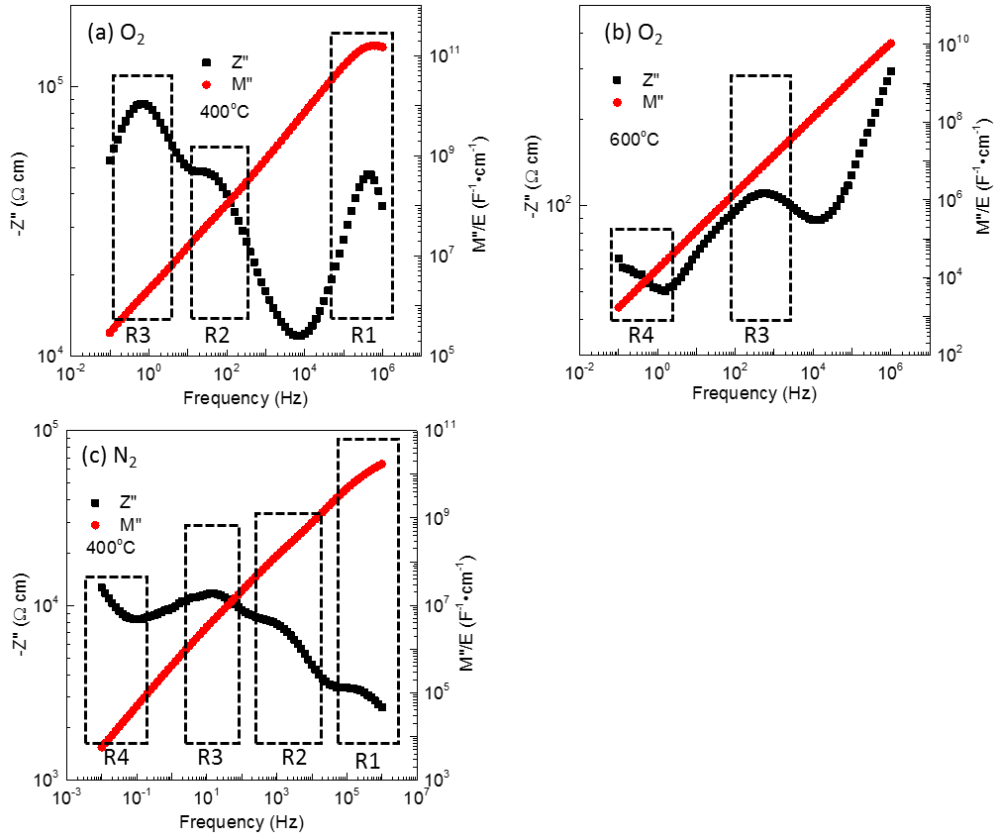


Figure 5-14.  $Z''$  and  $M''$  spectroscopic plots measured at (a) 400 and (b) 600 °C for  $x = 0$  annealed under  $O_2$  at 900 °C for 10 hours and (c) a pellet annealed under  $N_2$  at 900 °C for 10 hours.

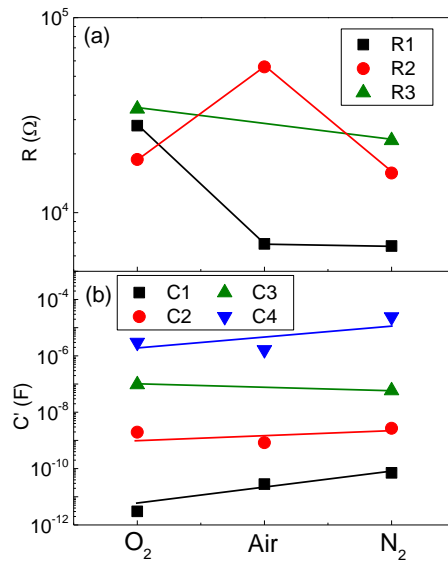


Figure 5-15. (a) Resistance and (b) capacitance values for  $N_2$  and  $O_2$  annealed  $x = 0$  at 400 °C.

From the above discussion of  $M''$  and  $Z''$  spectroscopic plots, a better understanding can be obtained for the different arcs in the  $Z^*$  plots. For  $N_2$  annealed samples, the high frequency distorted quarter circle is the bulk response (R1), the following distorted semicircle is formed by R2 and R3 and the low frequency spike is a typical Warburg semi-infinite linear diffusion response. For  $O_2$  annealed samples, the high frequency semicircle is R1 and the following two arcs are R2 and R3. In the case of R4, it is not shown at 300 °C but can be observed at higher temperatures, e.g. 600 °C.

Bulk conductivity Arrhenius plots of a comparison for  $N_2/O_2$  annealed  $x = 0$  samples with as-sintered  $x = 0$  and 0.02 samples, are shown in Figure 5-16.  $x = 0$  shows a slightly improved bulk conductivity when annealed in  $N_2$  compared to as-sintered samples, whereas  $O_2$  annealed samples are  $\sim 2$  orders of magnitude lower than  $N_2$  annealed/as sintered samples. The activation energy changes in the range  $\sim 0.63$  to 0.81 eV where  $N_2$  annealed samples possess the lowest value and  $O_2$  annealed sample possess the highest value.

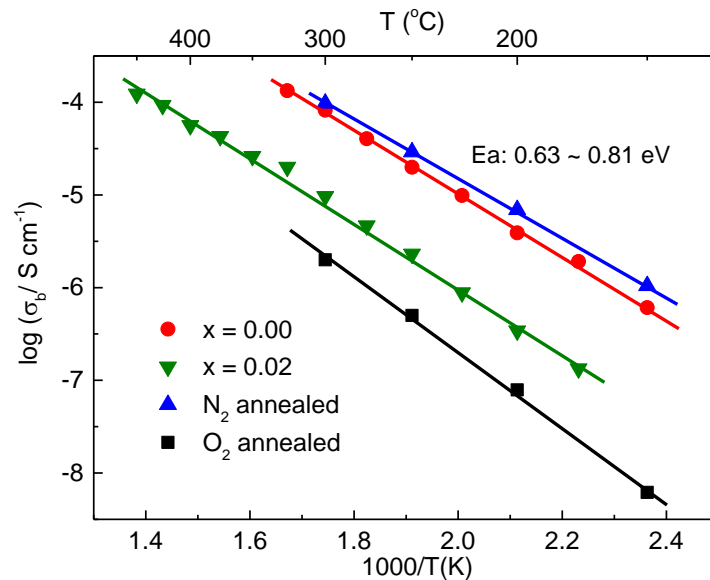


Figure 5-16. Comparison of bulk conductivity of  $x = 0$  ceramics after being annealed in  $O_2/N_2$  for 10h at 900 °C with as-sintered  $x = 0$  and 0.02 ceramics as reference.

$Z^*$  plots and  $Z''$ ,  $M''$  spectroscopic plots of selected x-series samples under different atmospheres are shown in Figure 5-17 and Figure 5-18, respectively. The R and C values in different atmospheres for these three samples are summarised in Figure 5-19. In terms of resistance for all three samples, R1 (bulk response) shows a very weak p-type behaviour (a small increase in  $Z''$  peak and shifting of  $M''$  peak towards low frequency with the change of flowing gas from  $O_2$  to  $N_2$ ) whereas R2 and R3 show clear  $pO_2$  dependence (p-type behaviour). On the other hand, no significant change was observed for the capacitance values when the flowing gas atmosphere changed from  $O_2$  to  $N_2$ .

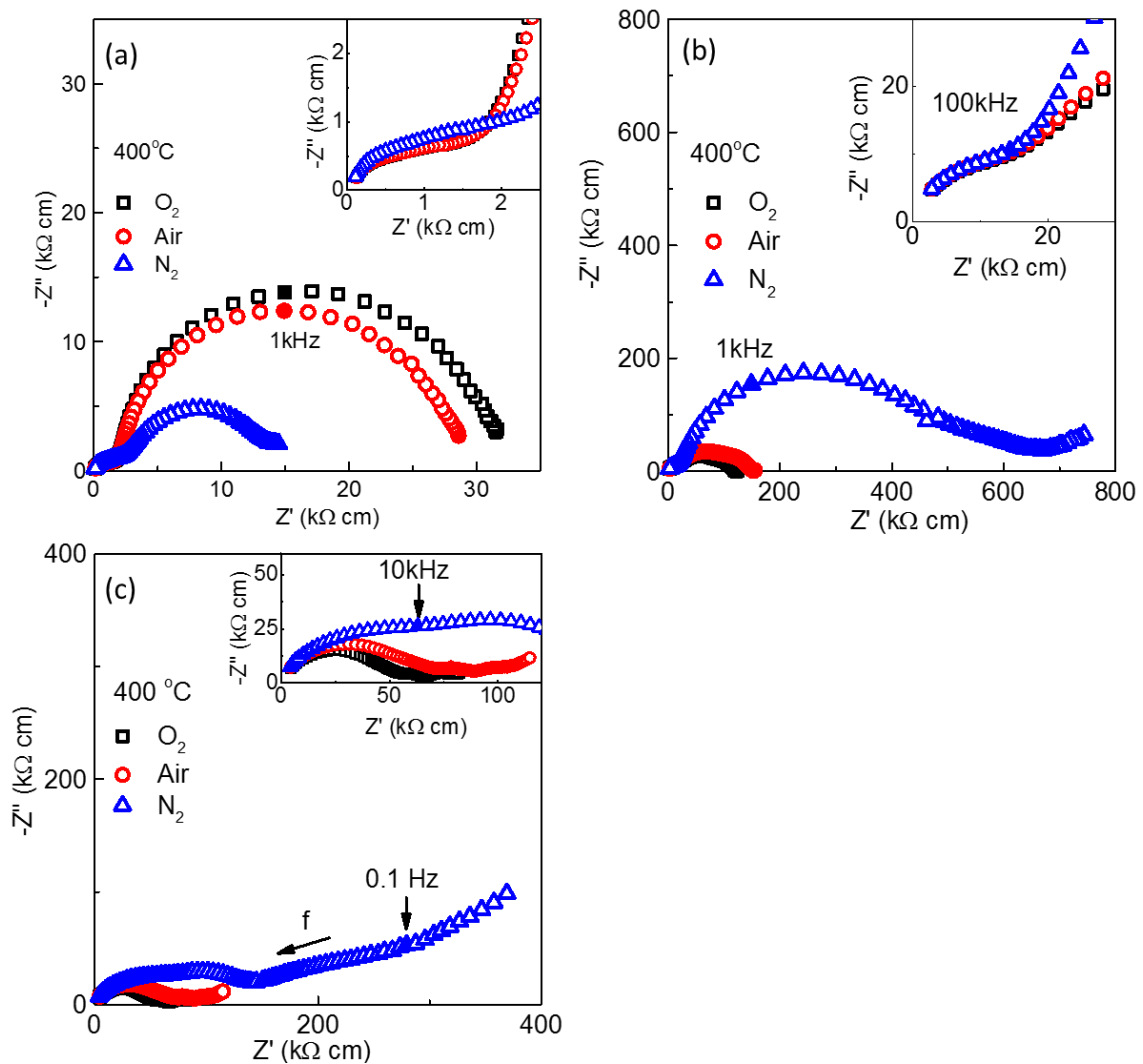


Figure 5-17.  $Z^*$  plots for (a)  $x = 0.00$  (b)  $x = -0.10$  and (c)  $x = 0.02$  under different

flowing gas atmospheres.

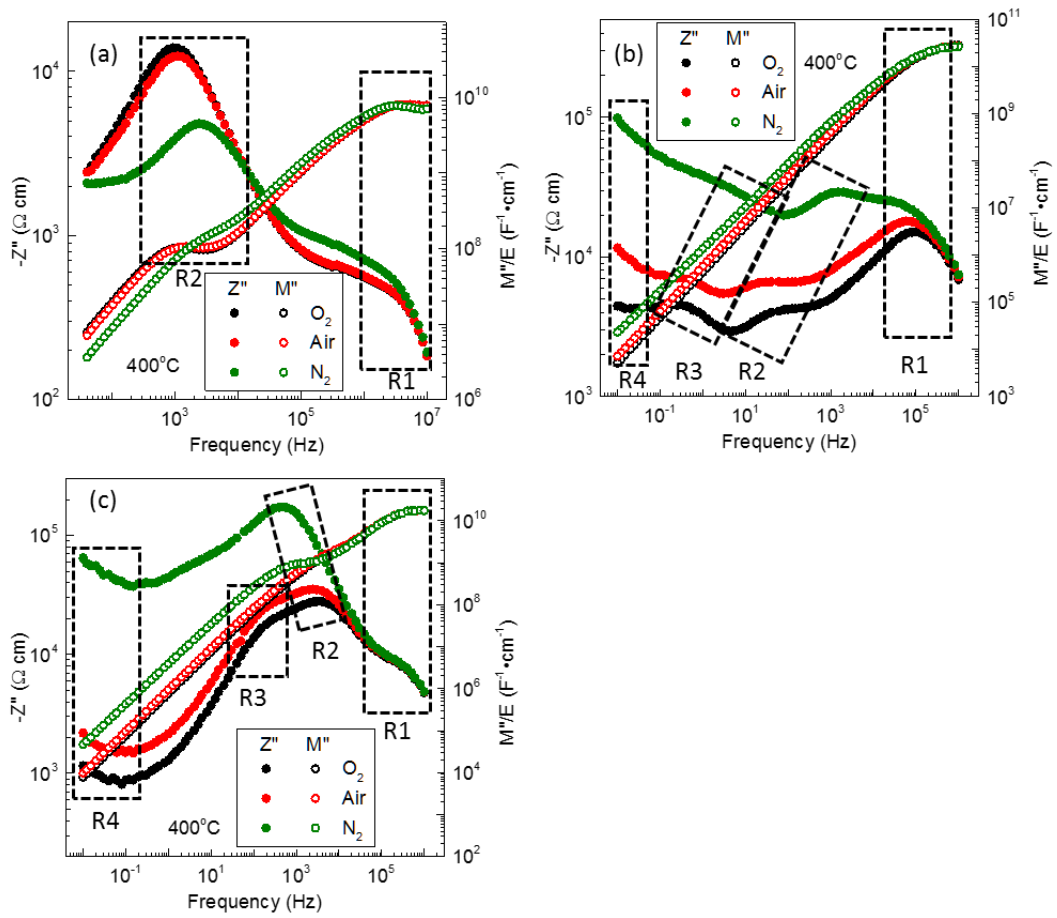


Figure 5-18.  $Z''$  and  $M''$  spectroscopic plots for (a)  $x = 0.00$  (b)  $x = -0.10$  and (c)  $x = 0.02$  under different flowing gas atmospheres.

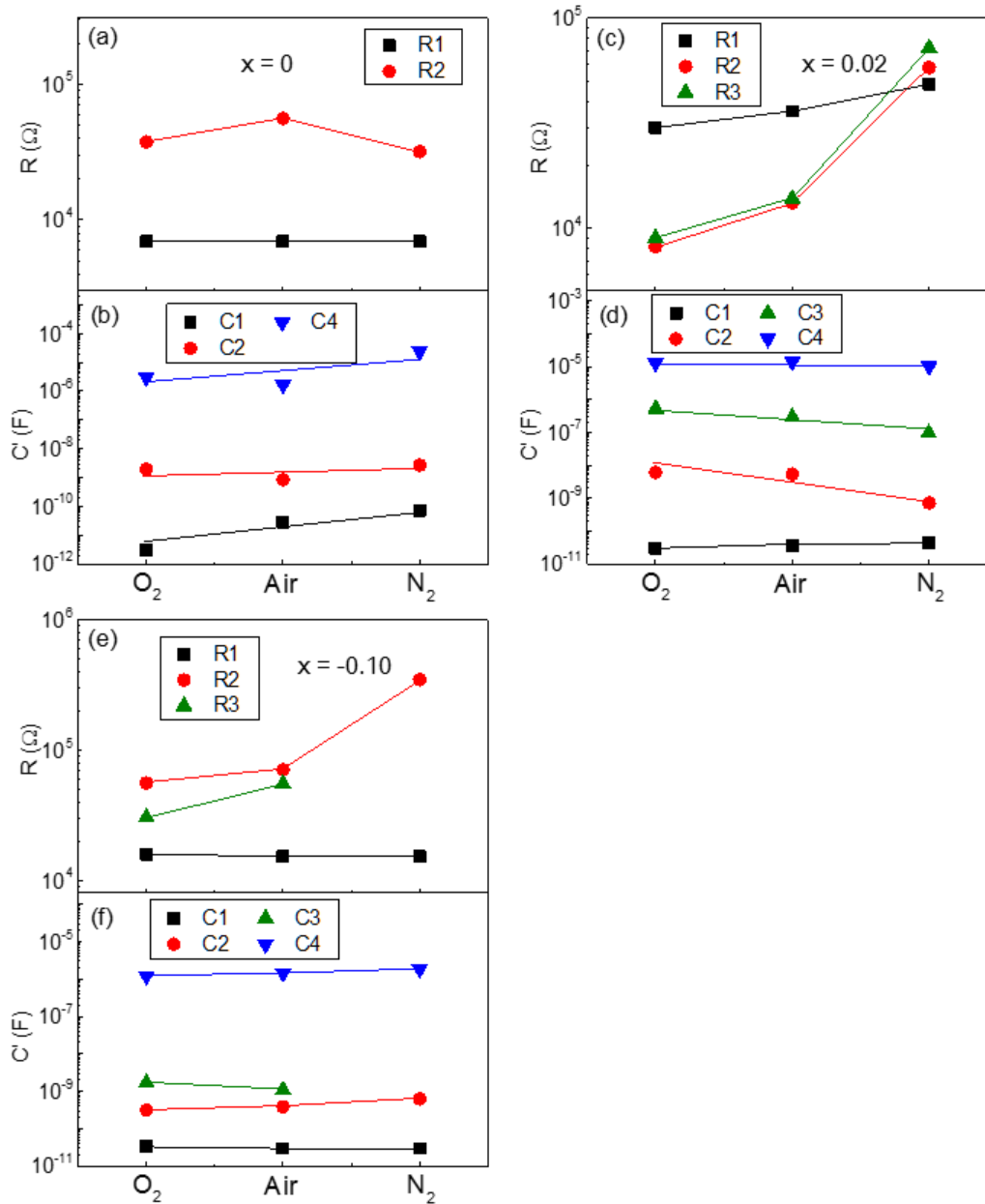


Figure 5-19. (a), (c), (e) Resistance and (b), (d), (f) capacitance for  $x = 0, 0.02$  and  $-0.10$  in different atmosphere at 400 °C.

A combination of EMF and  $^{18}O$  tracer diffusion measurements were used to verify the presence of oxide ion conduction in BiT, Figure 5-20. EMF shows a temperature dependent oxide ion transport number,  $t_{ion}$  which is modest ( $\sim 0.77$ ) at 600 °C but increases rapidly with temperature and reaches a peak value of  $\sim 0.94$  at  $\sim 675$  °C, the phase transition temperature. For any further increase of temperature,  $t_{ion}$  decreases

slowly. Generally speaking,  $t_{ion}$  of BiT remains relatively high with a value  $> 0.9$  in the range  $665 \sim 775$  °C.

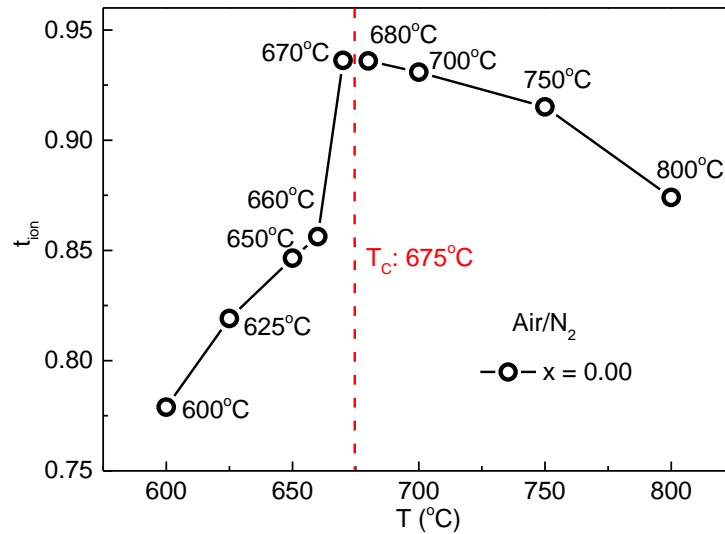


Figure 5-20.  $t_{ion}$  values between 600 and 800 °C for  $x = 0.00$ . The Curie temperature,  $T_c$ , is indicated in red.

$^{18}\text{O}$  tracer diffusion measurements were performed (R de Souza group, Germany) on both small and large grain  $x = 0$  samples to verify the oxide ion conduction and determine the influence of grain size on the oxygen diffusion in BiT. These two  $x = 0$  samples were sintered separately at different temperatures (2 hours at 1000 °C for the small grain sample and 2 hours at 1100 °C for the large grain sample) in order to obtain different grain size. The tracer diffusion coefficient,  $D^*$  at 550 °C is  $7.46 \times 10^{-10}$  cm<sup>2</sup>/s and  $2.55 \times 10^{-10}$  cm<sup>2</sup>/s for large and small grained (LG and SG) BiT, respectively, Figure 5-21. The total diffusion profile is  $\sim 150$   $\mu\text{m}$  for LG-BiT and  $\sim 100\mu\text{m}$  for SG-BiT. Calculated oxygen ion conduction from  $D^*$  with the Nernst–Einstein equation for LG- and SG-BiT is plotted in an Arrhenius plot together with the total conductivity (the total conductivity is  $1/R_{total}$  where  $R_{total} = R_1 + R_2 + R_3$ ) of BiT extracted from impedance data, Figure 5-22. In both cases, it is clear that the calculated conductivity is consistent with the total conductivity of BiT ceramics obtained from impedance measurements at the same temperature. It is worth to note that a change in the activation energy for

the total conductivity is observed at  $T_c$  during heating from  $\sim 0.67$  to  $0.88$  eV to  $\sim 0.38$  to  $0.39$  eV.

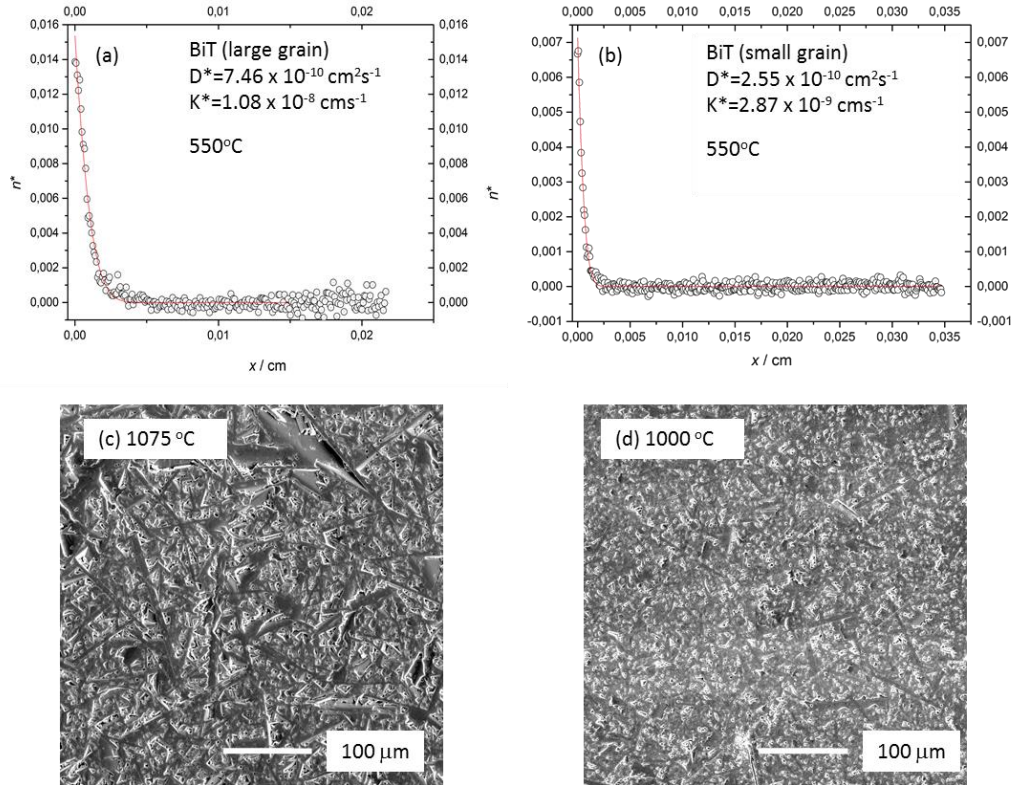


Figure 5-21.  $^{18}O$  tracer diffusion profile for a) large- and b) small-grained stoichiometric BiT after exchange at 549.8 °C for  $\sim 1298$  s with  $p^{18}O_2 \sim 200$  mbar with SEM micrographs of c) large- and d) small-grained ceramics.

A comparison of bulk conductivity for un-doped stoichiometric BiT and other known oxide ion conductors (electrolytes) is given in Figure 5-23.<sup>11</sup> The conductivity of BiT and NBT compare well to those of the best oxide ion conductors, and further improvements are expected with compositional optimisation by appropriate dopants.

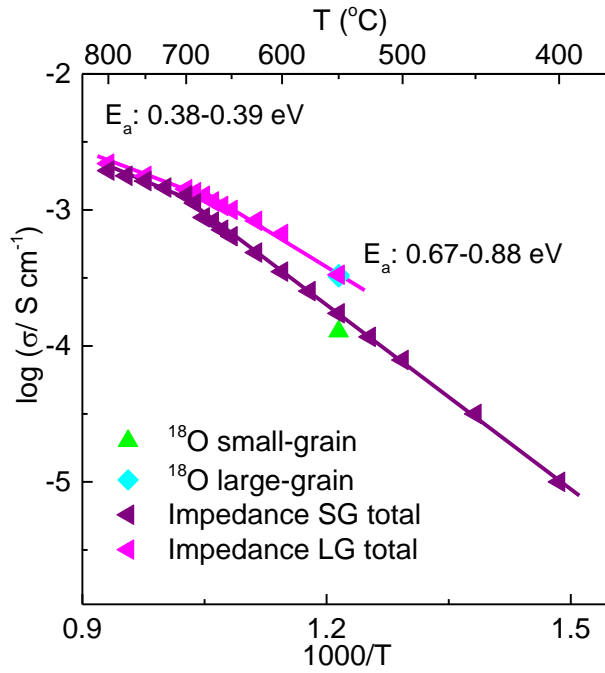


Figure 5-22. Arrhenius plot of total conductivity ( $1/[R1 + R2 + R3]$ ) values for large- and small-grained ceramics extracted from impedance data and compared with conductivity values calculated using the Nernst-Einstein equation from the  $D^*$  values obtained from  $\text{O}^{18}$  TOF-SIMS for the same ceramics.

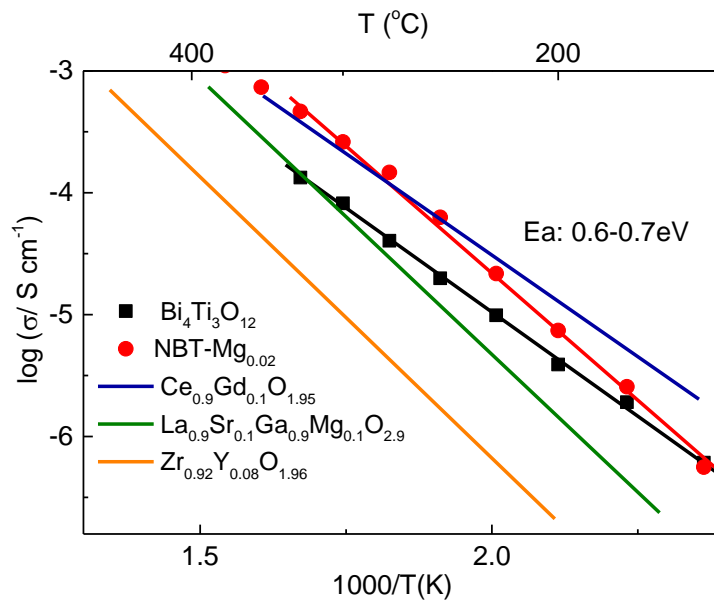
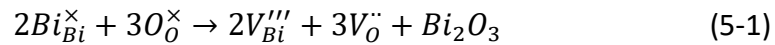


Figure 5-23. Comparison of  $\text{BiT}$  bulk conductivity with  $\text{Mg-NBT}$  and other known oxide ion conductors.

## 5.2. Discussion

The presence of oxide ion conduction in BiT has been proved by a combination of  $t_{ion}$  from EMF measurements and oxygen diffusion in TOF SIMs  $^{18}O$  measurements as well as the low frequency spike in  $Z^*$  plots from Impedance data, Figure 5-7 and Figure 5-20. The oxygen vacancies in the nominally stoichiometric BiT composition may be generated during sample processing owing to loss of  $Bi_2O_3$ :



It is presumable that more oxygen vacancies can be generated by either non-stoichiometry or acceptor doping to enhance the oxide ion conduction in BiT. However, unlike NBT, both Bi-deficient and Bi-rich samples in the x-series lead to a reduction in bulk conductivity, Figure 5-12. It is also worth noting that the influence of bulk conductivity caused by Bi non-stoichiometry in BiT is rather limited compared to undoped NBT.  $x = 0.02$  possesses the lowest bulk conductivity in un-doped BiTs which is about one order of magnitude lower than nominally stoichiometric BiT; further increases in Bi content lead to a subsequent increase in bulk conductivity, Figure 5-12. Alternatively, when annealing  $x = 0$  ceramics in  $O_2$  at  $900\text{ }^\circ\text{C}$  for 10 hours a lower bulk conductivity than  $x = 0.02$  can be obtained which indicates the excess  $Bi_2O_3$  in the starting composition can only partially compensate any oxygen vacancies. Therefore the formation of extrinsic oxygen vacancies in BiT cannot be completely attributed to Bi-loss during processing otherwise excess Bi should be able to eliminate most of the oxide ion conduction like in Bi-rich NBT. Intrinsic oxygen defects due to Frenkel or Schottky disorder is a possible explanation as it does not require any cation non-stoichiometry/dopant and is observed in many famous oxide ion conductors such as  $\delta\text{-}Bi_2O_3$  (oxygen deficient fluorite structure).<sup>12</sup>

On the other hand, samples with intentional Bi-deficiency ( $x < 0$ ) slightly reduce the bulk conductivity of BiT instead of enhancing it. It is clear that the attempt to

induce additional cation non-stoichiometry to generate more oxygen vacancies has a detrimental effect on the intrinsic defect mechanism and cause a reduction in bulk conductivity.

The above discussion indicates that both intrinsic and extrinsic oxygen defects can exist in BiT. The former significantly influences the bulk conductivity and cannot be compensated by extra Bi in starting material whereas the latter has a relatively small influence on bulk conductivity and can be compensated by extra Bi in starting material. The extrinsic oxygen vacancies in this study are generated due to the Bi-loss during processing but the attempt to induce additional Bi non-stoichiometry interrupt the formation of intrinsic oxygen defects. Again the Bi-loss is dependent on the processing procedure and conditions, thus Bi-deficient BiTs can be more conductive than nominally stoichiometric BiT with a different processing procedure.

It is worth noting that BiT with excessive  $\text{Bi}_2\text{O}_3$  ( $x > 0.02$ ) in the starting composition results in another increase in the bulk conductivity. With the presence of nano-size ( $\sim 500$  nm based on SEM back scattered electron images but could be different if investigated by TEM)  $\text{Bi}_2\text{O}_3$  secondary phase which is similar to the Bi over-doped NBT ( $x \geq 0.02$ , x-series, chapter 3). It is reasonable to explain the increase of bulk conductivity by the same two possible explanations, i.e. (i) a change in the Bi-content in the BiT main phase, and (ii) a space-charge model can be adopted in this system as well. The detailed discussion about these two explanations can be found in the discussion section in chapter 3.

EMF measurements shows a maximum  $t_{\text{ion}} \sim 0.94$  within a small temperature range  $670 \sim 680$  °C (Figure 5-20) which is consistent with the orthorhombic to tetragonal phase transition temperature. A change of activation energy from  $\sim 0.67$  to  $0.88$  eV to  $\sim 0.38$  to  $0.39$  eV can also be observed at the same temperature in the

Arrhenius type temperature dependent total conductivity plot in BiT which confirms a possible change in bulk conduction mechanism if this change is bulk-related, Figure 5-22. Furthermore, Fouskova et al. has reported that at  $T_c$  the ac conductivity of BiT single crystals show a rapid increase for the a-b plane whereas a rapid decrease is observed along the c-axis, Figure 1-21, which support the EMF results since the conduction in the a-b plane is dominated by oxide ion conduction whereas the c axis is dominated by electronic conduction, Figure 1-24.<sup>13</sup> They also show the conductivity along the c-axis increases substantially above  $\sim 700$  °C, therefore the decrease of  $t_{ion}$  above  $\sim 700$  °C is possibly due to increasing electronic conduction.

BiT keeps a relatively high  $t_{ion} \geq 0.93$  in the temperature range  $670 \sim 700$  °C. This range coincides with an 'intermediate *Cmca* phase' proposed by Zhou et al. which only exists in a small range  $670 \sim 695$  °C before it transforms to the *I4/mmm* phase. Thus the EMF and variable-temperature synchrotron X-ray diffraction results support each other about the existence of the intermediate *Cmca* phase and the favourability of oxide ion conduction and unfavourability of electronic conduction in this phase.

Compared with conducting NBT, the grain size become more of an issue in BiT since its grain size is highly sensitivity to small composition variations and the sintering temperature and the grain size varies within the range  $\sim 5 \mu\text{m}$  to  $\sim 0.1 \text{ mm}$ , Figure 5-4.<sup>18</sup>  $^{18}\text{O}$  tracer diffusion measurements show a different diffusion coefficient which changes from  $7.46 \times 10^{-10} \text{ cm}^2\text{s}^{-1}$  for large grained ceramics to  $2.55 \times 10^{-10} \text{ cm}^2\text{s}^{-1}$  for small grained ceramics which indicates the grain size does influence the oxygen migration in BiT ceramics, Figure 5-21. This result can be explained by a grain boundary effect where the grain boundaries act as a blocking barrier in the process of oxygen ion diffusion, therefore a large grain size sample with a smaller fraction of grain boundary possesses a higher oxygen diffusion coefficient than a smaller grain sized sample with a larger fraction of grain boundaries.

In terms of  $Z^*$  plots, the NBT data are well resolved and therefore the three responses observed in  $Z^*$  plots can be easily attributed to bulk, grain boundary and electrode effects. However, in the case of BiT, 4 different responses have been observed in  $Z''$  plots of non-stoichiometric as well as  $N_2$  and  $O_2$  annealed stoichiometric BiT ceramics, Figure 5-13 and Figure 5-14. Among them, R1 and R4 can be reasonably attributed to bulk and electrode effects, respectively but it is hard to assign R2 and R3 to particular components in the ceramics since they are sensitive to A-site nonstoichiometry and the annealing process in different  $pO_2$ 's. In general, R2 and R3 maybe many things such as a grain boundary response, an intergrowth (defect blocks of perovskite) of other Aurivillius phases or even a different component of the bulk response since the oxide ion conduction in BiT is anisotropic along different axes (favoured in the a-b plane but unfavoured along the c-axis). The associated capacitance components for R2 and R3 are in the range  $10^{-9} \sim 10^{-10}$  F for C2 and  $10^{-6} \sim 10^{-8}$  F for C3 and when annealing at low temperature ( $pO_2$  test), R1 is less  $pO_2$  dependent than R2 and R3 which means R1 possesses a larger share of 'ionic' conduction than R2 and R3. From the capacitance behaviour, C2 is consistent with a normal value for a grain boundary response. C3 possesses higher capacitance and R3 shows p-type like behaviour with a change of flowing gas from  $O_2$  to  $N_2$ . Therefore R3C3 may be attributed to an exchange process of oxygen between the  $O_2$  in the atmosphere and  $O^{2-}$  ions in ceramic since such an exchange process is certainly less favoured in a low  $pO_2$  atmosphere (e.g.  $N_2$ ) than in a high  $pO_2$  atmosphere (e.g.  $O_2$ ).

Takahashi et al. have used an equivalent circuit to try and separate the electronic and ionic contribution for the 'bulk' response in  $Z^*$  plots, Figure 5-24.<sup>14</sup> The equivalent circuit consists of two components, an ionic conduction pathway and a p-type electronic conduction pathway that are connected in parallel. They have discussed the possibility that a layered structure can cause an anisotropic electrical response but

they argue that since the grains were randomly oriented, the layered structure effect was negligible. They also state the influence of the grain boundary is expected to be very small at high temperatures and thus also to be negligible. However, this project shows these two assumptions may not be true. First, stoichiometric BiT annealed in  $O_2$  at  $900\text{ }^\circ\text{C}$  for 10 hours shows much better bulk electrical homogeneity and the different responses are well resolved compared to as-sintered BiT ceramics. This means the BiT ceramic only became more isotropic when the oxygen ion conduction is suppressed. Thus the bulk electrical anisotropy in as-sintered BiT cannot be neglected.

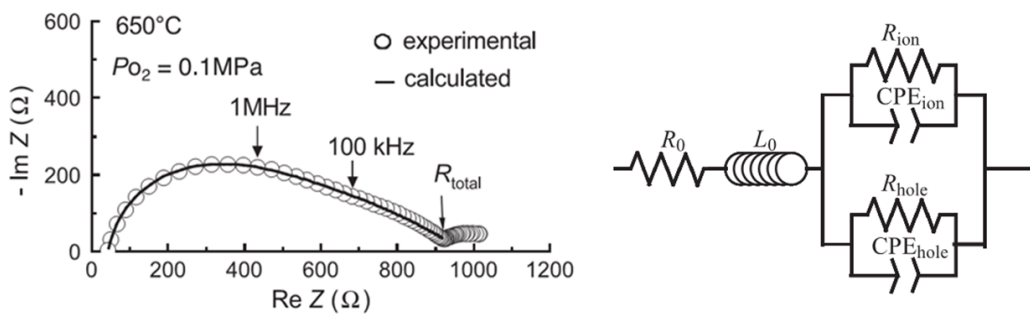


Figure 5-24.  $Z^*$  plot of BiT at  $650\text{ }^\circ\text{C}$  and the equivalent circuit used to fit it.<sup>14</sup>

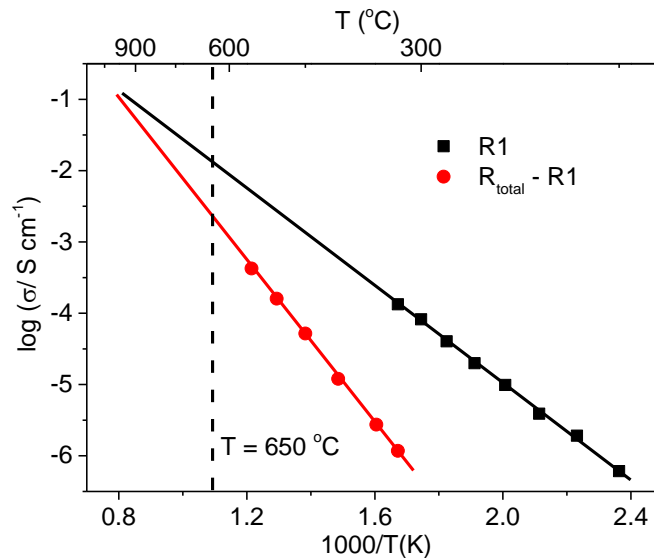


Figure 5-25. Comparison of  $R_1$  (bulk) and  $R_{\text{total}} - R_1$  for  $x = 0$  ceramic.

Second, a comparison of  $R_1$  (bulk response) and  $R_2 + R_3$  ( $R_{\text{total}} - R_1$ ) is shown in

Figure 5-25. It is clear that at 650 °C the total resistance is still dominated by R2 + R3 which is about 1 order of magnitude larger than R1. Therefore the so-called 'bulk' response as suggested by Takahashi et al actually contains multiple responses associated with the different components, each with their different activation energy which merge into a response that gives the appearance of a single, distorted semicircle at high temperature (650 °C in their case). The Arrhenius plot shown in Figure 5-25 indicates that the bulk (R1) dominates the total resistance of BiT ceramics at temperatures above 900 °C (assuming the activation energy for the bulk component doesn't change at  $T_C$ ). However, a change of activation energy is observed in Figure 5-22 at  $T_C$  where the activation energy of  $R_{total}$  changes from  $\sim 0.8$  to  $\sim 0.4$ . It is currently unclear if this change is caused by bulk, R2 or R3 but it will certainly influence the relation of them at temperatures  $> 675$  °C ( $T_C$ ).

### 5.3. Conclusions

BiT is potentially a good oxide ion conductor which possesses high oxide ion conduction. It is a mixed p-type and oxide ion conductor at low temperature but is nearly a pure oxide ion conductor (solid electrolyte) in the temperature range  $\sim 670$  to  $800$  °C with  $t_{ion} > 0.9$ . This high level of nearly 'pure' oxide ion conduction was confirmed by  $^{18}O$  TOF-SIMS measurements. Generally speaking, the Bi non-stoichiometry in BiT is limited and has little influence on bulk conduction. This is because BiT contains both extrinsic ( $Bi_2O_3$ -loss) and intrinsic (Schottky or Frenkel) oxygen vacancies and excess Bi can only compensate the extrinsic oxygen vacancies. Bi-deficient starting compositions lead to a reduction of bulk conductivity instead of an increase which may be attributed to a reduction in the intrinsic defects. Compared with NBT, the different responses in impedance results of BiT samples are poorly resolved and show considerable electrical inhomogeneity. This problem can be partially solved by suppressing the oxide ion conduction in BiT.

## 5.4. References

1. Dorrian, J. F., Newnham, R. E., Smith, D. K. & Kay, M. I. Crystal structure of  $\text{Bi}_4\text{Ti}_3\text{O}_{12}$ . *Ferroelectrics* **3**, 17–27 (1972).
2. Cummins, S. E. & Cross, L. E. Crystal symmetry, optical properties, and ferroelectric polarization of  $\text{Bi}_4\text{Ti}_3\text{O}_{12}$  single crystals. *Appl. Phys. Lett.* **10**, 14–16 (1967).
3. Newnham, R. E., Wolfe, R. W. & Dorrian, J. F. Structural basis of ferroelectricity in the bismuth titanate family. *Mater. Res. Bull.* **6**, 1029–1039 (1971).
4. Jardiel, T., Caballero, A. & Villegas, M. Aurivillius ceramics:  $\text{Bi}_4\text{Ti}_3\text{O}_{12}$ -based piezoelectrics. *J. Ceram. Soc. Japan* **116**, 511–518 (2008).
5. Kendall, K. Recent developments in perovskite-based oxide ion conductors. *Solid State Ionics* **82**, 215–223 (1995).
6. Vannier, R., Mairesse, G., Abraham, F. & Nowogrocki, G. Double substitutions in  $\text{Bi}_4\text{V}_2\text{O}_{11}$ . *Solid State Ionics* **70–71**, 248–252 (1994).
7. Noguchi, Y., Goto, T., Miyayama, M., Hoshikawa, A. & Kamiyama, T. Ferroelectric distortion and electronic structure in  $\text{Bi}_4\text{Ti}_3\text{O}_{12}$ . *J. Electroceramics* **21**, 49–54 (2008).
8. Takahashi, M., Noguchi, Y. & Miyayama, M. Electrical Conduction Mechanism in  $\text{Bi}_4\text{Ti}_3\text{O}_{12}$  Single Crystal. *Jpn. J. Appl. Phys.* **41**, 7053–7056 (2002).
9. Snedden, A., Lightfoot, P., Dinges, T. & Islam, M. S. Defect and dopant properties of the Aurivillius phase  $\text{Bi}_4\text{Ti}_3\text{O}_{12}$ . *J. Solid State Chem.* **177**, 3660–3665 (2004).
10. Hashimoto, T. & Moriwake, H. Oxygen vacancy formation energy and its effect on spontaneous polarization in  $\text{Bi}_4\text{Ti}_3\text{O}_{12}$ : A first-principles theoretical study. *Phys. Rev. B* **78**, 22–25 (2008).

11. Wachsman, E. D. & Lee, K. T. Lowering the Temperature of Solid Oxide Fuel Cells. *Science*, **334**, 935–939 (2011).
12. Harwig, H. A. On the Structure of Bismuthsesquioxide: The  $\alpha$ ,  $\beta$ ,  $\gamma$ , and  $\delta$ -phase. *Zeitschrift für Anorg. und Allg. Chemie* **444**, 151–166 (1978).
13. Fouskova, A. Dielectric Properties of Bismuth Titanate. *J. Appl. Phys.* **41**, 2834–2838 (1970).
14. Takahashi, M. Estimation of ionic and hole conductivity in bismuth titanate polycrystals at high temperatures. *Solid State Ionics* **172**, 325–329 (2004).

## 6. Chemical doping of $\text{Bi}_4\text{Ti}_3\text{O}_{12}$

As Bi non-stoichiometry can only cause very limited influence on the bulk conductivity, different dopants (i.e. donor, acceptor and isovalent) have been investigated to modify the functional properties of BiT, either as an electrolyte material or as a ferroelectric (dielectric) material. Among the three types of dopants, Nb donor doping on the Ti-site has been a common route to suppress the leakage current in BiT as reported in several previous studies.<sup>1-3</sup> Isovalent La-doping on the Bi-site has been reported to reduce  $T_C$  and therefore modify the ferroelectric properties.<sup>4-6</sup> Increased grain size and conductivity was reported for Sr acceptor doping on the Bi-site.<sup>7</sup> In this chapter, we reinvestigated these dopants and therefore Nb, Sr and La were adopted as donor, acceptor and isovalent dopants and their doping effects are discussed.

### 6.1. Nb-doped BiT

As shown in chapter 5, the difference in bulk conductivity caused by Bi non-stoichiometry is rather limited compared to NBT. Therefore Nb donor doping on the Ti-site was employed to further reduce the conductivity. A series of sample were prepared according to the general formula  $\text{Bi}_4\text{Ti}_{3-x}\text{Nb}_x\text{O}_{12+x/2}$  ( $0.000 < x \leq 0.250$ , x-series).

#### 6.1.1. Phase purity and microstructure

XRD patterns for all x-series samples are shown in Figure 6-1 and all observed peaks belong to the  $B1a1$  space group with no additional reflections. The lattice parameters calculated from the XRD patterns show a general trend from  $x = 0.000$  to  $0.150$  where  $a$  decreases and  $c$  increases with increasing Nb content whereas  $b$  remains almost unchanged, Figure 6-2. However,  $x = 0.250$  shows abnormal behaviour where  $a$ ,  $b$  and  $c$  all decrease rapidly which indicates the solid solution limit of Ti substituted by Nb is

in the range between  $x = 0.150$  and  $0.250$ . This result is supported by a combination of SEM and EDX which revealed a  $\text{Bi}_2\text{Ti}_2\text{O}_7$ -like pyrochlore-type phase to exist in  $x = 0.250$  ceramics, Figure 6-3 and Table 6-1. The average composition for the pyrochlore-type phase contains Bi on the A-site, Ti and Nb on the B-site with an average composition of  $\text{Bi}_2\text{Ti}_{1.73}\text{Nb}_{0.27}\text{O}_{7.13}$ .

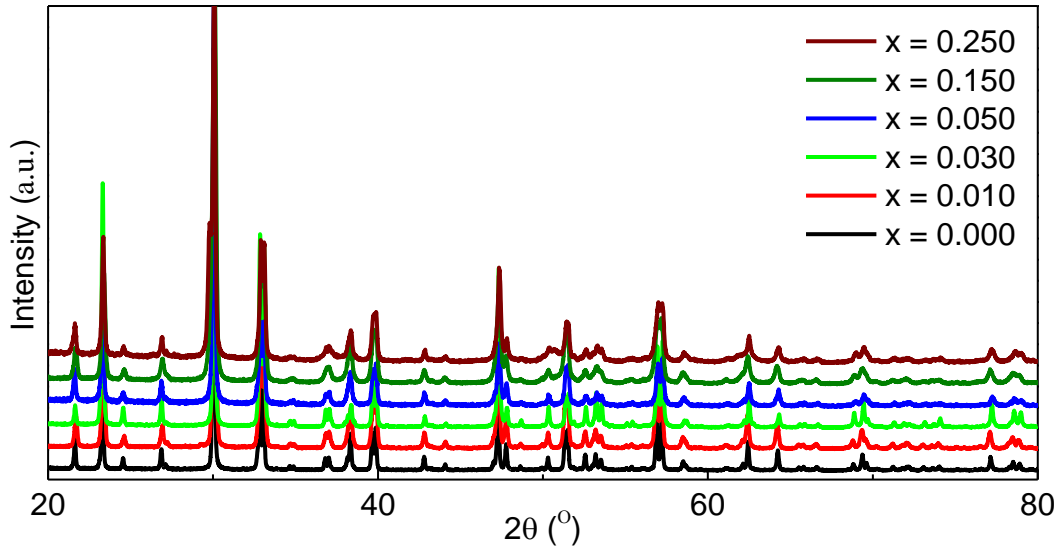


Figure 6-1. Room temperature X-ray powder diffraction data for  $\text{Bi}_4\text{Ti}_{3-x}\text{Nb}_x\text{O}_{12+x/2}$  crushed ceramics.

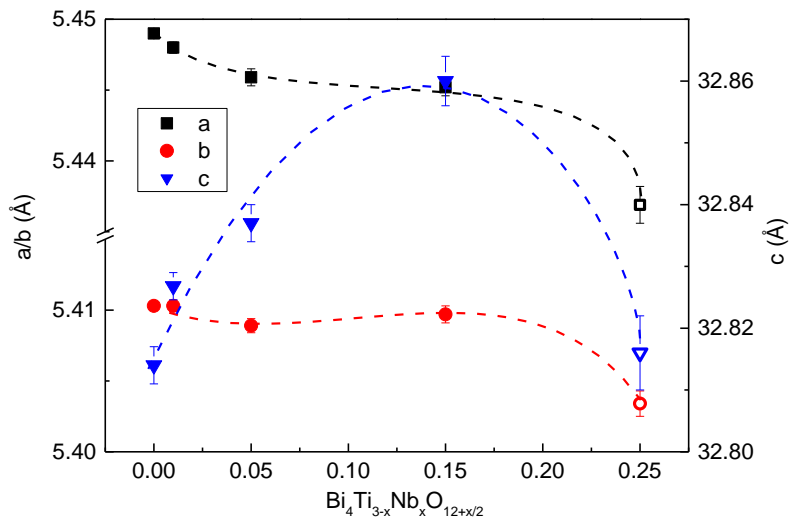


Figure 6-2. Lattice parameters  $a$ ,  $b$  and  $c$  versus  $x$  content for  $\text{Bi}_4\text{Ti}_{3-x}\text{Nb}_x\text{O}_{12+x/2}$  crushed ceramics (solid symbol: single phase; open symbol: multi-phase).

SEM images show a systematic decrease in grain size of Nb-BiT with increasing Nb content from  $\sim 100 \mu\text{m}$  for  $x = 0.000$  to  $< 1 \mu\text{m}$  for  $x = 0.250$  whereas a change of morphology from plate ( $x = 0.000$ ) to round grains ( $x > 0.000$ ), Figure 6-4.

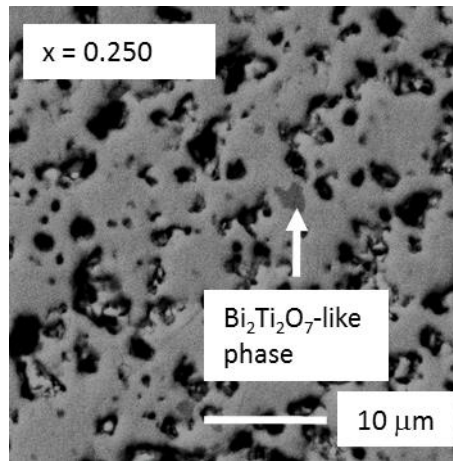


Figure 6-3. SEM back scattered electron images for  $x = 0.250$  ceramic showing the  $\text{Bi}_2\text{Ti}_2\text{O}_7$ -like secondary phase.

Table 6-1. Chemical composition (relative cation at%) of the main phase and secondary phase with associated error (standard deviation) by SEM/EDX of samples in the x-series.

Composition		Bi (at%)	Ti (at%)	Nb (at%)
<b>x = 0.000</b>	Main phase	56.8 ( $\pm 0.3$ )	43.2 ( $\pm 0.3$ )	N/A
	Theoretical value	57.1	42.9	N/A
<b>x = 0.050</b>	Main phase	56.3 ( $\pm 0.6$ )	42.4 ( $\pm 0.6$ )	1.3 ( $\pm 0.4$ )
	Theoretical value	57.1	42.2	0.7
<b>x = 0.150</b>	Main phase	56.8 ( $\pm 0.3$ )	40.3 ( $\pm 0.3$ )	2.9 ( $\pm 0.3$ )
	Theoretical value	57.1	41.2	1.7
<b>x = 0.250</b>	Main phase	56.9 ( $\pm 0.2$ )	39.8 ( $\pm 0.4$ )	3.3 ( $\pm 0.3$ )
	Theoretical value	57.1	40.1	2.8
	$\text{Bi}_2\text{Ti}_2\text{O}_7$ -like phase	49 ( $\pm 2$ )	44 ( $\pm 1$ )	7 ( $\pm 1$ )

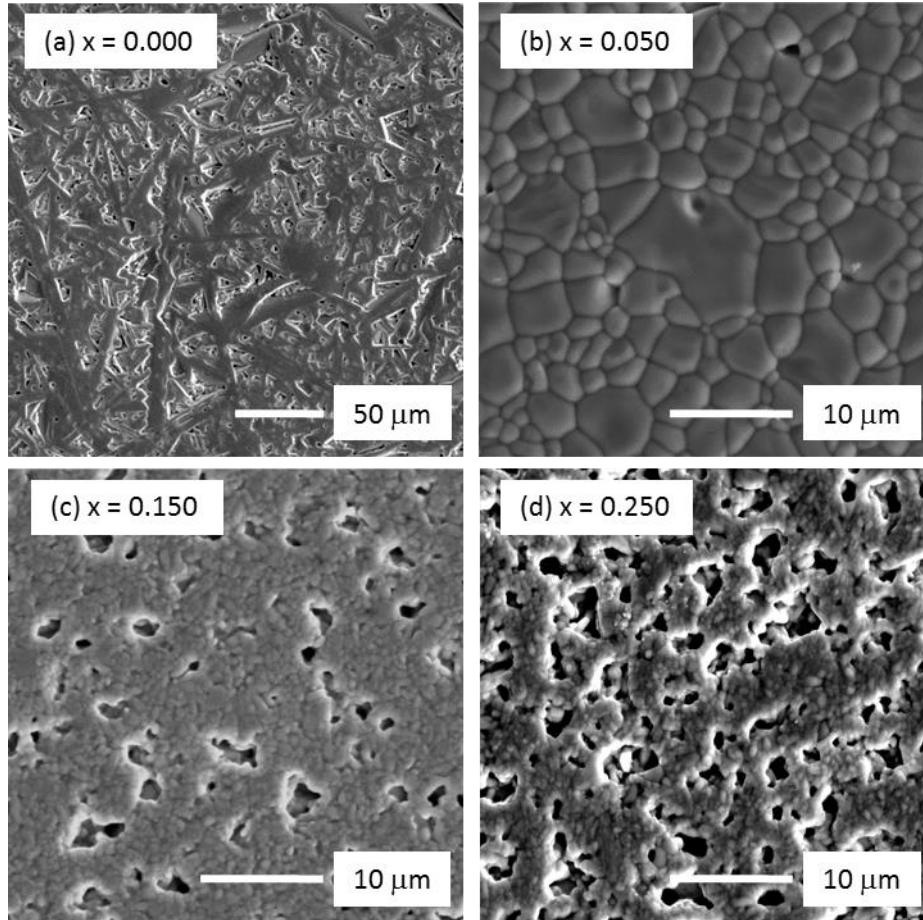


Figure 6-4. SEM micrographs for (a)  $x = 0.000$ , (b)  $x = 0.050$ , (c)  $x = 0.150$  and (d)  $x = 0.250$  ceramics. All samples were polished and thermally etched prior to SEM. The scale is different in (a) than in (b) to (d).

### 6.1.2. Electrical Properties

The temperature dependence of the permittivity,  $\epsilon_r$ , and the dielectric loss,  $\tan \delta$  are summarised in Figure 6-5. A rapid decrease of  $\epsilon_{r,\max}$  occurs with low levels of doping, i.e.  $x \geq 0.010$ . The  $\epsilon_{r,\max}$  changes from  $\sim 1800$  for un-doped BiT to  $\sim 750$  for  $x = 0.010$  and  $0.030$  and reaches a minimum value of  $\sim 450$  for  $x = 0.150$  whereas  $T_{\epsilon_r,\max}$  increases slightly ( $\sim 15$  °C) with Nb-doping, Figure 6-6.

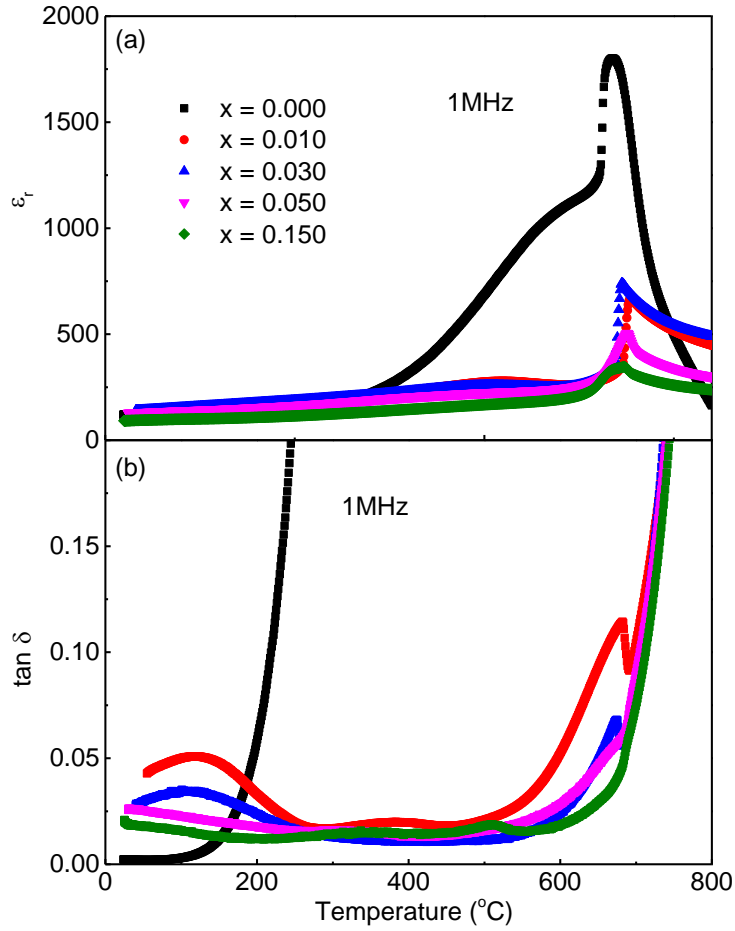


Figure 6-5. Temperature dependence of (a)  $\epsilon_r$  and (b)  $\tan \delta$  at 1 MHz for x-series ceramics.

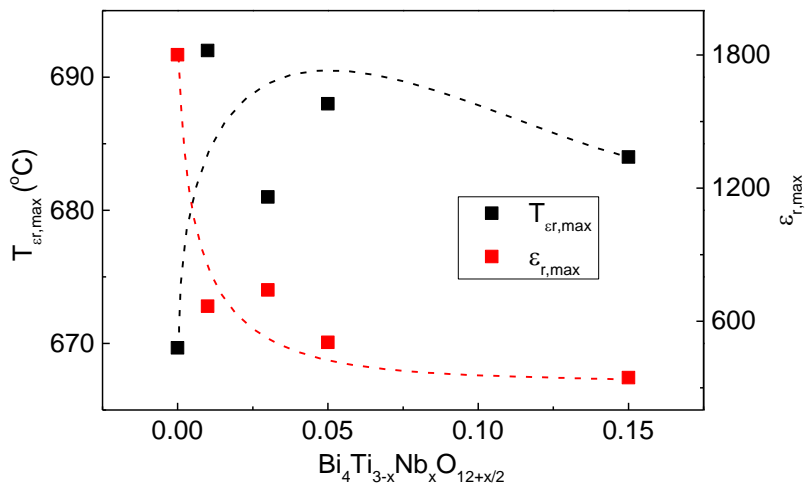


Figure 6-6. The influence of Nb-doping on the maximum permittivity,  $\epsilon_{r, \max}$  and the corresponding temperature,  $T_{\epsilon_r, \max}$  on x-series ceramics.

$Z^*$  plots for selected x-series samples are shown in Figure 6-7. As shown in Figure 5-6 in Chapter 5, three components are observed in  $Z^*$  plots for undoped BiT; a low frequency spike, followed by a distorted semi-circle then an incomplete semi-circle at high frequency. From the discussion in chapter 5, the low frequency spike and high frequency quarter circle can be attributed to an electrode effect and the bulk response, respectively. In the x-series, very low levels of doping ( $x = 0.005$ ) can lead to a significant increase in bulk resistivity, Figure 6-7 (a). For  $x \geq 0.01$ , the  $Z^*$  plots were dominated by a single arc associated with a bulk response ( $2.61 \times 10^{-11}$  F/cm) and a small low frequency spike ( $1.22 \times 10^{-8}$  F/cm) response associated with an electrode effect, Figure 6-8 (b). In general, the bulk resistivity of x-series samples increased with increasing Nb content and  $x = 0.150$  is the most resistive sample.

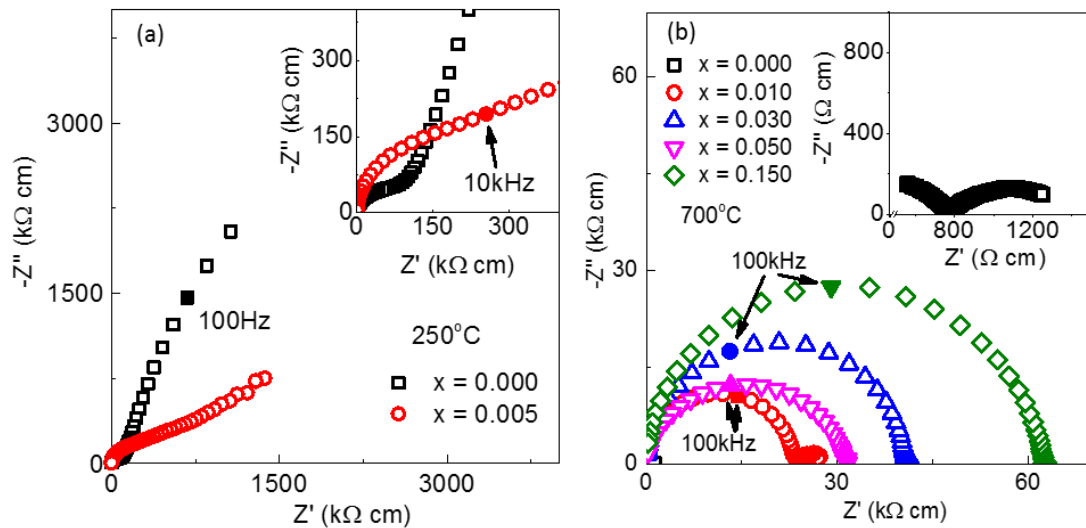


Figure 6-7.  $Z^*$  plots of selected x-series ceramics with (a) relatively low Nb-doping level (at 250 °C) and (b) high Nb-doping level (at 700 °C) .

Impedance measurements as a function of  $pO_2$  show two different responses for Nb-doped BiT. The bulk conductivity of samples with relatively low Nb-doping ( $x < 0.050$ ) increases with increasing  $pO_2$  indicating p-type conduction whereas with higher Nb-doping levels ( $x \geq 0.050$ ) the bulk conductivity increases with decreasing  $pO_2$  indicating n-type conduction.

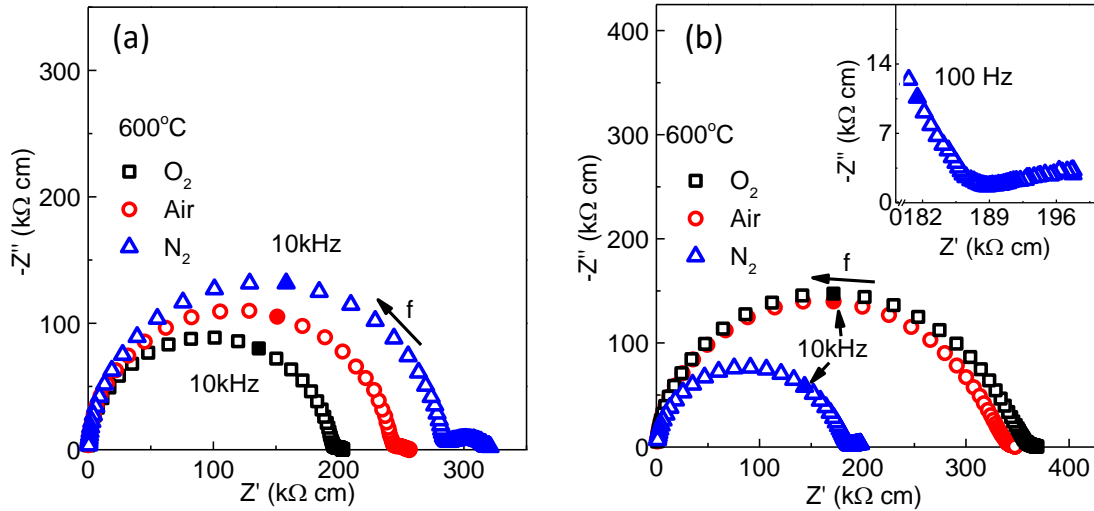


Figure 6-8.  $Z^*$  plots for (a)  $x = 0.010$  and (b)  $x = 0.050$  under different flowing gas atmospheres at  $600\text{ }^\circ\text{C}$ .

Based on the impedance spectroscopy data, the bulk conductivity (extracted from the  $M''$  peak due to the difficulty in resolving the bulk response from  $Z^*$  plots for low Nb-doped samples) of  $x$ -series samples are summarised in an Arrhenius plot shown in Figure 6-9. With Nb-doping, BiT changes from a conductor to an insulator. The bulk conductivity initially decreases with increasing Nb content and then it remains at a similar level for  $x \geq 0.050$ . A significant difference in activation energy for the bulk conductivity is also observed with increasing Nb content from a value of  $\sim 0.60$  eV for undoped BiT to  $\sim 0.70$  to  $\sim 1.60$  eV for low levels of Nb doping and to  $\sim 1.70$  eV for high levels of Nb-doping. The activation energy for high level Nb-doped samples with  $x \geq 0.050$  ( $\sim 1.7$  eV) is close to half of the reported BiT optical band gap,  $E_g$ , of  $\sim 3.0$ – $3.35$  eV, indicating  $x \geq 0.050$  samples are presumably dominated by intrinsic electronic conduction.<sup>8,9</sup>

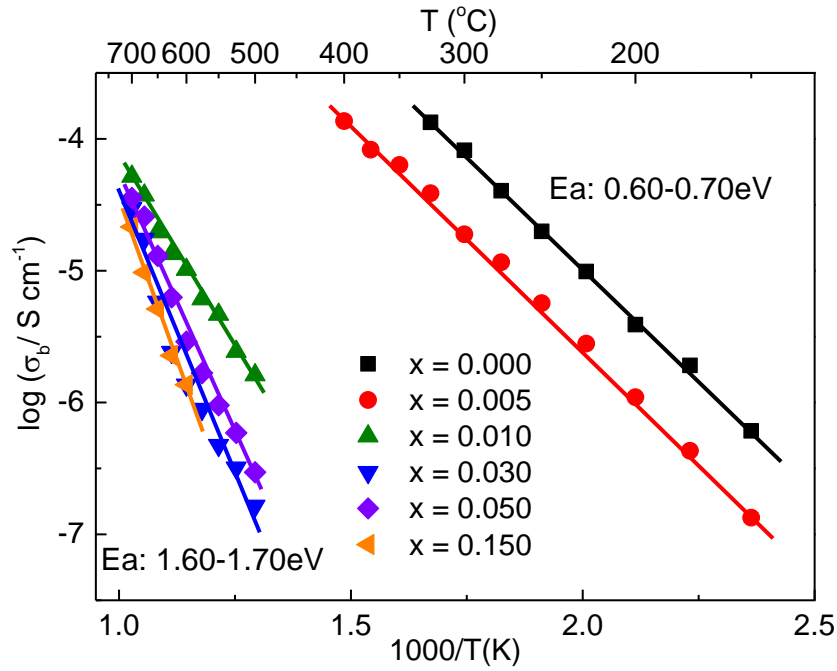


Figure 6-9. Arrhenius plot of bulk conductivity,  $\sigma_b$ , versus reciprocal temperature for selected x-series ceramics. Activation energy,  $E_a$ , values for  $\sigma_b$  are included.

EMF measurements confirmed the lack of oxide ion conduction in Nb-doped BiT.  $x = 0.030$  ceramics have  $t_{\text{ion}} \sim 0.27$  at 600  $^{\circ}\text{C}$  and it decreases with increasing temperature, Figure 6-10. Compared with undoped BiT, the oxide ion conduction is significantly suppressed.

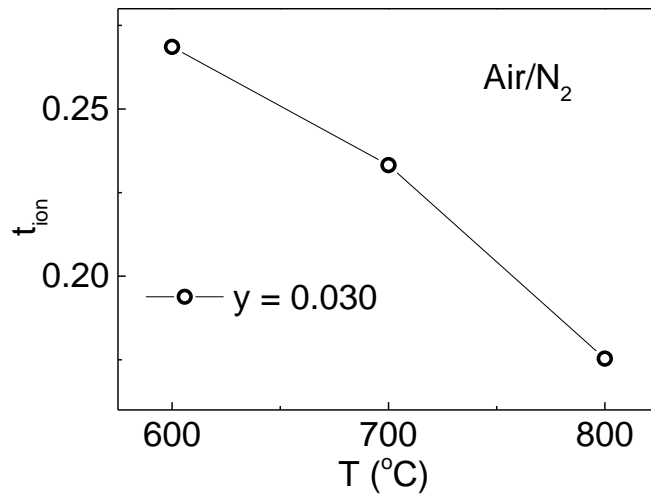


Figure 6-10.  $t_{\text{ion}}$  values between 600 and 800  $^{\circ}\text{C}$  for  $x = 0.030$ .

## 6.2. La doped BiT

Nominally stoichiometric BiT exhibits nearly pure oxide ion conduction with  $t_{\text{ion}} \sim 0.94$  near  $T_c$ . However, the  $T_c$  of BiT is rather high ( $\sim 675$  °C) for applications like intermediate temperature SOFCs. La-doping on the Bi-site is known to be able to significantly reduce  $T_c$  with a relatively low level of doping and has been employed to modify the Curie temperature.<sup>4-6</sup> It is interesting therefore to investigate if the high oxide ion conduction can be retained whilst reducing  $T_c$  in La-doped BiT. Samples with La-doping are labelled as the  $\gamma$ -series based on the general formula  $\text{Bi}_{4-\gamma}\text{La}_\gamma\text{Ti}_3\text{O}_{12}$  ( $0 \leq \gamma \leq 2$ ).

### 6.2.1. Phase purity and microstructure

The phase purity of La-doped BiT was examined by a combination of XRD and SEM/EDX. The XRD patterns for  $\gamma$ -series samples are shown in Figure 6-11. No additional reflections are observed in any pattern but with increasing La content some of the split peaks start to merge indicating a possible increase in crystal symmetry, see inset in Figure 6-11. The lattice parameters (Figure 6-12) show a consistent trend where  $c$  increases continuously with increasing  $\gamma$  content whereas  $a$  and  $b$  initially approach each other and then decrease with increasing  $\gamma$  and eventually the cell becomes tetragonal ( $I4/mmm$ ) for  $\gamma = 2.00$ .

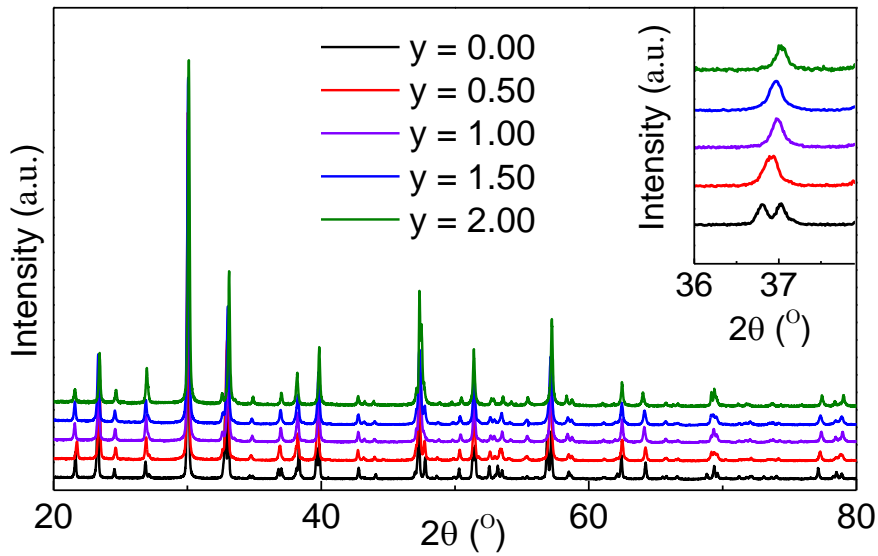


Figure 6-11. Room temperature X-ray powder diffraction data for the  $\text{Bi}_{4-y}\text{La}_y\text{Ti}_3\text{O}_{12}$  series.

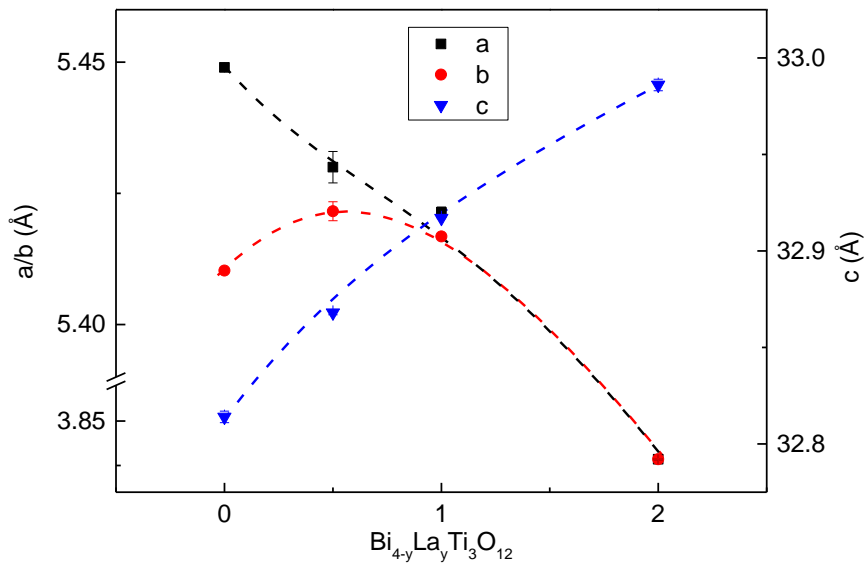


Figure 6-12. Lattice parameters  $a$ ,  $b$  and  $c$  as a function of  $y$  content for the  $\text{Bi}_{4-y}\text{La}_y\text{Ti}_3\text{O}_{12}$  series.

EDX results show a systematic increase in La content in the main phase with an increase of  $\text{La}_2\text{O}_3$  in the starting composition, Table 6-2. For  $y < 1.50$ , the La content is in reasonable agreement with the theoretical value with a small error. However, for  $y = 1.50$  there is a discrepancy between the theoretical and experimental values and for

$y = 2.00$  the experimental error becomes significantly larger which may indicate an uneven distribution of La. In addition, La-doping on the Bi-site also suppresses grain growth and leads to a significant decrease in grain size with increasing La content, Figure 6-13.

Table 6-2. Chemical composition (relative cation at%) and associated error (standard deviation) by SEM/EDX for the  $\text{Bi}_{4-y}\text{La}_y\text{Ti}_3\text{O}_{12}$  series.

Composition		Bi (at%)	Ti (at%)	La (at%)
<b>y = 0.00</b>	Main phase	56.8 ( $\pm 0.3$ )	43.2 ( $\pm 0.3$ )	N/A
	Theoretical value	57.1	42.9	N/A
<b>y = 0.50</b>	Main phase	49 ( $\pm 3$ )	44 ( $\pm 3$ )	7 ( $\pm 1$ )
	Theoretical value	50.0	42.9	7.1
<b>y = 1.00</b>	Main phase	42.6 ( $\pm 0.7$ )	42.6 ( $\pm 0.7$ )	14.7 ( $\pm 0.3$ )
	Theoretical value	42.9	42.9	14.3
<b>y = 1.50</b>	Main phase	33.1 ( $\pm 0.2$ )	42.5 ( $\pm 0.5$ )	24.4 ( $\pm 0.4$ )
	Theoretical value	35.7	42.9	21.4
<b>y = 2.00</b>	Main phase	24 ( $\pm 7$ )	44 ( $\pm 3$ )	32 ( $\pm 4$ )
	Theoretical value	28.6	42.9	28.6

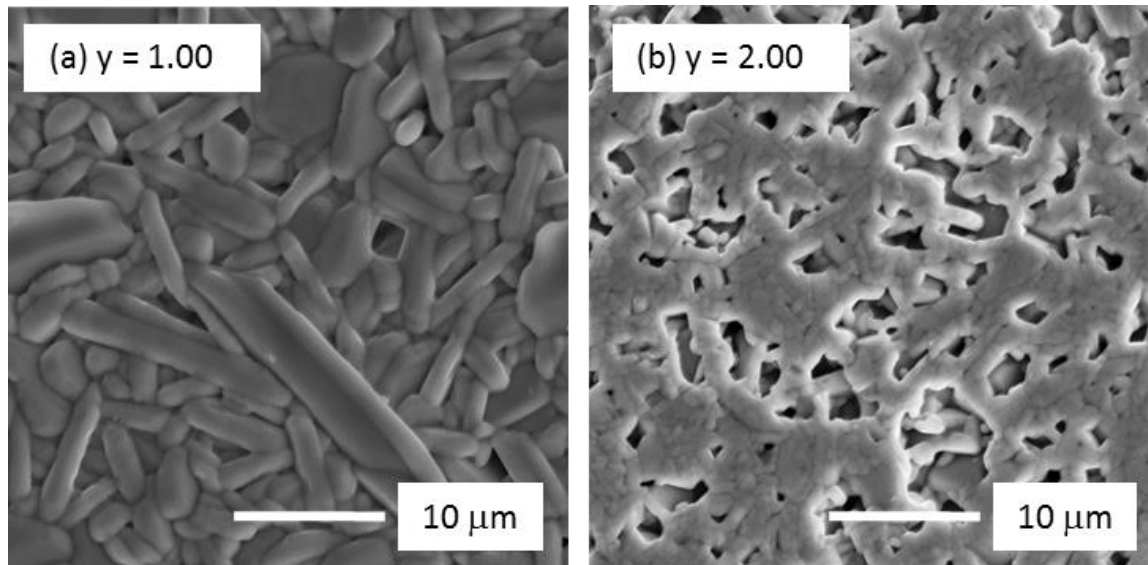


Figure 6-13. SEM micrographs of (a)  $y = 1.00$  and (b)  $y = 2.00$ . All samples were polished and thermally etched prior to SEM.

#### 6.2.2. Electrical properties

A summary of  $\epsilon_r$  and  $\tan \delta$  versus temperature is shown in Figure 6-14. With La doping a dramatic decrease in both  $\epsilon_{r,\max}$  and  $T_{\epsilon_r,\max}$  occurs.  $T_{\epsilon_r,\max}$  is reduced from  $\sim 675$  °C for un-doped samples to  $\sim 200$  °C for  $y = 1.00$  and a further increase of La content leads to a  $T_{\epsilon_r,\max}$  below room temperature, Figure 6-15.  $\epsilon_{r,\max}$  also decreases from  $\sim 1800$  for undoped samples to  $\sim 300$  for  $y = 1.00$  and the temperature dependent  $\epsilon_r$  becomes much flatter as  $T_{\epsilon_r,\max}$  is below room temperature. On the other hand,  $\tan \delta$  is reduced by La-doping but even for  $y = 2.00$  the loss is still much higher when compared with the x-series samples (Nb-doped) with  $\tan \delta > 0.2$  above 500 °C.

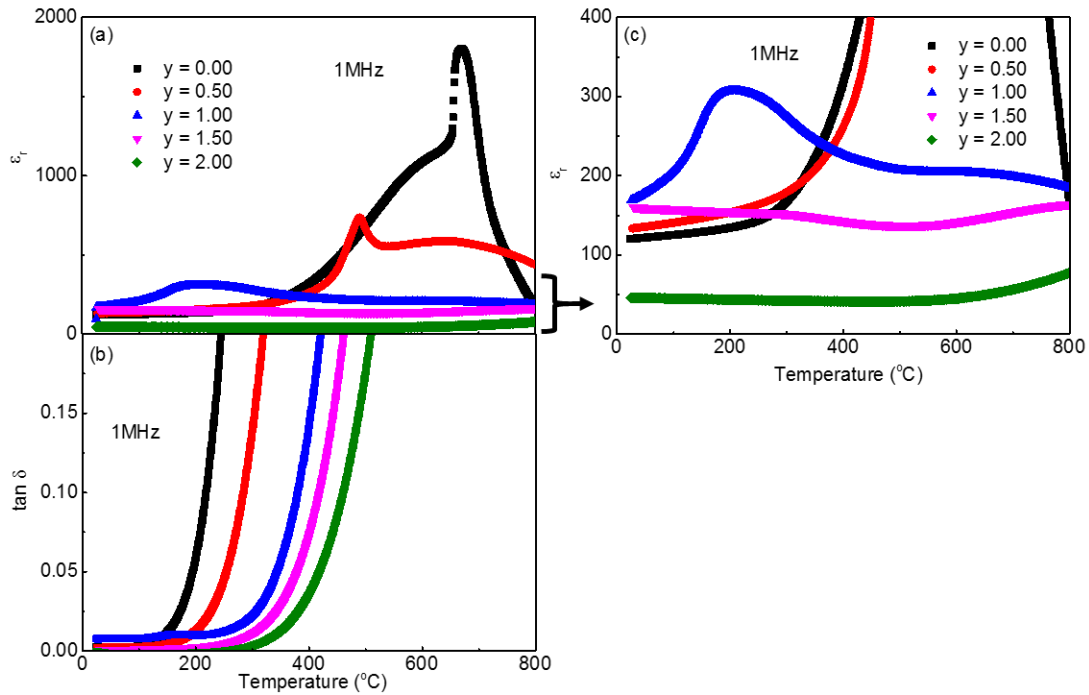


Figure 6-14. Temperature dependence of (a)  $\epsilon_r$  and (b)  $\tan \delta$  at 1 MHz for  $\text{Bi}_{4-y}\text{La}_y\text{Ti}_3\text{O}_{12}$  series; (c) expanded scale of (a) to show the low permittivity range.

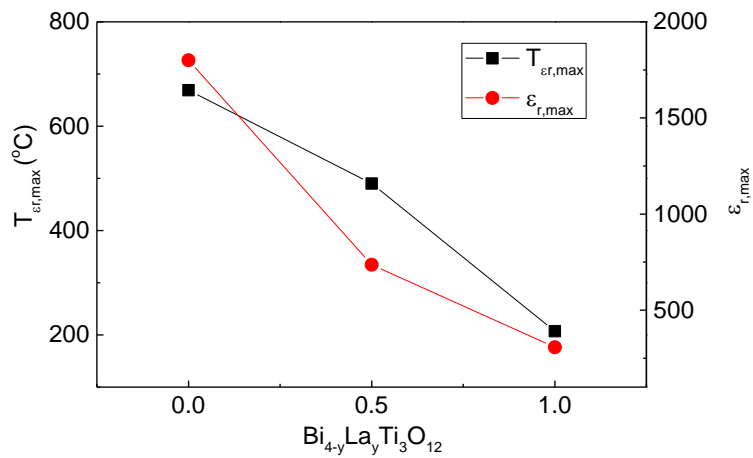


Figure 6-15. The influence of La-doping on the (a) maximum permittivity,  $\epsilon_{r,\max}$  and the corresponding temperature,  $T_{\epsilon_{r,\max}}$ .

$Z^*$  plots obtained from selected samples at 500 °C are shown in Figure 6-16. All samples in the  $y$ -series consist of a low frequency spike, followed by a distorted semi-circle then an incomplete semi-circle at high frequency.  $Z''$  and  $M''$  spectroscopic plots for  $y = 1.00$  and  $2.00$  indicate the two arcs can be considered as two parallel RC

elements connected in series with each RC from a different response, Figure 6-16 (c) and (d). For  $y = 2.00$ , the capacitance for the high frequency quarter circle and the lower frequency distorted semicircle are  $3.89 \times 10^{-12}$  F/cm and  $2.35 \times 10^{-10}$  F/cm. Following the discussion from Chapter 5, these values show that the quarter circle is a bulk response and the semicircle is attributed to a grain boundary response. The low frequency spike is consistent with the Warburg diffusion behaviour and therefore is an electrode effect. It is clearly shown from the  $Z^*$  plots that the bulk resistivity increases considerably with La-doping. It is worth mentioning that the low frequency spike which indicates the presence of ionic conduction is observed in all  $y$ -series samples, Figure 6-17.

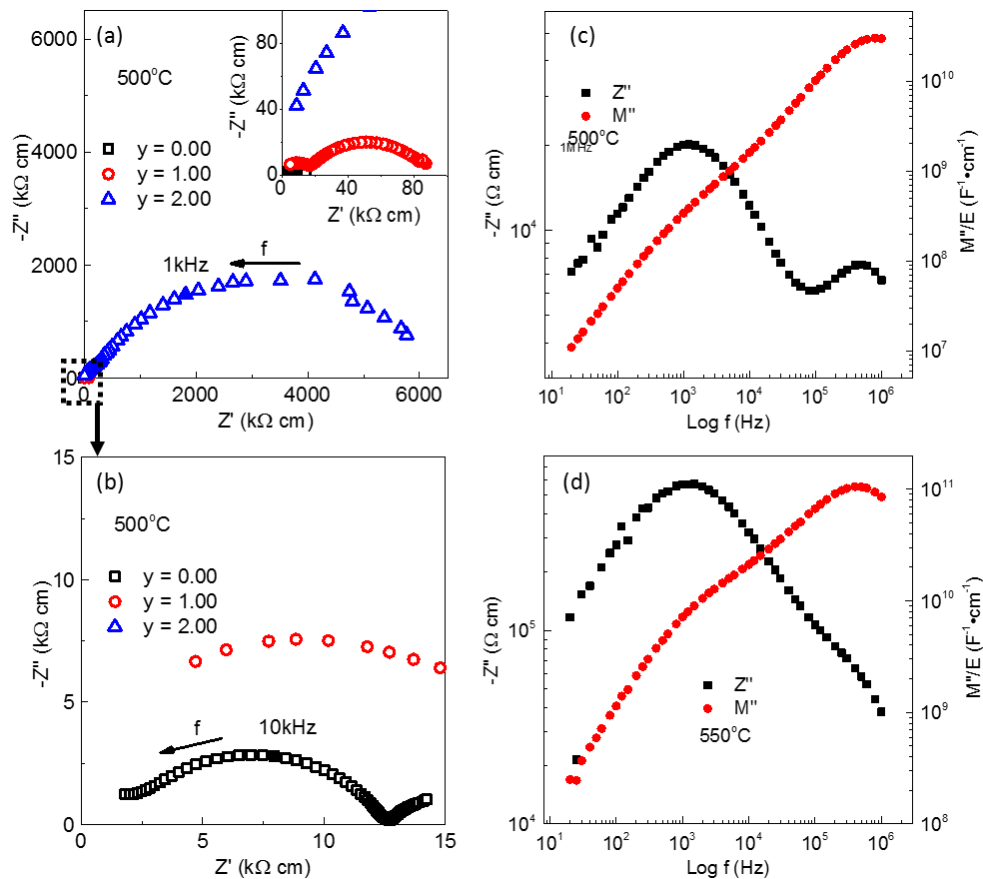


Figure 6-16. (a)  $Z^*$  plots (500 °C) for selected  $y$ -series samples and (b) expanded scale to highlight the response from  $y = 0.00$  and  $1.00$ .  $Z''$  and  $M''$  spectroscopic plots for (c)  $y = 1.00$  (500 °C) and (d)  $y = 2.00$  (550 °C).

Impedance measurements performed in various  $pO_2$ 's for  $\gamma = 1.50$  showed an increase in the grain boundary conductivity with increasing  $pO_2$ , Figure 6-17 (a) indicating p-type behaviour. There is poor resolution of the bulk and grain boundary arc responses in the  $Z^*$  plots and it is difficult to identify whether or not the bulk response is changing with  $pO_2$  using these plots, see inset in Figure 6.15 (a). In this case,  $M''$  spectroscopic plots were used to extract bulk resistivity values, Figure 6-17 (b). The calculated resistivity (at 550 °C) under  $O_2$ , Air and  $N_2$  was 13, 20 and 23  $k\Omega \cdot cm$ , respectively. Therefore, the presence of p-type conduction was confirmed. In addition, the low frequency spike indicates La-doped BiT is a mixed conductor with both ionic and p-type electronic conduction.

The bulk conductivity (extracted from  $M''$  spectroscopic peaks) for the  $\gamma$ -series of samples is summarised in an Arrhenius plot, Figure 6-18. The conductivity decreases continuously with increasing La content. The difference in bulk conductivity between  $\gamma = 0.00$  and 2.00 is  $\sim 3$  orders of magnitude. However, opposite to other insulating BiT or NBT samples, the activation energy for the whole  $\gamma$ -series remains relatively similar ( $\sim 0.65$  to  $0.75$  eV for all  $\gamma$ -series samples).

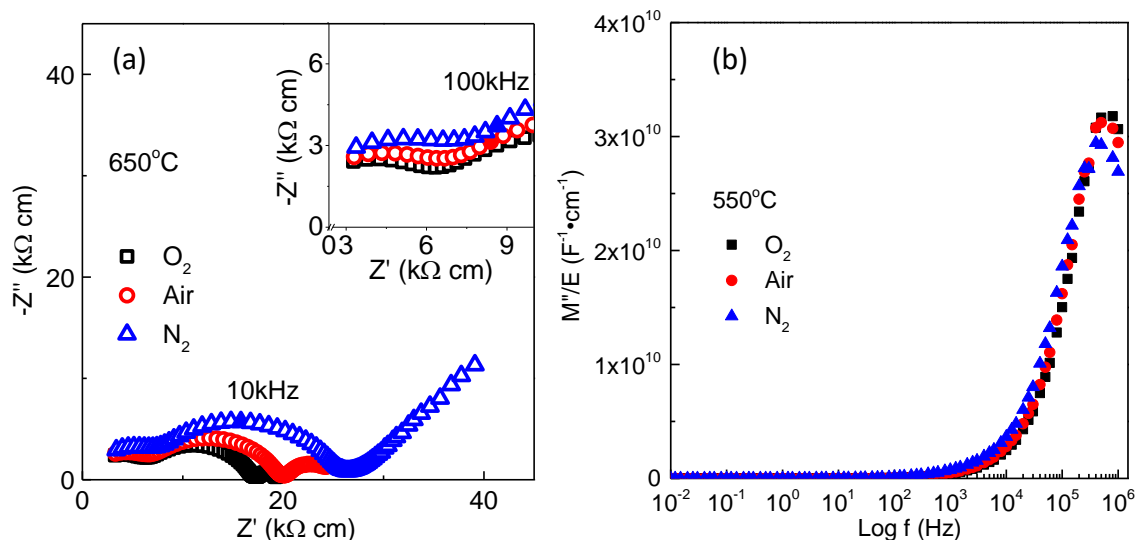


Figure 6-17. a)  $Z^*$  plots (650 °C) and b)  $M''$  spectroscopic plots (550 °C) for  $\gamma = 1.50$  under different atmospheres.

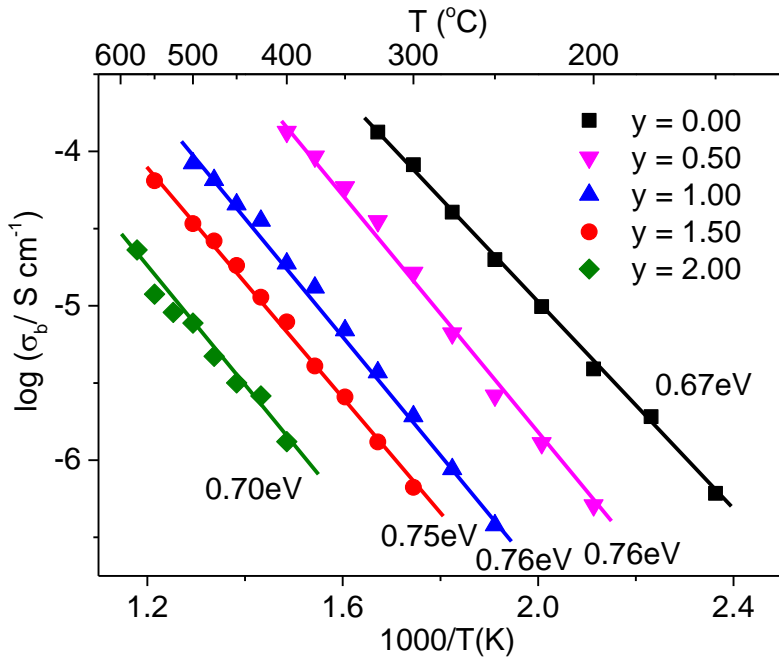


Figure 6-18. Arrhenius plot of bulk conductivity,  $\sigma_b$ , versus reciprocal temperature for  $y$ -series ceramics. Activation energy,  $E_a$ , values for  $\sigma_b$  are included.

Figure 6-19 shows the temperature dependence of  $t_{ion}$  for  $y = 0.50$  in comparison with undoped BiT. With La doping, the maximum  $t_{ion}$  temperature is reduced and  $t_{ion}$  at 600 °C increases from  $\sim 0.77$  for  $y = 0.00$  to  $\sim 0.93$  for  $y = 0.50$ . Above 600 °C,  $t_{ion}$  of  $y = 0.50$  decreases slowly with increasing temperature but still remains  $> 0.9$  until  $\sim 700$  °C.

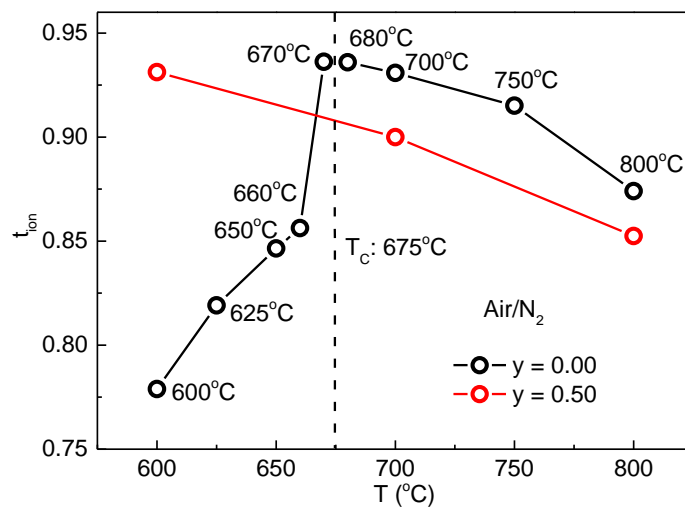


Figure 6-19.  $t_{ion}$  values between 600 and 800 °C for  $y = 0.00$  and 0.50.

## 6.3. Sr-doping

In attempts to enhance the bulk conductivity, Sr was adopted as an acceptor dopant on the Bi-site in an attempt to increase the level of oxygen deficiency in BiT. The slightly larger size of Sr than Bi was also considered to be able to modify  $T_C$  and obtain a higher  $t_{ion}$  at lower temperatures similar to La-doping. Samples in this series were synthesized based on the general formula  $Bi_{4-z}Sr_zTi_3O_{12-z/2}$  ( $0 \leq z \leq 0.40$ , z-series).

### 6.3.1. Phase purity and microstructure

XRD patterns for this series are shown in Figure 6-20 and no additional reflections were observed in the range  $0 \leq z \leq 0.20$ . For  $z = 0.40$ , both  $Bi_2O_3$  (space group  $P\bar{4}2_1c$ ) and  $TiO_2$  (space group  $P3_121$ ) were identified as secondary phases based on the XRD patterns. The calculated lattice parameters are shown in Figure 6-21. Among the three axes,  $a$  decreases and  $c$  increases with increasing  $z$  content whereas  $b$  remains almost unchanged. A rapid decrease of  $c$  is observed for  $z = 0.20$  which may indicate the actual solid solution limit is in the range between  $z = 0.12$  and  $0.20$ .

The existence of  $Bi_2O_3$  was confirmed by SEM/EDX results on a polished (without thermal etching)  $z = 0.40$  sample, Figure 6-22. SEM back scattered electron images show a bright secondary phase which indicates a higher atomic number than the matrix. EDX analysis showed a secondary phase with a higher Bi content than the matrix which confirms the existence of a Bi-rich secondary phase, Table 6-3. The large error values associated with the EDX analysis of the secondary phase are due to the distribution of the Bi-rich phase since most of the signal was from the BiT matrix due to the very small size of the secondary phase regions. On the other hand, no Ti-rich secondary phase was observed maybe due to the size and even distribution of that secondary phase. It is worth noting that despite the presence of secondary phases, the Sr content in the bulk increases systematically with increasing  $SrCO_3$  in the starting

composition. A significant change is observed for the grain size which decreases with increasing Sr content, Figure 6-23.

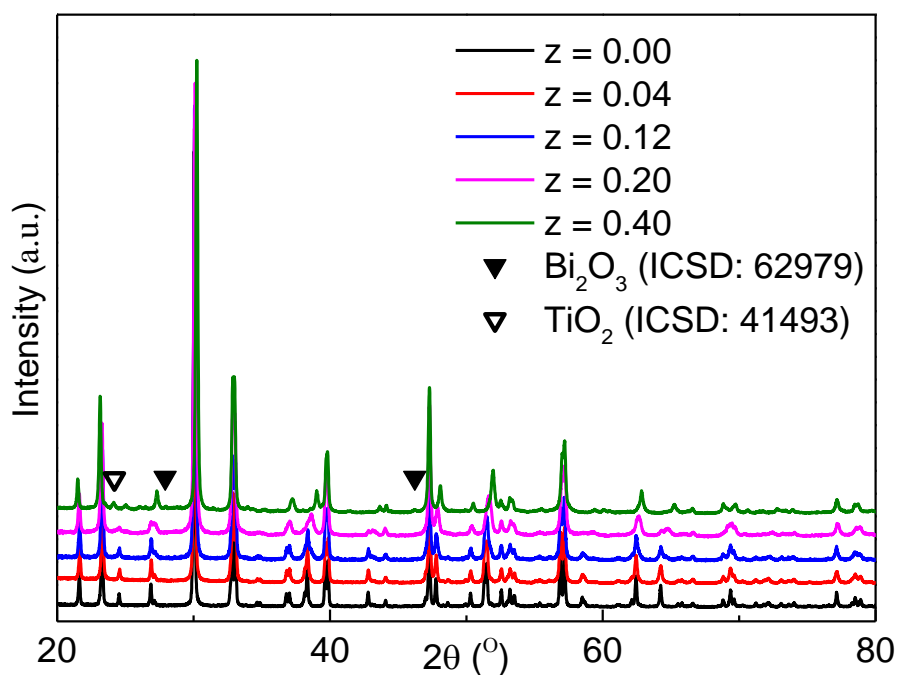


Figure 6-20. Room temperature X-ray powder diffraction data for Bi<sub>4-z</sub>Sr<sub>z</sub>Ti<sub>3</sub>O<sub>12-z/2</sub> ceramics.

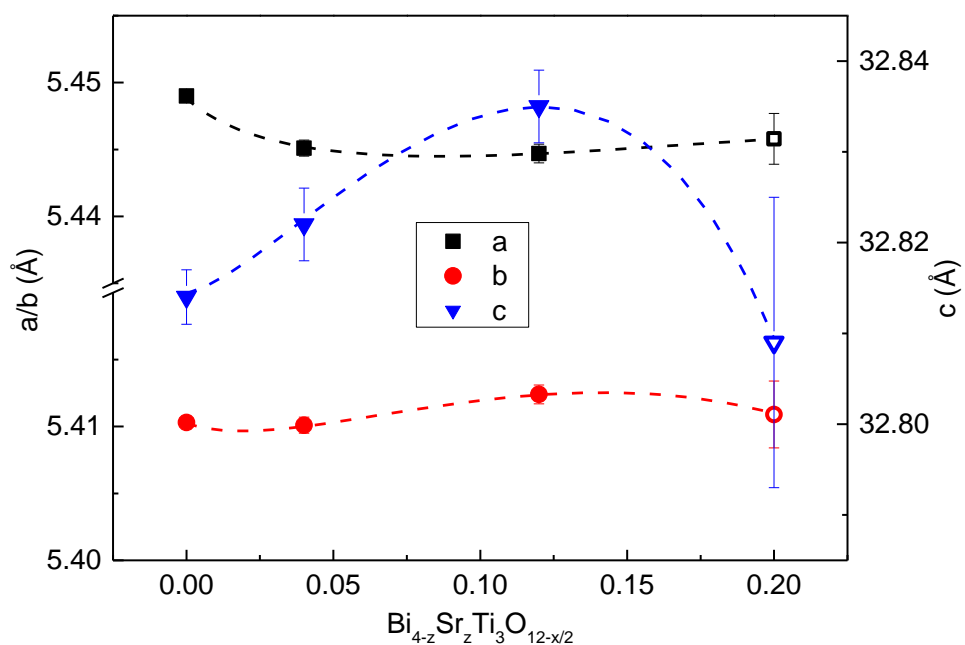


Figure 6-21. Lattice parameters a, b and c as a function of z content (solid symbol: single phase; open symbol: multi-phase).

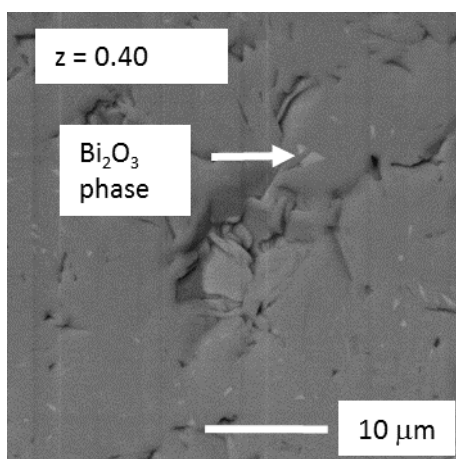


Figure 6-22. SEM back scattered electron images for  $z = 0.40$  (polished without thermal etching) showing the  $\text{Bi}_2\text{O}_3$  secondary phase.

Table 6-3. Bulk chemical composition (relative cation at%) and associated error (standard deviation) by SEM/EDX of the main and secondary phases present in selected  $z$ -series ceramics.

Composition		Bi (at%)	Ti (at%)	Sr (at%)
<b><math>z = 0.00</math></b>	Main phase	56.8 ( $\pm 0.3$ )	43.2 ( $\pm 0.3$ )	N/A
	Theoretical value	57.1	42.9	N/A
<b><math>z = 0.04</math></b>	Main phase	56.3 ( $\pm 0.8$ )	43.1 ( $\pm 0.6$ )	0.6 ( $\pm 0.4$ )
	Theoretical value	56.7	42.9	0.4
<b><math>z = 0.12</math></b>	Main phase	55.2( $\pm 0.3$ )	43.3 ( $\pm 0.3$ )	1.5 ( $\pm 0.5$ )
	Theoretical value	55.8	42.9	1.3
<b><math>z = 0.20</math></b>	Main phase	54.0 ( $\pm 0.9$ )	43.2 ( $\pm 0.5$ )	2.8 ( $\pm 0.7$ )
	Theoretical value	54.9	42.9	2.2
<b><math>z = 0.40</math></b>	Main phase	52 ( $\pm 2$ )	43 ( $\pm 1$ )	5 ( $\pm 1$ )
	Theoretical value	52.7	42.9	4.4
	Bi-rich phase	68 ( $\pm 7$ )	28 ( $\pm 7$ )	3 ( $\pm 1$ )

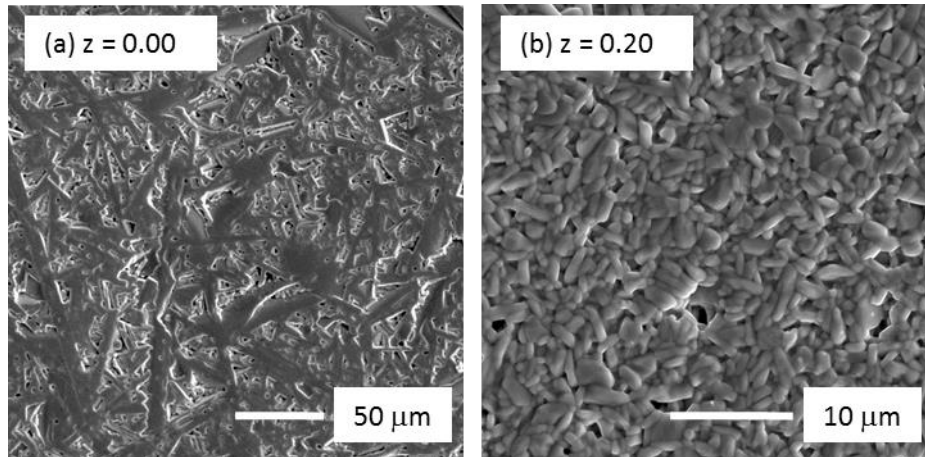


Figure 6-23. SEM micrographs of (a)  $z = 0.00$  and (b)  $z = 0.20$ . All samples were polished and thermally etched prior to SEM.

### 6.3.2. Electrical properties

For z-series samples, the relative permittivity maximum,  $\epsilon_{r,\max}$  decreases from  $\sim 1800$  for undoped BiT to  $\sim 1500$  with increasing z, Figure 6-24 and Figure 6-25. On the other hand, the temperature for  $\epsilon_{r,\max}$ ,  $T_{\epsilon_{r,\max}}$  initially decreases with increasing Sr content and then remains at  $\sim 600$  °C for  $z \geq 0.12$ . The dielectric loss,  $\tan \delta$  for the z-series samples is high with a value of  $> 0.2$  at temperatures above 300 °C. At higher temperatures,  $\tan \delta$  decreases with increasing Sr content.

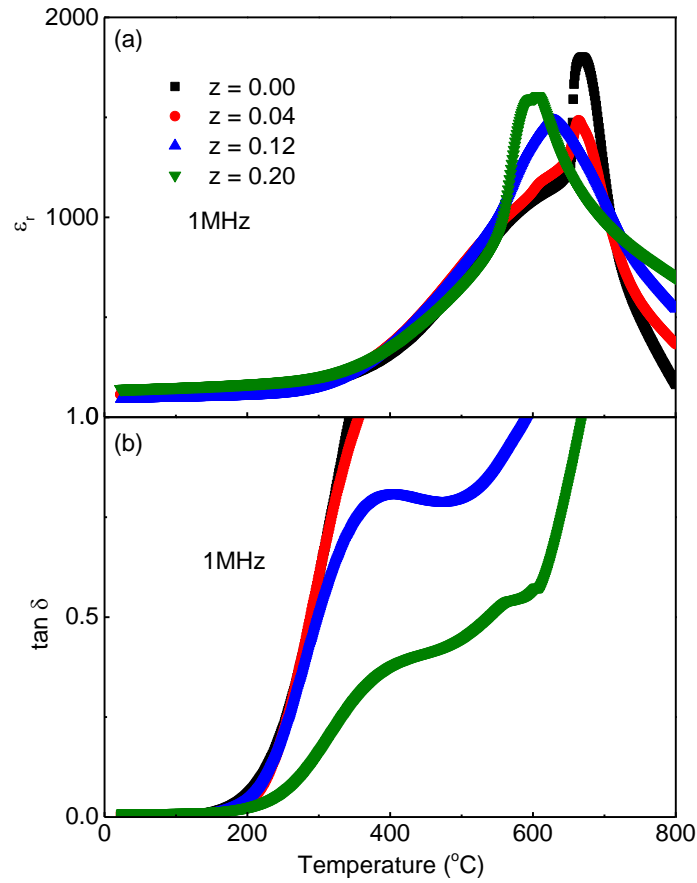


Figure 6-24. Temperature dependence of (a)  $\epsilon_r$  and (b)  $\tan \delta$  at 1 MHz for Sr-doped BiTs.

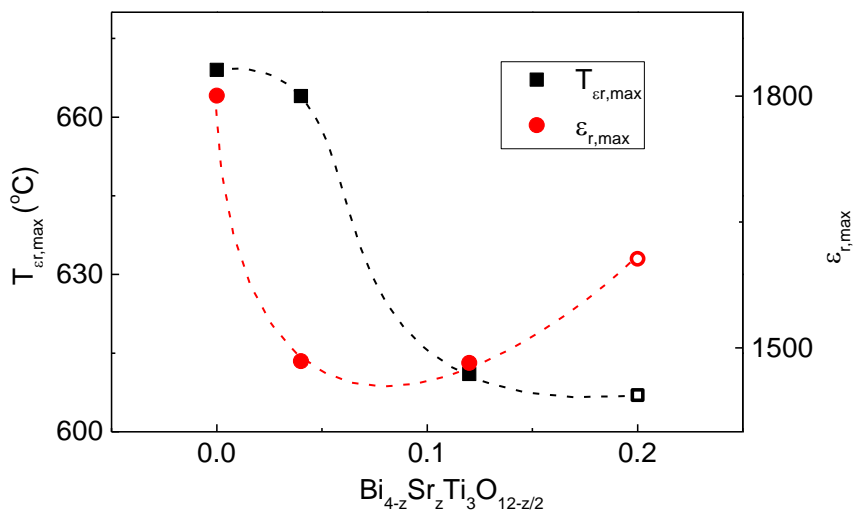


Figure 6-25. Summary of (a) maximum permittivity,  $\epsilon_{r, \max}$  and the corresponding temperature,  $T_{\epsilon_r, \max}$  with the change of Sr content in the z-series of ceramics. (solid symbol: single phase; open symbol: multi-phase).

$Z^*$  and  $Z''$  &  $M''$  spectroscopic plots for the z-series are shown in Figure 6-26. In Figure 6-26 (a) and its insert, samples with  $z \leq 0.12$  possess a low frequency spike, followed by a distorted semi-circle then an incomplete semi-circle at high frequency. Capacitance values associated with these three arcs are in the range of  $\sim 1 \times 10^{-5}$  F/cm,  $\sim 1 \times 10^{-10}$  F/cm and  $\sim 1 \times 10^{-12}$  F/cm which indicates they are an electrode effect, a grain boundary and a bulk response, respectively. With increasing Sr content, the bulk response starts to merge with the grain boundary response and eventually a single arc is observed for  $z = 0.20$ . The  $Z''$  and  $M''$  spectroscopic plots for the z-series samples are shown in Figure 6-26 (b). Two responses are observed in both the  $Z''$  and  $M''$  plots which are referred to as R1C1 (bulk) for the high frequency response and R2C2 (grain boundary) for the low frequency response. A significant change is observed in the  $M''$  spectroscopic where the  $M''$  peak for R1 decreases whereas the  $M''$  peak for R2 increases with increasing Sr content which means C1 increases whereas C2 decreases with increasing Sr content. In addition, the  $Z''$  of R2 also increases with increasing Sr content which indicates a more resistive grain boundary.

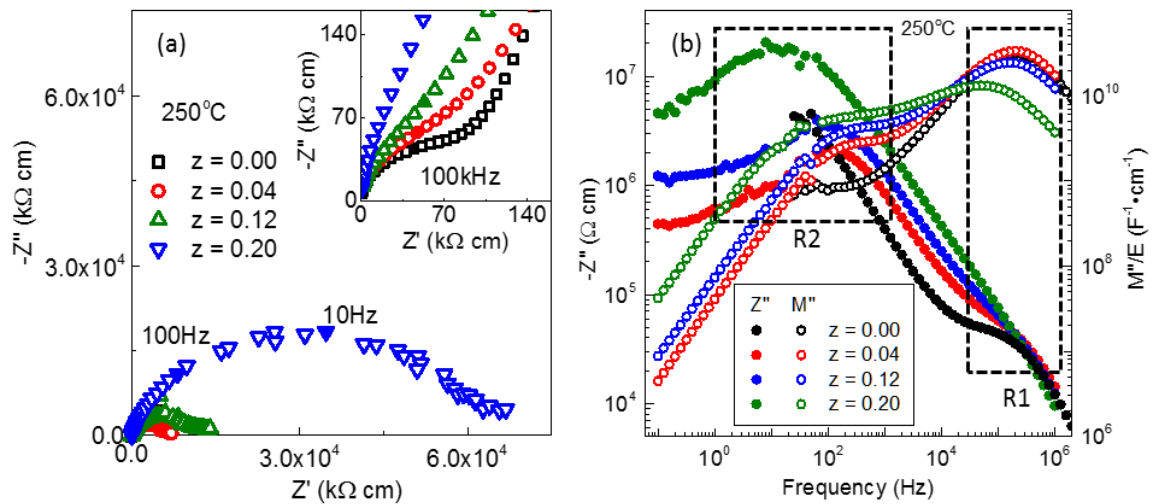


Figure 6-26. a)  $Z^*$  plots, and b)  $Z''$  and  $M''$  spectroscopic plots for  $0 \leq z \leq 0.20$  ceramics at 250 °C.

The influence of  $pO_2$  on the impedance response of  $z = 0.20$  is shown in Figure

6-27. The insert of Figure 6-27 (a) shows it is rather hard to decide the influence of  $pO_2$  on the bulk conductivity based on  $Z^*$  plots, therefore  $M''$  spectra were employed to extract the bulk resistivity (at 400 °C) which was calculated to be  $\sim 720 \Omega \cdot \text{cm}$  in  $N_2$  and  $1134 \Omega \cdot \text{cm}$  in  $O_2$  which indicates n-type bulk conduction.

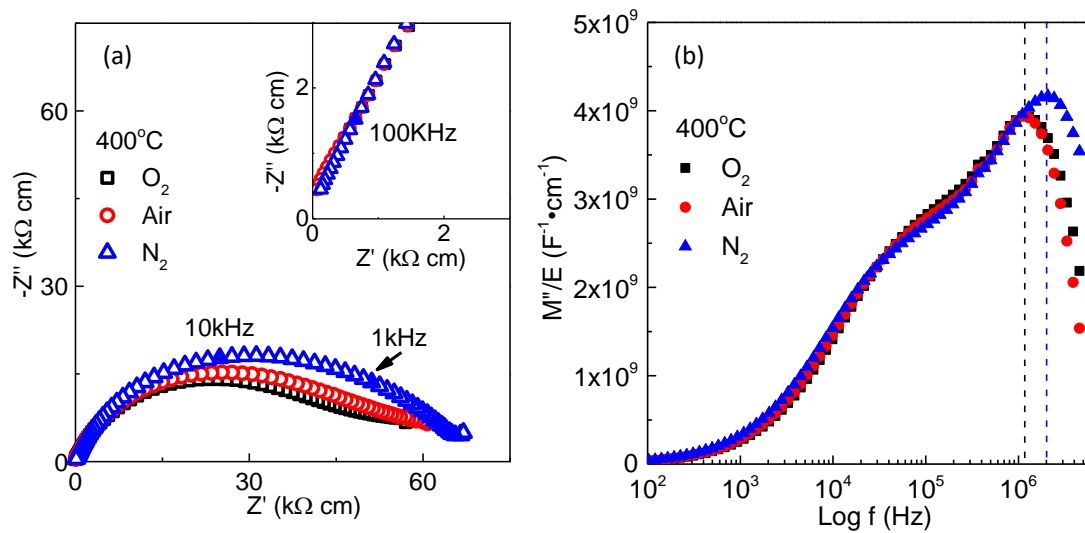


Figure 6-27. a)  $Z^*$  plots and b)  $M''$  spectroscopic plots for  $z = 0.20$  at 400 °C under different atmospheres.

The temperature dependent bulk conductivity of samples (extracted from  $M''$  data) in the  $z$ -series is summarised in an Arrhenius plot, Figure 6-28. For a low doping level ( $0 \leq z \leq 0.20$ ) the Sr-doped BiTs retain relatively high bulk conductivity with a small change in activation energy which increased from  $\sim 0.63$  eV for  $z = 0.00$  to  $\sim 0.8$  eV for Sr doped BiTs.

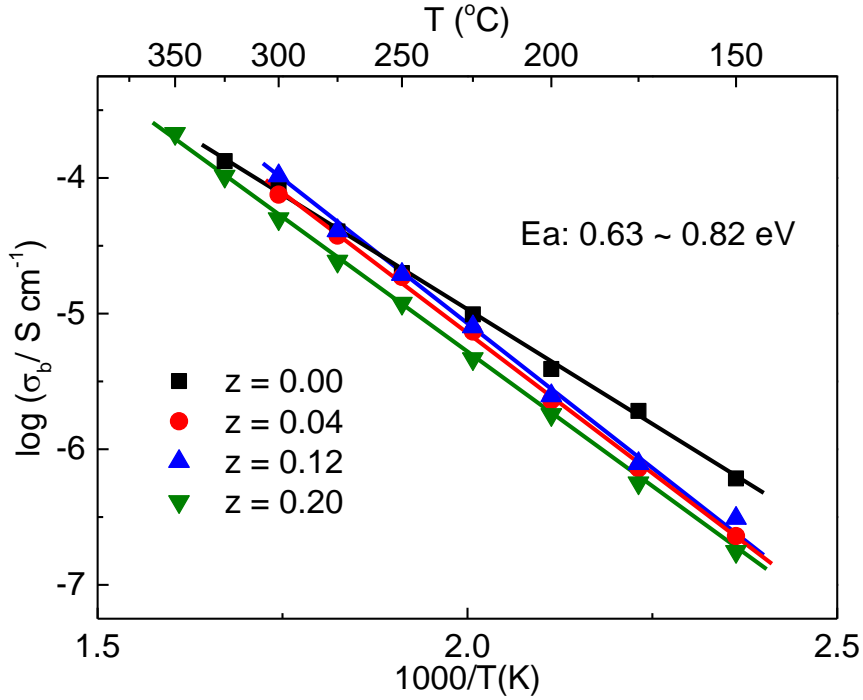
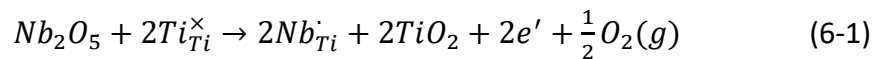


Figure 6-28. Arrhenius plot of bulk conductivity,  $\sigma_b$ , versus reciprocal temperature for Sr doped BiTs. Activation energy,  $E_a$ , values for  $\sigma_b$  are included.

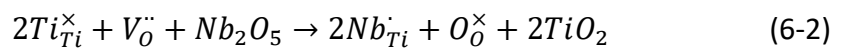
#### 6.4. Discussion

Nb doping on the Ti-site was used to suppress leakage current. The lattice parameters show an abnormal change when  $x = 0.250$  (Figure 6-2) is reached and SEM/EDX determine the existence of a pyrochlore-type phase at  $x = 0.250$  (Figure 6-3 and Table 6-1). The solid solution limit of the x series should therefore be in the range  $0.150 \leq x < 0.250$ .

Two different compensation mechanisms are possible in the x-series, either electronic doping



or ionic charge compensation:

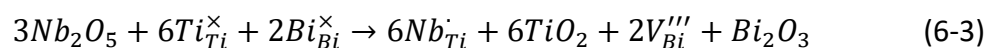


The experimental results reveal the bulk conductivity and  $\tan \delta$  decrease

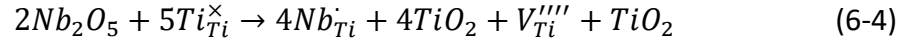
dramatically with Nb-doping, Figure 6-6 and Figure 6-9. Furthermore, the bulk activation energy for conduction of BiT with high levels of Nb doping is  $\sim 1.70$  eV indicating the conduction is predominately intrinsic electronic conduction. Therefore the ionic charge compensation mechanism (6-2) is adopted in the x-series. This is also supported by EMF measurements which show a significant decrease of  $t_{ion}$  at 700 °C from  $\sim 0.94$  for undoped BiT to  $\sim 0.23$  for  $x = 0.030$ , Figure 6-10.

The Nb content required to fully suppress the oxide ion conduction is in the range 0.01  $\sim$  0.03. It can be calculated that the oxygen non-stoichiometry in nominal stoichiometric BiT is in the range of 0.005  $\sim$  0.0150. However, unlike NBT, the Bi non-stoichiometry in BiT cannot be determined directly from this data since the existence of intrinsic oxygen vacancies in BiT has already been proposed in Chapter 5. Nevertheless, this result demonstrates the relative level of oxygen vacancies in BiT (0.42  $\sim$  1.25 %) is even lower than in NBT (0.83  $\sim$  1.67 ‰). Therefore the mobility of oxygen ions in BiT should also be very high to promote such high oxygen ion conductivity.

With a further increase of Nb doping level the activation energy for bulk conduction remains close to half the intrinsic band gap value and no sign of any significant increase of bulk conductivity was observed, Figure 6-9. This indicates the absence of any electronic compensation mechanism (6-1). From this point of view, the excess Nb beyond the required amount to fill the oxygen vacancies may take another mechanism different from (6-1) and (6-2). For example, cation vacancies can also compensate the charge difference between  $Nb^{5+}$  and  $Ti^{4+}$  while not introduce any significant variation in bulk conductivity such as



or



The secondary phases produced by these two mechanisms ( $Bi_2O_3$  and  $TiO_2$ ) could exist but below the detectable limit of XRD and SEM/EDX, therefore not shown in the observed results. Thus the doping mechanism(s) at higher Nb levels remain unknown. Further structural studies and the detection of low levels of secondary phases will require neutron diffraction and TEM to gain a full understanding about the doping mechanism(s) in Nb-doped BiT.

La-doping on the Ti-site was adopted in this project to reduce  $T_C$  to obtain a higher  $t_{ion}$  at lower temperature. It is known that the solid solution limit of La-doping in BiT is high. In general, the reported solid solution limit for La-doping has a value  $y \geq 2$ .<sup>10,11</sup> The highest doping level adopted in this project was  $y = 2.00$  and all samples were single-phase by XRD and SEM/EDX, Figure 6-11 and Table 6-2. The only exception is the EDX result for  $x = 0.150$  which shows a relatively larger deviation between the observed and theoretical value. The origin(s) of this error is currently unknown but may be due to inter growth of a phase with a high La content. LCR results show that La-doping can effectively lower  $T_C$  (Figure 6-14 and Figure 6-15), however, the downside of La-doping is the bulk conductivity of BiT also decreases with increasing La content as shown in Figure 6-18. The bulk conductivity systematically decreases with increasing La-content whereas the activation energy of all samples in the  $y$ -series remains similar and in the range  $0.63 \sim 0.76$  eV which indicates the conduction mechanism is unchanged, Figure 6-18.

For a material, its conductivity can be calculated as

$$\sigma = nq\mu$$

where  $n$  is the charge carrier concentration,  $q$  is the electrical charge of charge carrier

and  $\mu$  is the mobility of the charge carrier. Since the conduction mechanism is unchanged, the type of charge carrier ( $q$ ) should remain unchanged. Therefore a smaller  $n$  and/or  $\mu$  is expected to be responsible for the reduced bulk conductivity. It is well known in the literature to use La-doping to suppress leakage current in BiT since it is less volatile and can improve the chemical stability of the adjacent oxide ions to suppress the formation of oxygen vacancies.<sup>12</sup> In other words, the charge carrier concentration  $n$  is reduced in this case. However, as discussed above and in Chapter 5, the Bi-loss during processing is only partially responsible for the oxygen vacancies. Therefore the cation polarisability and weak Bi-O bonds of Bi ion which enhance the mobility of the oxide ion ( $\mu$ ) and is an important factor and may be a more dominant factor than the volatility of Bi ( $n$ ) in terms of leading to oxide ion conduction in BiT. The effect of reduced bulk conductivity can be the result of a combination of the two above mentioned mechanisms.

EMF results show that with 12.5 at% La doping ( $y = 0.50$ ,  $T_C \sim 490$  °C) the  $t_{ion}$  at 600 °C has increased from  $\sim 0.77$  to  $\sim 0.93$  which confirms the maximum  $t_{ion}$  is related to the phase transition temperature, Figure 6-19. The LCR result shows  $T_C$  for  $y = 0.50$  is  $\sim 490$  °C also, as discussed in Chapter 5, the maximum  $t_{ion}$  of BiT may related to the *Cmca* intermediate phase. Since  $t_{ion}$  for  $y= 0.50$  at 600 °C is still high ( $\sim 0.93$ ), therefore this existence range of this intermediate phase may extended by La doping. Further structure studies such as neutron diffraction are required to prove this assumption.

This improvement made La-doped BiT a potential good electrolyte material for intermediate temperature SOFCs. However, as discussed above, the drawback of La-doped BiT to be used as an electrolyte material is the decreasing bulk conductivity with increasing La content. Figure 6-29 shows the  $T_C$  and bulk conductivity at 300 °C with different La contents. A linear function was used to simulate the trend of bulk conductivity whereas a single exponential decay function was used for  $T_C$ . The results

show to obtain a  $T_c = 600\text{ }^\circ\text{C}$ ,  $y = 0.22$  is required. With  $y = 0.22$  the bulk conductivity at  $300\text{ }^\circ\text{C}$  is reduced to  $\sim 45\%$  of the bulk conductivity of  $y = 0.00$ . Since the activation energy for all  $y$ -series samples are relatively similar to each other, it can be reasonable estimated at  $600\text{ }^\circ\text{C}$  the bulk conductivity of  $y = 0.22$  is still  $\sim 45\%$  of  $x = 0$ . As shown in figure 5-23 in Chapter 5, the estimated bulk conductivity for  $y = 0$  at  $600\text{ }^\circ\text{C}$  is  $\sim 8.7 \times 10^{-3}\text{ S/cm}$ , therefore the bulk conductivity at  $600\text{ }^\circ\text{C}$  for  $y = 0.22$  is  $\sim 3.9 \times 10^{-3}\text{ S/cm}$  which is comparable to those of the best electrolyte material at  $600\text{ }^\circ\text{C}$  such as LSGM ( $\sim 3.2 \times 10^{-2}\text{ S/cm}$ ) and YSZ ( $\sim 3 \times 10^{-2}\text{ S/cm}$ ).<sup>13</sup> However, all these numbers are estimated based on low temperature data because the bulk response is beyond the measurement window at high temperatures (e.g.  $600\text{ }^\circ\text{C}$ ). Further work is therefore still required to overcome the influence of the electrical microstructures (i.e. resistive thin layer effects) associated with BiT-based ceramics if they are to be considered as potentially useful electrolytes for ITSOFCs.

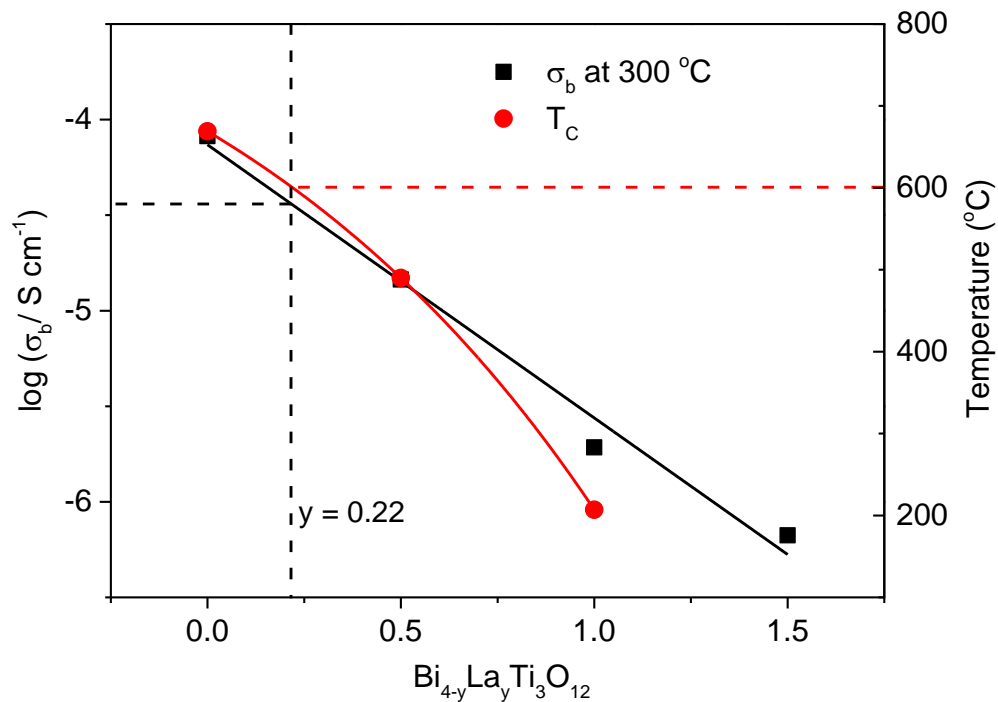
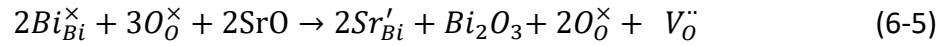
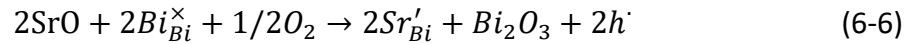


Figure 6-29. The variation of bulk conductivity at  $300\text{ }^\circ\text{C}$  and  $T_c$  versus  $y$  in  $\text{Bi}_{4-y}\text{La}_y\text{Ti}_3\text{O}_{12}$  ceramics.

Since the larger La ion doping on the Bi-site can significantly decrease  $T_C$  of BiT, the Sr ion which possesses a larger size and lower valence compared to the Bi ion may therefore be employed to replace Bi to reduce  $T_C$  as well as to generate more oxygen vacancies according to the equation:



or an electronic acceptor-doping mechanism is also possible:



For the z-series of samples, a  $Bi_2O_3$  secondary phase is observed in both XRD and SEM/EDX results for  $z = 0.40$ , Figure 6-20 and Figure 6-22. However, an abnormality in the lattice parameters is observed for  $z = 0.20$  and a similar  $T_{Er,max}$  exists for  $z = 0.12$  and  $0.20$  therefore suggesting the solid solution limit should be between  $z = 0.12$  and  $0.20$ , Figure 6-21.

Impedance results demonstrate the bulk conductivity of the z-series samples remains relatively similar from  $z = 0.00$  to  $0.20$ , whereas the activation energy increased slightly from  $\sim 0.63$  eV for  $z = 0.00$  to  $\sim 0.82$  eV for  $z = 0.20$ , Figure 6-28. Compared with the y-series, in both series the activation energy increased and  $T_C$  decreased with doping. However, the bulk conductivity remains unchanged with low levels of Sr doping. From the viewpoint of bulk conductivity, Sr-doping has only a minor influence on the bulk conductivity which excludes the possibility of an electronic acceptor-doping mechanism. Therefore the fact that bulk conductivity of BiT remain unchanged indicates either the generated oxygen vacancies have only little contribution to the oxide ion conduction or the additional Sr causes intergrowths of other phase(s) that have been undetected by XRD and SEM/EDX. For the former explanation, the generated oxygen vacancies may interact strongly with the Sr dopant and get trapped therefore have no contribution to the bulk conductivity. For the latter explanation, the intergrowth of Aurivillius phase(s) such as  $SrBi_4Ti_4O_{15}$  and  $Sr_4Bi_4Ti_7O_{24}$  can be formed which left the bulk composition unchanged.<sup>14,15</sup> Again, structural

studies and in-depth phase analysis using neutron diffraction and TEM are required in order to gain a better understanding of the Sr-doping mechanism(s) in BiT.

In general, all three dopants discussed in this chapter achieve the desired purpose for them. As discussed above, in order to be used as an electrolyte material, the two most important properties for BiT are the bulk conductivity  $\sigma_b$  and the Curie temperature  $T_C$  where  $t_{ion}$  is close to unity. From the three different dopants, it can be observed that a larger sized dopant on the Bi-site can effectively reduce  $T_C$  (La, Sr); the solid solution limit for aliovalent dopants is rather limited (Nb, Sr) and the cation polarisability and weak Bi-O bonds of Bi ion is more important than the oxygen vacancies generated by Bi-loss during processing in term of oxide ion conduction in BiT (Nb, La).

## 6.5. Conclusions

BiT is potentially a good electrolyte and ferroelectric material. La-doping on the Bi-site can be used to lower  $T_C$  and makes BiT a potentially good oxygen ion conductor at lower temperatures. Sr-doping can also be used to lower  $T_C$  while maintaining the bulk conductivity but the solid solution window is rather limited ( $z < 0.20$ ) compared to La. Nb-doping on the Ti-site can eliminate oxygen vacancies and minimise the leakage conduction to provide excellent BiT-based dielectric materials.

## 6.6. References

1. Roy, M., Bala, I., Barbar, S. K., Jangid, S. & Dave, P. Synthesis, structural and electrical properties of La and Nb modified  $\text{Bi}_4\text{Ti}_3\text{O}_{12}$  ferroelectric ceramics. *J. Phys. Chem. Solids* **72**, 1347–1353 (2011).
2. Duran-Martin, P. & Voisard, C. Study and control of the conductivity of Nb-doped  $\text{Bi}_4\text{Ti}_3\text{O}_{12}$  for high temperature piezoelectric applications. *Boletín la Soc. ...* **582**, (1999).

3. Shulman, H. S., Damjanovic, D. & Setter, N. Niobium Doping and Dielectric Anomalies in Bismuth Titanate. *J. Am. Ceram. Soc.* **83**, 528–532 (2004).
4. Park, B. H. *et al.* Lanthanum-substituted bismuth titanate for use in non-volatile memories. *Nature* **401**, 682–684 (1999).
5. Jiang, a. Q., Hu, Z. X. & Zhang, L. D. The induced phase transformation and oxygen vacancy relaxation in La-modified bismuth titanate ceramics. *Appl. Phys. Lett.* **74**, 114–116 (1999).
6. Shimazu, M., Tanaka, J., Muramatsu, K. & Tsukioka, M. Phase transition in the family  $\text{La}_x\text{Bi}_{4-x}\text{Ti}_3\text{O}_{12}$ : In relation to lattice symmetry and distortion. *Journal of Solid State Chemistry* **35**, 402–406 (1980).
7. Shulman, H. S., Testorf, M., Damjanovic, D. & Setter, N. Microstructure, Electrical Conductivity, and Piezoelectric Properties of Bismuth Titanate. *J. Am. Ceram. Soc.* **79**, 3124–3128 (1996).
8. Gu, H. *et al.* Synthesis and optical properties of highly c-axis oriented  $\text{Bi}_4\text{Ti}_3\text{O}_{12}$  thin films by sol-gel processing. *Thin Solid Films* **283**, 81–83 (1996).
9. Goto, T., Noguchi, Y., Soga, M. & Miyayama, M. Effects of Nd substitution on the polarization properties and electronic structures of bismuth titanate single crystals. *Mater. Res. Bull.* **40**, 1044–1051 (2005).
10. Frit, B. & Mercurio, J. P. The crystal chemistry and dielectric properties of the Aurivillius family of complex bismuth oxides with perovskite-like layered structures. *J. Alloys Compd.* **188**, 27–35 (1992).
11. Newnham, R. E., Wolfe, R. W. & Dorrian, J. F. Structural basis of ferroelectricity in the bismuth titanate family. *Mater. Res. Bull.* **6**, 1029–1039 (1971).
12. Kim, S. J. *et al.* Direct observation of oxygen stabilization in layered ferroelectric  $\text{Bi}_{3.25}\text{La}_{0.75}\text{Ti}_3\text{O}_{12}$ . *Appl. Phys. Lett.* **91**, 62913 (2007).
13. Ishihara, T., Sammes, N. M. & Yamamoto, O. in *High Temperature and Solid*

*Oxide Fuel Cells* 83–117 (Elsevier, 2003). doi:10.1016/B978-185617387-2/50021-0

14. Hervoche, C. H. *et al.* Structural Behavior of the Four-Layer Aurivillius-Phase Ferroelectrics  $\text{SrBi}_4\text{Ti}_4\text{O}_{15}$  and  $\text{Bi}_5\text{Ti}_3\text{FeO}_{15}$ . *J. Solid State Chem.* **164**, 280–291 (2002).
15. Zurbuchen, M. A. *et al.* Synthesis, structure, and electrical behavior of  $\text{Sr}_4\text{Bi}_4\text{Ti}_7\text{O}_{24}$ . *J. Appl. Phys.* **107**, 24106 (2010).

## 7. Non-stoichiometry in the perovskite phase

### ' $K_{0.5}Bi_{0.5}TiO_3$ '

$K_{0.5}Bi_{0.5}TiO_3$ , KBT, is a ferroelectric material which possesses a mixed A-site perovskite structure similar to NBT with Na replaced by K. However, the crystal structure is much simpler for KBT than NBT and its phase transformations are similar to  $BaTiO_3$  and not as complex as NBT.<sup>1-3</sup> On heating, KBT changes from a tetragonal ( $P4mm$ ) cell to a Cubic cell ( $Pm-3m$ ) at  $\sim 380$  °C.<sup>4</sup> KBT has been widely studied as a candidate for ferroelectric and piezoelectric applications due to its relatively high  $T_C$ .<sup>5-9</sup> Since K is in the same group as Na in the periodic table it shares a lot of similar properties in many aspects. Therefore oxide ion conduction with a mechanism similar to NBT may be expected to occur in KBT. In this project the potential of KBT as an oxide ion conductor has been investigated.

As discussed in Chapter 3, the electrical properties of NBT are highly sensitive to low levels of Na and Bi non-stoichiometry. Thus the effect of both Bi and K non-stoichiometry on the electrical properties of KBT have been studied. In this chapter, Bi non-stoichiometric samples with general formula  $K_{0.5}Bi_{0.5+x}TiO_{3+3x/2}$  ( $-0.01 \leq x \leq 0.01$ ) are referred to as x-series samples whereas K non-stoichiometric samples with general formula  $K_{0.50+y}Bi_{0.50}TiO_{3+1/2y}$  ( $-0.01 \leq y \leq 0.05$ ) are referred to as y-series samples.

In this project, micron-sized  $TiO_2$  reagent powder (the same as used for the NBT synthesis) was initially used as a starting material to synthesise KBT. However, the density of the obtained ceramics via the solid state route was rather poor ( $\sim 80$  % of theoretical density) and dense pellets are required for EMF measurements to prevent any gas leakage through porosity. In the literature, a prolonged dwelling time for sintering ( $\geq 20$  hours) is normally reported to obtain dense KBT ceramics but the volatility of both  $K_2O$  and  $Bi_2O_3$  makes it hard to control the final stoichiometry using

such prolonged dwelling periods. Therefore nano-sized  $\text{TiO}_2$  reagent powder was used in an attempt to obtain dense KBT ceramics. In this case, subscripts are used to distinguish KBT ceramics prepared from the two different kinds of  $\text{TiO}_2$  starting material. For example,  $x_{\text{nano}}$  and  $x_{\text{micro}}$  indicate x-series samples prepared with nano- and micron-sized  $\text{TiO}_2$  powder, respectively.

## 7.1. Phase purity and microstructure

### 7.1.1.x-series samples

A combination of XRD and SEM/EDX was employed to determine the phase purity and microstructure of the x-series ceramics. XRD patterns obtained from crushed ceramics are shown in Figure 7-1. For all x-series samples (either prepared using nano-sized or micron-sized  $\text{TiO}_2$  powders), all reflections are consistent with the tetragonal  $P4mm$  structure of KBT at room temperature with no additional reflections.

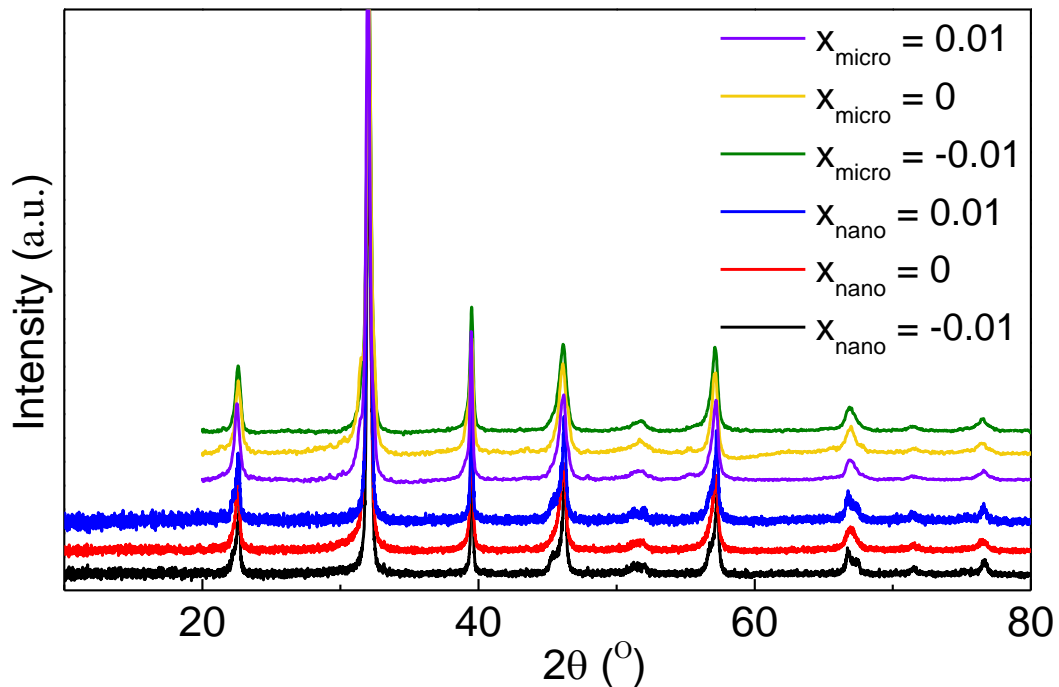


Figure 7-1. Room temperature X-ray powder diffraction data of crushed pellets for the  $x_{\text{nano}}$ -series ceramics.

The lattice parameters for  $x_{\text{nano}}$ -series samples are shown in Figure 7-2. The lattice parameters for  $x_{\text{nano}} = 0$  and 0.01 are relatively similar whereas  $x_{\text{nano}} = -0.01$  possesses a smaller  $a$  and a larger  $c$ .

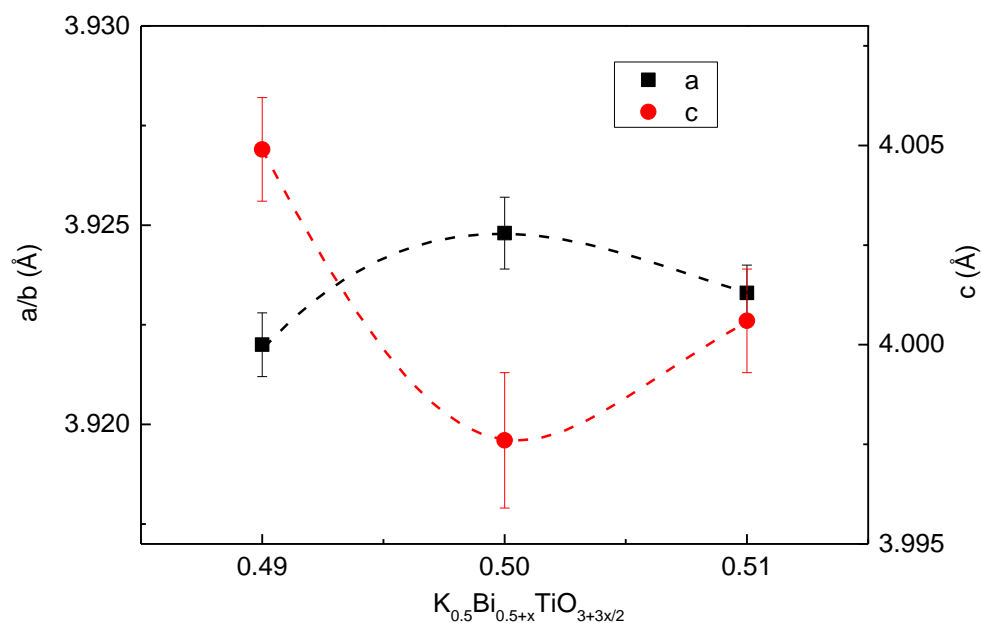


Figure 7-2. Lattice parameters  $a$ ,  $b$  and  $c$  versus  $x$  content for  $x_{\text{nano}}$ -series crushed ceramics.

A combination of SEM and EDX reveals there are secondary phases present (Figure 7-5 and Figure 7-6). For  $x_{\text{nano}}$ -series samples, a rod shaped secondary phase was observed in all three compositions by SEM, as shown in Figure 7-5. EDX results show the secondary phase has a high K and Bi content with a K:Bi ratio of 1:3 and very limited Ti content (Table 7-1). To the best of our knowledge, the only oxide consistent with this ratio is  $\text{K}_2\text{Ti}_6\text{O}_{13}$ . It is worth to note that SEM shows a relatively large amount of this  $\text{K}_2\text{Ti}_6\text{O}_{13}$  phase distributed on the observed surface; it is hard to understand why the XRD pattern of crushed pellets do not show reflections from this phase. The natural surface of sintered pellets of all three compositions in the  $x$ -series were then measured using XRD. The results show the presence of  $\text{K}_2\text{Ti}_6\text{O}_{13}$  in all of them (Figure 7-3) and the reflections from  $\text{K}_2\text{Ti}_6\text{O}_{13}$  can be significantly reduced by a gentle polish of the

pellet surface (Figure 7-4). Combined with the crushed pellet results, it shows that the  $K_2Ti_6O_{13}$  phase primarily exists as a thin layer close to the surface of the KBT pellets and the volume fraction of this secondary phase in the ceramics is rather low.

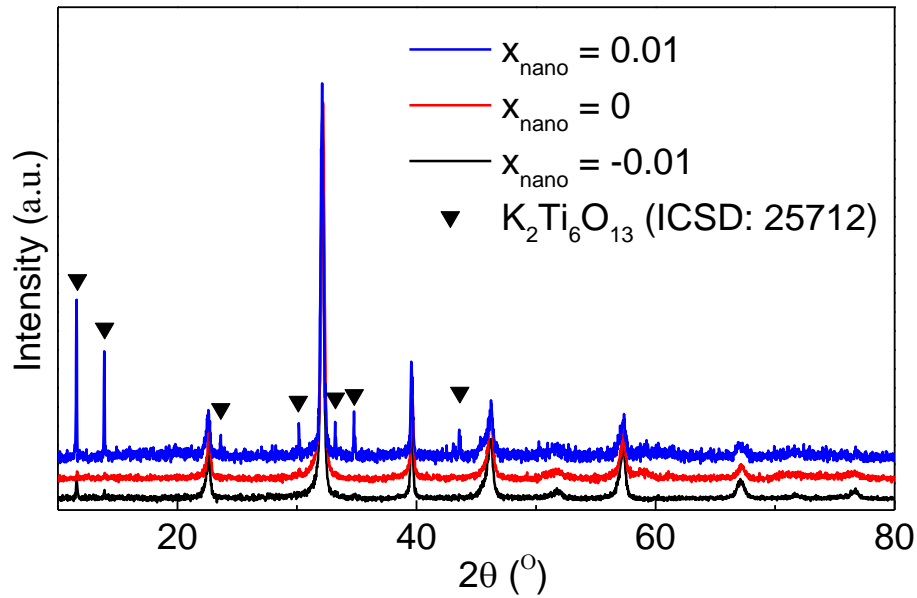


Figure 7-3. Room temperature X-ray diffraction data of pellet surfaces for the  $x_{nano}$ -series.

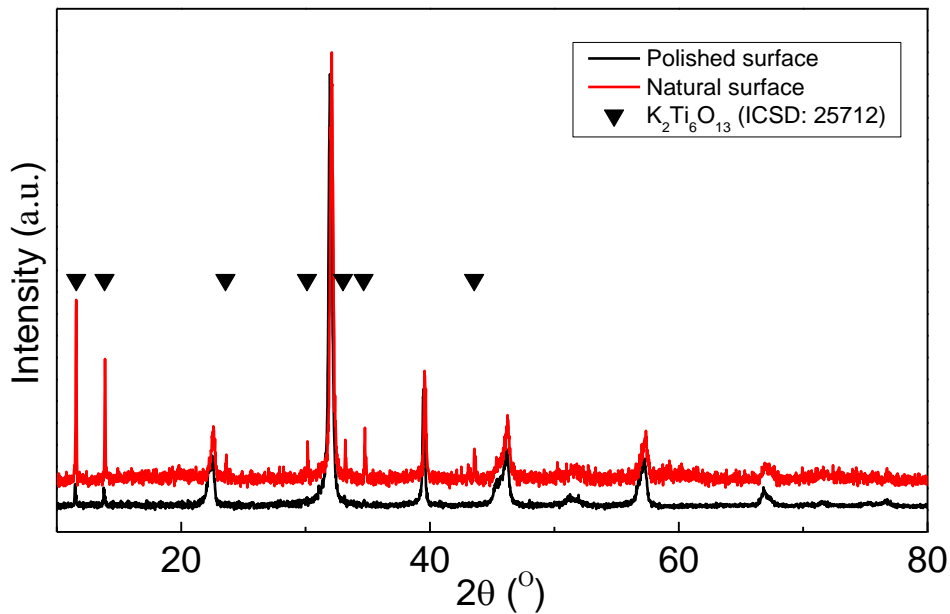


Figure 7-4. A comparison of a natural surface and a polished surface of  $x_{nano} = 0.01$ .

For the  $x_{\text{micro}}$ -series samples, the SEM images show a significant amount of porosity (Figure 7-6), especially for  $x_{\text{micro}} = 0$  and 0.01 which indicates a low density. The  $\text{K}_2\text{Ti}_6\text{O}_{13}$  phase has also been observed in the  $x_{\text{micro}}$ -series with a similar morphology as in the  $x_{\text{nano}}$ -series but with a much finer size.

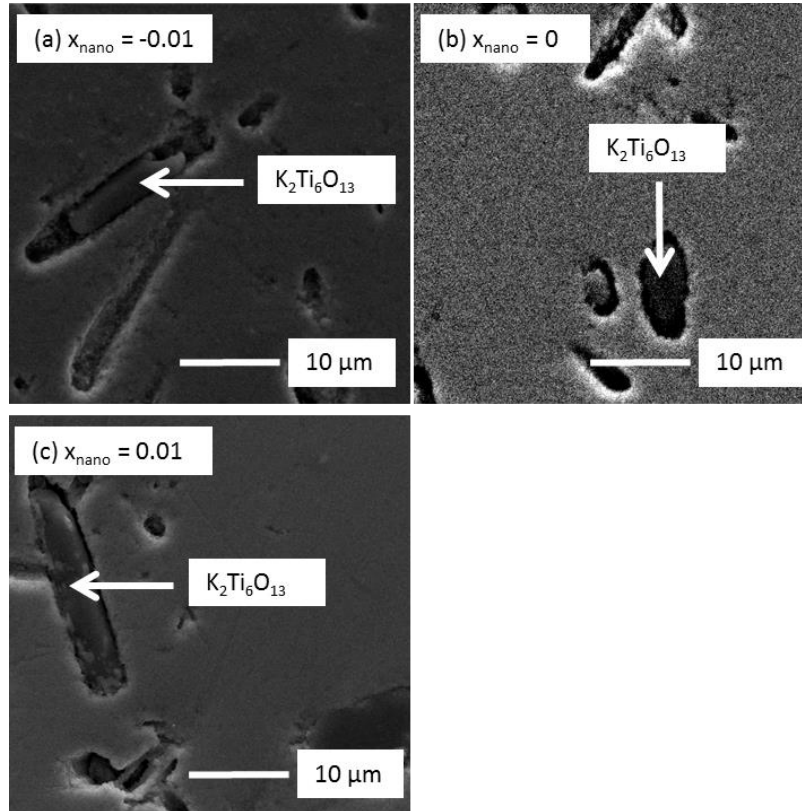


Figure 7-5. SEM Secondary electron images for (a)  $x = -0.01$ , (b)  $x = 0.00$ , (c)  $x = 0.01$  for  $x_{\text{nano}}$ -series ceramics. (Polished without thermal etching)

The unpolished (natural) surfaces of as-sintered pellets have been used to determine the grain size and morphology instead of polished and thermal etched ceramics because the KBT grain growth is very slow even with thermal etching at the sintering temperature. The grain size of KBT ceramics prepared with nano-sized  $\text{TiO}_2$  is significantly smaller compared to NBT and BiT. For samples in this series, the grain sizes vary in the range 50 ~ 500 nm and show no significant difference between ceramics with different starting composition. The morphology of KBT grains remains cuboid-like for all samples (Figure 7-7).

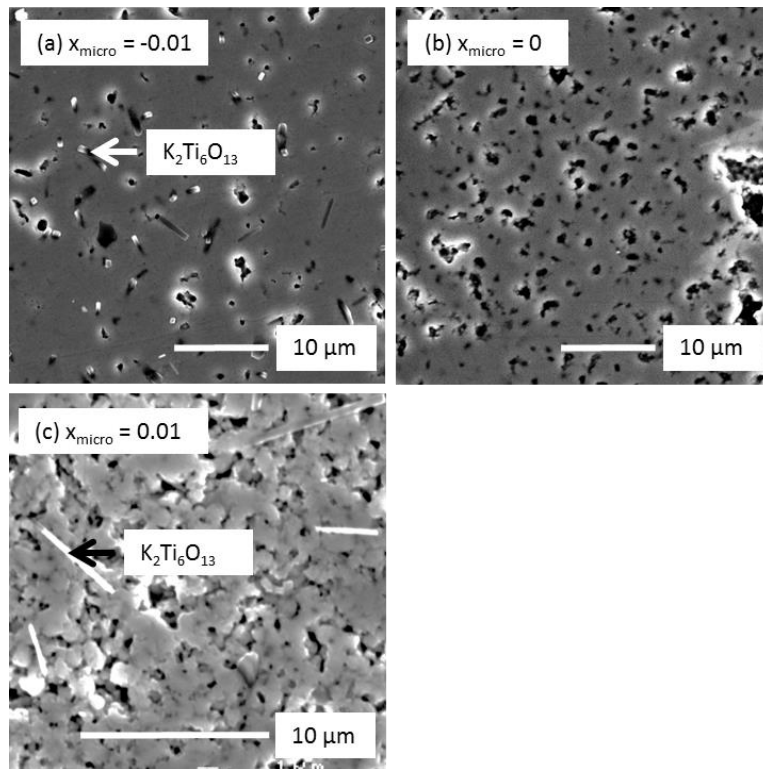


Figure 7-6. SEM Secondary electron images for (a)  $x = -0.01$ , (b)  $x = 0.00$ , (c)  $x = 0.01$  for  $x_{\text{micro}}$ -series ceramics. (Polished without thermal etching)

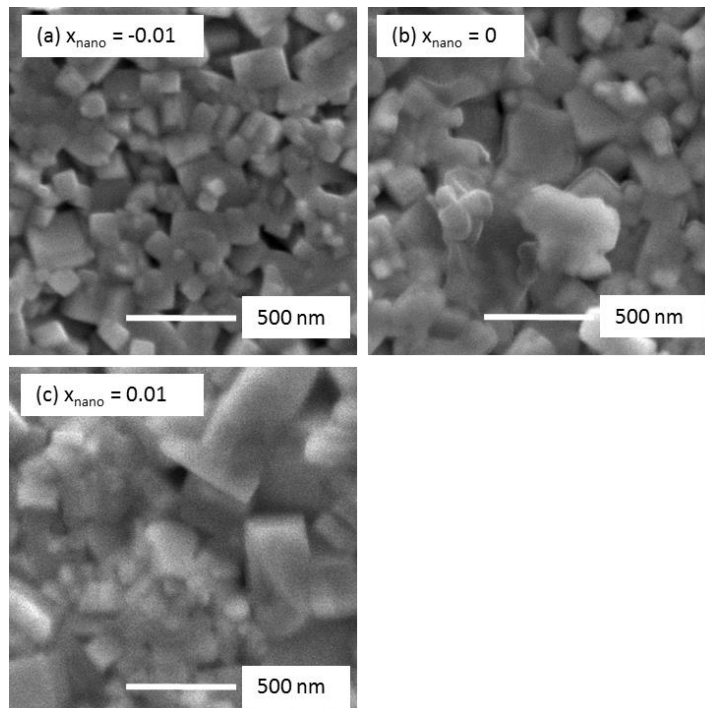


Figure 7-7. SEM micrographs for (a)  $x_{\text{nano}} = -0.01$ , (b)  $x_{\text{nano}} = 0.00$ , (c)  $x_{\text{nano}} = 0.01$  pellet (natural surfaces).

Table 7-1. Chemical composition (relative cation at%) of the main phase and associated error (standard deviation) by SEM/EDX of selected samples in the  $x_{\text{nano}}$ -series.

Composition		Bi (at%)	Ti (at%)	K (at%)
$x_{\text{nano}} = -0.01$	Main phase	26.6 ( $\pm 0.3$ )	48.4 ( $\pm 1.2$ )	25.0 ( $\pm 1.1$ )
	$\text{K}_2\text{Ti}_6\text{O}_{13}$	1.9 ( $\pm 0.5$ )	73.0 ( $\pm 0.5$ )	25.1 ( $\pm 0.2$ )
$x_{\text{nano}} = 0$	Main phase	26.2 ( $\pm 0.4$ )	48.4 ( $\pm 1.4$ )	25.3 ( $\pm 1.5$ )
	$\text{K}_2\text{Ti}_6\text{O}_{13}$	1.5 ( $\pm 0.6$ )	73.9 ( $\pm 0.9$ )	24.6 ( $\pm 0.9$ )
$x_{\text{nano}} = 0.01$	Main phase	26.9 ( $\pm 0.4$ )	47.4 ( $\pm 0.8$ )	25.7 ( $\pm 0.6$ )
	$\text{K}_2\text{Ti}_6\text{O}_{13}$	1.4 ( $\pm 0.8$ )	74.2 ( $\pm 0.7$ )	24.4 ( $\pm 1.2$ )
$\text{K}_{0.5}\text{Bi}_{0.5}\text{TiO}_3$		25	50	25
$\text{K}_2\text{Ti}_6\text{O}_{13}$		0	75	25

### 7.1.2. $\gamma$ -series samples

XRD patterns of crushed pellets in the  $\gamma$ -series showed no evidence of any secondary phases, all observed reflections can be indexed on the tetragonal  $P4mm$  structure (Figure 7-8). The lattice parameters (Figure 7-9) for  $\gamma_{\text{nano}} = 0$  and 0.02 are relatively similar to each other whereas  $\gamma_{\text{nano}} = -0.01$  possess a much smaller  $c$ .

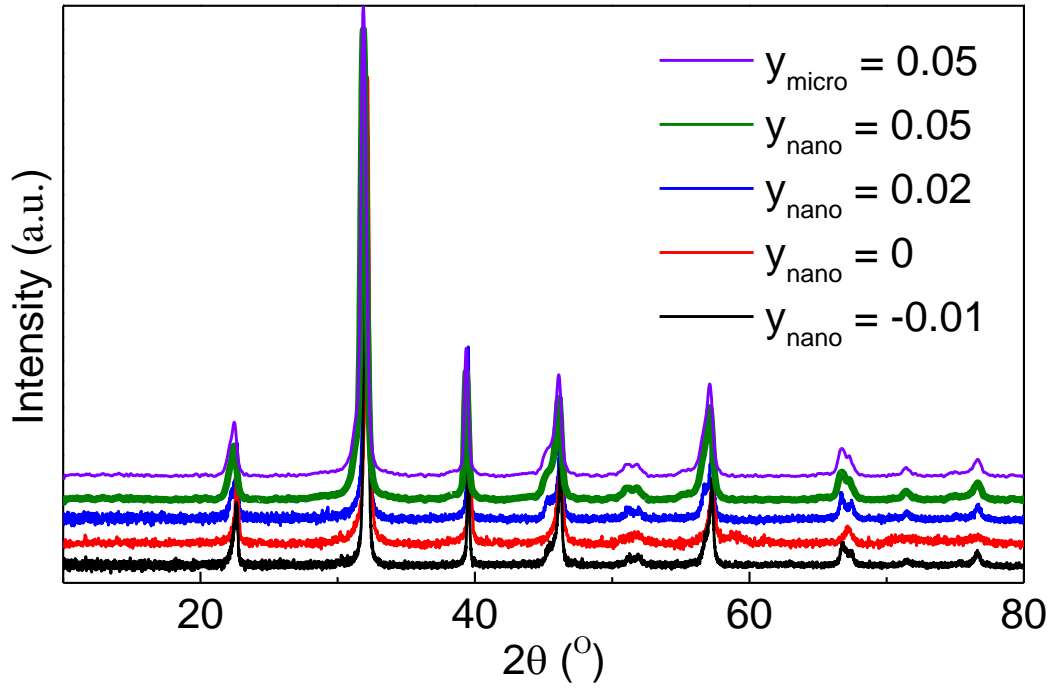


Figure 7-8. Room temperature X-ray powder diffraction data for y-series ceramics.

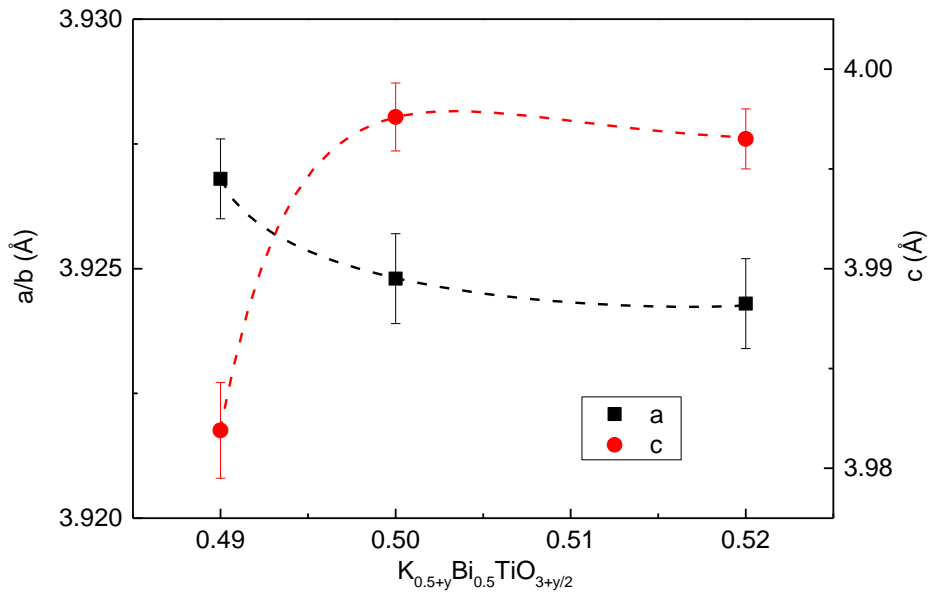


Figure 7-9. Lattice parameters  $a$ ,  $b$  and  $c$  versus  $x$  content for  $y_{\text{nano}}$ -series crushed ceramics.

On the other hand, similar to the x-series samples, SEM and EDX detected the existence of  $\text{K}_2\text{Ti}_6\text{O}_{13}$  in the surface layer of KBT which is not observed in the XRD patterns of crushed pellets (Figure 7-10).  $y_{\text{micro}}$ -series ceramics also show a more

porous structure than  $\gamma_{\text{nano}}$ -series ceramics. The bulk composition of  $\gamma_{\text{nano}}$ -series ceramics again remains almost unchanged for ceramics with different starting compositions (Table 7-2). The average grain size of the  $\gamma_{\text{nano}}$ -series samples was not influenced by the starting composition which is about 50 ~ 500 nm for both K-rich and K-deficient samples (Figure 7-11).

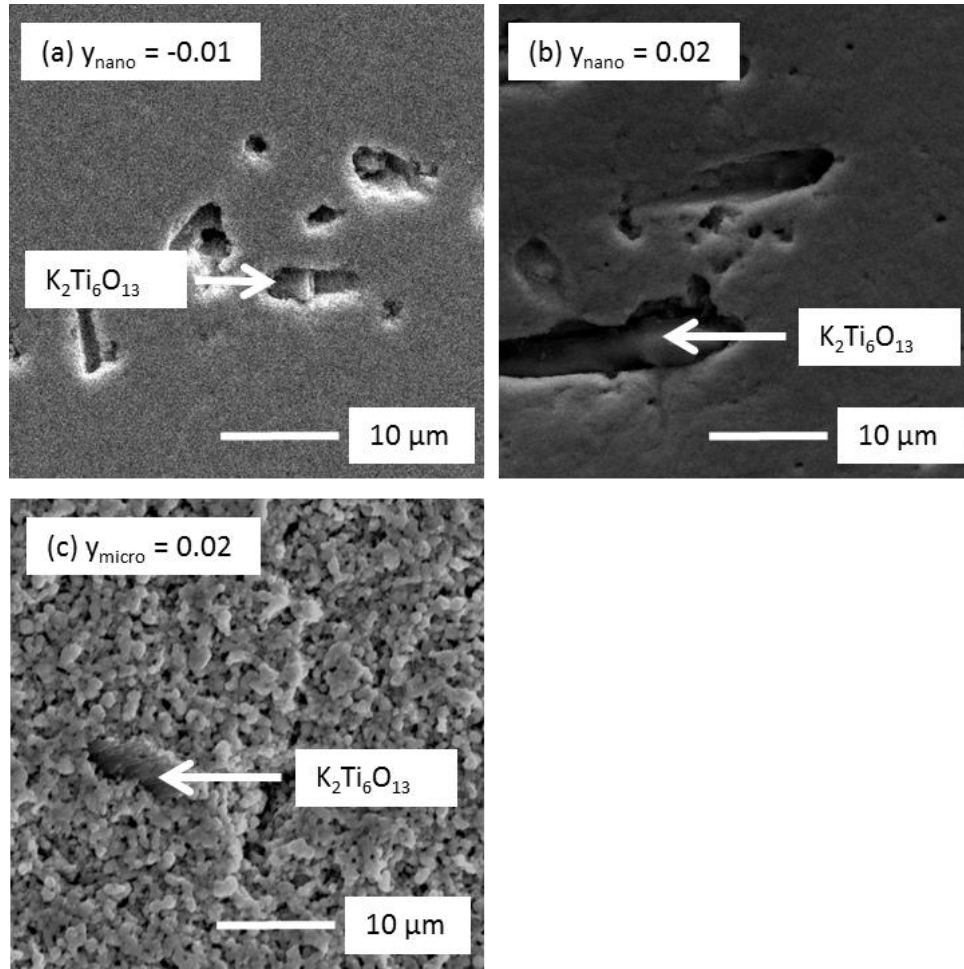


Figure 7-10. SEM images for (a)  $\gamma_{\text{nano}} = -0.01$ , (b)  $\gamma_{\text{nano}} = 0.02$  and (c)  $\gamma_{\text{micro}} = 0.02$  (polished without thermal etching) showing the  $\text{K}_2\text{Ti}_6\text{O}_{13}$  secondary phase.

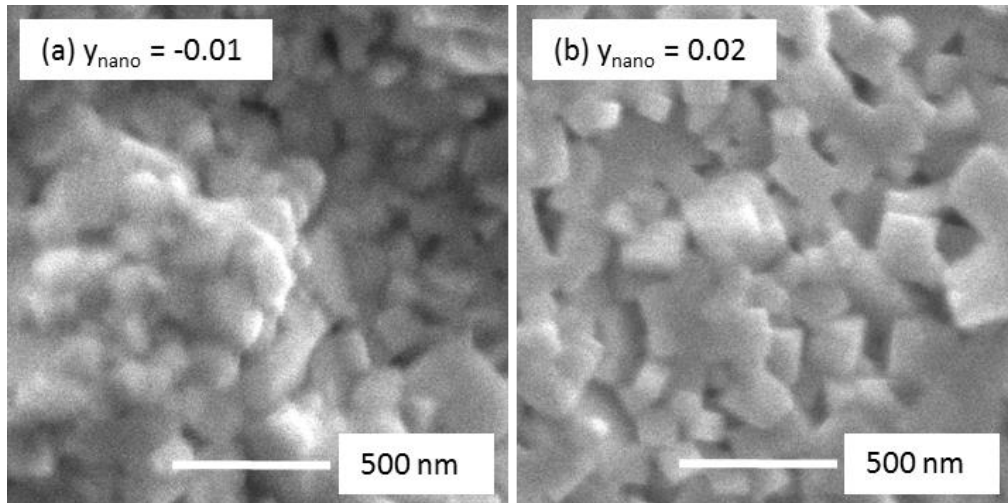


Figure 7-11. SEM micrographs of (a)  $y_{\text{nano}} = -0.01$  and (b)  $y_{\text{nano}} = 0.02$  pellet (natural) surfaces.

Table 7-2. Bulk chemical composition (relative cation at%) and associated error (standard deviation) by SEM/EDX of the main and secondary phases present in selected  $y$ -series ceramics.

Composition		Bi (at%)	Ti (at%)	K (at%)
$y_{\text{nano}} = -0.01$	Main phase	26.3 ( $\pm 0.3$ )	48.6 ( $\pm 0.9$ )	25.1 ( $\pm 0.5$ )
	$\text{K}_2\text{Ti}_6\text{O}_{13}$	1.4 ( $\pm 0.5$ )	73.6 ( $\pm 0.4$ )	25.0 ( $\pm 0.2$ )
$y_{\text{nano}} = 0$	Main phase	26.2 ( $\pm 0.4$ )	48.4 ( $\pm 1.4$ )	25.3 ( $\pm 1.5$ )
	$\text{K}_2\text{Ti}_6\text{O}_{13}$	1.5 ( $\pm 0.6$ )	73.9 ( $\pm 0.9$ )	24.6 ( $\pm 0.9$ )
$y_{\text{nano}} = 0.02$	Main phase	26.4 ( $\pm 0.2$ )	47.6 ( $\pm 0.2$ )	26.0 ( $\pm 0.2$ )
	$\text{K}_2\text{Ti}_6\text{O}_{13}$	3 ( $\pm 2$ )	71 ( $\pm 4$ )	26 ( $\pm 2$ )
$\text{K}_{0.5}\text{Bi}_{0.5}\text{TiO}_3$		25	50	25
$\text{K}_2\text{Ti}_6\text{O}_{13}$		0	75	25

## 7.2. Electrical properties

The temperature dependence of permittivity,  $\epsilon_r$  and dielectric loss,  $\tan \delta$  are shown in

Figure 7-12. For  $x_{\text{micro}}$ -series, a permittivity peak was observed which corresponds to the Curie temperature,  $T_C$ , whereas for  $x_{\text{nano}}$ -series, the peak is much lower and broadened. As shown in Figure 7-13, the maximum permittivity,  $\epsilon_{r,\text{max}}$  for  $x_{\text{micro}} = -0.01$ , 0 and 0.01 are  $\sim 2000$ , 3700 and 3400, respectively. The corresponding temperature,  $T_{\epsilon_r,\text{max}}$  is  $\sim 375$  °C for  $x_{\text{micro}} = 0$  and increased to 385 and 392 °C for  $x_{\text{micro}} = -0.01$  and 0.01. On the other hand, the value for the lower temperature peak in the  $x_{\text{nano}}$ -series samples was only half of the  $x_{\text{micro}}$ -series with a value  $\sim 1800$  for  $x_{\text{nano}} = 0$  and 0.01 whereas it decreased to  $\sim 1500$  for  $x = -0.01$  (Figure 7-13 (c)). It is rather hard to decide  $T_{\epsilon_r,\text{max}}$  for the  $x_{\text{nano}}$ -series samples since the peak is very board.

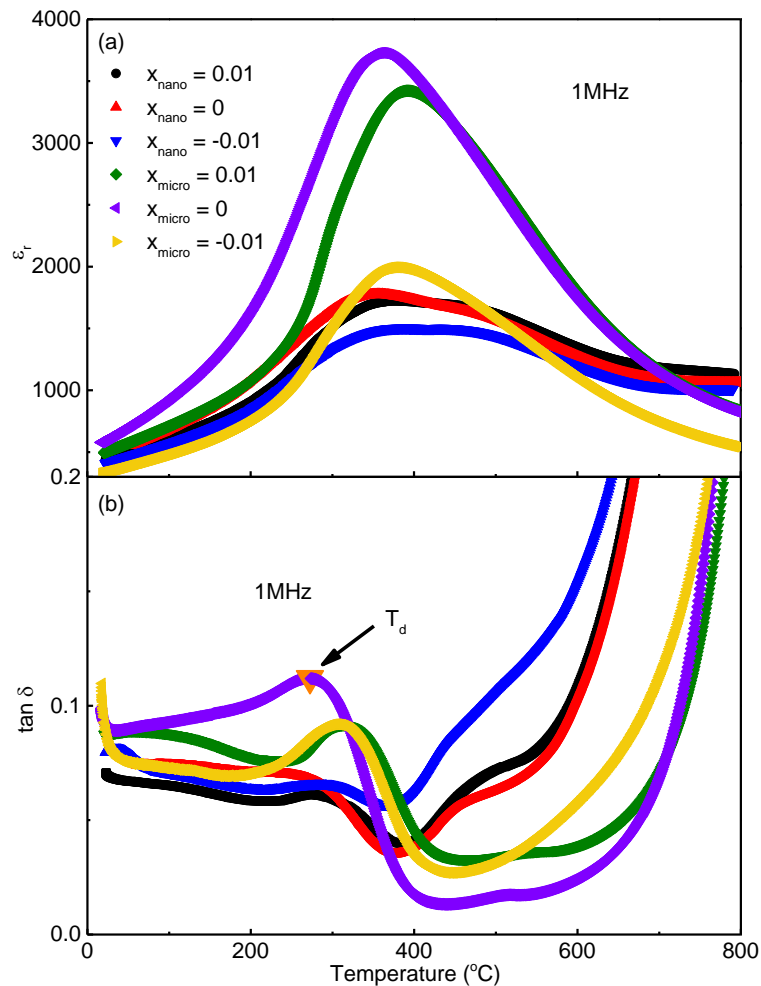


Figure 7-12. Temperature dependence of (a)  $\epsilon_r$  and (b)  $\tan \delta$  at 1 MHz for  $x$ -series ceramics.

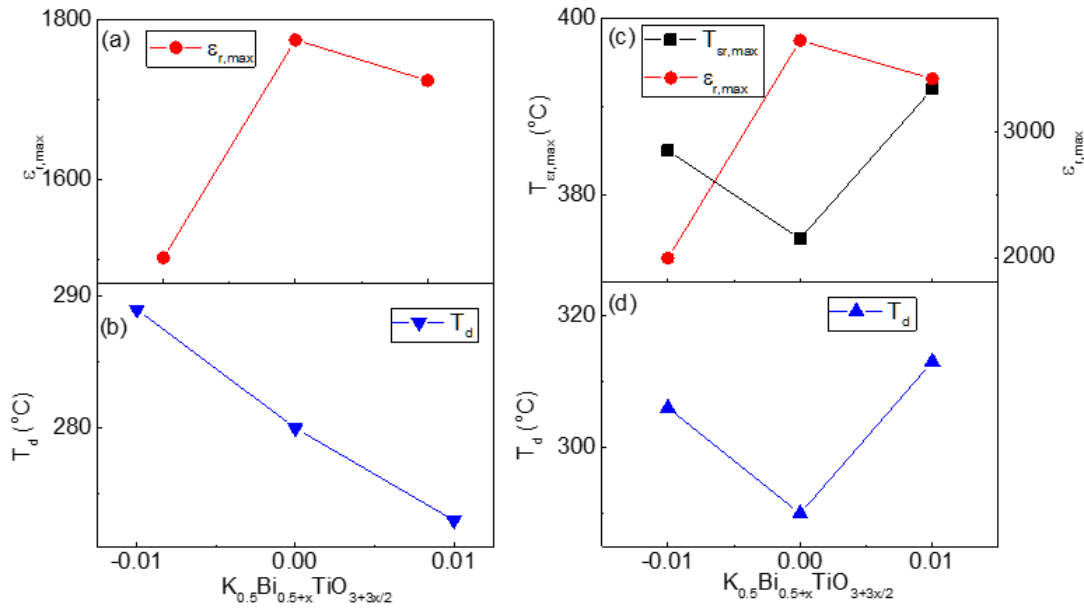


Figure 7-13. The change of (a), (c) maximum permittivity,  $\epsilon_{r,max}$  and (b), (d) the depolarization temperature,  $T_d$  with Bi non-stoichiometry.

$\tan \delta$  remains low at  $< 0.15$  from room temperature to  $\sim 600$  °C for all samples in the x-series (Figure 7-12 (b)). Samples in the  $x_{nano}$ -series possess a higher loss than the  $x_{micro}$ -series. In both series,  $x = -0.01$  possesses a slightly higher  $\tan \delta$  at temperature  $> 400$  °C compared to  $x = 0$  and  $0.01$ . The depolarisation temperature,  $T_d$  which has been taken as the temperature corresponding to the peak maximum of the ramp in  $\tan \delta$  before  $T_C$  decreases continuously with increasing Bi content (Figure 7-13 (b) and (d)).

The temperature dependent  $\epsilon_r$  and  $\tan \delta$  for the y-series samples are summarised in Figure 7-14 and Figure 7-15. Generally speaking,  $\epsilon_{r,max}$  decreases with increasing K content. For the  $y_{nano}$ -series,  $y_{nano} = -0.01$  possesses the highest  $\epsilon_{r,max}$  of  $\sim 1800$  which is slightly higher than  $y_{nano} = 0$ , with further increasing K-content  $\epsilon_r$  decreases continuously and the lowest value is reached at  $x = 0.05$  with  $\epsilon_{r,max} \sim 280$  (Figure 7-16). In the case of the  $y_{micro}$ -series,  $y_{micro} = 0$  has the highest  $\epsilon_{r,max} \sim 3700$  whereas  $y_{micro} = 0.05$  has the lowest  $\epsilon_{r,max} \sim 250$ . It can be seen that the increase in K content may influence the lattice polarisability and/or the ferroelectric domain wall motion in KBT

and results in lower permittivity. The maximum temperature  $T_{\epsilon_r, \max}$  is rather hard to determine for all  $y$ -series samples since with increasing K content the permittivity peak becomes increasingly broad.

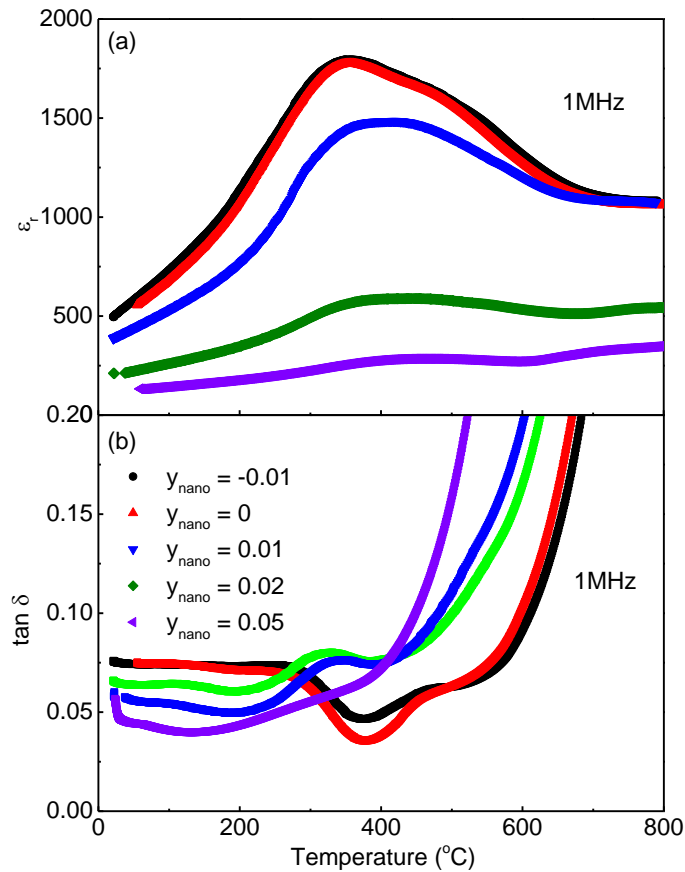


Figure 7-14. Temperature dependence of (a)  $\epsilon_r$  and (b)  $\tan \delta$  at 1 MHz for  $y_{\text{nano}}$ -series ceramics.

$\tan \delta$  remains relatively similar for all  $y$ -series samples in the temperature range room temperature to 400 °C. Above 400 °C,  $\tan \delta$  increases with increasing K content in the starting composition. The depolarization temperature,  $T_d$  for the nano-series increases from  $\sim 250$  °C for  $y_{\text{nano}} = -0.01$  to  $\sim 350$  °C for  $y_{\text{nano}} = 0.02$  whereas for the micron-series, it increases from  $\sim 270$  °C for  $y_{\text{micro}} = 0$  to  $\sim 310$  °C for  $y_{\text{micro}} = 0.05$ . It was not possible to obtain  $T_d$  for  $y_{\text{nano}} = 0.05$  because  $\tan \delta$  is rather flat in the temperature range RT to 400 °C before starting to increase rapidly.

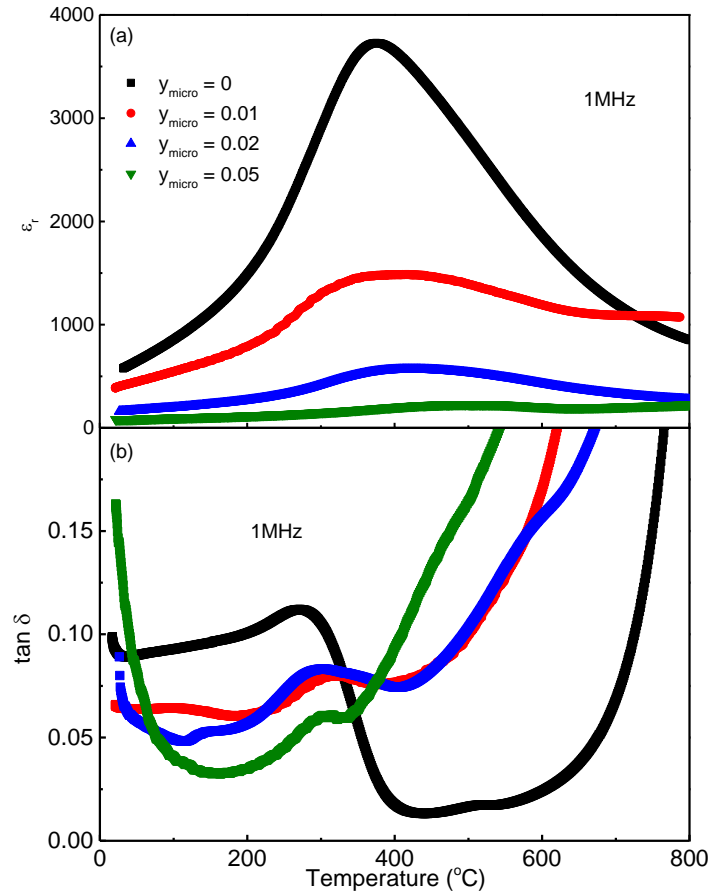


Figure 7-15. Temperature dependence of (a)  $\epsilon_r$  and (b)  $\tan \delta$  at 1 MHz for  $y_{\text{micro}}$ -series ceramics.

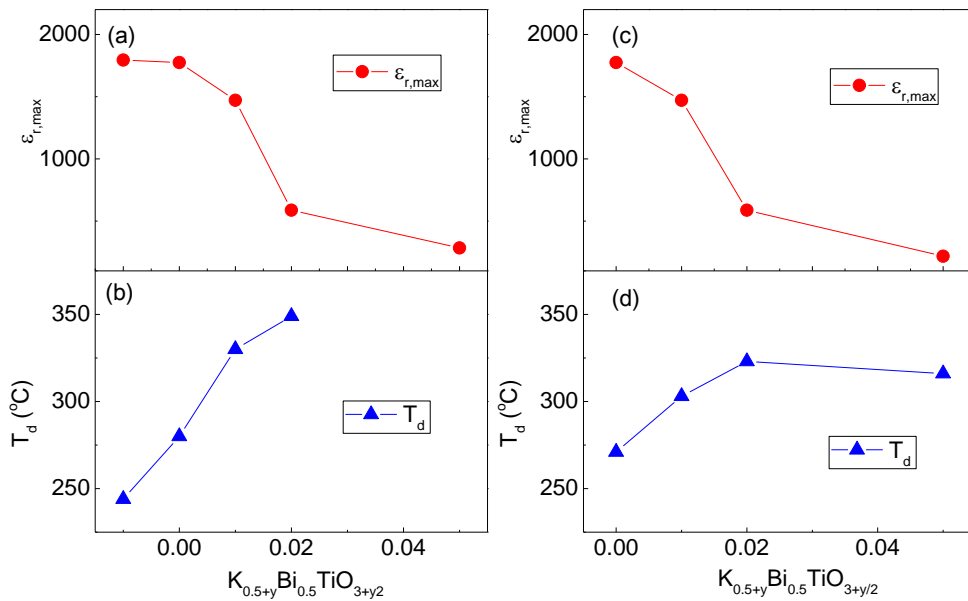


Figure 7-16. The change of (a), (c) maximum permittivity,  $\epsilon_{r,\text{max}}$  and (b), (d) the depolarization temperature,  $T_d$  with K non-stoichiometry.

$Z^*$  plots for  $x_{\text{nano}}$ -series samples are shown in Figure 7-17 (a). For  $x_{\text{nano}} = 0$  and  $-0.01$ , the  $Z^*$  plots consist of a high frequency semicircle with a low frequency spike. For  $x_{\text{nano}} = 0.01$  an additional arc can be observed between the semicircle and spike.  $Z''$  and  $M''$  spectroscopic plots are presented to verify the different responses (Figure 7-17 (c-d)). Only one component was observed in the  $M''$  spectroscopic plots for all three samples whereas two components are observed in the corresponding  $Z''$  spectroscopic plots. In addition, there is an abnormal response in the range  $\sim 1$  to  $10$  Hz with an extra arc observed for  $x = 0.01$ .

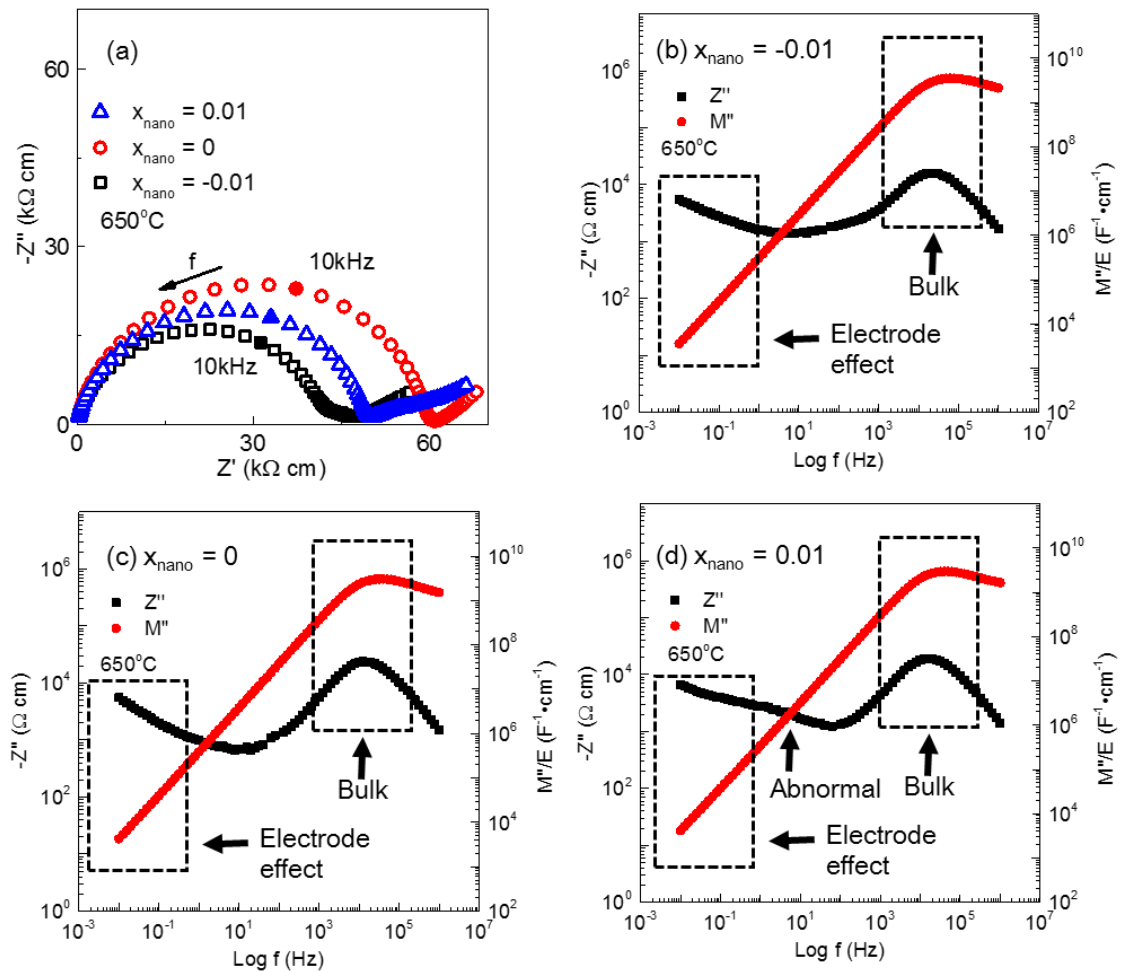


Figure 7-17. a)  $Z^*$  plots for  $x_{\text{nano}}$ -series samples and  $Z''$ ,  $M''$  spectroscopic plots for (b)  $x_{\text{nano}} = -0.01$ , (c)  $x_{\text{nano}} = 0$  and (d)  $x_{\text{nano}} = 0.01$  at  $650$  °C.

For the  $x_{\text{micro}}$ -series, the  $Z^*$  plots consist of a high frequency semicircle with a low

frequency spike for all three samples (Figure 7-18).  $Z''$  spectroscopic plots also show two responses similar to the  $x_{\text{nano}}$ -series samples.

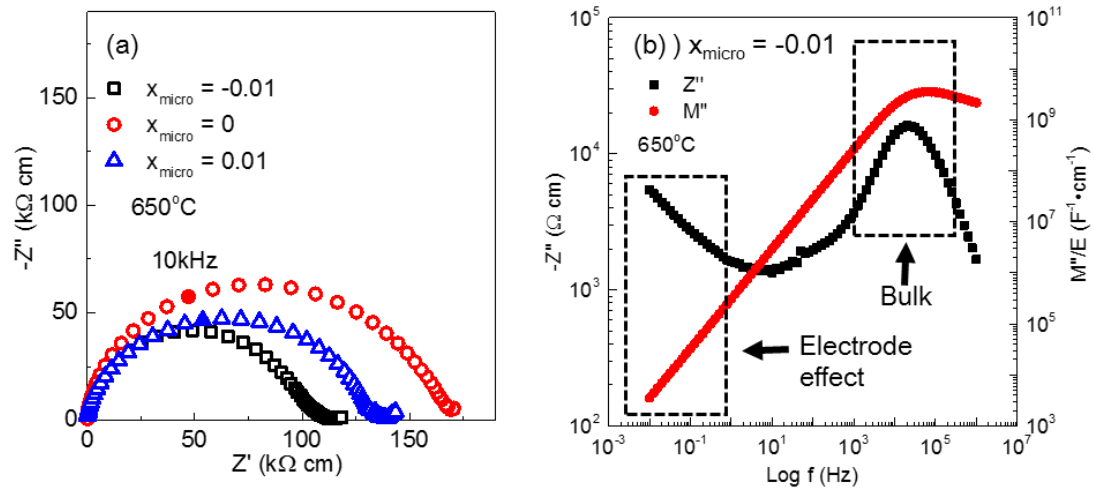


Figure 7-18. a)  $Z^*$  plots for  $x_{\text{micro}}$ -series samples and (b)  $Z''$ ,  $M''$  spectroscopic plot for  $x = -0.01$ .

Extracted capacitance values associated for all  $x$ -series samples show a value in the range  $\sim 1.1 \times 10^{-10}$  F/cm for the high frequency semicircle,  $\sim 1 \times 10^{-8}$  F/cm for the abnormal response and  $\sim 1 \times 10^{-6}$  F/cm for the low frequency spike. The capacitance for the high frequency incomplete arc is consistent with permittivity values from the LCR meter (1050  $\sim$  1200 in permittivity or  $0.93 \sim 1.06 \times 10^{-10}$  F/cm in capacitance) which indicates this arc is associated with a bulk response. With the high capacitance and the spike-like behaviour, the low frequency spike is a typical Warburg semi-infinite linear diffusion response that can be attributed to an electrode effect. The abnormal response for  $x = 0.01$  is most likely to be a thin-layer response (grain boundary or surface layer) based on the associated capacitance value.

For the  $x$ -series, the bulk conductivity is high for the  $x_{\text{nano}}$ -series samples and low for the  $x_{\text{micro}}$ -series samples. However, the starting Bi non-stoichiometry results in a

limited difference in bulk conductivity within the same series. For the  $x_{\text{nano}}$ -series,  $x = 0$  possesses the highest bulk resistivity ( $\sim 60 \text{ k}\Omega\cdot\text{cm}$ ) whereas  $x = -0.01$  is the least resistive sample ( $\sim 40 \text{ k}\Omega\cdot\text{cm}$ ). For the  $x_{\text{micro}}$ -series, again  $x = 0$  possesses the highest bulk resistivity ( $\sim 160 \text{ k}\Omega\cdot\text{cm}$ ) whereas  $x = -0.01$  is the least resistive sample ( $\sim 120 \text{ k}\Omega\cdot\text{cm}$ ).

A significant difference in frequency corresponding to the  $Z''$  and  $M''$  maximum ( $\Delta f_{\text{max}}$ ) has been noticed for both the  $x_{\text{nano}}$  and  $x_{\text{micro}}$ -series samples. As shown in Figure 7-19, the  $\Delta f_{\text{max}}$  of  $x_{\text{nano}} = -0.01$  is always larger than  $x_{\text{micro}} = -0.01$ , although in general  $\Delta f_{\text{max}}$  decreases with increasing temperature. The existence of  $\Delta f_{\text{max}}$  normally indicates the existence of electrical heterogeneity. Therefore, it can be seen that KBT prepared with micron-sized  $\text{TiO}_2$  possesses a more electrically homogeneous microstructure compared to those prepared with nano-sized  $\text{TiO}_2$ .

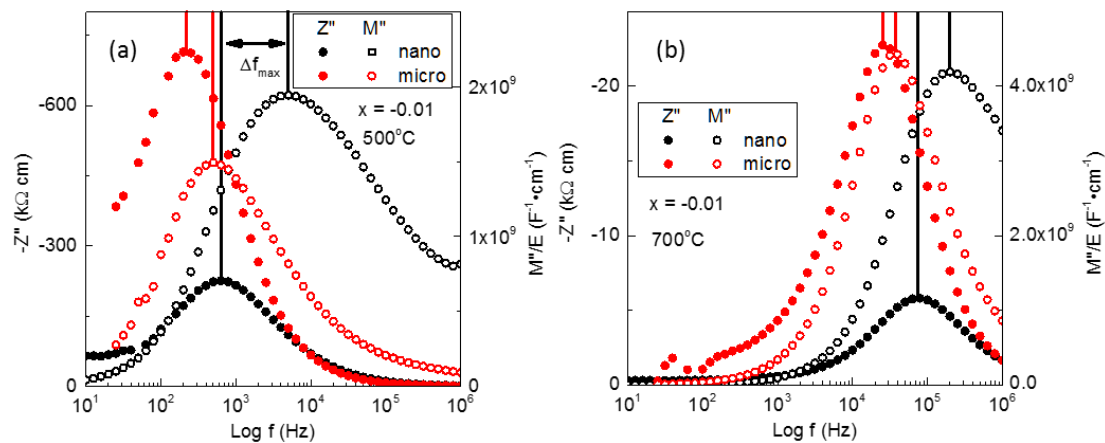


Figure 7-19.  $Z''$  and  $M''$  spectroscopic plots for  $x_{\text{nano}} = -0.01$  and  $x_{\text{micro}} = -0.01$  at (a)  $500 \text{ }^\circ\text{C}$  and  $700 \text{ }^\circ\text{C}$ . The difference in time constant between the  $Z''$  and  $M''$  peaks,  $\Delta f_{\text{max}}$  is marked.

$Z^*$  plots for y-series samples measured at  $600 \text{ }^\circ\text{C}$  are shown in Figure 7-20. Similar to the x-series, y-series samples are also dominated by one semicircle ( $\sim 1 \times 10^{-10} \text{ F/cm}$ ) associated with the bulk response and a small low frequency spike response ( $\sim 1 \times 10^{-6} \text{ F/cm}$ ) associated with an electrode effect. Again the bulk conductivity is high for the

$y_{\text{nano}}$ -series samples and low for the  $y_{\text{micro}}$ -series samples. However, the bulk conductivity clearly increases with increasing K content. For the  $y_{\text{nano}}$ -series,  $y_{\text{nano}} = 0.05$  possesses the lowest bulk resistivity ( $\sim 2.4 \text{ k}\Omega\cdot\text{cm}$ ) in this series which is more than 1 order of magnitude lower than the stoichiometric  $y_{\text{nano}} = 0$  ( $\sim 60 \text{ k}\Omega\cdot\text{cm}$ ). For the  $y_{\text{micro}}$ -series,  $y_{\text{micro}} = 0.05$  possesses the lowest bulk resistivity ( $\sim 50 \text{ k}\Omega\cdot\text{cm}$ ) whereas  $y = 0$  possesses the highest bulk resistivity ( $\sim 160 \text{ k}\Omega\cdot\text{cm}$ ).

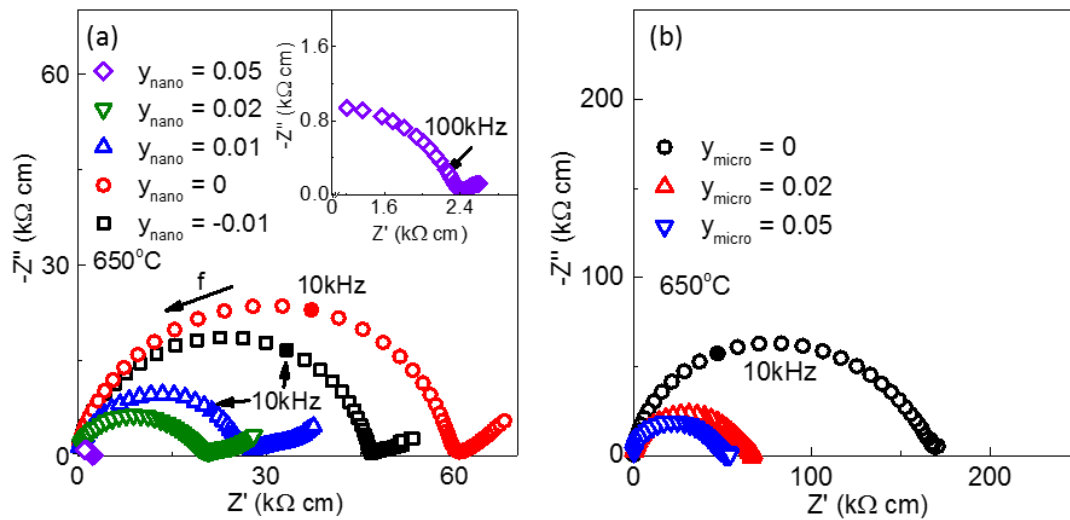


Figure 7-20.  $Z^*$  plots for (a)  $y_{\text{nano}}$  and (b)  $y_{\text{micro}}$ -series samples at  $650 \text{ }^\circ\text{C}$ .

Based on the impedance spectroscopy data, bulk conductivity of KBT samples are summarised in an Arrhenius plot with  $\text{Na}_{0.5}\text{Bi}_{0.5}\text{TiO}_3$  (conducting NBT) and  $\text{Na}_{0.5}\text{Bi}_{0.51}\text{TiO}_{3.014}$  (insulating NBT) as reference (Figure 7-21 and Figure 7-22). The bulk conductivity of  $x_{\text{nano}}$ -series samples are all in between conducting and insulating NBT and are about two orders of magnitude lower than conducting NBT whereas the difference in bulk conductivity within this series is limited. It is worth to note that  $x_{\text{nano}} = -0.01$  (0.92 eV) shows a much lower activation energy compared to  $x_{\text{nano}} = 0$  and 0.01 ( $\sim 1.3 \text{ eV}$ ). Nominal K non-stoichiometry introduces a significant difference in the bulk conductivity which is more than one order of magnitude between  $y_{\text{nano}} = 0$  and  $y_{\text{nano}} = 0.05$ . The bulk activation energy also decreases with increasing K content from  $\sim 1.50$

eV for  $y_{\text{nano}} = 0$  to  $\sim 1.28$  eV for  $y_{\text{nano}} = 0.05$ , suggesting a possible change in conduction mechanism.

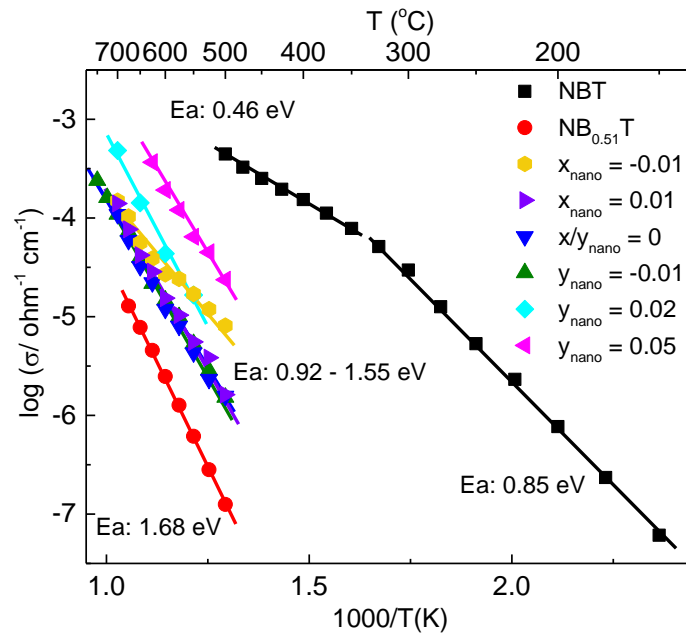


Figure 7-21. Arrhenius plot of bulk conductivity,  $\sigma_b$ , versus reciprocal temperature for  $x_{\text{nano}}$ - and  $y_{\text{nano}}$ -series ceramics with  $\text{Na}_{0.5}\text{Bi}_{0.5}\text{TiO}_3$  (NBT) and  $\text{Na}_{0.5}\text{Bi}_{0.51}\text{TiO}_{3.014}$  ( $\text{NB}_{0.51}\text{T}$ ) as reference. Activation energy,  $E_a$ , values for  $\sigma_b$  are included.

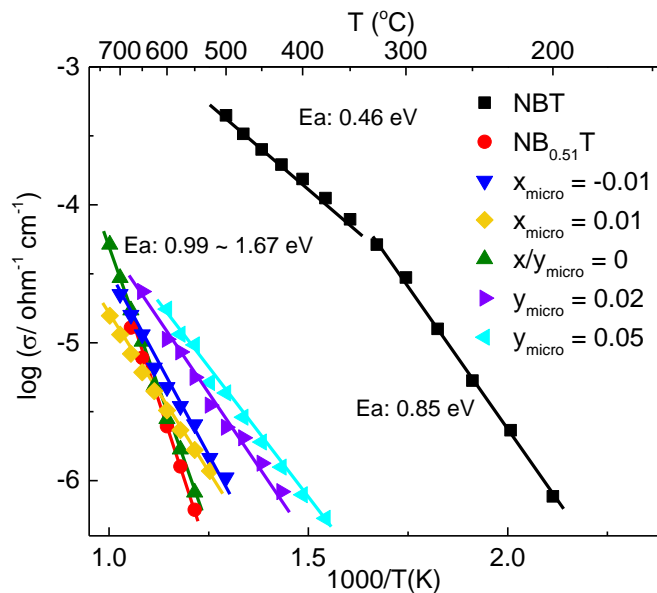


Figure 7-22. Arrhenius plot of bulk conductivity,  $\sigma_b$ , versus reciprocal temperature for  $x_{\text{micro}}$ - and  $y_{\text{micro}}$ -series ceramics with  $\text{Na}_{0.5}\text{Bi}_{0.5}\text{TiO}_3$  (NBT) and  $\text{Na}_{0.5}\text{Bi}_{0.51}\text{TiO}_{3.014}$  ( $\text{NB}_{0.51}\text{T}$ ) as reference. Activation energy,  $E_a$ , values for  $\sigma_b$  are included.

The  $x_{\text{micro}}$  and  $y_{\text{micro}}$ -series samples generally follow the same trend as the nano-series but with lower bulk conductivity. All  $x_{\text{micro}}$ -series samples possess a similar bulk conductivity to NB0.51T with a small difference in bulk activation energy. For the  $y_{\text{micro}}$ -series samples, the bulk conductivity increases with increasing K content and the difference can be  $\sim 1$  order of magnitude. The activation energy also decreases with increasing K content from  $\sim 1.67$  eV for  $y_{\text{micro}} = 0$  to  $\sim 1.02$  eV for  $y_{\text{micro}} = 0.05$ .

Isothermal bulk conductivity of KBT ceramics at 600 °C versus the K/Bi ratio in the starting composition is shown in Figure 7-23. In general, the nano-series samples possess a bulk conductivity  $\sim 1$  order of magnitude higher than corresponding micro-series sample. In terms of A-site non-stoichiometry, both the nano- and micron-series samples follow a similar trend which shows nominally stoichiometric KBT ( $x$  or  $y = 0$ ) are the most resistive samples and the bulk conductivity increases with increasing K content in the starting composition.

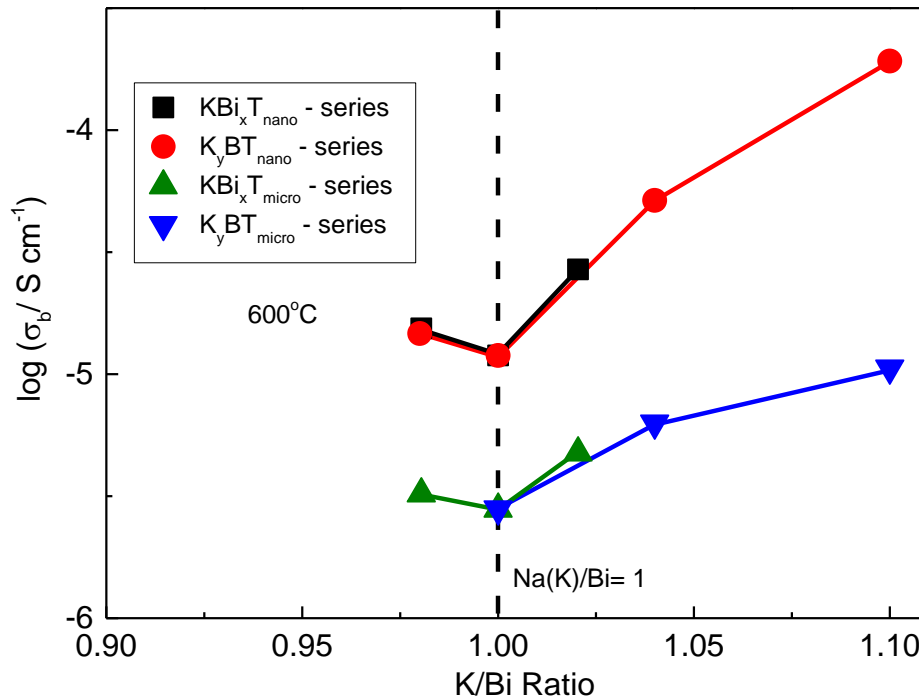


Figure 7-23. Bulk conductivity of A-site non-stoichiometric KBTs at 600 °C versus K/Bi ratio in the starting composition.

### 7.3. Ionic conduction in KBT

As discussed in the previous section, a low frequency spike has been observed in the  $Z^*$  plot for all KBT samples. This response is consistent with the Warburg semi-infinite linear diffusion which indicates the existence of ionic conduction. However, so far the type of the ionic charge carrier is not clear. It can be one of/a combination of oxide ion, proton or K ion. In order to verify the charge carrier, a series of measurements have been employed including  $pO_2/pH_2O$  dependence of the impedance response and EMF measurements.

The results of  $pO_2$  dependent impedance measurements for the x-series samples are shown in Figure 7-24. For  $x_{nano}$ -series samples, the high frequency bulk response is independent of  $pO_2$  on switching the flowing gas from  $O_2$  to  $N_2$  whereas clear n-type behaviour is observed for  $x_{micro} = 0$ . The low frequency response in  $x_{nano} = 0.01$  increases with decreasing  $pO_2$ .

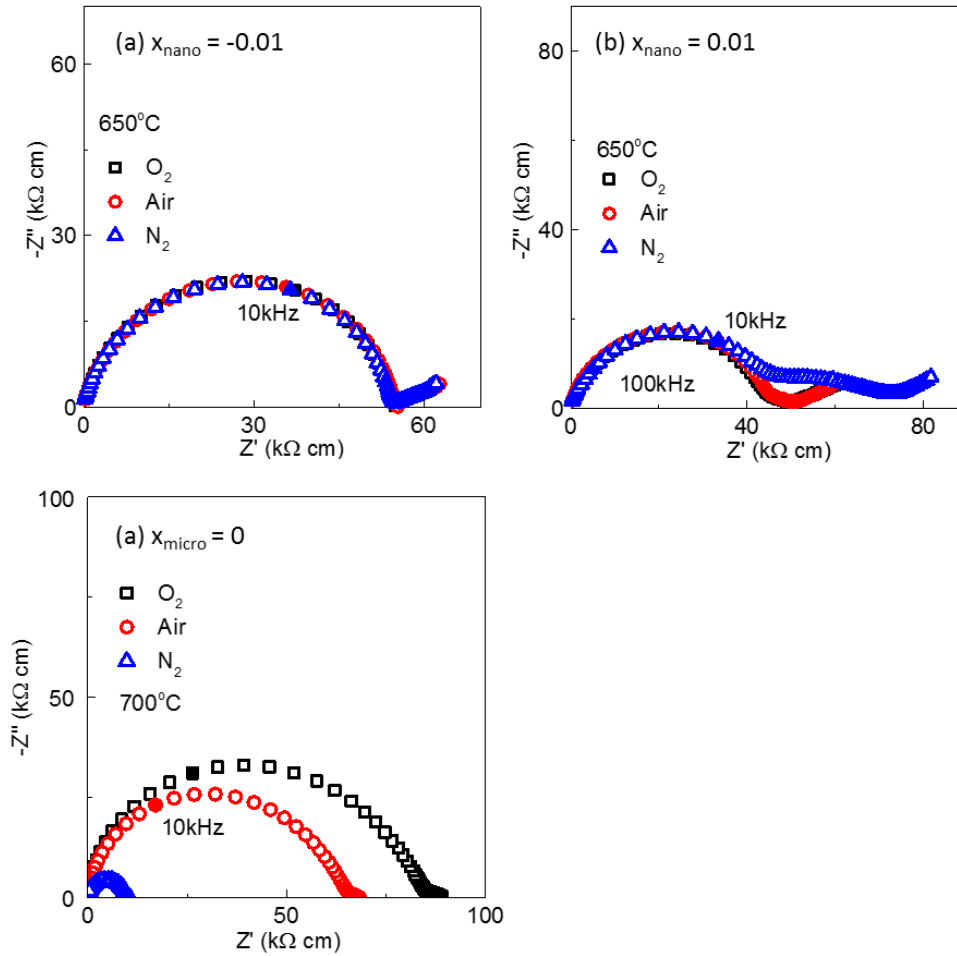


Figure 7-24.  $Z^*$  plots for (a)  $x = -0.01$  and (b)  $x = 0.01$  under different atmospheres at 650 °C and (c)  $x_{\text{micro}} = 0$  under different atmospheres at 700 °C.

$p_{\text{O}_2}$  tests of  $\gamma$ -series samples showed similar behaviour of the bulk conductivity as the  $x$ -series samples when changing the flowing gas from O<sub>2</sub> to N<sub>2</sub> (Figure 7-25). The bulk conductivity of  $\gamma_{\text{nano}}$ -series samples is less sensitive to the change of  $p_{\text{O}_2}$  from O<sub>2</sub> to N<sub>2</sub> than  $\gamma_{\text{micro}}$ -series samples. The independence of the high frequency bulk response for the nano-series samples supports the suggestion that these samples are dominated by ionic conduction.

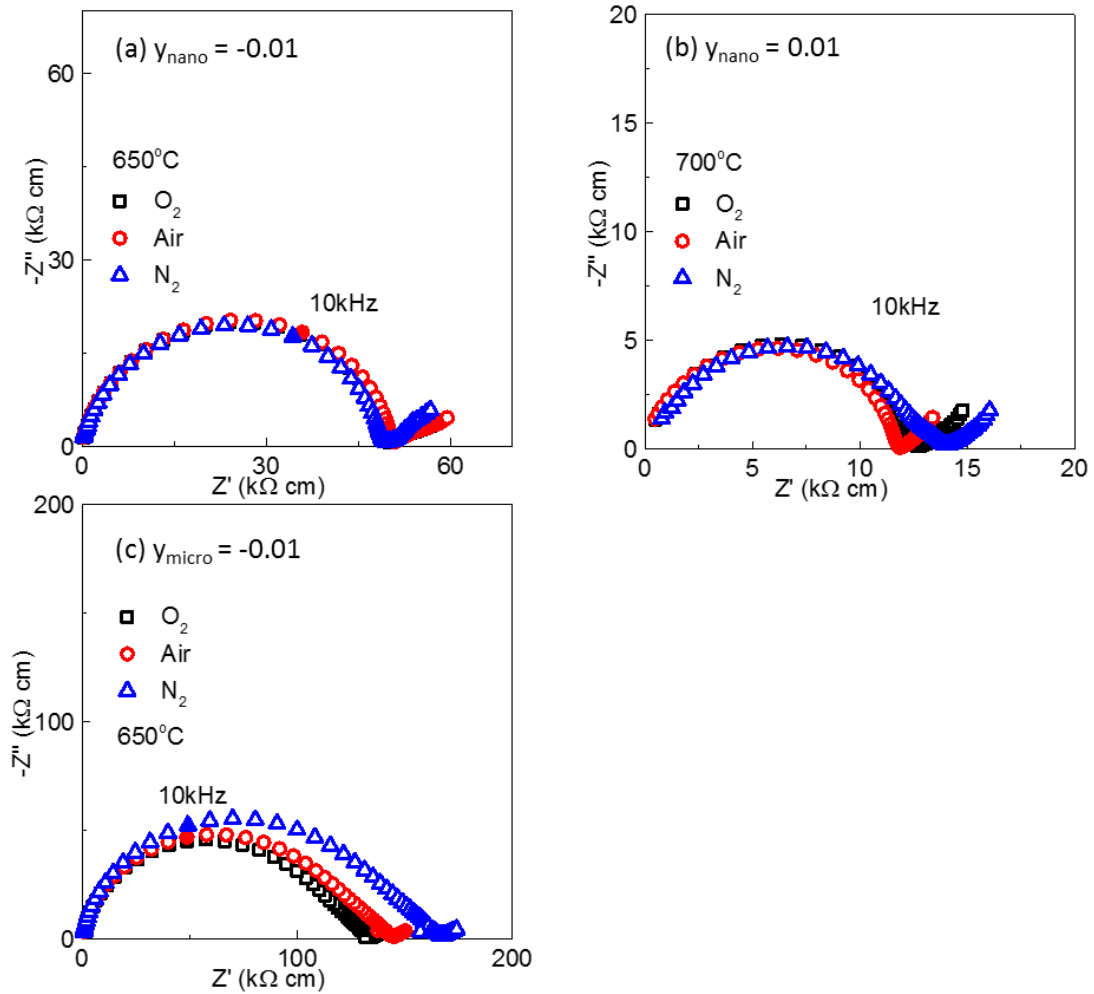


Figure 7-25.  $Z^*$  plots for (a)  $y_{\text{nano}} = -0.01$  and (b)  $y_{\text{nano}} = 0.01$  and  $y_{\text{micro}} = -0.01$  under different atmospheres.

Since ionic conduction has been proved in KBT ceramics, EMF measurements were required to verify the type of ionic charge carrier and to determine the level of oxide ion conduction. EFM results for selected KBT samples are shown in Figure 7-26. The obtained oxygen ion transport number  $t_{\text{ion}}$  is rather low,  $\sim 0.05 - 0.2$ . During the EMF measurements, the outside of YSZ tube is normally exposed to air whereas different pre-dried gases (e.g.  $\text{N}_2$ ,  $\text{O}_2$ ) are flowing through the inside of the tube to generate a  $p\text{O}_2$  gradient. However, for KBT samples, a negative voltage was observed when only dry air was flowing inside the YSZ tube. The negative voltage suggested there were other charge carrier(s) in KBT which establish a voltage before a  $p\text{O}_2$  gradient has been

built-up.<sup>10</sup> Considering the difference in water content between dry air and normal air, proton conduction is a reasonable option. For all the previous EMF measurements performed on NBT and BiT ceramics, the  $pO_2$  gradient is generated by flowing dry  $N_2$  inside the YSZ tube while keeping the outside of the YSZ tube in laboratory Air.  $t_{ion}$  could therefore be underestimated since part of the voltage generated by oxide ion conduction is cancelled out by proton conduction. Consequently, an EMF measurement using dry air instead of laboratory air was employed to prevent (reduce) the  $pH_2O$  gradient across the sample. In this case, a much higher positive voltage and therefore  $t_{ion}$  was obtained ( $\sim 0.5$ ) for  $x_{nano} = -0.01$  compared to that measured in laboratory air. This provides strong evidence for the presence of proton conduction in KBT (Figure 7-27).

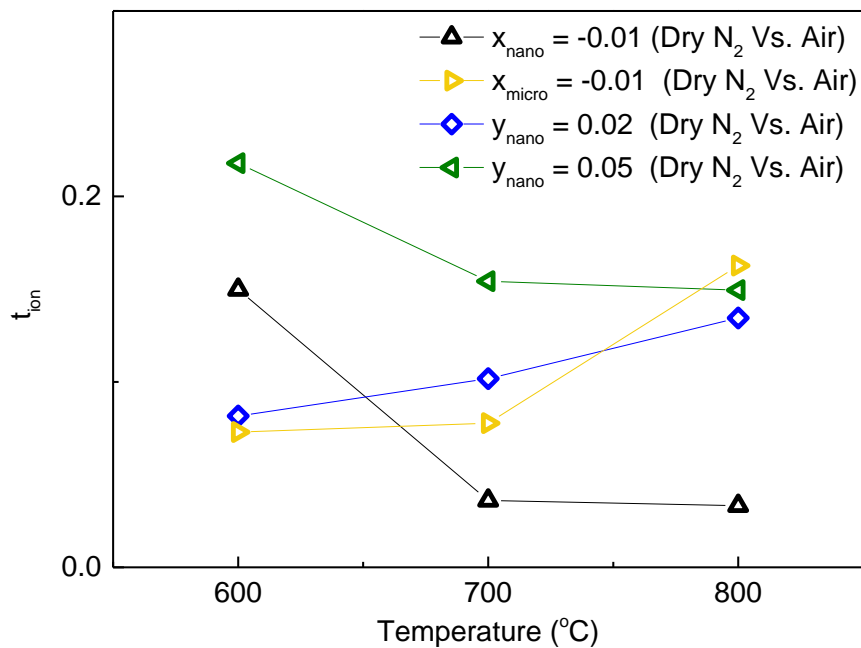


Figure 7-26.  $t_{ion}$  values between 600 and 800 °C for selected x- and y-series samples. (Dry  $N_2$ /Air: gas was pre-dried before use; Air: laboratory (normal) Air)

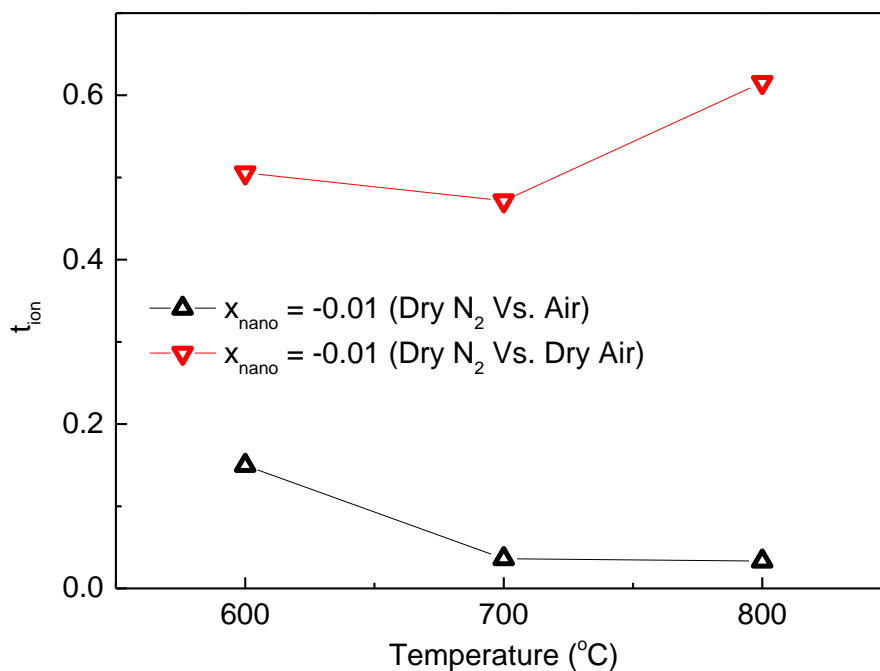


Figure 7-27.  $t_{ion}$  values between 600 and 800 °C for  $x_{nano} = -0.01$  under dry and normal air. (Dry  $N_2$ /Air: gas was pre-dried before use; Air: laboratory (normal) Air)

A  $pH_2O$  test was performed to confirm the proton conduction by flowing wet air (generated by passing air through a bubbler filled with water and placed in a 70 °C water bath) while recording impedance measurements. Figure 7-28 shows the  $Z^*$  plots and  $M''$  spectroscopic plots of  $\gamma = 0$  and 0.05 at room temperature under wet/dry flowing air. In both  $\gamma = 0$  and 0.05, the samples exposed to wet air consist of a high frequency semicircle and a low frequency spike whereas the  $Z^*$  plot of samples exposed to dry air show only a large spike for the whole frequency range. For wet air exposed samples, the extracted capacitance associated with the high frequency semicircle and low frequency spike are  $\sim 5 \times 10^{-11}$  F/cm and  $1 \times 10^{-6}$  F/cm, respectively. The capacitance for the high frequency incomplete arc is consistent with permittivity values from the LCR meter ( $\sim 500$  or  $4.4 \times 10^{-11}$  F/cm in capacitance) indicating this arc is associated with bulk response whereas the spike is consistent with a Warburg semi-infinite linear diffusion response. On the other hand, the large spike for the dry air samples also possess a capacitance associated with a bulk response ( $\sim 5 \times 10^{-11}$  F/cm).

A spike in  $Z^*$  plot indicates a large bulk resistivity which can be almost seen as infinite (a vertical spike) at this temperature, therefore the bulk for both  $y = 0$  and  $0.05$  are significantly reduced under a wet air atmosphere and ionic conduction is present. The  $M''$  spectroscopic plots also suggest that in dry air the bulk response for both  $y_{\text{nano}} = 0$  and  $0.05$  are too resistive to be detected by impedance whereas in wet air the bulk conductivity becomes much higher.

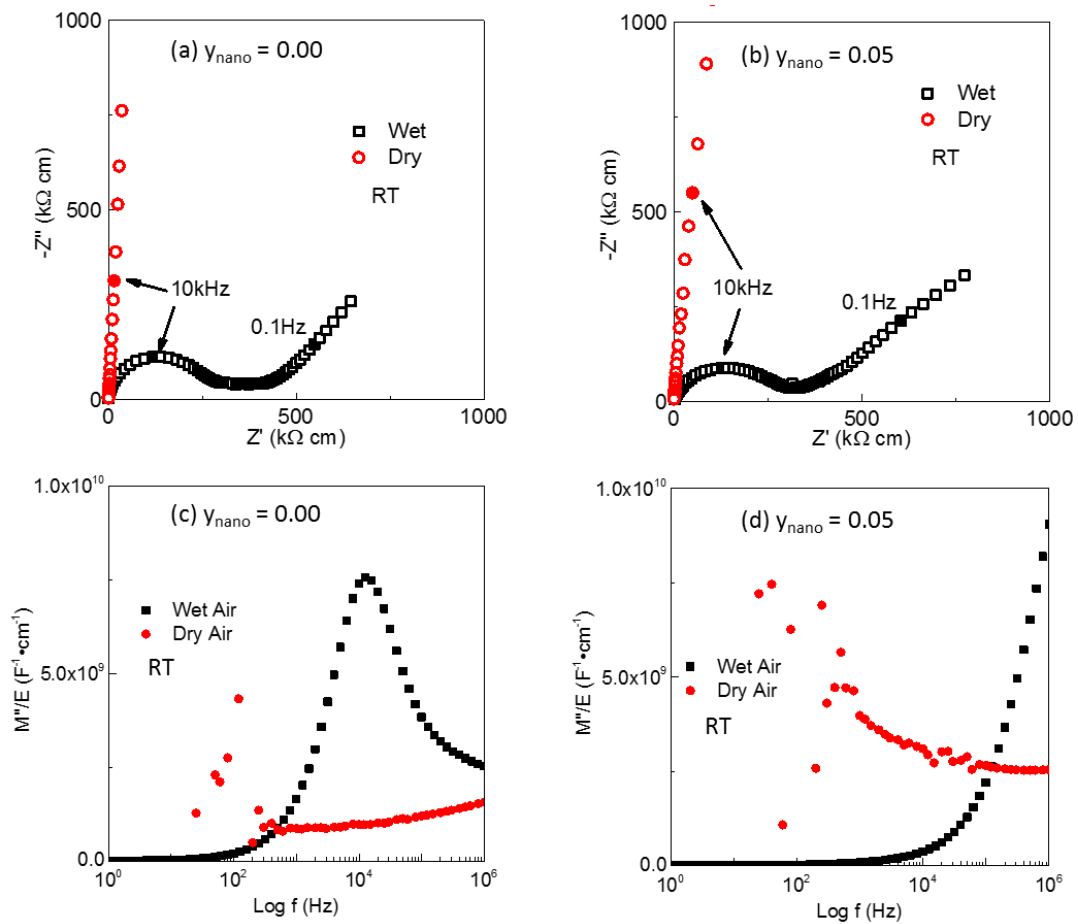


Figure 7-28.  $Z^*$  plots for (a)  $y_{\text{nano}} = 0$  and (b)  $y_{\text{nano}} = 0.05$ ;  $M''$  spectroscopic plots for (c)  $y_{\text{nano}} = 0$  and (d)  $y_{\text{nano}} = 0.05$  under different  $\text{pH}_2\text{O}$  atmospheres.

Some studies have suggested that in the oxide ion conducting electrolyte  $\text{Ce}_{0.9}\text{Gd}_{0.1}\text{O}_{2-x}$  (GDC) the predominated proton conduction is attributed to a surface pathway (lateral pellet surfaces) instead of passing through the grains within the ceramic.<sup>11,12</sup> In order to determine if this is also the case in KBT, a  $y_{\text{nano}} = 0.02$  pellet

with a ring electrode has been adopted (insert of Figure 7-29 (a)). The hole in the middle of the electrode is required to expose the pellet to moisture and the lateral pellet surfaces were sealed with Silicone grease to prevent direct contact of moisture. The results show that despite the lateral pellet surfaces being covered by Silicone grease, the conductivity increased significantly after exposure to a wet atmosphere (Figure 7-29 (a)). A modest change has been observed for the high frequency response which indicates the proton conduction can be attributed to volumetric grains instead of a surface layer (Figure 7-29 (b)). As a comparison, stoichiometric NBT was also measured in wet atmosphere, Figure 7-30. The  $Z^*$  plot consistent with a high frequency arc corresponding to bulk response and a low frequency spike corresponding to an electrode effect. The result shows NBT possess a relatively low bulk conductivity at room temperature than KBT and starts to increase above  $\sim 150^\circ\text{C}$ , Figure 7-31.

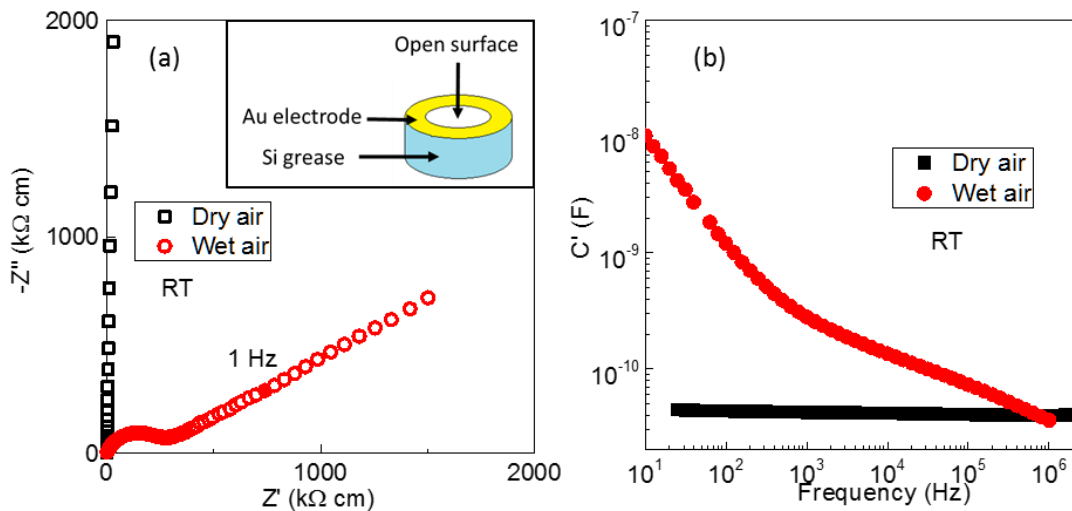


Figure 7-29. (a)  $Z^*$  plots and (b)  $C'$  spectroscopic plots for  $y_{\text{nano}} = 0.02$  with a ring electrode (insert in (a)) at room temperature.

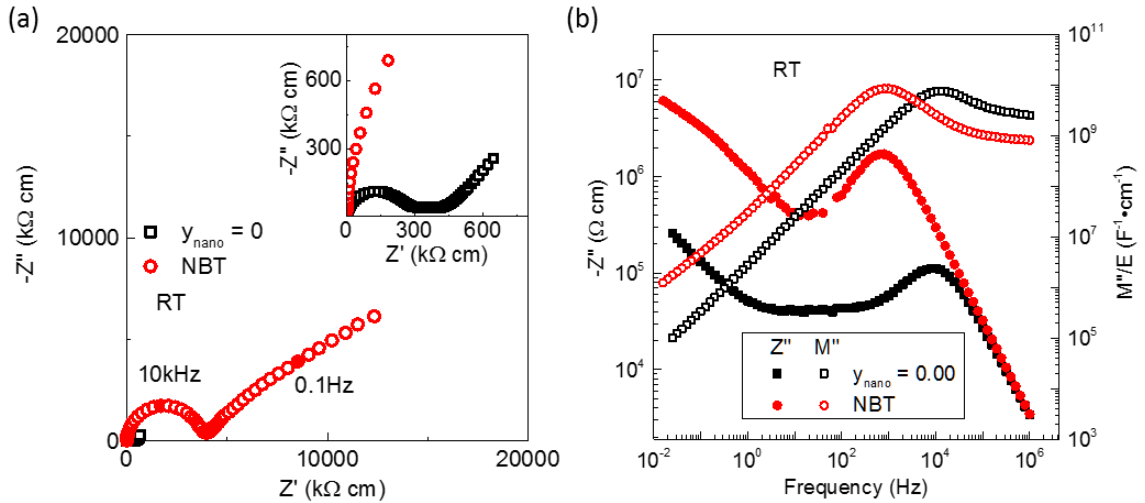


Figure 7-30. (a)  $Z^*$  plots and (b)  $Z''$  and  $M''$  spectroscopic plots for  $y_{\text{nano}} = 0.00$  and NBT in wet air at room temperature.

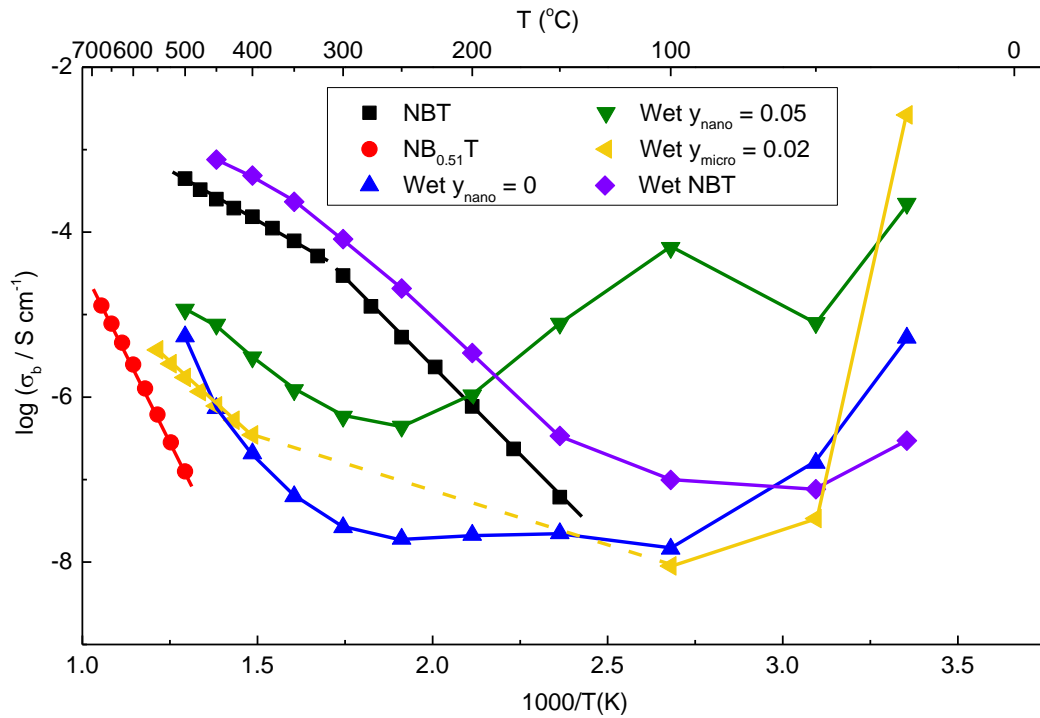


Figure 7-31. Arrhenius plot of  $\sigma_b$  of selected  $y$ -series samples and stoichiometric NBT under a high  $p_{\text{H}_2\text{O}}$  atmosphere.  $\text{Na}_{0.5}\text{Bi}_{0.5}\text{TiO}_3$  (NBT) and  $\text{Na}_{0.5}\text{Bi}_{0.51}\text{TiO}_{3.014}$  ( $\text{NB}_{0.51}\text{T}$ ) are presented as reference.

The bulk conductivity of KBT ceramics under wet atmosphere are summarised in an Arrhenius plot in Figure 7-31. A high bulk conductivity at lower temperatures has been observed for all measured samples. For the nano-series samples ( $y_{\text{nano}} = 0$  and

0.05), the bulk conductivity initially decreases with increasing temperature and then remains relatively stable in the range 100 ~ 300 °C. With a further increase in temperature the bulk conductivity starts to increase again.  $y_{\text{micro}} = 0.02$  has an even higher bulk conductivity at room temperature than  $y_{\text{nano}} = 0.05$ . However, its bulk conductivity decreases rapidly with increasing temperature and becomes too resistive for the instrument to measure in the range ~ 100 to 400 °C. It worth to note that  $y_{\text{nano}} = 0.05$  possess a much higher bulk conductivity than  $y_{\text{nano}} = 0$  for the whole temperature range. Figure 7-32 shows a comparison of KBT ceramics under wet and dry atmosphere. The bulk conductivity at high temperature (> 500 °C) shows no significant influence of pH<sub>2</sub>O.

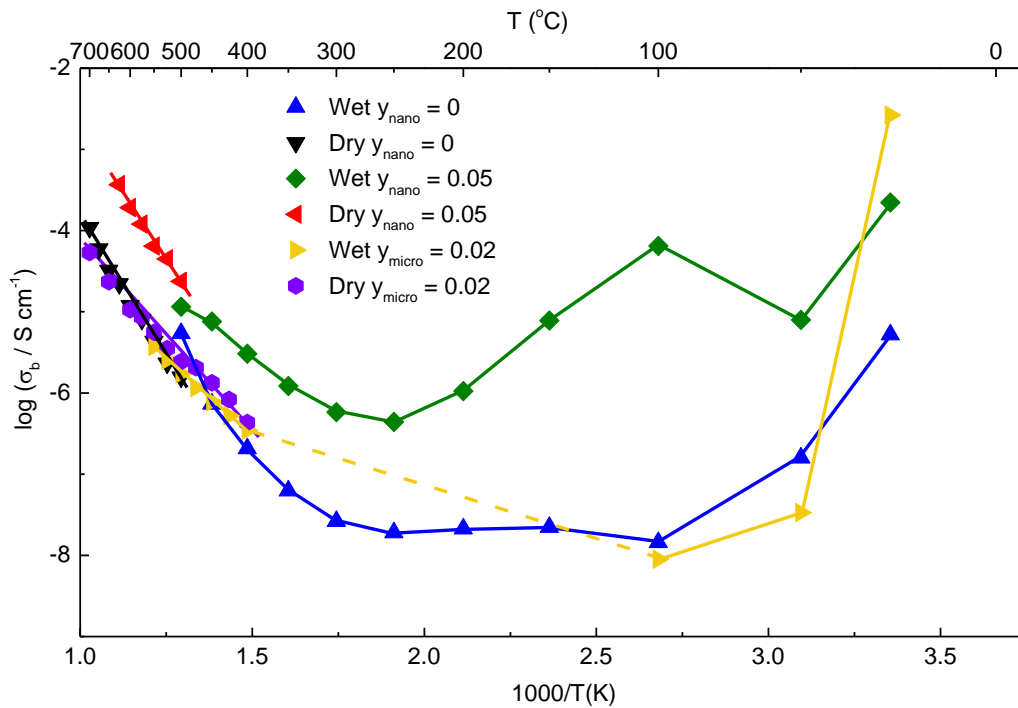


Figure 7-32. Arrhenius plot of  $\sigma_b$  of selected wet and dry KBT ceramics.

## 7.4. Discussion

For all samples in this chapter, a small amount of  $K_2Ti_6O_{13}$  secondary phase was detected within a thin layer close to the surface of sintered pellet. However, as stated

by König et al., the formation of this phase is related to the thermal decomposition of KBT.<sup>13</sup> From the point of view of electrical properties, both permittivity and bulk conductivity change systematically with the change of starting composition. Thus it is hard to determine the solid solution limit for A-site non-stoichiometry in KBT, especially in consideration of the vaporization of  $K_2O$  and  $Bi_2O_3$ .

For all nano-series KBT ceramics, a broadened peak has been observed in the temperature dependent permittivity plot compared to the micro series samples, Figure 7-12 and Figure 7-14. A maximum peak value is reached in the range from  $\sim 380$  °C which is consistent with the reported  $T_C$  of KBT to  $\sim 400$  °C.<sup>4</sup> However, the situation is much better for the micron-series samples which shows a relatively sharp peak, Figure 7-15. The maximum permittivity for the secondary phase  $K_2Ti_6O_{13}$  is at  $\sim 300$  °C with a value of 60 which is obviously not the reason for this broadening.<sup>14</sup> One possibility is such a broadened peak may be generated due to the more significant electrical heterogeneity of the nano-series KBTs compared to the micro-series which has been proved by the  $\Delta f_{max}$  as shown in Figure 7-19. Such electrical heterogeneity of KBT can lead to a broadening of the permittivity peak and therefore lower the peak value.

The bulk conductivity of KBT is not as sensitive to A-site nonstoichiometry as NBT. Generally speaking the bulk conductivity of KBTs follows two trends. Firstly, for the starting composition, nano-series samples are always more conductive than micro-series samples, Figure 7-23. Secondly, the bulk conductivity of KBT ceramics increase with increasing K content. It is worth to note that the proton conduction is enhanced with excess K in starting material as shown in Figure 7-31, therefore this increase in bulk conductivity should be related to the increase of proton conduction.

The difference in  $TiO_2$  particle size from micron-sized to nano-sized starting

material can lead to several other differences. KBT ceramics synthesized with nano-sized  $\text{TiO}_2$  possess a higher density (> 90%) and a relatively  $p\text{O}_2$  independent (within  $\text{O}_2$  to  $\text{N}_2$ ) bulk conductivity. On the other hand, the density of KBT ceramics synthesised with micron-sized  $\text{TiO}_2$  is much lower (70 ~ 80%). Such a difference in density may cause by the higher specific surface area for nano- $\text{TiO}_2$  which has a higher surface energy that benefits the densification at high temperature. In addition, the higher conductivity in nano-series KBTs also helps the sintering process via the higher ionic mobility of the ions.

The bulk conductivity of the micro-series samples are more  $p\text{O}_2$  dependent and also possess better electrical homogeneity than the nano-series samples, Figure 7-24 and Figure 7-19. As shown in Figure 7-31, nano-series samples possess a higher bulk conductivity at intermediate temperature (100 ~ 400 °C) than micro-series samples under a wet atmosphere which means the nano-series samples can keep the protons (absorbed water) to a higher temperature than micron-series samples. This is probably due to the higher density and lower porosity in nano-series samples.

The most obvious difference between KBT and NBT is the lack of high level oxide ion conduction. As discussed in chapter 3, computer simulations suggest the cation polarisability, weak Bi-O bonds and local atomistic configurations in NBT are all important factors that favour oxygen ion migration. From this point of view, KBT also has these benefits and should have the potential to possess a high level of oxide ion conduction. Therefore differences exist between KBT and NBT that must be critical for oxide ion conduction.

Firstly, the existence of  $\text{K}_2\text{Ti}_6\text{O}_{13}$  phase has been observed in all samples of KBT ceramics in this project. König et al. suggest the formation of  $\text{K}_2\text{Ti}_6\text{O}_{13}$  is due to thermal decomposition and the evaporation of K and Bi which only appear on the surface

layer.<sup>13</sup> For KBT ceramics in this project, the formation of  $K_2Ti_6O_{13}$  phase cannot be avoided despite sacrificial powder with the same composition being used to cover pellets during sintering. From the NBT results we understand the oxide ion conduction can be highly sensitive to very low levels of A-site non-stoichiometry. Therefore the formation of  $K_2Ti_6O_{13}$  will deplete the KBT main phase of K and Ti which may then increase the actual Bi-content in the final product which leads to lower bulk conduction.

Secondly, despite the chemical similarity between K and Na, the size difference between them leads to different polymorphic structures. The  $BO_6$  octahedra in KBT do not have any tilting, therefore the Bi ions in KBT is not off-centered as in NBT and invariable Bi-O bond lengths are obtained in KBT and therefore the existence of the weak Bi-O bonds does not occur in KBT.<sup>15</sup>

Thirdly, in terms of saddle-point configurations, for NBT the migration energy barrier of different pathways are different. The Bi-Bi-Ti saddle-point is reported to have the lowest barrier (0.22 eV) whereas the Na-Na-Ti saddle-point has the highest barrier (1.3 eV).<sup>16</sup> However, the measured activation energy for conducting NBT from impedance data is 0.6 ~ 0.8 eV which is in agreement with the Na-Bi-Ti pathway where the migration energy barrier is 0.6 to 0.85 eV. Therefore it is reasonable to believe the oxide ion migration is mainly controlled by the Na-Bi-Ti pathway. If it is the same case in KBT, then a larger and heavier K ion certainly will be less favourable to displace away from the mobile oxygen ions and introduces a higher activation energy which could be high enough to make the K-Bi-Ti pathway considerably less favourable for oxygen ion migration. In this case, the only pathway with a low energy barrier for oxygen migration is the Bi-Bi-Ti saddle-point. Such a reduction in number of possible pathways for oxygen diffusion is certainly unfavourable for oxide ion conduction.

## 7.5. Conclusions

Compared to NBT, the bulk conductivity of KBT is relatively insensitive to A-site non-stoichiometry and high levels of oxide ion conduction is absent in undoped KBT samples in this project. Nano-sized and micro-sized TiO<sub>2</sub> reagent powders can lead to a difference in ceramic density, electrical homogeneity and level of bulk conduction in sintered KBT ceramics. Nano-series KBT possess a higher ceramic density, increased electrical heterogeneity and higher bulk conduction than the corresponding micron-series samples. Combined with EMF data, KBT has been determined to be a mixed conductor with mixed ionic/electronic conduction where the bulk conduction in wet atmospheres at low temperature can be predominated by proton conduction. The proton conduction in KBT is controlled by the K content in the starting material; higher K contents lead to higher proton conduction. Consequently, the bulk conductivity also increase with increasing K content.

## 7.6. References

1. Pronin, I. P., Parfenova, N. N., Zaitseva, N. V, Isupov, V. A. & Smolenskii, G. A. Phase transitions in solid solutions of sodium--bismuth and potassium--bismuth titanates. *Sov. Phys. Solid State* **24**, 1060–1062 (1982).
2. Jones, G. O., Kreisel, J. & Thomas, P. A. A structural study of the (Na<sub>1-x</sub>K<sub>x</sub>)<sub>0.5</sub>Bi<sub>0.5</sub>TiO<sub>3</sub> perovskite series as a function of substitution (x) and temperature. *Powder Diffraction* **17**, 301–319 (2002).
3. Ivanova, V. V, Kapyshev, A. G., Venevtsev, Y. N. & Zhdanov, G. S. X-ray determination of the symmetry of elementary cells of the ferroelectric materials (K<sub>0.5</sub>Bi<sub>0.5</sub>)TiO<sub>3</sub> and (Na<sub>0.5</sub>Bi<sub>0.5</sub>)TiO<sub>3</sub> and of high-temperature phase transitions in (K<sub>0.5</sub>Bi<sub>0.5</sub>)TiO<sub>3</sub>. *Izv. Akad. Nauk SSSR* **26**, 354–356 (1962).

4. Emel'yanov, S. M., Raevskii, I. P. & Prokopalo, O. I. Nature of phase transitions in potassium bismuth titanate. *Sov. Phys. solid state* **25**, 889–890 (1983).
5. Bengagi, M., Morini, F., El Maaoui, M. & Marchet, P. Structure and electrical properties in the  $K_{1/2}Bi_{1/2}TiO_3$ - $K_{1/2}Bi_{1/2}ZrO_3$  solid solution (KBT-KBZ). *Phys. status solidi* **209**, 2063–2072 (2012).
6. Bennett, J. *et al.* Multiferroic properties of  $BiFeO_3$ - $(K_{0.5}Bi_{0.5})TiO_3$  ceramics. *Mater. Lett.* **94**, 172–175 (2013).
7. Bennett, J. *et al.* Variation of Piezoelectric Properties and Mechanisms Across the Relaxor-Like /Ferroelectric Continuum in  $BiFeO_3$ - $(K_{0.5}Bi_{0.5})TiO_3$ - $PbTiO_3$  Ceramics. *IEEE Trans. Ultrason. Ferroelectr. Freq. Control* **62**, 33–45 (2015).
8. Bennett, J., Bell, A. J., Stevenson, T. J. & Comyn, T. P. Exceptionally large piezoelectric strains in  $BiFeO_3$ - $(K_{0.5}Bi_{0.5})TiO_3$ - $PbTiO_3$  ceramics. *Scr. Mater.* **68**, 491–494 (2013).
9. Bennett, J., Bell, a. J., Stevenson, T. J. & Comyn, T. P. Tailoring the structure and piezoelectric properties of  $BiFeO_3$ - $(K_{0.5}Bi_{0.5})TiO_3$ - $PbTiO_3$  ceramics for high temperature applications. *Appl. Phys. Lett.* **103**, 152901 (2013).
10. Han, D. *et al.* Transport properties of acceptor-doped barium zirconate by electromotive force measurements. *Int. J. Hydrogen Energy* **41**, 14897–14908 (2016).
11. Pérez-Coll, D. & Mather, G. C. Electrical transport at low temperatures in dense nanocrystalline Gd-doped ceria. *Solid State Ionics* **181**, 20–26 (2010).
12. Tandé, C., Pérez-Coll, D. & Mather, G. C. Surface proton conductivity of dense nanocrystalline YSZ. *J. Mater. Chem.* **22**, 11208 (2012).

13. König, J. *et al.* The thermal decomposition of  $K_{0.5}Bi_{0.5}TiO_3$  ceramics. *J. Eur. Ceram. Soc.* **29**, 1695–1701 (2009).
14. Vikram, S. V., Phase, D. M. & Chandel, V. S. High-T C phase transition in  $K_2Ti_6O_{13}$  lead-free ceramic synthesised using solid-state reaction. *J. Mater. Sci. Mater. Electron.* **21**, 902–905 (2010).
15. Otoničar, M., Škapin, S. D., Jančar, B., Ubič, R. & Suvorov, D. Analysis of the Phase Transition and the Domain Structure in  $K_{0.5}Bi_{0.5}TiO_3$  Perovskite Ceramics by In Situ XRD and TEM. *J. Am. Ceram. Soc.* **93**, 4168–4173 (2010).
16. He, X. & Mo, Y. Accelerated Materials Design of  $Na_{0.5}Bi_{0.5}TiO_3$  Oxygen Ionic Conductors Based on First Principles Calculations. *Phys. Chem. Chem. Phys.* **17**, 18035–18044 (2015).

## 8. General discussion

In this project, the effect of A-site non-stoichiometry in NBT, BiT and KBT systems has been discussed. The results have shown that the electrical behaviour of these three systems are rather different from each other, especially in respect to A-site non-stoichiometry. The bulk conductivity of undoped conducting (type 1), intermediate (type 2) and insulating (type 3) NBTs are shown in Figure 8-1. The range of different types of NBTs are marked with different shaded colour regions (type 1-blue, type 2-orange and type 3-green).

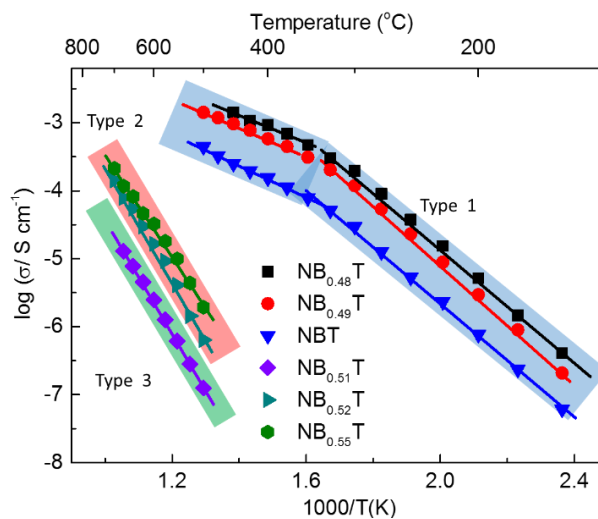


Figure 8-1. Arrhenius plot of  $\sigma_b$  versus reciprocal temperature for selected NBTs

Figure 8-2 compares the bulk conductivity of undoped KBT and BiT samples with the three types of NBT samples. It is clear that for KBT samples, the bulk conductivity is generally within the same magnitude as type 2 and 3 NBT whereas for BiT samples the bulk conductivities are similar to type 1 NBT. In both cases, the A-site non-stoichiometry can only cause a relatively small variation in bulk conductivity compared with NBT. A-site non-stoichiometry in NBT can dramatically change the bulk conductivity from an insulator to a conductor with  $\sim 3$  orders of magnitude difference (Figure 8-4) Whereas the bulk conductivity difference caused by A-site non-

stoichiometry in KBT and BiT is only  $\sim 1$  order of magnitude, Figure 8-3 and Figure 8-4, respectively. At 300 oC, the bulk conductivity of insulating NBTs have exceed the detectable limit of our impedance spectroscopy and therefore only conducting NBTs are shown in Figure 8-3.

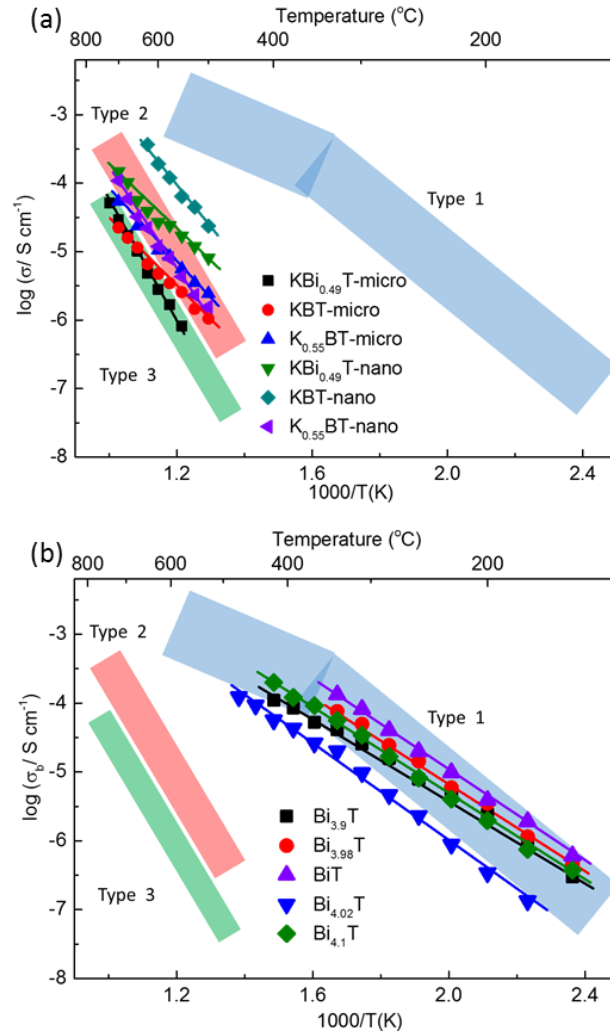


Figure 8-2. Arrhenius plot of  $\sigma_b$  versus reciprocal temperature for selected (a) KBTs and (b) BiTs with the shaded regions of the three NBT types.

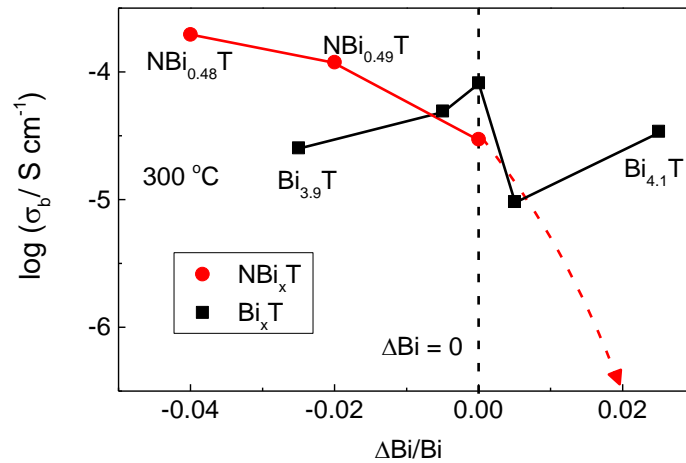


Figure 8-3. Bulk conductivity of selected NBTs and BiTs at 600 °C versus relative Bi non-stoichiometry in starting compositions.

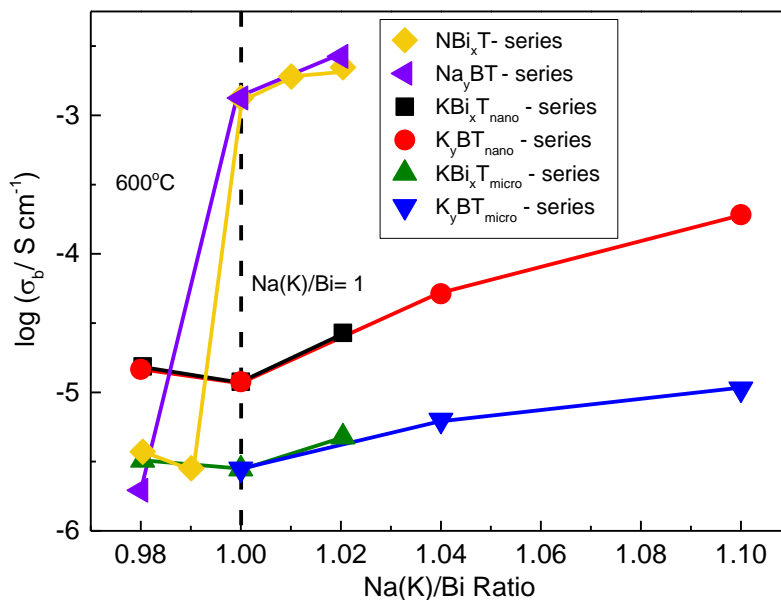


Figure 8-4. Bulk conductivity of A-site non-stoichiometric KBTs at 600 °C versus K/Bi ratio in starting compositions.

The origin of supreme oxide ion conduction in NBT has been discussed in Chapter 3 and 4 which is related to the cation polarisability, weak Bi-O bonds and local atomistic configurations.<sup>1</sup> KBT and BiT were initially chosen to study because they are both related to the perovskite structure and chemically similar to NBT. However, the results show that their electrical properties are significantly different to NBT and to each other.

For KBT, the Na ion in NBT is replaced by the K ion. As discussed in the literature

review, KBT has the same amount of Bi and a random distribution of A-site cations like in NBT.<sup>2</sup> However, the bulk conductivity of KBTs remain insulating compared to NBT with different A-site non-stoichiometry. The size difference between K and Na may be the key factor here which influences the oxide ion conduction.

NBT differs to (Ba,Sr)TiO<sub>3</sub>-related titanates both structurally and electrically, however, the phase transition sequence of KBT is more like (Ba,Sr)TiO<sub>3</sub> instead of NBT. The structure of KBT does not have any octahedral tilting, therefore the Bi ions in KBT has a normal coordination number rather than a reduced coordination number as in NBT.<sup>3</sup> As result the Bi-O bond length remain the same in KBT and stronger Bi-O bonds can be obtained. Secondly, the energy barrier for different types of saddle point in NBT has been calculated and the energy barrier for the Na-Bi-Ti saddle point is consistent with the experimental activation energy (at least below T<sub>m</sub>) which indicates it is the major pathway for oxygen migration.<sup>4</sup> Since K is much larger and heavier than Na, it is reasonable to predict that the energy barrier for the K-Bi-Ti saddle point is higher than the Na-Bi-Ti saddle point and leads to a lower oxide ion conduction in KBT. Apart from the size effect, K is also more difficult to process and more volatile than Na which may lead to a higher loss during processing. Since no K-rich phase has been observed even in K<sub>0.55</sub>BT, the true K content in the final sintered KBT ceramics is still unknown and could still be slightly K deficient.

On the other hand, BiT samples have a bulk conductivity similar to type 1 NBTs with an even lower activation energy. Again the A-site non-stoichiometry can only cause limited influence to the bulk conductivity of BiT. As discussed in Chapter 5, the insensitivity to A-site non-stoichiometry is mainly due to the existence of intrinsic defects which cannot be compensated by extra Bi<sub>2</sub>O<sub>3</sub> in the starting material. However, the pathway for oxygen migration and site of oxygen vacancies in BiT remain unknown. In the literature there is controversy about whether the oxygen vacancies exist only in

$[\text{Bi}_2\text{O}_2]^{2+}$  layer, perovskite block or both.<sup>5-7</sup> Therefore the oxygen ion migration pathway in BiT also has the possibility to be one or a combination of the perovskite blocks,  $[\text{Bi}_2\text{O}_2]^{2+}$  layers and the interface between the perovskite blocks and  $[\text{Bi}_2\text{O}_2]^{2+}$  layers. As shown in Figure 8-2 (b), the bulk conductivity and activation energy of BiT is very similar to type 1 NBT which may imply that the migration of oxygen ion of BiT is in a similar environment as in NBT, i.e. the perovskite blocks. However, computer modelling suggests that the energy barrier for Bi-Bi-Ti saddle point in NBT is very low,  $\sim 0.22$  eV.<sup>4</sup> However, this values does not agree with our experimental results which show an activation energy of  $0.6 \sim 0.7$  eV. It is also worth to note that at low temperature BiT possess a mixed p-type and oxide ion conduction which means the real activation energy for oxide ion conduction in BiT could be higher than the values observed in our experiments. Therefore neutron diffraction and TEM are required to determine the site(s) of the oxygen vacancies which is the key factor to understand the oxide ion conduction in BiT.

## References

1. Li, M. *et al.* A family of oxide ion conductors based on the ferroelectric perovskite  $\text{Na}_{0.5}\text{Bi}_{0.5}\text{TiO}_3$ . *Nat. Mater.* **13**, 31–5 (2014).
2. Isupov, V. A. Ferroelectric  $\text{Na}_{0.5}\text{Bi}_{0.5}\text{TiO}_3$  and  $\text{K}_{0.5}\text{Bi}_{0.5}\text{TiO}_3$  Perovskites and Their Solid Solutions. *Ferroelectrics* **315**, 123–147 (2005).
3. Otoničar, M., Škapin, S. D., Jančar, B., Ubič, R. & Suvorov, D. Analysis of the Phase Transition and the Domain Structure in  $\text{K}_{0.5}\text{Bi}_{0.5}\text{TiO}_3$  Perovskite Ceramics by In Situ XRD and TEM. *J. Am. Ceram. Soc.* **93**, 4168–4173 (2010).
4. He, X. & Mo, Y. Accelerated Materials Design of  $\text{Na}_{0.5}\text{Bi}_{0.5}\text{TiO}_3$  Oxygen Ionic

- Conductors Based on First Principles Calculations. *Phys. Chem. Chem. Phys.* **17**, 18035–18044 (2015).
5. Noguchi, Y., Miwa, I., Goshima, Y. & Miyayama, M. Defect Control for Large Remanent Polarization in Bismuth Titanate Ferroelectrics -- Doping Effect of Higher-Valent Cations --. *Jpn. J. Appl. Phys.* **39**, L1259–L1262 (2000).
  6. Hashimoto, T. & Moriwake, H. Oxygen vacancy formation energy and its effect on spontaneous polarization in  $\text{Bi}_4\text{Ti}_3\text{O}_{12}$ : A first-principles theoretical study. *Phys. Rev. B* **78**, 92106 (2008).
  7. Jovalekić, C., Pavlović, M., Osmokrović, P. & Atanasoska, L. X-ray photoelectron spectroscopy study of  $\text{Bi}_4\text{Ti}_3\text{O}_{12}$  ferroelectric ceramics. *Appl. Phys. Lett.* **72**, 1051–1053 (1998).

## 9. Conclusions

This project was focused on investigating the electrical properties of A-site, Bi-containing perovskite-based materials. The starting point of the project was based on following the previous work in our group performed by Dr. Ming Li on the A-site complex perovskite material  $\text{Na}_{0.5}\text{Bi}_{0.5}\text{TiO}_3$  (NBT) where it had been reported that NBT possesses surprising and pronounced bulk oxide ion conduction that is highly sensitive to low levels of A-site non-stoichiometry in the nominal starting composition.

This project began with a more extensive study on the NBT system regarding Na non-stoichiometry in undoped materials and the effect of dopants which include both acceptor- ( $\text{Mg}^{2+} \rightarrow \text{Ti}^{4+}$ ,  $\text{Na}_{0.5}\text{Bi}_{0.5}\text{Ti}_{1-x}\text{Mg}_x\text{O}_{3-x}$ ) and donor-doping ( $\text{Nb}^{5+} \rightarrow \text{Ti}^{4+}$ ,  $\text{Na}_{0.5}\text{Bi}_{0.5}\text{Ti}_{1-x}\text{Nb}_x\text{O}_{3+x/2}$ ). It has been shown that for un-doped NBT, the bulk conductivity (oxide ion conduction) is strongly dependent on the Na/Bi ratio in the nominal starting composition rather than a simple A-site rich/deficient concept. This is because of the different defect mechanisms for Na or Bi non-stoichiometry. In general, samples with a Na/Bi ratio  $\geq 1$  exhibit high, nearly pure oxygen ion conduction with a low activation energy ( $< 0.9$  eV) for bulk conduction, whereas samples with a Na/Bi ratio  $< 1$  are electronic insulators with a high activation energy ( $\sim 1.6$  eV) for bulk conduction. Mg acceptor doping on the Ti-site has limited solubility but it can further increase the oxide ion conduction by  $\sim 0.5$  an order of magnitude compared to  $\text{NB}_{0.48}\text{T}$ . Mg doping also extends the bulk electrolyte (oxide ion conduction) window to lower  $p\text{O}_2$  and reduces the required sintering temperature to obtain dense NBT ceramics. On the other hand, low levels of Nb donor doping ( $\geq 0.005$ ) are enough to minimise oxide ion conduction in NBT and leads to an n-type electronic predominated bulk conduction ( $t_{\text{ion}} \leq 0.07$ ) at elevated temperature,  $> 600$  °C. Further increases in Nb doping does not introduce any significant level of electronic conduction and Nb-doped NBT are excellent dielectric materials. It is worth to note that, a so called intermediate NBT

with mixed oxide ion and n-type conduction and  $t_{\text{ion}}$  close to half can be obtained by either starting with an extremely Bi-rich, un-doped NBT composition ( $\text{Bi} \geq 0.52$ ) or a very low level of Nb doping ( $0.002 \sim 0.003$ ).

A high level of oxide ion conduction has also been found in the Aurivillius phase  $\text{Bi}_4\text{Ti}_3\text{O}_{12}$  (BiT). Un-doped BiT shows mixed p-type and oxide ion conduction at low temperature but near pure oxide ion conduction around  $T_c$  ( $675^\circ\text{C}$ ). Unlike NBT, the Bi nonstoichiometry in BiT can only cause a limited variation in bulk conductivity. This is probably because the existence of intrinsic defects in BiT which is not generated by Bi-loss during processing. Different doping mechanisms have also been studied in BiT; isovalent doping ( $\text{La}^{3+} \rightarrow \text{Bi}^{3+}$ ,  $\text{Bi}_{4-x}\text{La}_x\text{Ti}_3\text{O}_{12}$ ), acceptor doping ( $\text{Sr}^{2+} \rightarrow \text{Bi}^{3+}$ ,  $\text{Bi}_{4-x}\text{Sr}_x\text{Ti}_3\text{O}_{12-2/x}$ ) on the Bi-site and donor doping ( $\text{Nb}^{5+} \rightarrow \text{Ti}^{4+}$ ,  $\text{Bi}_4\text{Ti}_{3-x}\text{Nb}_x\text{O}_{12+x/2}$ ) on Ti-site. La-doping can lower  $T_c$  and makes BiT a potentially good oxygen ion conductor at lower temperatures but it also systematically suppresses the bulk conductivity with increasing La content. Sr-doping on the Bi-site can also reduce  $T_c$  while maintaining the bulk conductivity. However, its solubility in BiT is rather limited. Nb-doping on the Ti-site behaves similar as that in NBT which can fill up oxygen vacancies and therefore suppress the oxide ion conduction without introducing any significant level of electronic conduction.

$\text{K}_{0.5}\text{Bi}_{0.5}\text{TiO}_3$  (KBT) also possesses a perovskite structure but the electrical properties are significantly different when compared to NBT. KBT has been determined to be a mixed ionic-electronic conductor but the ionic conduction can be dominated by proton conduction at lower temperatures ( $< 600^\circ\text{C}$ ). The proton conduction is controlled by the K/Bi ratio in the nominal starting composition. Samples with a K/Bi ratio  $> 1$  exhibit higher proton conductivity whereas samples with a lower K/Bi ratio  $\leq 1$  exhibit lower proton conduction. The oxide ion conduction in KBT is significantly lower than conducting NBT and nominal A-site non-stoichiometry has only a limited

influence on the electrical properties.

## 10. Future Work

The results obtained in this project reveal that both NBT and BiT are good oxygen-ion conducting electrolytes whereas KBT is a mixed conductor with mixed electronic-oxide ion and/or proton conduction. Among these three materials, the NBT system has been relatively well investigated. However, the crystal chemistry and polymorphism of NBT remains an issue to be fully resolved and this hinders a more complete understanding of its structure-composition-electrical property relationships and the possible oxide-ion conduction pathway(s). There are several interesting issues, including; what is the crystal structure and/or polymorphism around 320 °C (permittivity maximum and change of bulk conduction activation energy) and what is the significant crystal structure difference between conducting and insulating NBTs? Electrically it is worth to investigate the possibility to further increase the bulk oxide ion conduction, either by elemental doping (eg Ga for Ti) or by forming solid solutions with other perovskites (eg BiGaO<sub>3</sub>). Processing methods to reduce the grain boundary resistivity is an important topic in the development of NBT-based ceramic electrolytes that has not been investigated.

The EMF and <sup>18</sup>O TOF-SIMS diffusion results show that BiT is a good oxide ion conductor around T<sub>C</sub>. However, as discussed in Chapter 5 and 6, the Z\* plots of BiT are not as well resolved as in NBT and KBT and BiT ceramics are electrically heterogeneous. The absolute values of bulk conductivity for BiT at high temperature are still not clear and it would therefore be worthy to perform electrical measurements on single crystals.

The oxide ion conduction mechanism in BiT is another topic worthy of study. As discussed in Chapter 8, there is a lot of controversy existing in the literature (as discussed in the literature review) regarding the location of oxygen vacancies and the

location of dopants such as La within the structure.<sup>1-5</sup> The former is especially important here since it can provide information about the oxygen migration pathway, e.g. whether the oxygen ions migrate through the perovskite blocks or the  $[\text{Bi}_2\text{O}_2]^{2+}$  layers or the interface between them. Computer simulations suggest the energy required for oxygen migration is very high ( $\sim 1.6$  eV) which is certainly in clear disagreement with the results in this project.<sup>2</sup> Therefore structural and atomistic simulation studies are required in order to reveal the location of the oxygen vacancies or interstitials, the oxygen migration pathway and the energy barriers for different pathways to get a better understanding about the oxide ion conduction mechanism in BiT.

For KBT, it has been determined that its bulk ionic conduction can be dominated by a combination of oxide ions and proton conduction. However, it is rather hard to accurately measure the contribution from each mechanism since the proton conduction is highly sensitive to the  $\text{pH}_2\text{O}$  of the surrounding atmosphere at relatively low temperatures ( $< 600$  °C). Therefore, it is worth to quantify the contribution from different charge carriers, i.e. oxide ion, proton and electron/hole.  $^{18}\text{O}$  diffusion via TOF-SIMS can be used to calculate the oxide ion conduction and EMF measurements with controlled  $\text{pO}_2$  and  $\text{pH}_2\text{O}$  can be used to estimate the proton conduction.

As discussed in Chapter 8, structural and computer simulation studies are required to obtain information such as the favoured site(s) for oxygen vacancies, the energy barrier(s) for oxygen migration and saddle points in order to explain why oxide ion conduction readily exists in NBT but is less favourable in KBT.

The results obtained in this project reveal that both NBT and BiT are potentially good oxygen-ion conducting electrolytes. Therefore it is worth to start investigating applications (e.g. SOFC) based on these new electrolyte materials. From a more

general point of view, since A-site Bi benefits oxide ion conduction in perovskite and related materials, other Bi-containing oxides are worth investigating for their potential to be used as electrolytes (pure oxide ion conductor) or electrodes (mixed oxide ion conductor) for various applications.

## References

1. Vannier, R., Mairesse, G., Abraham, F. & Nowogrocki, G. Double substitutions in  $\text{Bi}_4\text{V}_2\text{O}_{11}$ . *Solid State Ionics* **70–71**, 248–252 (1994).
2. Snedden, A., Lightfoot, P., Dinges, T. & Islam, M. S. Defect and dopant properties of the Aurivillius phase  $\text{Bi}_4\text{Ti}_3\text{O}_{12}$ . *J. Solid State Chem.* **177**, 3660–3665 (2004).
3. Hashimoto, T. & Moriwake, H. Oxygen vacancy formation energy and its effect on spontaneous polarization in  $\text{Bi}_4\text{Ti}_3\text{O}_{12}$ : A first-principles theoretical study. *Phys. Rev. B* **78**, 92106 (2008).
4. Jovalekić, C., Pavlović, M., Osmokrović, P. & Atanasoska, L. X-ray photoelectron spectroscopy study of  $\text{Bi}_4\text{Ti}_3\text{O}_{12}$  ferroelectric ceramics. *Appl. Phys. Lett.* **72**, 1051–1053 (1998).
5. Park, B. H. *et al.* Differences in nature of defects between  $\text{SrBi}_2\text{Ta}_2\text{O}_9$  and  $\text{Bi}_4\text{Ti}_3\text{O}_{12}$ . *Appl. Phys. Lett.* **74**, 1907–1909 (1999).